Imaging the Earth's near surface with dense seismic observation

Thesis by

Yan Yang

In Partial Fulfillment of the Requirements for
the degree of
Doctor of Philosophy

CALIFORNIA INSTITUTE OF TECHNOLOGY
Pasadena, California

2025
Defended July 8, 2024

Yan Yang
ORCID: 0000-0002-6105-2918

To my grandparents.

ACKNOWLEDGEMENTS

I am deeply grateful for the past five years at the Caltech Seismo Lab, where I had the privilege of working with welcoming, talented individuals.

I thank my Ph.D. advisor, Zhongwen, for being a knowledgeable, innovative, optimistic, critical, respectful, and supportive mentor, as well as a role model seismologist. I thank my advisor, Rob, for guiding me with his invaluable experience and wisdom in geophysics and geology, and for always providing effective emotional support. I thank my advisor, Zach, for introducing me to the cutting-edge field of machine learning with his numerous brilliant ideas. Outside the Seismo Lab, I am also thankful to Ruby for generously sharing her time and insights to help me with my research projects and career development.

In addition to the faculty I have directly worked with, I appreciate learning from Jennifer, Nadia, Mike, Mark, Joann, Jean-Philippe, and Allen during courses, seminars, and coffee hours. Special thanks to the Seismo Lab staff, especially Donna, Kim, and Priscilla, for making my life much easier.

I am fortunate to have met wonderful people who have enriched my Ph.D. experience. My fellow cohorts: Ojashvi, Jimmy, Kai, and Ben; my weekend dinner carpool: Yida, Cijin, Jiaqi, and Mo; my officemates: Jack, Olivia, Vasilije, and Rajani. I value the academic and social interactions I've had over the years with Voon, Zhe, Xin, Ethan, Ettore, Jack, Jorge, Jiuxun, Zefeng, Wenbo, Zhichao, Jiaxuan, Hongyu, Caifeng, Valeria, Qian, Wei, Pond, Auden, Eli, and many other peers. I appreciate the tremendous help from Zhigang, Sunny, and Weiqiang during my job applications.

Finally, I want to express my deepest gratitude to my family. As an only child, my parents have given me their full love and have been immensely supportive throughout my years of schooling. My husband, Qiushi, has always brought me positive energy, making me happier every day over the past eight years.

ABSTRACT

Understanding the Earth's near surface is critical for assessing seismic hazards and ensuring environmental sustainability. In this thesis, I explore the use of advanced observation and analysis techniques for near-surface imaging with big seismic data.

Chapters 2-6 focus on the applications of Distributed Acoustic Sensing (DAS). DAS is an emerging sensing technology that transforms fiber-optic cables into dense seismic arrays. In Chapter 2, I introduce a high-performance Python tool for computing seismic ambient noise cross-correlation with large volumes of DAS data. In Chapter 3, I perform ambient noise tomography using a DAS array in Ridgecrest, California, to resolve spatial variation of the near-surface structure, revealing its correlation with earthquake ground shaking amplification. In Chapter 4, I use surface wave scattering observed in the DAS noise cross-correlation for fault zone detection and characterization. In Chapter 5, I analyze three years of DAS noise cross-correlation to monitor seismic velocity changes, providing insights into vadose zone soil moisture dynamics and water resource management in the context of climate change. In Chapter 6, I use a DAS array at the South Pole to characterize firn structure for a better understanding of cryosphere mass balance.

Chapters 7 and 8 focus on imaging geological structures in the urban Los Angeles region using dense arrays of geophones. Chapter 7 uses converted S-to-p phases recorded by a dense network of low-cost accelerometers to map the basin depth. Chapter 8 investigates shallow seismicity in the Long Beach area to illuminate complex fault structures.

In Chapters 9 and 10, I apply a state-of-the-art machine learning framework known as a neural operator for solving seismic wave equations. The trained neural operator enables full seismic waveform modeling with substantial advancements over conventional numerical techniques including its fast speed, generalizability, and convenient differentiability for full waveform inversion.

PUBLISHED CONTENT AND CONTRIBUTIONS

* indicates equal contribution.

Shen, Z.*, **Yang, Y.***, Fu, X., Adams, K. H., Biondi, E., & Zhan, Z. Fiber-optic seismic sensing of vadose zone soil moisture dynamics. *Nature Communications.* (Accepted).
Y.Y. participated in the conception of the project, developed the methodology, analyzed the data, made the figures, and wrote the manuscript.

Yang, Y., Zhan, Z., Karrenbach, M. H., Reid-McLaughlin, A., Biondi, E., Wiens, D. A., & Aster, R. C. (2024). Characterizing South Pole Firn Structure with Fiber Optic Sensing. *Geophysical Research Letters*, 51, e2024GL109183. https://doi.org/10.1029/2024GL109183
Y.Y. participated in the conception of the project, developed the methodology, analyzed the data, made the figures, and wrote the manuscript.

Yang, Y., Gao, A. F., Azizzadenesheli, K., Clayton, R. W., & Ross, Z. E. (2023). Rapid Seismic Waveform Modeling and Inversion With Neural Operators. *IEEE Transactions on Geoscience and Remote Sensing*, 61, 1–12. https://doi.org/10.1109/TGRS.2023.3264210
Y.Y. participated in the conception of the project, developed the methodology, analyzed the data, made the figures, and wrote the manuscript.

Yang, Y., & Clayton, R. W. (2023). Shallow Seismicity in the Long Beach–Seal Beach, California Area. *Seismological Research Letters*. https://doi.org/10.1785/0220220358
Y.Y. participated in the conception of the project, developed the methodology, analyzed the data, made the figures, and wrote the manuscript.

Yang, Y., Zhan, Z., Shen, Z., & Atterholt, J. (2022). Fault Zone Imaging With Distributed Acoustic Sensing: Surface-To-Surface Wave Scattering. *Journal of Geophysical Research: Solid Earth*, 127(6), e2022JB024329. https://doi.org/10.1029/2022JB024329
Y.Y. participated in the conception of the project, developed the methodology, analyzed the data, made the figures, and wrote the manuscript.

Yang, Y., Atterholt, J. W., Shen, Z., Muir, J. B., Williams, E. F., & Zhan, Z. (2022). Sub-Kilometer Correlation Between Near-Surface Structure and Ground Motion Measured With Distributed Acoustic Sensing. *Geophysical Research Letters*, 49(1), e2021GL096503. https://doi.org/10.1029/2021GL096503
Y.Y. participated in the conception of the project, developed the methodology, analyzed the data, made the figures, and wrote the manuscript.

Yang, Y.*, Gao, A. F.*, Castellanos, J. C.*, Ross, Z. E., Azizzadenesheli, K., & Clayton, R. W. (2021). Seismic Wave Propagation and Inversion with Neural Operators. *The Seismic Record*, 1(3), 126–134. https://doi.org/10.1785/0320210026
Y.Y. participated in the conception of the project, developed the methodology, analyzed the data, and made the figures.

TABLE OF CONTENTS

Chapter 1

INTRODUCTION

Earth’s near surface, the top tens of meters of the upper crust, is a dynamic zone undergoing rapid spatiotemporal changes due to a variety of environmental and human interactions. Understanding the Earth's near surface is crucial for assessing seismic hazards and ensuring environmental sustainability. Seismic imaging, which converts recorded seismic waves into detailed images of the Earth’s interior, is a vital tool in this endeavor. Accurately resolving the near surface requires high-density, high-frequency seismic observation, which faces challenges such as high costs, logistical difficulties, and computational burdens.

To address these challenges, solutions have been proposed for both seismic sources and receivers. Ambient noise interferometry, a well-established technique, uses long-period natural vibrations or high-frequency anthropogenic noise to turn receivers into virtual sources, providing low-cost, noninvasive, repetitive seismic sources. The emerging technique of distributed acoustic sensing (DAS) repurposes telecommunication fibers into meter-spacing strain sensors, offering dense coverage and continuous monitoring in urban, subsea, and glacial environments. With advances in these cost-effective seismic sources and receivers, near surface imaging and monitoring can be achieved at unprecedented resolution.

Handling the vast amount of data from dense seismic observation requires enhanced computational capabilities and advanced algorithms to extract useful information. Machine learning has emerged as a promising approach to overcome these computational challenges, facilitating tasks such as phase picking, data compression, and detecting unseen patterns.

In this thesis, I focus on improving our understanding of the near surface using dense seismic observation including DAS data and advanced data analysis techniques such as machine learning. Although the topics may appear diverse, the chapters are organized purposefully.

I begin with Chapter 2, where I present a high-performance Python tool that leverages PyTorch to accelerate noise cross-correlation workflow using graphic processing unit (GPU) setups. The computation of ambient noise cross-correlation for large volumes of DAS data is fundamental for most passive imaging and monitoring tasks, yet it is the most time-consuming step. The tool I provide in Chapter 2 forms the basis for the work in Chapters 3-5, and it is also versatile enough to be adapted to any seismic dataset.

After the 2019 M7.1 Ridgecrest earthquake, a telecommunication fiber-optic cable across the city of Ridgecrest was converted into an 8-km DAS array. The array has been operational for five years and is still operational today, providing long-term, high-quality, continuous recordings, including aftershocks and anthropogenic noise. This valuable ambient noise data has been used in Chapters 3-5. In Chapter 3, I use noise cross-correlation to image the near-surface structure along the fiber path at high resolution, which can readily explain the lateral variations in earthquake shaking amplification at sub-kilometer scales. In Chapter 4, I report the observation of surface wave scattering in the noise cross-correlation. I use the scattered waves to detect small faults and characterize their properties. In Chapter 5, I use years of noise cross-correlation data to map seismic velocity changes over large spatiotemporal scales. The results provide a new method for monitoring vadose zone soil moisture dynamics, capturing sub-seasonal precipitation events and prolonged drought conditions, quantifying vadose zone water loss during the drought.

In addition to the use of urban dark fibers, DAS is unlocking new field measurements in harsh and remote environments. In Chapter 6, I shift focus to a DAS array at the South Pole, using both ambient noise and active seismic sources. I study the seismic velocity profile of the firn (compacted snow layers) to improve firn density estimation for the East Antarctic region, which is crucial for understanding cryosphere mass balance and climate change impacts.

I turn to dense seismic observation of local earthquakes in urban settings in Chapters 7 and 8. In Chapter 7, I analyze converted seismic phases observed by a dense network of low-cost strong-motion sensors to map the depth of the Los Angeles (LA) basin. In Chapter 8, I detect and locate seismicity using dense nodal arrays in the Long Beach area to reveal the complex nature of shallow faults and their associated seismic hazards.

The case studies of dense seismic observation presented in Chapters 3-8 are primarily limited to phase information. Fully exploiting seismic data requires considering the full complexity of wave propagation, which comes at great computational expense, especially for higher frequencies.

To address this challenge, in Chapters 9 and 10, I explore a state-of-the-art machine learning concept known as a neural operator. I present a prototype framework for accelerated simulation of seismic wave propagation using this paradigm. The results demonstrate the accuracy, efficiency, and generalizability of this novel method for full waveform modeling. This method also enables automatic differentiation for convenient full-waveform inversion.

Chapter 2

A PYTHON TOOL FOR SEISMIC AMBIENT NOISE WITH DAS DATA ON MULTIPLE GPUS

Abstract

We introduce a Python tool designed for ambient noise seismology with Distributed Acoustic Sensing (DAS) data on both central processing unit (CPU) and graphic processing unit (GPU) platforms. This development aims to tackle the high computation arising from processing vast volumes of DAS data. Our code leverages the advanced features of the modern PyTorch package. It is user-friendly and optimizes both preprocessing and cross-correlation tasks, showing significant acceleration when utilizing GPUs compared to CPU-only computations. We also provide postprocessing tools including surface wave dispersion analysis and seismic velocity change measurements. While we demonstrate the code's capabilities using a public DAS dataset, it's versatile enough for adaption to any seismic dataset.

2.1 Introduction

Ambient noise cross-correlation stands as a cornerstone technique in modern seismology. By cross-correlating continuous noise signals recorded at different stations, empirical Green's functions are extracted (Shapiro & Campillo, 2004; Shapiro et al., 2005; Snieder, 2004). Its well-established applications offer invaluable insights into the dynamic processes shaping our planet, spanning from detailed structural imaging of the near-surface to upper mantle (Diez et al., 2016; Lin et al., 2013; Nakata et al., 2015; Yao et al., 2006), to monitoring temporal changes in subsurface properties (Clements & Denolle, 2018; Illien et al., 2021; Mao et al., 2022; Mordret et al., 2016; Sens-Schönfelder & Wegler, 2006; Wang et al., 2017).

The demand for near-surface imaging requires high-frequency noise cross-correlation, which necessitates "Large-N" arrays characterized by dense deployments with high sampling rates. On the other hand, prolonged subsurface monitoring calls for "Large-T" arrays designed for extended durations, sometimes spanning years. Distributed acoustic sensing (DAS) is an emerging technique that can turn preexisting telecommunication fiber-optic cables into cost-effective, long-term, dense seismic arrays (Lindsey & Martin, 2021; Parker et al., 2014; Zhan, 2020). Ambient noise imaging and monitoring with DAS has been shown successful in near-surface imaging (Cheng et al., 2021; Dou et al., 2017; Martin et al., 2021; Spica et al., 2020; Tribaldos et al., 2019; Yang, Atterholt, et al., 2022) and subsurface monitoring (Rodríguez Tribaldos & Ajo-Franklin, 2021; Yang & Zhan, 2022). Given the large spatial and temporal size inherent in DAS recordings, the computation of noise cross-correlations for DAS becomes a data-intensive task, underscoring the need for efficient computational tools (Martin, 2021).

Ambient noise cross-correlation has been implemented through a myriad of tools and platforms, evolving from low-level languages like C and Fortran (Bensen et al., 2007; Herrmann, 2013) to more modern vectorized languages like Python, MATLAB, and Julia (Clements & Denolle, 2020; Jiang & Denolle, 2020; Lecocq et al., 2014; Makus & Sens-Schönfelder, 2024). This shift is driven by the ease of use, flexibility, and the expansive ecosystems of libraries and tools these languages offer, for example, NumPy (Harris et al., 2020), SciPy (Virtanen et al., 2020), and ObsPy (Beyreuther et al., 2010). Another notable change in the field has been the move from central processing unit (CPU) to graphic processing unit (GPU), enhancing the efficiency of the cross-correlation step (Clements & Denolle, 2020; Fichtner et al., 2017). Amidst these transitions, the central challenge has always been navigating the tradeoff between computational efficiency and development agility. In this context, PyTorch stands out (Paszke et al., 2019). PyTorch, built mainly on C++ but with a Python interface, is a well-established framework in the machine learning community for processing large datasets, renowned for its optimized computing capabilities and performance-driven design. It not only addresses the efficiency-agility tradeoff but also offers a versatile computing environment. Unlike CUDA, which is limited to NVIDIA GPUs, PyTorch is adaptable, running on CPUs, NVIDIA GPUs, and even non-NVIDIA GPUs. Its native support for multi-GPU acceleration further amplifies its suitability for data-intensive tasks like ambient noise cross-correlation.

In this chapter, we present a Python tool that leverages PyTorch for ambient noise cross-correlation. Utilizing the public Ridgecrest DAS dataset hosted by the Southern California Earthquake Data Center (SCEDC) on Amazon Web Services (AWS), we illustrate the code's workflow and validate the effectiveness of our cross-correlation results. Furthermore, our package provides integrated tools for subsequent analyses, including dispersion analysis and velocity change (dv/v) measurements derived from the computed cross-correlation functions.

2.2 Workflow

Ambient noise cross-correlation is typically characterized by a structured workflow, which can be broadly divided into two primary phases: preprocessing and cross-correlation (Bensen et al., 2007; Clements & Denolle, 2020; Fichtner et al., 2017). Following the cross-correlation, the derived noise correlation functions (NCFs) can be used for further analyses, such as dispersion analysis or dv/v measurements. A schematic representation of our general workflow is in Figure 2.1, with detailed introductions provided in the subsequent sections.

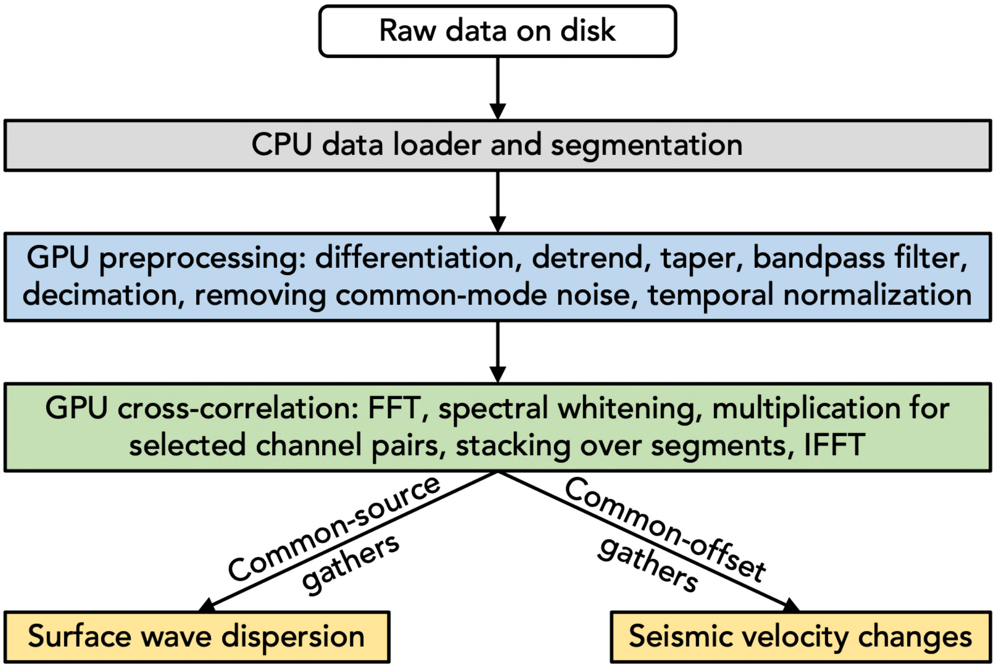

Figure 2.1: The workflow of seismic ambient noise analysis with DAS data: preprocessing, cross-correlation, and postprocessing.

2.2.1 Preprocessing

The package can read raw DAS data stored on disk in formats such as SEG-Y, SAC, H5, or custom formats with defined function to read data. Once read into CPU memory, the data is reshaped into segments of the desired length and then transferred to the chosen computing device, either CPUs or GPUs, depending on the configuration. This transition between computational environments, such as moving data between CPUs and GPUs, is handled seamlessly and efficiently using PyTorch (Paszke et al., 2019).

Preprocessing is an essential step in ambient noise cross-correlation. Its primary aim is to emphasize broad-band ambient noise through minimizing the influence of earthquake signals and instrumental irregularities that can mask the ambient noise. Standard preprocessing steps include removing instrument response, demeaning, detrending, applying a band-pass filter, temporal normalization, and spectral whitening (Bensen et al., 2007). When dealing with DAS data, we integrate two supplementary steps. At the very first step, if the raw data is strain, we differentiate strain to yield strain rate, effectively eliminating steps in the waveform caused by fading (e.g., Figure 2.5 in Willis et al., 2021). After all the single-trace based preprocessing, we detrend across the channel axis to eliminate common-mode noise. This is crucial as it significantly reduces the strong energy at a 0-time lag in the resulting NCFs (e.g., Figure 2.8 in Willis et al., 2021). All preprocessing tasks are implemented using the PyTorch package (Paszke et al., 2019), allowing fast implementation on either CPU or GPUs. We have placed the spectral whitening step—typically the final step of preprocessing—within the cross-correlation phase. By executing it between the Fast Fourier Transform (FFT) and Inverse Fast Fourier Transform (IFFT) operations, we achieve greater computational efficiency.

2.2.2 Cross-correlation

After preprocessing, we proceed to the cross-correlation, which is usually the most computationally intensive step and typically scales quadratically with respect to both the number of channels and the number of time steps. Typically, to expedite the process, calculations are performed in the frequency domain, taking advantage of the efficiency of the FFT. The Fourier spectrum is computed using the torch.fft.rfft module, which computes discrete Fourier transforms via the real FFT, offering a speed advantage over conventional FFTs. We then perform the spectral whitening, which enhances the signal-to-noise ratio by equalizing the amplitude spectrum. For selected channel pairs that we want to cross-correlate, we multiply the whitened Fourier transform of the first signal by the complex conjugate of the whitened Fourier transform of the second signal, the cross-spectrum is stacked in the frequency domain over desired time periods and finally transformed back to the time domain to produce the noise NCFs. Post-IFFT, the two-sided time-domain NCFs is generated, adhering to a specified maximum lag time. Notably, the entire process in PyTorch is streamlined and the individual functions can be easily modified, making it accessible even for those new to the framework.

In the cross-correlation phase, we maintain flexibility in the selection of channel pairs for correlation and the stacking intervals. For example, in the context of dispersion analysis, we may want to use common-source NCFs for a better track of phase velocities. Conversely, for dv/v analysis, cross-correlations cannot be indiscriminately stacked over extended periods. Rather, there's a need to retain NCFs that are stacked at more frequent intervals—weekly, daily, or even hourly. This frequent stacking, while beneficial for analysis, presents a storage challenge. To address this, rather than processing all potential channel pairs, a more strategic approach can be adopted. By focusing solely on cross-correlating those with common offsets, we can achieve a more storage-efficient method but also retain the spatial resolution essential for accurate dv/v measurements.

2.2.3 Phase velocity dispersion analysis

Surface wave dispersion is one of the most important applications of computed NCFs. We offer functions to measure phase velocity dispersion using a beamforming approach. For any given channel within the DAS array, we construct a common-source gather of NCFs. A subarray of proximate channels are taken as receivers and any distant channel can be a virtual source. The NCFs are then bandpass filtered into successive narrow frequency bands. For a given phase velocity, we employ the shift-and-stack method to calculate the stacked energy corresponding to this velocity. By applying this method across successive narrow frequency bands and velocities, we can construct a frequency-velocity image that shows the stacked energy for each frequency-velocity pairing. The dispersion curve is determined through an auto-search algorithm, which identifies the optimal local phase velocity that aligns with the local maximum energy in the frequency-velocity image. By taking multiple virtual sources, we can produce several measurements of the dispersion curves. This approach yields an averaged representation of the curve and offers a method to gauge the uncertainty associated with these measurements.

2.2.4 dv/v measurements

Coda wave interferometry (CWI) is a technique commonly used to measure small changes in seismic velocity (dv/v) by analyzing the coda waves that follow the direct seismic arrivals across consecutive days or months (Mao et al., 2022; Obermann et al., 2013; Snieder, 2004). While CWI is highly sensitive to small changes in the medium, it relies on scattered waves that can be influenced by numerous factors, making the interpretation of results complex. In contrast, ballistic wave interferometry uses direct, unscattered seismic waves that travel along predictable paths, reducing the ambiguity associated with scattered wave paths (Mordret et al., 2020). The fine channel spacing of DAS enables the use of direct high-frequency surface waves for dv/v measurements, resolving changes in the top few meters. Recent research indicates that subsurface velocity changes in the top few meters, as measured by high-frequency waves, can exhibit variations of several percent (Qin et al., 2022; Rodríguez Tribaldos & Ajo-Franklin, 2021). These variations are discernible even in the early arrivals of direct surface waves. Such changes can be measured through cross-spectrum of NCFs over consecutive time periods. We provide a simple function to calculate cross-spectrum of direct waves in the NCFs. This method involves analyzing the phase differences between pairs of seismic signals for a certain frequency band. By computing the cross-spectrum of these signal pairs, phase shifts can be extracted, which are directly related to the time delays between the signals. These time delays, in turn, provide an estimate of the relative velocity change.

2.3 Performance and example

We evaluated the performance of our package for preprocessing and cross-correlation computation using various computational setups. For preprocessing, we compared CPU implementations using NumPy and SciPy, as well as both CPU and GPU implementations using PyTorch. The tests were performed on a randomly generated dataset with a size of (300, 180000), representing 300 channels at 50 Hz over one hour.

For cross-correlation, prior Python-based packages, such as SeisMIC (Makus & Sens-Schönfelder, 2024) and NoisePy (Jiang & Denolle, 2020), have implemented the Fast Fourier Transform (FFT) using NumPy and SciPy. In our performance evaluation, we compared the speed of cross-correlation using NumPy, SciPy, and PyTorch. All tests were conducted on the same random dataset, and cross-correlation was performed for 1,000 random channel pairs. The key difference among the tests was the implementation of the FFT process: numpy.fft.rfft, scipy.fft.rfft, and torch.fft.rfft. For PyTorch, we conducted evaluations on both a single CPU and a single GPU.

Figure 2.2 illustrates the time taken for preprocessing and cross-correlation. While the computation times for the three packages on the CPU were relatively consistent, with PyTorch slightly outperforming the others, the GPU implementation of PyTorch demonstrated a speedup of approximately three orders of magnitude. This significant enhancement highlights the potential for substantial optimization in the most computationally demanding step of cross-correlation. The tests were conducted on an Intel Xeon Gold 6230 CPU and an NVIDIA Tesla P100 GPU with 16 GB of video random access memory (VRAM).

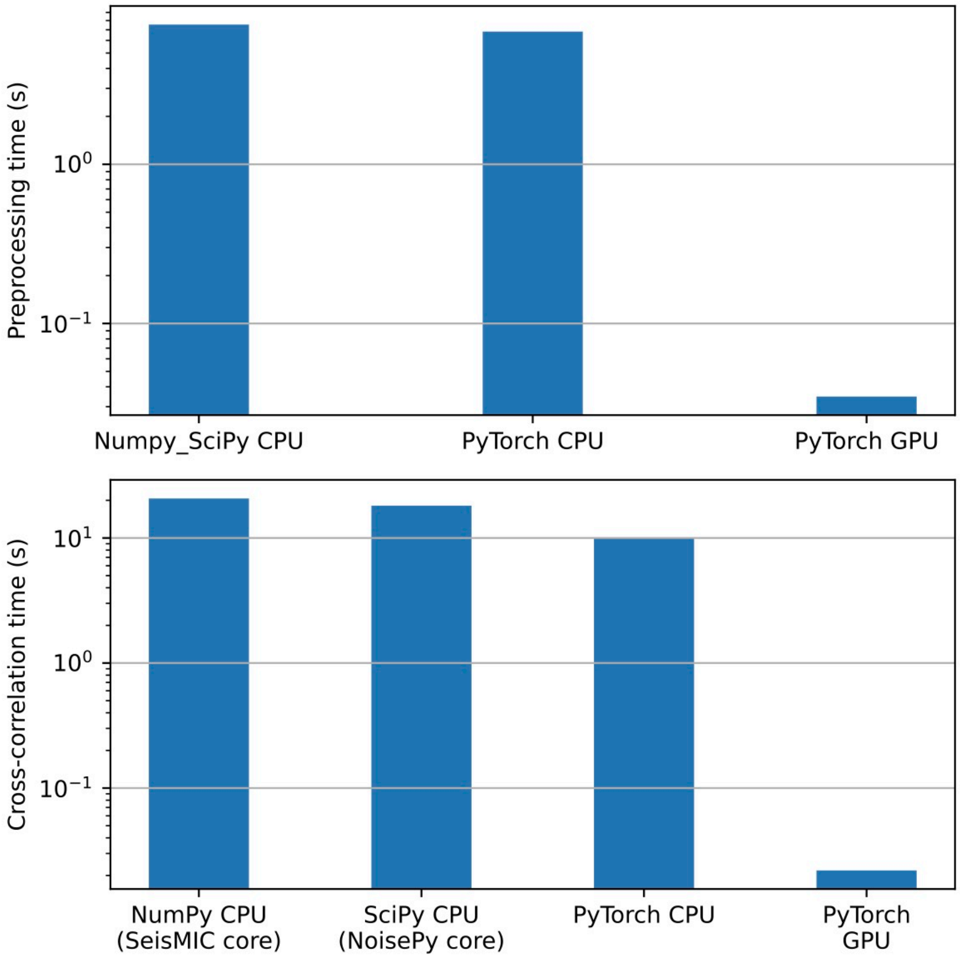

Figure 2.2: Comparison of computation speeds using NumPy, SciPy, and PyTorch on a single CPU and a single GPU. The preprocessing time is measured for data with 300 channels and 180,000 samples (50 Hz for 1 hour). The cross-correlation time is measured for 1,000 random channel pairs with a 30-second time lag.

We apply the Python code to a publicly available DAS dataset hosted by SCEDC. This data was recorded between 2020/06/23 and 2020/07/29 along a fiber-optic cable running between Ridgecrest and Inyokern airport. We compute NCFs following the workflow described above. Figure 2.3 shows the common-source gather of NCFs. Notable are the signals of moving vehicles at approximately 20 m/s and surface waves ranging from 200 to 1,000 m/s.

Body waves and fault zone scattered surface waves are discernible on some sections, as detailed by Atterholt et al., (2022) and Yang, Zhan, et al., (2022).

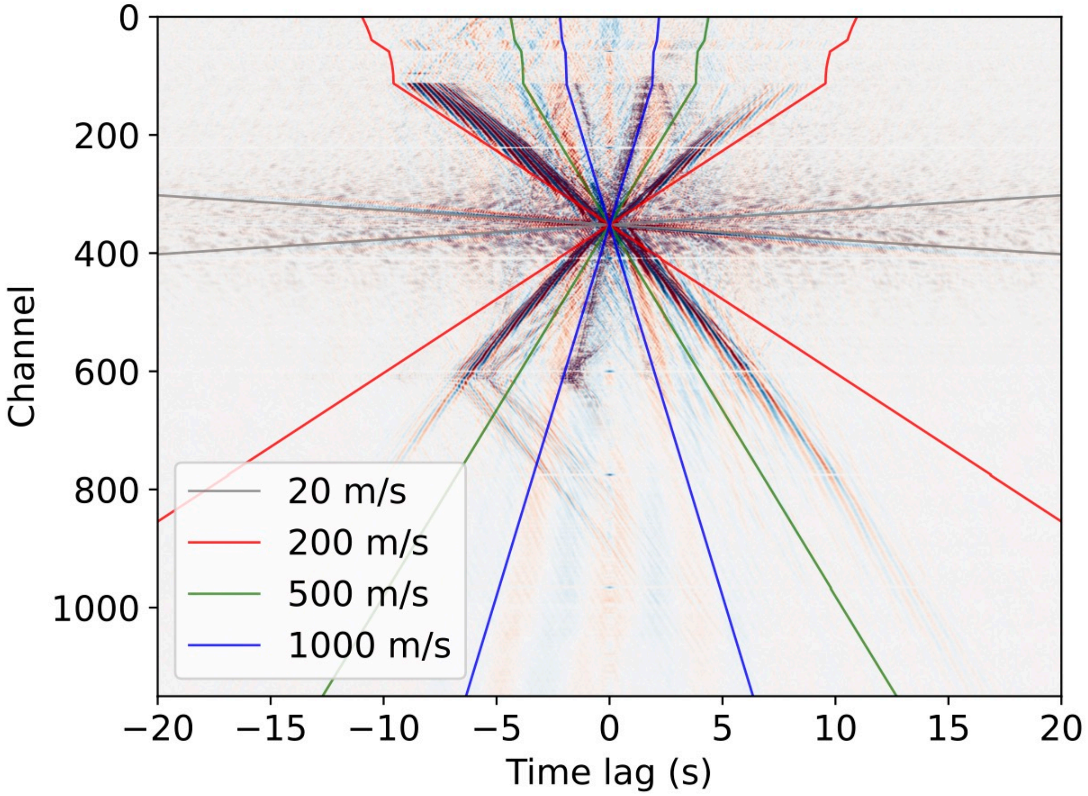

Figure 2.3: Stack of one-month NCFs from the Ridgecrest DAS array. Travel times corresponding to group velocities ranging from 200 m/s to 1 km/s are indicated by colored lines.

For further analysis on the NCFs, we employed the beamforming technique for surface wave dispersion on the computed NCFs. Figure 2.4 illustrates a sample waveform, the computed frequency-velocity energy image at 1-10 Hz, and the automatically tracked dispersion curve. The detailed subsurface model derived from the dispersion analysis across the entire array has shown strong correlation with the site amplification during earthquakes (Yang, Atterholt, et al., 2022).

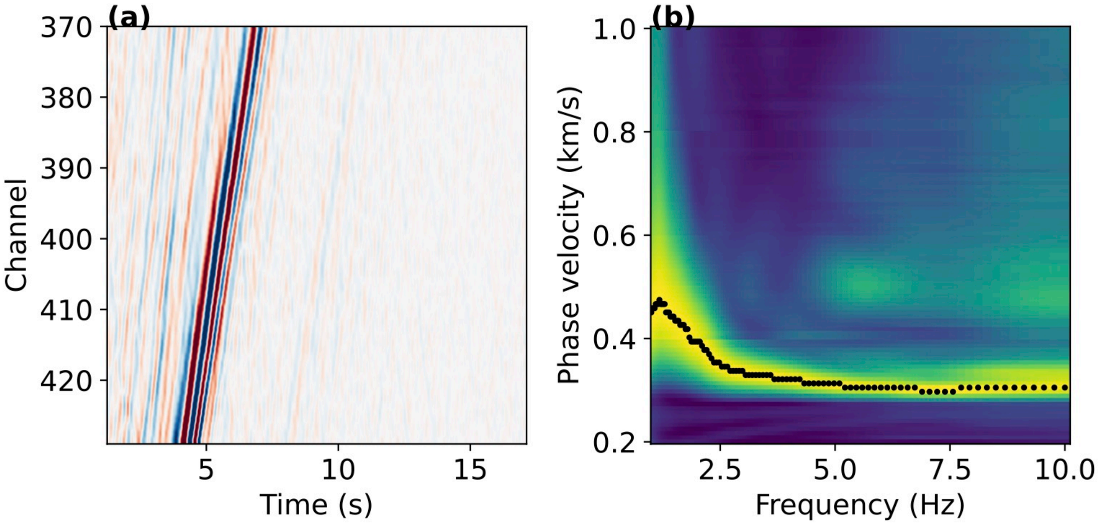

Figure 2.4: Applications on the computed common-source NCFs. (a) A subarray of common-source NCFs for local phase velocity measurements. (b) Rayleigh wave phase velocity dispersion measured by the beamforming approach.

To validate the dv/v measurements, we constructed a synthetic dataset by introducing a 1% dt/t variation to the NCF. These synthetic daily NCFs were further modified with 20% peak-to-peak noise. A 1-second window was used for the cross-spectrum analysis. The measurements closely matched the ground truth, as shown in Figure 2.5. For real data, we applied the method to 1.5 years of DAS data from June 2021 to December 2022. The seasonal variation of dv/v is clearly visible, and the measurements are consistent across nearby channel pairs (Figure 2.6).

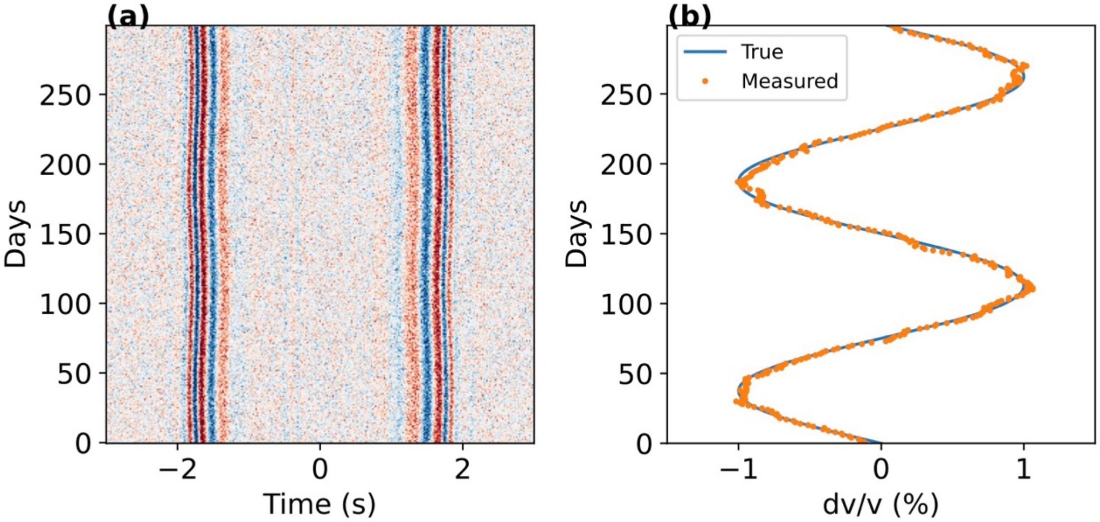

Figure 2.5: Applications on the synthetic NCFs. (a) A synthetic dataset representing daily stacked NCFs, which is made up with 1% dt/t in a sinusoidal shift and added with 20% noise. (b) dv/v measured by cross-spectrum approach compared with the true dv/v in the synthetic data.

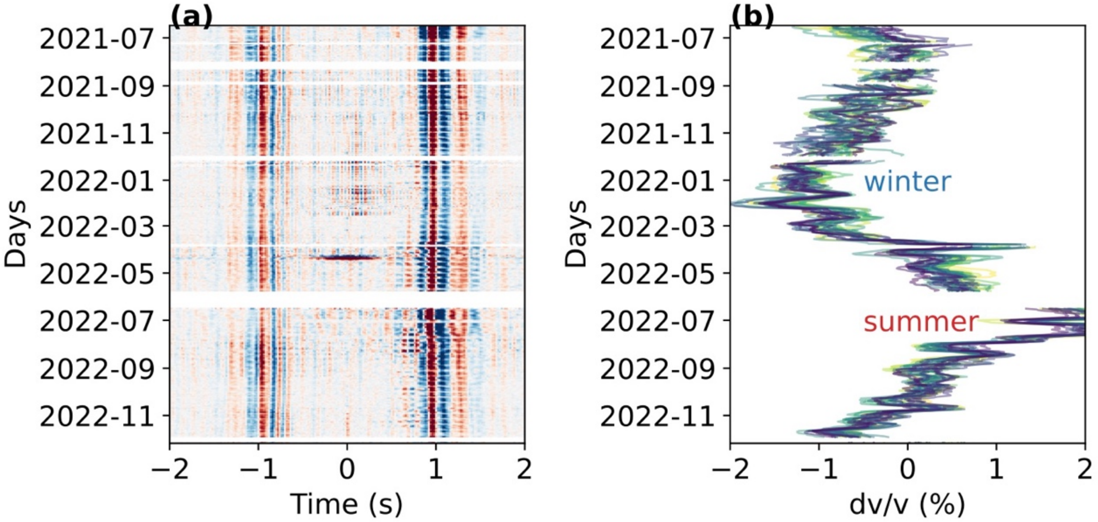

Figure 2.6: Applications on the computed common-offset NCFs. (a) A real dataset representing daily stacked NCFs between channel 200 and 230. (b) dv/v measured for 25 common-offset channel pairs around channel 200.

2.4 Discussion

The speed of our code largely benefits from PyTorch. Originating from the machine learning domain, PyTorch has been renowned for its adeptness in managing and processing extensive datasets. Its architecture is optimized for high-performance computations, making it an ideal choice for tasks like cross-correlation in frequency domain. Python, as a vectorized language, offers versatility and user-centric design. Its open-source nature, coupled with a vast library ecosystem, provides a platform for researchers to modify and adapt code according to their own research needs. When Python's flexibility is combined with PyTorch's computational capabilities, we aim to offer a tool that is both functional and adaptable. Researchers are not just limited to using predefined functions; they can expand and modify, tailoring the code to address specific challenges. As the seismology community continues to grow and diversify, there will be an increasing demand for tools that are accessible to both experienced researchers and those new to the field. We hope our code, with its user-friendly design, sets a precedent for future software developments, emphasizing the importance of both efficiency and adaptability.

DAS datasets are inherently large, often encompassing thousands of channels and boasting high sampling rates. Such datasets present not only computational challenges, but also intricate issues related to data transfer. This transfer process includes moving data between CPU and GPU memory and managing input/output (I/O) operations between the disk and memory. While GPU-based cross-correlation is remarkably fast, the time taken to transfer data from the CPU to the GPU can offset the computational speed gains. Therefore, it's crucial to design these transfers based on specific needs. A balanced approach is essential: raw data files shouldn't be so small that they necessitate excessive I/O operations, nor so large that they consume an inordinate amount of memory in CPU to GPU transfer. We advocate for the use of Solid-State Drives (SSDs) during processing, as they can significantly expedite data read/write operations, thereby alleviating some of the challenges associated with data transfer. Our package is designed to work efficiently on servers with multiple CPUs and GPUs. As the field of big-data seismology grows, cloud computing emerges as a promising solution to circumvent extensive data transfers. In recent years, there's been a noticeable trend in seismology research towards leveraging cloud system for processing voluminous seismic datasets (MacCarthy et al., 2020; Ni et al., 2021; Zhu et al., 2023).

While our tool only offers basic functions for dispersion analysis and dv/v measurements, the Python ecosystem has a variety of specialized packages for more advanced seismological analyses. For dispersion analysis, methods such as multi-channel analysis of surface waves, frequency–wavenumber transform, and frequency–Bessel transform, have been extensively documented and implemented in various Python packages (Fichtner et al., 2023; Jiang & Denolle, 2020; Li et al., 2021). Similarly, for dv/v measurements, techniques like the windowed cross correlation, trace stretching, moving window cross spectrum, and wavelet-based methods offer refined insights (Jiang & Denolle, 2020; Lecocq et al., 2014; Mao et al., 2020; Mikesell et al., 2015; Yuan et al., 2021; Makus & Sens-Schönfelder, 2024). Our code's design allows for potential integration with these advanced tools, giving researchers the option to expand upon our basic tools and delve deeper into Python's seismological toolset.

2.5 Conclusions

We presented a Python tool for Seismic Ambient Noise seismology with DAS, leveraging the computational capabilities of PyTorch. The significant acceleration achieved through GPU utilization, as compared to CPU-only computations, highlights the potential of our approach in addressing data-intensive tasks in seismology. The challenges of data transfer and I/O operations in large DAS datasets were also acknowledged, emphasizing the need for strategic data management and the potential benefits of cloud computing in future seismological studies. As the field progresses, such Python tools will be pivotal, offering a balance between computational efficiency and versatility, ensuring that researchers can effectively tackle the complexities of modern seismological data.

References

Atterholt, J., Zhan, Z., & Yang, Y. (2022). Fault Zone Imaging With Distributed Acoustic Sensing: Body-To-Surface Wave Scattering. *Journal of Geophysical Research: Solid Earth*, *127*(11), e2022JB025052. https://doi.org/10.1029/2022JB025052

Bensen, G. D., Ritzwoller, M. H., Barmin, M. P., Levshin, A. L., Lin, F., Moschetti, M. P., et al. (2007). Processing seismic ambient noise data to obtain reliable broad-band surface wave dispersion measurements. *Geophysical Journal International*, *169*(3), 1239–1260. https://doi.org/10.1111/j.1365-246X.2007.03374.x

Beyreuther, M., Barsch, R., Krischer, L., Megies, T., Behr, Y., & Wassermann, J. (2010). ObsPy: A Python Toolbox for Seismology. *Seismological Research Letters*, *81*(3), 530–533. https://doi.org/10.1785/gssrl.81.3.530

Cheng, F., Chi, B., Lindsey, N. J., Dawe, T. C., & Ajo-Franklin, J. B. (2021). Utilizing distributed acoustic sensing and ocean bottom fiber optic cables for submarine structural characterization. *Scientific Reports*, *11*(1), 1–14. https://doi.org/10.1038/s41598-021-84845-y

Clements, T., & Denolle, M. A. (2018). Tracking Groundwater Levels Using the Ambient Seismic Field. *Geophysical Research Letters*, *45*(13), 6459–6465. https://doi.org/10.1029/2018GL077706

Clements, T., & Denolle, M. A. (2020). SeisNoise.jl: Ambient Seismic Noise Cross Correlation on the CPU and GPU in Julia. *Seismological Research Letters*, *92*(1), 517–527. https://doi.org/10.1785/0220200192

Diez, A., Bromirski, P. D., Gerstoft, P., Stephen, R. A., Anthony, R. E., Aster, R. C., et al. (2016). Ice shelf structure derived from dispersion curve analysis of ambient seismic noise, Ross Ice Shelf, Antarctica. *Geophysical Journal International*, *205*(2), 785–795. https://doi.org/10.1093/gji/ggw036

Dou, S., Lindsey, N., Wagner, A. M., Daley, T. M., Freifeld, B., Robertson, M., et al. (2017). Distributed Acoustic Sensing for Seismic Monitoring of The Near Surface: A Traffic-Noise Interferometry Case Study. *Scientific Reports*, *7*(1), 11620. https://doi.org/10.1038/s41598-017-11986-4

Fichtner, A., Ermert, L., & Gokhberg, A. (2017). Seismic Noise Correlation on Heterogeneous Supercomputers. *Seismological Research Letters*, *88*(4), 1141–1145. https://doi.org/10.1785/0220170043

Fichtner, A., Hofstede, C., N. Kennett, B. L., Nymand, N. F., Lauritzen, M. L., Zigone, D., & Eisen, O. (2023). Fiber-Optic Airplane Seismology on the Northeast Greenland Ice Stream. *The Seismic Record*, *3*(2), 125–133. https://doi.org/10.1785/0320230004

Harris, C. R., Millman, K. J., van der Walt, S. J., Gommers, R., Virtanen, P., Cournapeau, D., et al. (2020). Array programming with NumPy. *Nature*, *585*(7825), 357–362. https://doi.org/10.1038/s41586-020-2649-2

Herrmann, R. B. (2013). Computer Programs in Seismology: An Evolving Tool for Instruction and Research. *Seismological Research Letters*, *84*(6), 1081–1088. https://doi.org/10.1785/0220110096

Illien, L., Andermann, C., Sens-Schönfelder, C., Cook, K. L., Baidya, K. P., Adhikari, L. B., & Hovius, N. (2021). Subsurface Moisture Regulates Himalayan Groundwater Storage and Discharge. *AGU Advances*, *2*(2), e2021AV000398. https://doi.org/10.1029/2021AV000398

Jiang, C., & Denolle, M. A. (2020). NoisePy: A New High-Performance Python Tool for Ambient-Noise Seismology. *Seismological Research Letters*, *91*(3), 1853–1866. https://doi.org/10.1785/0220190364

Lecocq, T., Caudron, C., & Brenguier, F. (2014). MSNoise, a Python Package for Monitoring Seismic Velocity Changes Using Ambient Seismic Noise. *Seismological Research Letters*, *85*(3), 715–726. https://doi.org/10.1785/0220130073

Li, Z., Zhou, J., Wu, G., Wang, J., Zhang, G., Dong, S., et al. (2021). CC-FJpy: A Python Package for Extracting Overtone Surface-Wave Dispersion from Seismic Ambient-Noise Cross Correlation. *Seismological Research Letters*, *92*(5), 3179–3186. https://doi.org/10.1785/0220210042

Lin, F. C., Li, D., Clayton, R. W., & Hollis, D. (2013). High-resolution 3D shallow crustal structure in Long Beach, California: Application of ambient noise tomography on a dense seismic array. *Geophysics*, *78*(4). https://doi.org/10.1190/geo2012-0453.1

Lindsey, N. J., & Martin, E. R. (2021). Fiber-Optic Seismology. *Annual Review of Earth and Planetary Sciences*, *49*(1), 309–336. https://doi.org/10.1146/annurev-earth-072420-065213

MacCarthy, J., Marcillo, O., & Trabant, C. (2020). Seismology in the Cloud: A New Streaming Workflow. *Seismological Research Letters*, *91*(3), 1804–1812. https://doi.org/10.1785/0220190357

Makus, P., & Sens-Schönfelder, C. (2024). SeisMIC - an Open Source Python Toolset to Compute Velocity Changes from Ambient Seismic Noise. Seismica, 3(1). https://doi.org/10.26443/seismica.v3i1.1099

Mao, S., Mordret, A., Campillo, M., Fang, H., & van der Hilst, R. D. (2020). On the measurement of seismic traveltime changes in the time–frequency domain with wavelet cross-spectrum analysis. *Geophysical Journal International*, *221*(1), 550–568. https://doi.org/10.1093/gji/ggz495

Mao, S., Lecointre, A., van der Hilst, R. D., & Campillo, M. (2022). Space-time monitoring of groundwater fluctuations with passive seismic interferometry. *Nature Communications*, *13*(1), 4643. https://doi.org/10.1038/s41467-022-32194-3

Martin, E. R. (2021). A linear algorithm for ambient seismic noise double beamforming without explicit crosscorrelations. *Geophysics*, *86*(1), F1–F8. https://doi.org/10.1190/geo2019-0847.1

Martin, E. R., Lindsey, N. J., Ajo-Franklin, J. B., & Biondi, B. L. (2021). Introduction to Interferometry of Fiber-Optic Strain Measurements. In *Distributed Acoustic Sensing in Geophysics* (pp. 111–129). American Geophysical Union (AGU). https://doi.org/10.1002/9781119521808.ch9

Mikesell, T. D., Malcolm, A. E., Yang, D., & Haney, M. M. (2015). A comparison of methods to estimate seismic phase delays: numerical examples for coda wave interferometry. *Geophysical Journal International*, *202*(1), 347–360. https://doi.org/10.1093/gji/ggv138

Mordret, A., Mikesell, T. D., Harig, C., Lipovsky, B. P., & Prieto, G. A. (2016). Monitoring southwest Greenland’s ice sheet melt with ambient seismic noise. *Science Advances*, *2*(5), e1501538. https://doi.org/10.1126/sciadv.1501538

Mordret, A., Courbis, R., Brenguier, F., Chmiel, M., Garambois, S., Mao, S., et al. (2020). Noise-based ballistic wave passive seismic monitoring – Part 2: surface waves. *Geophysical Journal International*, *221*(1), 692–705. https://doi.org/10.1093/gji/ggaa016

Nakata, N., Chang, J. P., Lawrence, J. F., & Boué, P. (2015). Body wave extraction and tomography at Long Beach, California, with ambient-noise interferometry. *Journal of Geophysical Research: Solid Earth*, *120*(2), 1159–1173. https://doi.org/10.1002/2015JB011870

Ni, Y., Denolle, M., & Swinski, J.-P. (2021). Cloud-Optimized ASDF-H5 for Seismology. *AGU Fall Meeting 2021*, *2021*, S15E-0297.

Obermann, A., Planès, T., Larose, E., Sens-Schönfelder, C., & Campillo, M. (2013). Depth sensitivity of seismic coda waves to velocity perturbations in an elastic heterogeneous medium. *Geophysical Journal International*, *194*(1), 372–382. https://doi.org/10.1093/gji/ggt043

Parker, T., Shatalin, S., & Farhadiroushan, M. (2014). Distributed Acoustic Sensing - A new tool for seismic applications. *First Break*, *32*(2), 61–69.

Paszke, A., Gross, S., Massa, F., Lerer, A., Bradbury, J., Chanan, G., et al. (2019, December 3). PyTorch: An Imperative Style, High-Performance Deep Learning Library. arXiv. https://doi.org/10.48550/arXiv.1912.01703

Qin, L., Steidl, J. H., Qiu, H., Nakata, N., & Ben-Zion, Y. (2022). Monitoring Seasonal Shear Wave Velocity Changes in the Top 6 m at Garner Valley in Southern California With Borehole Data. *Geophysical Research Letters*, *49*(23), e2022GL101189. https://doi.org/10.1029/2022GL101189

Rodríguez Tribaldos, V., & Ajo-Franklin, J. B. (2021). Aquifer Monitoring Using Ambient Seismic Noise Recorded With Distributed Acoustic Sensing (DAS) Deployed on Dark Fiber. *Journal of Geophysical Research: Solid Earth*, *126*(4), 1–20. https://doi.org/10.1029/2020JB021004

Sens-Schönfelder, C., & Wegler, U. (2006). Passive image interferometry and seasonal variations of seismic velocities at Merapi Volcano, Indonesia. *Geophysical Research Letters*, *33*(21). https://doi.org/10.1029/2006GL027797

Shapiro, N. M., & Campillo, M. (2004). Emergence of broadband Rayleigh waves from correlations of the ambient seismic noise. *Geophysical Research Letters*, *31*(7). https://doi.org/10.1029/2004GL019491

Shapiro, Nikolai M., Campillo, M., Stehly, L., & Ritzwoller, M. H. (2005). High-Resolution Surface-Wave Tomography from Ambient Seismic Noise. *Science*, *307*(5715), 1615–1618. https://doi.org/10.1126/science.1108339

Snieder, R. (2004). Extracting the Green's function from the correlation of coda waves: A derivation based on stationary phase. *Physical Review E - Statistical Physics, Plasmas, Fluids, and Related Interdisciplinary Topics*. https://doi.org/10.1103/PhysRevE.69.046610

Spica, Z. J., Perton, M., Martin, E. R., Beroza, G. C., & Biondi, B. (2020). Urban Seismic Site Characterization by Fiber-Optic Seismology. *Journal of Geophysical Research: Solid Earth*, *125*(3), 1–29. https://doi.org/10.1029/2019JB018656

Tribaldos, V. R., Ajo-Franklin, J., Dou, S., Lindsey, N., Ulrich, C., Robertson, M., et al. (2019). *Surface Wave Imaging using Distributed Acoustic Sensing Deployed on Dark Fiber: Moving Beyond High Frequency Noise* (preprint). EarthArXiv. https://doi.org/10.31223/osf.io/jb2na

Virtanen, P., Gommers, R., Oliphant, T. E., Haberland, M., Reddy, T., Cournapeau, D., et al. (2020). SciPy 1.0: fundamental algorithms for scientific computing in Python. *Nature Methods*, *17*(3), 261–272. https://doi.org/10.1038/s41592-019-0686-2

Wang, Q. Y., Brenguier, F., Campillo, M., Lecointre, A., Takeda, T., & Aoki, Y. (2017). Seasonal Crustal Seismic Velocity Changes Throughout Japan. *Journal of*

Geophysical Research: Solid Earth, *122*(10), 7987–8002. https://doi.org/10.1002/2017JB014307

Willis, M. E., Ellmauthaler, A., Wu, X., & LeBlanc, M. J. (2021). Important Aspects of Acquiring Distributed Acoustic Sensing (DAS) Data for Geoscientists. In *Distributed Acoustic Sensing in Geophysics* (pp. 33–44). American Geophysical Union (AGU). https://doi.org/10.1002/9781119521808.ch2

Yang, Y., & Zhan, Z. (2022). Fiber seismic monitoring of the dry Owens Lake. *AGU Fall Meeting 2022*, *2022*, S22B-04.

Yang, Y., Zhan, Z., Shen, Z., & Atterholt, J. (2022). Fault Zone Imaging With Distributed Acoustic Sensing: Surface-To-Surface Wave Scattering. *Journal of Geophysical Research: Solid Earth*, *127*(6), e2022JB024329. https://doi.org/10.1029/2022JB024329

Yang, Y., Atterholt, J. W., Shen, Z., Muir, J. B., Williams, E. F., & Zhan, Z. (2022). Sub-Kilometer Correlation Between Near-Surface Structure and Ground Motion Measured With Distributed Acoustic Sensing. *Geophysical Research Letters*, *49*(1), e2021GL096503. https://doi.org/10.1029/2021GL096503

Yao, H., van der Hilst, R. D., & de Hoop, M. V. (2006). Surface-wave array tomography in SE Tibet from ambient seismic noise and two-station analysis - I. Phase velocity maps. *Geophysical Journal International*, *166*(2), 732–744. https://doi.org/10.1111/j.1365-246X.2006.03028.x

Yuan, C., Bryan, J., & Denolle, M. (2021). Numerical comparison of time-, frequency- and wavelet-domain methods for coda wave interferometry. *Geophysical Journal International*, *226*(2), 828–846. https://doi.org/10.1093/gji/ggab140

Zhan, Z. (2020). Distributed Acoustic Sensing Turns Fiber-Optic Cables into Sensitive Seismic Antennas. *Seismological Research Letters*, *91*(1), 1–15. https://doi.org/10.1785/0220190112

Zhu, W., Hou, A. B., Yang, R., Datta, A., Mousavi, S. M., Ellsworth, W. L., & Beroza, G. C. (2023). QuakeFlow: a scalable machine-learning-based earthquake monitoring workflow with cloud computing. *Geophysical Journal International*, *232*(1), 684–693. https://doi.org/10.1093/gji/ggac355

Chapter 3

SUB-KILOMETER CORRELATION BETWEEN NEAR-SURFACE STRUCTURE AND GROUND MOTION MEASURED WITH DISTRIBUTED ACOUSTIC SENSING

Yang, Y., Atterholt, J. W., Shen, Z., Muir, J. B., Williams, E. F., & Zhan, Z. (2022). Sub-Kilometer Correlation Between Near-Surface Structure and Ground Motion Measured With Distributed Acoustic Sensing. *Geophysical Research Letters*, 49(1), e2021GL096503. https://doi.org/10.1029/2021GL096503

Abstract

Earthquake ground motion depends strongly on near-surface structure, which is challenging to image in urban areas at high resolution. Distributed acoustic sensing (DAS) is an emerging technique that provides a scalable solution by converting pre-existing fiber-optic cables into dense seismic arrays. After the July 2019 M7.1 Ridgecrest earthquake, we converted an underground dark fiber across the city of Ridgecrest, CA, into a DAS array. The recorded aftershocks show substantial lateral variability in site amplification over only 8-km in distance. To understand the cause of such variability, we used three months of continuous data, dominated by traffic-generated seismic noise, to image near-surface structure along the fiber path. We find that the lateral variations of earthquake shaking correlate well with the shallow shear velocity model at sub-kilometer scales, in particular micro-basins filled with soft sediments. These results highlight the great potential of DAS for high-resolution seismic hazard mapping in urban areas.

3.1 Introduction

Populated urban areas tend to be located in sedimentary basins with broad flat land and favorable positions near water bodies (Wirth et al., 2019). However, shallow soft sediments with low shear velocity can trap seismic energy and amplify earthquake shaking (Aki, 1993; Singh et al., 1988). Characterizing near-surface structure and quantifying ground motion is critical to mapping the seismic risk of urban regions. Estimating seismic hazard is usually accomplished with empirically derived ground-motion models (GMMs) with site characteristics, usually Vs30 (the time-averaged shear velocity in the upper 30 meters), which can be empirically inferred from local tomography models, geologic units and topography gradients, but is often sparse and uneven spatially (Allen & Wald, 2009; Wills et al., 2000; Yong et al., 2012). In the last few decades, several important earthquakes, such as the 1985 Mexico City (Campillo et al., 1990), 1989 Loma Prieta (Hanks & Brady, 1991), 2010 Haiti (Hough et al., 2010), and 2015 Nepal (Rajaure et al., 2017) earthquakes, showed highly variable and localized site amplification at kilometer or sub-kilometer scales. Mapping seismic hazard at such fine scales requires high-resolution, high-frequency seismic experiments. Dense nodal seismic arrays have been popular in recent years for this application and have demonstrated the ability to extract shallow crustal structure at high resolution (Lin et al., 2013; Nakata et al., 2015; Schmandt & Clayton, 2013), though sometimes with space constraints and short-term deployment limitations.

Distributed acoustic sensing (DAS) is an emerging technique that can turn pre-existing telecommunication fiber-optic cables into cost-effective, long-term dense seismic arrays in urban or harsh environments with remote operation (Lindsey & Martin, 2021; Zhan, 2019). DAS works by applying optical interferometry to the laser light back-scattered from intrinsic inhomogeneities within an optical fiber to measure strain or strain rate along the fiber. With an effective channel spacing of a few meters, DAS can record unaliased high-frequency wavefields and allow near-surface imaging at a resolution of several tens of meters. In practice, DAS has been used successfully for near-surface ambient noise imaging with traffic as noise sources (Ajo-Franklin et al., 2019; Dou et al., 2017; Spica et al., 2020).

On 4th July 2019, an M6.4 earthquake occurred in Ridgecrest, California, followed by an M7.1 mainshock 34 hours later. As a rapid response, five days after the mainshock, we gained access to 10-km of underground dark fiber in the city of Ridgecrest and converted it into a DAS array of 1250 channels with 8-meter spacing (Figure 3.1). The Ridgecrest DAS array recorded numerous local magnitude (Ml) >2 events with high fidelity and has detected six times more aftershocks than the standard earthquake catalog within the first three months

(Li et al., 2021). The continuous DAS data also allow ambient noise tomography for near-surface structures. With DAS data for both the aftershocks and ambient seismic noise, we have a unique opportunity to evaluate the spatial variability of the earthquake ground motions and its relation to small-scale shallow subsurface structure. In this paper, we will focus on the 8-km segment along W Inyokern Road which has approximately straight line geometry in the east-west direction.

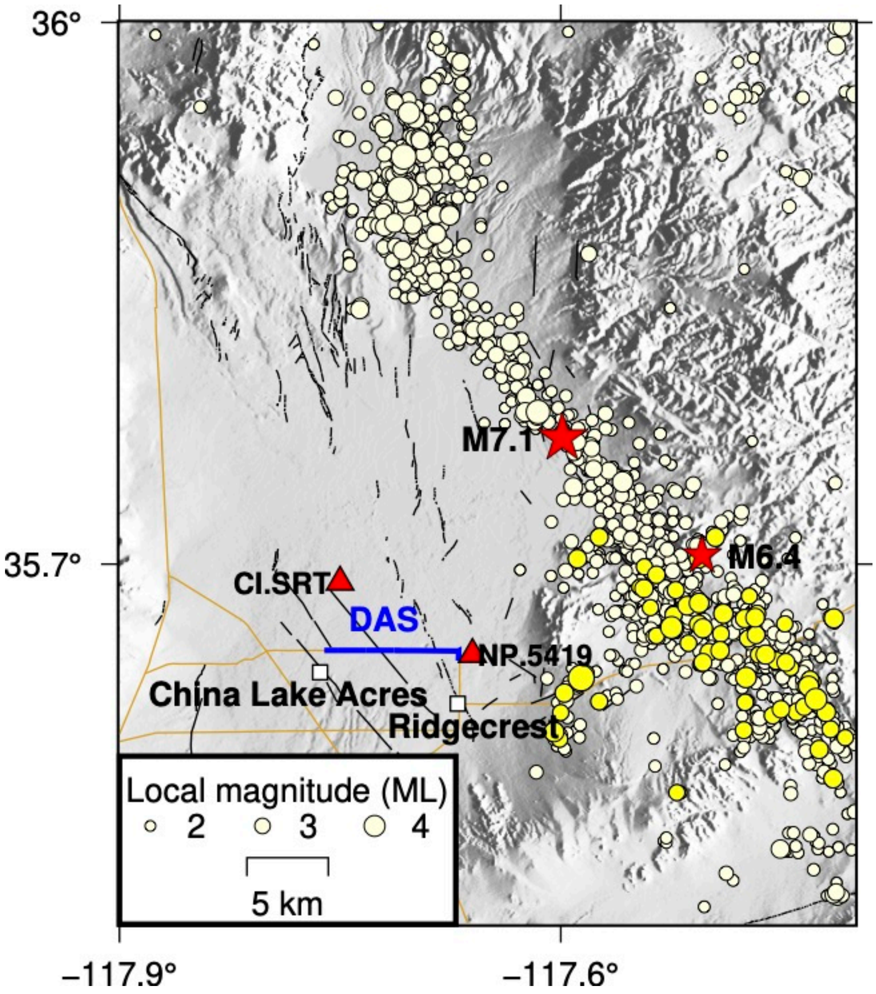

Figure 3.1: The location map of the Ridgecrest DAS array. The ground trace of the Ridgecrest DAS array is shown in blue. ~1600 local magnitude (Ml) >2 aftershocks during July 10th - October 4th are shown in circles (catalog source: https://service.scedc.caltech.edu/ftp/catalogs/SCSN/), with the yellow circles showing

M>3 events in a narrow back azimuth range that are used in the site amplification inversion . The M7.1 mainshock and the M6.4 foreshock are marked with the red stars. The two nearby seismic stations CI.SRT and NP.5419 are shown in red triangles. The main roads are plotted in golden lines. The fault zones are marked with black lines (data source: U.S. Geological Survey and New Mexico Bureau of Mines and Mineral Resources, Quaternary fault and fold database for the United States, accessed August 1, 2019, at: https://www.usgs.gov/natural-hazards/earthquake-hazards/faults).

3.2 Methods

3.2.1 Conversion from DAS strain to ground acceleration

Seismic hazard and site amplification studies usually focus on ground motions (i.e., displacement, velocity, and acceleration), while DAS measures the along-fiber strain field averaged over a finite gauge length. For a monochromatic plane wave, the relationship between acceleration $\ddot{u}$ and strain rate $\dot{\varepsilon}$ is given by:

$$\ddot{u} = c\dot{\varepsilon} = \frac{\omega}{k}\dot{\varepsilon}, \tag{3.1}$$

where c is apparent phase velocity, ω is angular frequency, k is wavenumber (e.g., Yu et al., 2019). To apply conventional methods for site amplification estimation and compare with previous results, we need to convert our measured strain to acceleration, by differentiation to strain rate and correcting for the waves' apparent phase velocity, which varies for different seismic phases ranging from fast body waves to slow surface and scattered waves. The conversion from strain rate to acceleration can be accomplished through spatial integration with one co-located seismometer (Wang et al., 2018), f-k rescaling (Lindsey et al., 2020), or slowness determination based on slant stacking (Lior et al., 2021). Due to the lack of a co-located seismometer and the strong locally scattered waves in the Ridgecrest, none of these methods work well. In this work we use the Cartesian coronae framework of the Fast Discrete Curvelet Transform (FDCT) to convert the strain rate to particle motions. Recently, the FDCT was successfully applied to denoise DAS records and shows some promise in other DAS preprocessing steps (Atterholt et al., 2021). As part of the FDCT, the f-k domain is compartmentalized into tiles corresponding to different velocity ranges and scales. This compartmentalization is special because it uses a parabolic scaling relationship that yields more tiles at finer scales. The FDCT framework thus provides a convenient basis with which to remove or modify DAS data according to velocity and scale. Under this framework we can easily mute high velocity phases without interfering with other phases. We can also improve the stability of the strain rate to ground motion conversion by applying equation (3.1) using the median velocity of each tile instead of using different velocities for all pixels in the f-k domain. Here, this framework is particularly advantageous, because the parabolic scaling ensures that the median velocity approximation becomes more precise as resolution improves at finer scales. In this work, we perform the strain rate to ground motion conversion using a Cartesian coronae framework constructed using 8 scales with 16 tiles at the coarsest scale; the parabolic scaling relationship prescribes the rest of the tiling using just these two parameters. For these conversions, we mute all tiles that abut the wavenumber axis, i.e., tiles with k~0.

3.2.2 Separation of source, path and site effects

The observed ground motion variability is a combination of source, path, and site effects. With multiple events recorded at all channels along the cable, we are able to use a generalized inversion to separate the site response from all the event-receiver pairs' observations (Andrews, 1986). We use 71 M>3 events in a back azimuth range of 60-120° during 3 months after the Ridgecrest mainshock. We pick P and S waves based on the arrival times predicted by the SCSN catalog and the CVM-S4.26 model (Lee et al., 2014). S waves are more critical for ground motions and have higher SNR than P waves in our data (Li et al., 2021), so we focus on S wave amplification here. We cut the waveform to 2 sec before and 10 sec after the picked S wave arrival times and calculate power spectral density at equal intervals of 0.03 in log frequency, and then smooth it with a running average for every 8 samples. Following Andrews (1986), the spectral amplitudes $O_{ij}(f)$ observed at frequency f, recording channel j for event i can be written as:

$$O_{ij}(f) = E_j(f)P_{ij}(f)S_i(f), \tag{3.2}$$

where E, P, S are earthquake source effect, path effect and site effect, respectively. The assumption here is that the S-wave heterogeneity is not super important except in the very shallow layers where we have site amplification. By taking the logarithm and simplifying the path effect as geometric attenuation for S waves, the source and site terms can be solved with a linear inversion. The detailed inversion method is described in Text S1. For the site effects, we also take moving averages over 30 channels to get rid of unrealistic spikes due to ground coupling issues. Due to the lack of frequency constraint and little variation with frequency, we only focus on the site amplification averaged in [0.5, 5] Hz, in which the S wave energy dominates and is critical for most low and mid-rise buildings.

3.2.3 Ambient noise tomography

In ambient noise tomography, we follow the conventional workflow that was developed over the last decade for crustal imaging for larger scale and longer period data (Bensen et al., 2007). Preprocessing includes removing mean and linear trends, down-sampling to 50 Hz, band pass filtered to [0.1, 10] Hz. Then, a running-absolute-average temporal normalization and spectral whitening are applied to each 1-hour data segment. After cross-correlation and normalization in frequency domain, the cross-correlation functions were transformed back to time domain and stacked over three months. We use beamforming to search for the phase velocity that maximizes the stacked energy of the shifted waveforms for each narrow frequency band in 1-10 Hz. Given a virtual source, for each channel, we take a subarray of channels around it to measure the local phase velocity dispersion (Figure 3.2a). The subarray size is determined by the wavelength at each period. Since every channel can be treated as a virtual source, there are hundreds of virtual sources that can provide an average measurement with the standard deviation taken as uncertainty. Rayleigh-wave phase velocity is most sensitive to shear-wave velocity structure at a depth around one-third to one half of the wavelength (Forsyth et al., 1998; Haney & Tsai, 2015). Therefore, the phase velocity in this study is sensitive to the shear velocity in the top 200 meters assuming 600 m/s velocity at 1 Hz. We use a level set tomography approach based on a geologically motivated model parameterization (Muir et al., 2021; Muir & Tsai, 2020). The model is parameterized by a small number of interfaces defined by the level set method and Gaussian random fields inside each layer. This model parameterization has fewer effective parameters and allows spatial continuity, thus providing a simplified and more interpretable model. After testing different model parameters, we aim at a 3-layer model with 2 interfaces. The velocity in each layer is parameterized as 2D Gaussian random field. The Gaussian random field parameters of the three layers are given in Table 3.S1. After 10 times of realization with randomly generated prior models, we take the average inversion results as the final model and the standard deviation as the model uncertainty.

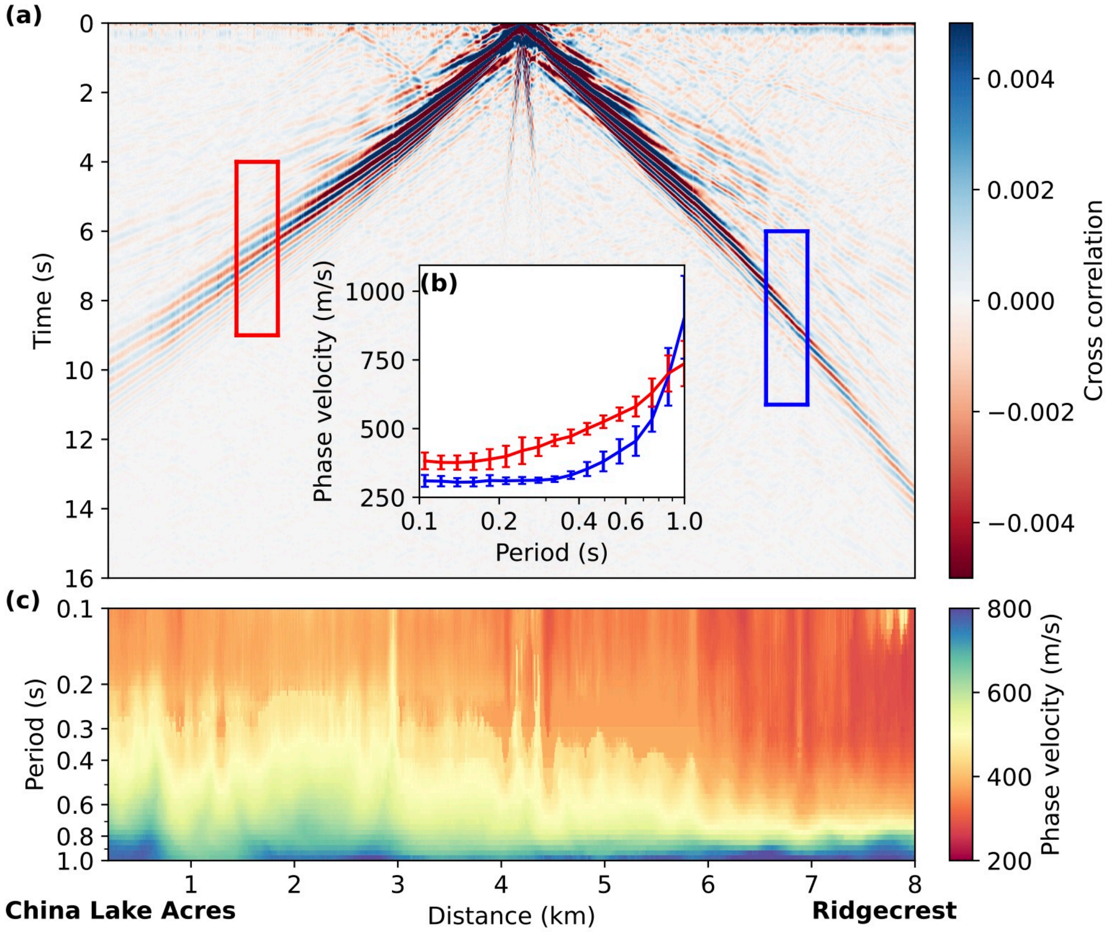

Figure 3.2: Near-surface imaging procedures. (a) A common shot gather with virtual source in the middle of the cable. (b) Phase velocity dispersion curves measured by beamforming with a section of channels in the red and blue rectangles in (a). The error bars are given by the standard deviation of the dispersion measured from all other channels as virtual sources (c) Phase velocity map along the cable. Each column is averaged from all the channels as virtual sources.

3.3 Results and discussion

3.3.1 Localized site amplification revealed by Ridgecrest aftershocks

Although the entire DAS array is in the sedimentary basin of Indian Wells Valley and with little topographic slope, the recorded earthquake shaking shows strong and consistent lateral variation (Figure 3.3a and Figure 3.S1). Conversion from strain rate to ground motion reduces the overall gradient in spectral amplitude along the cable by mitigating slow scattered surface waves, but the converted ground acceleration wavefield still shows an apparent amplification factor of 2 between the west and the east ends (Figure 3.3b). The systematic trend in the apparent amplification is not likely caused by the cable-ground coupling given the uniform installation along the entire cable. Furthermore, similar apparent amplifications are also observed at the two seismic stations close to the two ends of the Ridgecrest DAS array: CI.SRT (4 km away) and NP.5419 (500 m away) (Figure 3.1). The spectral acceleration of the two stations shows a similar amplitude difference (a factor of two), as in the DAS-converted acceleration after correcting the geometrical spreading effect (Figure 3.3d and Figure 3.S2). We recognize that the absolute amplitudes of the DAS-converted acceleration are still systematically different from those from the seismometers (Figure 3.3d), which has also been reported on previous DAS experiments and attributed to the fiber-ground coupling and the cable properties (Jousset et al., 2018; Lindsey et al., 2020; Paitz et al., 2020). Here we focus on the relative amplitudes along the cable to estimate site effects, but calibration should be required for future work where absolute amplitude information is desired. The red line in Figure 3.4a shows the inverted site amplification profile, normalized to the channel with the lowest amplification factor. The site amplification generally increases from west to east and has a factor of three difference over only an 8-km distance. The strongest amplification peak appears in the east end while the lowest amplification is at 2-3 km, with a secondary broad amplification peak between 0 and 2 km.

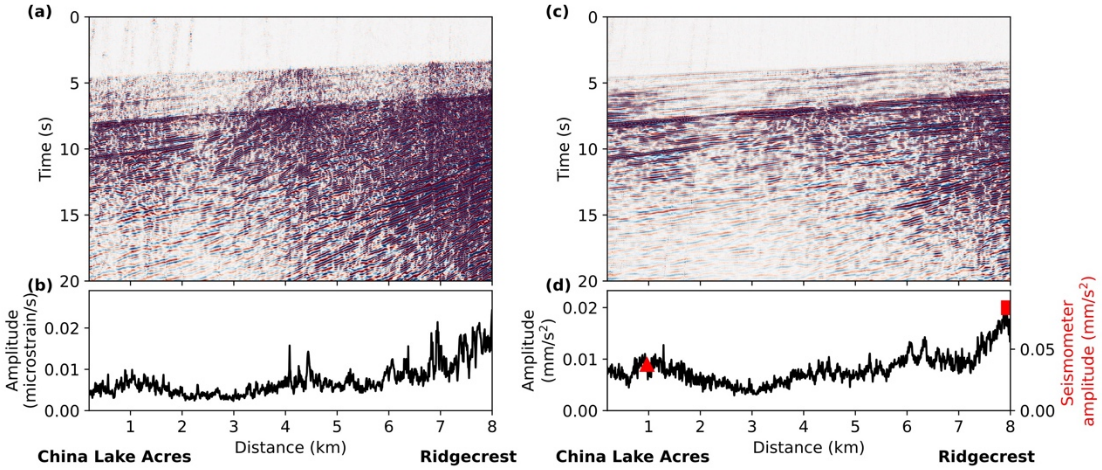

Figure 3.3: Comparison between strain rate and converted acceleration of an M3 earthquake that occurred on UTC 17:09:22, July 21st, 2019. (a) DAS measured strain rates; (b) Average spectral strain rate in [0.5, 5] Hz of the waveform in (a); (c) Converted ground acceleration; (d) Average spectral acceleration in [0.5, 5] Hz of the waveform in (c). The average spectral acceleration of the two stations CI.SRT and NP.5419 are shown in the red triangle and the red square, respectively. The distances of the two stations are projected to their nearest DAS channels. The amplitudes of the two stations are shown in the y axis on the right due to different instrument scaling. Geometric spreading is compensated in (b) and (d). This amplification factor is commonly observed among many events.

3.3.2 Subsurface imaging with traffic noise

Our continuous DAS array also allows us to image the near-surface structure that may be the cause of the S wave amplification pattern observed above. While numerous aftershocks were recorded (Li et al., 2021), the continuous data are still dominated by urban noise from vehicles with weekly periodicity (Figure 3.S3), due to the proximity of the cable to Highway 395. With cross-correlations stacked over three months, the Rayleigh wave fundamental mode can be clearly tracked, with the asymmetric bending of arrival times suggesting strong velocity variability (Figure 3.2a). With all channels as virtual sources, we are able to construct a phase velocity map at 1-10 Hz with uncertainties mostly below 40 m/s (Figure 3.2b and 3.4c). The inverted shear velocity model shows strong lateral variation along the 8-

km DAS profile (Figure 3.4b). A 60-meter thick top layer with shear velocity as low as 270 m/s occupies the east end of the cable (6-8 km) and diminishes to less than 20 meters thick at the distance of 2-3 km, where a high-velocity anomaly also appears at 50-100 m depth. A secondary micro-basin is visible in the westernmost 1.5 km of the profile (Figure 3.4b). Regional velocity models from traveltime tomography here have low resolution in the shallow crust (White et al., 2021). Without available borehole data, the Vs30 model based on local geology and terrain is largely smoothed and unable to disclose any variation along the 8-kilometer profile (McPhillips et al., 2020; Thompson et al., 2014, Figure 3.4a). Our near-surface velocity model has two orders of magnitude higher resolution (~200 m horizontal resolution in the top layer) and therefore is suitable for fine-scale ground motion estimation.

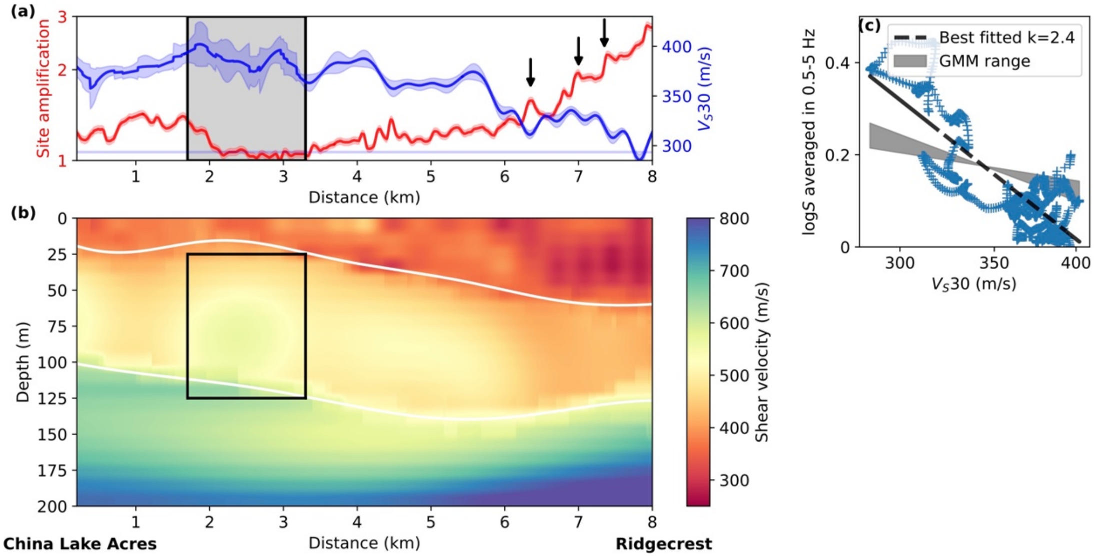

Figure 3.4: Site amplification profile and near-surface shear velocity model. (a) The red line shows site amplification averaged in [0.5, 5] Hz and normalized to the channel at 3-km distance with the lowest amplification, with the red shaded area showing uncertainty from bootstrapping. The blue line shows Vs30 computed from the velocity model in (b), with the blue shaded area showing the 2 times standard deviation from 10 realizations of inversion. The black arrows show some small-scale anti-correlation while the gray shaded area shows a region with poor anti-correlation between site amplification and Vs30; (b)

The three-layer shear velocity model from ambient noise imaging, with the two interfaces outlined in the white lines. The black box outlines a high-velocity anomaly corresponding to the gray shaded area in (a). (c) Log-log relationship between the Vs30 and site amplification (blue crosses) with the best fitted k shown in the black line. The range of the GMM predicted site amplification variation in [0.5, 5] Hz is plotted in the gray shaded area (Bayless & Abrahamson, 2019).

3.3.3 Fine-scale correlation between site amplification and velocity structure

Most modern GMMs take Vs30 as the principal site parameter either directly or as the basis for site classification into categories (Douglas, 2014). The site amplification model with respect to Vs30 generally consists of a linear term as a function of Vs30 alone and nonlinear terms that account for soil effects. Because the shaking is generally weak for the aftershocks studied here, we focus on the linear term which is typically given as a power law with exponent k:

$$\log_{10} S = -k\log_{10}\left(\frac{V_S 30}{V_{S_{ref}}}\right), \tag{3.3}$$

where $V_{S_{ref}}$ is the Vs30 at a reference site on rocks, k is a coefficient estimated by regression, S is the site amplification factor commonly assessed for peak ground acceleration (PGA) or response spectrum at different periods. Recent studies also start to use horizontal-component Fourier amplitude spectrum instead of response spectra values to build the GMMs (Bayless & Abrahamson, 2019), which is easier to constrain with seismological methods. As shown in Figure 3.3a, our Vs30 measurements show a remarkable anti-correlation with the earthquake site amplification, both at long wavelength over the 8-km profile and at sub-km scales (annotated by black arrows in Figure 3.4a). Fitting our site amplification and Vs30 results using equation (3.3) gives a good linear relation with a correlation coefficient of 0.81 (Figure 3.4c). Previous research indicates that the relationship between horizontal amplification factor and Vs30 may have a large scatter even in log space (e.g., Castellaro et al., 2008). Our site amplification and Vs30 results show that, while Vs30 is not a perfect single-variable predictor of site amplification, it performs notably well on a small scale. However, the fitted k = 2.4 is much larger than the typical values (0.2-0.8) in the

[0.5, 5] Hz band from the BA18 GMM (Bayless & Abrahamson, 2019, Figure 3.4c), which means stronger shaking variability than expected from the Vs30 profile. One important reason is that prior empirical equations are regressed from broader regions based on the ergodic assumption without any locally-specific corrections (Bradley, 2015). The systematic deviation from the regressed ergodic GMM suggests that non-ergodic correction terms are necessary to characterize local site amplification here in the Ridgecrest city. Our findings suggest that DAS provides an easy way to perform a local non-ergodic GMM calibration.

DAS imaging can provide further information beyond the Vs30. Recently other empirical site parameters representing the shear velocity structure deeper than Vs30 have been integrated into GMMs, such as the depth to the 1 km/s velocity horizon ($Z_{1.0}$) (Chiou & Youngs, 2014) or the depth to the 2.5 km/s horizon ($Z_{2.5}$) (Campbell & Bozorgnia, 2014). Indeed, our results also indicate the site amplification correlated with structure deeper than 30 m. At 2-3 km distance, the lowest site amplification is not correlated with the highest Vs30 (Figure 3.4a), but appears to be related to the high-velocity anomaly at 50-100 m depth (Figure 3.4b). We propose that with DAS's ability to recover more structure information than Vs30 without the need to wait for earthquakes, we can identify other quantities that can better characterize site effects and predict ground motion with physics-based approaches such as forward modeling.

3.4 Conclusions

With the Ridgecrest DAS data, we extract site amplification from earthquake aftershocks and perform near-surface imaging with traffic-generated seismic noise. Our results demonstrate that DAS-based noise tomography is capable of capturing subsurface structural heterogeneities that cause ground shaking variability at sub-kilometer scales. Such fine-scale seismic hazard microzonation can significantly improve urban seismic risk management. Although the physics linking the shallow structure and site amplification quantitatively requires further investigation, the observation we report here highlights the potential of DAS for high-resolution urban seismic hazard mapping as an efficient and inexpensive tool.

Supplementary Material

Generalized inversion for site effect

Following Andrews (1986), the spectral amplitudes $O_{ij}(f)$ observed at frequency f, recording channel i for event j can be written as:

$$O_{ij}(f) = E_j(f)P_{ij}(f)S_i(f), \tag{3.S1}$$

where E, P, S are earthquake source effect, path effect and site effect, respectively. The assumption here is that the S-wave heterogeneity is not super important except in the very shallow layers where we have site amplification. By taking the logarithm and simplifying the path effect as geometric attenuation for S waves, we have:

$$\log O_{ij} + \log r_{ij} = \log E_j + \log S_i, \tag{3.S2}$$

where r is the epicentral distance. The equation above can be written in matrix form as $\boldsymbol{Gm} = \boldsymbol{d}$:

$$\begin{bmatrix} 1 & 0 & \dots & 0 & 1 & 0 & \dots & 0 \\ 1 & 0 & \dots & 0 & 0 & 1 & \dots & 0 \\ \dots & \dots & \dots & \dots & \dots & \dots & \dots & \dots \\ 1 & 0 & \dots & 0 & 0 & 0 & \dots & 1 \\ 0 & 1 & \dots & 0 & 1 & 0 & \dots & 0 \\ \dots & \dots & \dots & \cdots & \dots & \dots & \dots & \dots \\ 0 & 0 & \dots & 1 & 0 & 0 & \dots & 1 \end{bmatrix} \begin{bmatrix} \log S_1 \\ \log S_2 \\ \dots \\ \log S_M \\ \log E_1 \\ \log E_2 \\ \dots \\ \log E_N \end{bmatrix} = \begin{bmatrix} \log O_{11} + \log r_{11} \\ \log O_{12} + \log r_{12} \\ \dots \\ \log O_{1N} + \log r_{1N} \\ \log O_{21} + \log r_{21} \\ \dots \\ \log O_{MN} + \log r_{MN} \end{bmatrix}$$

where N is the number of earthquakes; M is the number of stations; $\boldsymbol{m}$ is a vector with $M + N$ elements, consisting of $\log E_j$ and $\log S_i$; $\boldsymbol{d}$ is a vector with $M * N$ elements, consisting $\log O_{ij} + \log r_{ij}$ for all earthquake-station pairs. $\boldsymbol{G}$ is a sparse matrix with either 0 or 1 elements, each row of $\boldsymbol{G}$ is corresponding to one earthquake-station pair. Since $\boldsymbol{G}$ and $\boldsymbol{d}$ are known, this equation for $\boldsymbol{m}$ can be solved with $\boldsymbol{m} = (\boldsymbol{G}^T\boldsymbol{G})^{-1}\boldsymbol{G}^T\boldsymbol{d}$.

Table 3.S1: The Gaussian random field parameters of the subsurface velocity model.

Variable (from top to bottom)	Standard deviation	Horizontal correlation length	Vertical correlation length
Layer 1 velocity	50 m/s	200 m	50 m
Interface 1 depth	20 m	2 km	
Layer 2 velocity	10 m/s	800 m	50 m
Interface 2 depth	20 m	4 km	
Layer 3 velocity	10 m/s	4 km	50m

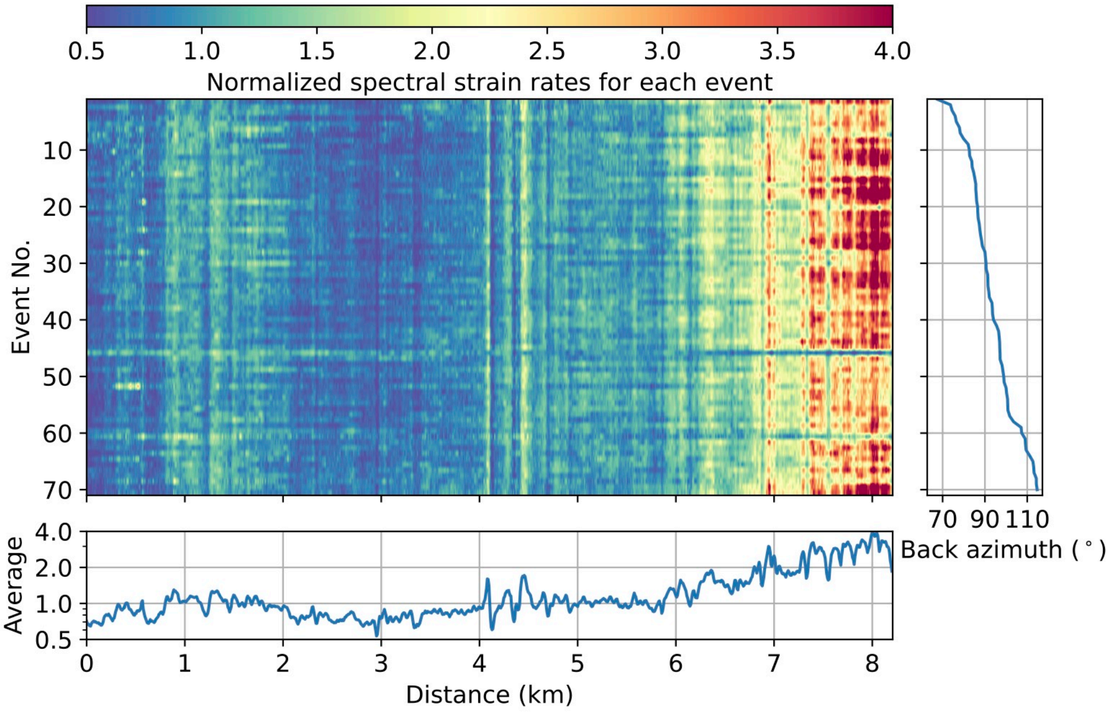

Figure 3.S1: Lateral variation of DAS recorded ground strain rate of Ridgecrest aftershocks (the yellow circles in Figure 3.1). The spectral strain rate is averaged in [0.5, 5] Hz and for each event, the amplitude is spectral normalized to the median amplitude of all channels. The events are sorted by their back azimuths to the center of the array as shown in the right panel. The averaged strain rate over all events is shown in the bottom panel.

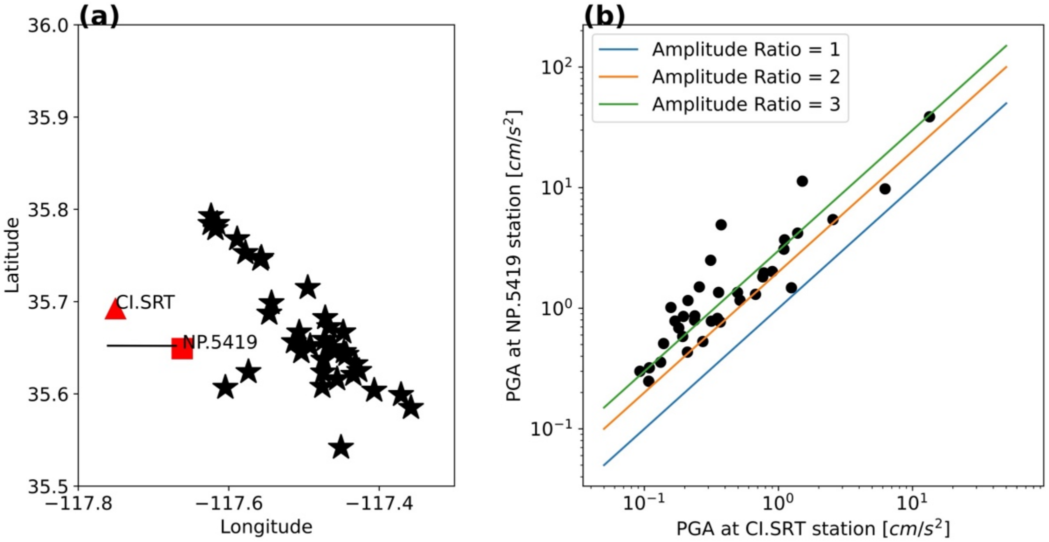

Figure 3.S2: The peak ground acceleration (PGA) ratio between station NP.5419 and CI.SRT after correction for hypocentral distance and back azimuth. (a) Map view of the seismometer stations (in the triangles), DAS array (in the black line) and the recorded M>3 events (in the black stars); (b) Scatter plot of the PGA at the two stations, with the lines representing different amplitude ratios.

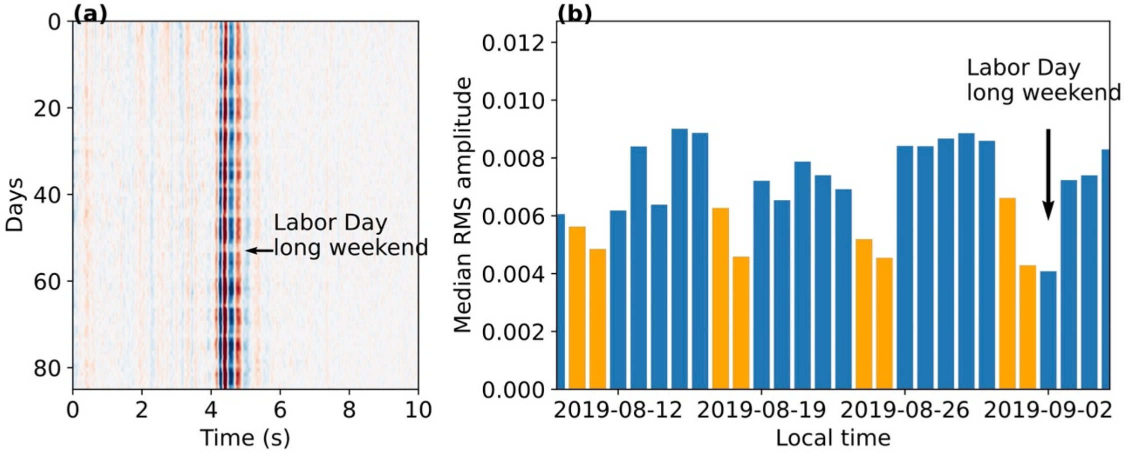

Figure 3.S3: Daily noise pattern with weekly periodicity. (a) Noise cross-correlation between channel No.450 and No.300 over the three months. (b) Median of daily root mean square amplitude recorded at channel No. 200. The orange bars are corresponding to the weekends.

The low amplitude due to the Labor Day long weekend is marked in both panels.

References

Ajo-Franklin, J. B., Dou, S., Lindsey, N. J., Monga, I., Tracy, C., Robertson, M., et al. (2019). Distributed Acoustic Sensing Using Dark Fiber for Near-Surface Characterization and Broadband Seismic Event Detection. *Scientific Reports*, *9*(1), 1–14. https://doi.org/10.1038/s41598-018-36675-8

Aki, K. (1993). Local site effects on weak and strong ground motion. *Tectonophysics*. https://doi.org/10.1016/0040-1951(93)90262-I

Allen, T. I., & Wald, D. J. (2009). On the Use of High-Resolution Topographic Data as a Proxy for Seismic Site Conditions (VS30). *Bulletin of the Seismological Society of America*, *99*(2A), 935–943. https://doi.org/10.1785/0120080255

Andrews, D. J. (1986). Objective Determination of Source Parameters and Similarity of Earthquakes of Different Size (pp. 259–267). https://doi.org/10.1029/GM037p0259

Atterholt, J., Zhan, Z., Shen, Z., & Li, Z. (2021). A unified wavefield partitioning approach for distributed acoustic sensing. *Geophysical Journal International*. https://doi.org/10.1093/gji/ggab407

Bayless, J., & Abrahamson, N. A. (2019). Summary of the BA18 ground-motion model for fourier amplitude spectra for crustal earthquakes in California. *Bulletin of the Seismological Society of America*, *109*(5), 2088–2105. https://doi.org/10.1785/0120190077

Bensen, G. D., Ritzwoller, M. H., Barmin, M. P., Levshin, A. L., Lin, F., Moschetti, M. P., et al. (2007). Processing seismic ambient noise data to obtain reliable broad-band surface wave dispersion measurements. *Geophysical Journal International*, *169*(3), 1239–1260. https://doi.org/10.1111/j.1365-246X.2007.03374.x

Bradley, B. A. (2015). Systematic ground motion observations in the Canterbury earthquakes and region-specific non-ergodic empirical ground motion modeling. *Earthquake Spectra*, *31*(3), 1735–1761. https://doi.org/10.1193/053013EQS137M

Campbell, K. W., & Bozorgnia, Y. (2014). NGA-West2 ground motion model for the average horizontal components of PGA, PGV, and 5% damped linear acceleration response spectra. *Earthquake Spectra*, *30*(3), 1087–1114. https://doi.org/10.1193/062913EQS175M

Campillo, M., Sánchez-Sesma, F. J., & Aki, K. (1990). Influence of small lateral variations of a soft surficial layer on seismic ground motion. *Soil Dynamics and Earthquake Engineering*, *9*(6), 284–287. https://doi.org/10.1016/S0267-7261(05)80014-4

Castellaro, S., Mulargia, F., & Rossi, P. L. (2008). Vs30: Proxy for seismic amplification? *Seismological Research Letters*, *79*(4), 540–543. https://doi.org/10.1785/gssrl.79.4.540

Chiou, B. S. J., & Youngs, R. R. (2014). Update of the Chiou and Youngs NGA model for the average horizontal component of peak ground motion and response spectra. *Earthquake Spectra*, *30*(3), 1117–1153. https://doi.org/10.1193/072813EQS219M

Dou, S., Lindsey, N., Wagner, A. M., Daley, T. M., Freifeld, B., Robertson, M., et al. (2017). Distributed Acoustic Sensing for Seismic Monitoring of the Near Surface: A Traffic-

Noise Interferometry Case Study. *Scientific Reports*, *7*(1). https://doi.org/10.1038/s41598-017-11986-4

Douglas, J. (2014). Ground motion prediction equations 1964--2014. *PEER Report 2011*, *102*.

Forsyth, D. W., Webb, S. C., Dorman, L. M., & Shen, Y. (1998). Phase Velocities of Rayleigh Waves in the MELT Experiment on the East Pacific Rise. *Science*, *280*(5367), 1235–1238. https://doi.org/10.1126/science.280.5367.1235

Haney, M. M., & Tsai, V. C. (2015). Nonperturbational surface-wave inversion: A Dix-type relation for surface waves. *Geophysics*, *80*(6), EN167–EN177. https://doi.org/10.1190/GEO2014-0612.1

Hanks, C., & Brady, A. G. (1991). The Loma Prieta earthquake, ground motion, and damage in Oakland, Treasure Island, and San Francisco. *Bulletin of the Seismological Society of America*, *81*(5), 2019–2047.

Hough, S. E., Altidor, J. R., Anglade, D., Given, D., Janvier, M. G., Maharrey, J. Z., et al. (2010). Localized damage caused by topographic amplification during the 2010 M7.0 Haiti earthquake. *Nature Geoscience*, *3*(11), 778–782. https://doi.org/10.1038/ngeo988

Jousset, P., Reinsch, T., Ryberg, T., Blanck, H., Clarke, A., Aghayev, R., et al. (2018). Dynamic strain determination using fibre-optic cables allows imaging of seismological and structural features. *Nature Communications*, *9*(1). https://doi.org/10.1038/s41467-018-04860-y

Lee, E. J., Chen, P., Jordan, T. H., Maechling, P. B., Denolle, M. A. M., & Beroza, G. C. (2014). Full-3-D tomography for crustal structure in Southern California based on the scattering-integral and the adjoint-wavefield methods. *Journal of Geophysical Research: Solid Earth*, *119*(8), 6421–6451. https://doi.org/10.1002/2014JB011346

Li, Z., Shen, Z., Yang, Y., Williams, E., Wang, X., & Zhan, Z. (2021). Rapid Response to the 2019 Ridgecrest Earthquake With Distributed Acoustic Sensing. *AGU Advances*, *2*(2). https://doi.org/10.1029/2021av000395

Lin, F. C., Li, D., Clayton, R. W., & Hollis, D. (2013). High-resolution 3D shallow crustal structure in Long Beach, California: Application of ambient noise tomography on a dense seismic array. *Geophysics*, *78*(4). https://doi.org/10.1190/geo2012-0453.1

Lindsey, N. J., & Martin, E. R. (2021). Fiber-Optic Seismology. *Annual Review of Earth and Planetary Sciences*, *49*(1), 309–336. https://doi.org/10.1146/annurev-earth-072420-065213

Lindsey, N. J., Rademacher, H., & Ajo-Franklin, J. B. (2020). On the Broadband Instrument Response of Fiber-Optic DAS Arrays. *Journal of Geophysical Research: Solid Earth*, *125*(2), 1–16. https://doi.org/10.1029/2019JB018145

Lior, I., Sladen, A., Mercerat, D., Ampuero, J. P., Rivet, D., & Sambolian, S. (2021). Strain to ground motion conversion of distributed acoustic sensing data for earthquake magnitude and stress drop determination. *Solid Earth*, *12*(6), 1421–1442. https://doi.org/10.5194/se-12-1421-2021

McPhillips, D. F., Herrick, J. A., Ahdi, S., Yong, A. K., & Haefner, S. (n.d.). Updated Compilation of VS30 Data for the United States: U.S. Geological Survey data release. Retrieved from https://doi.org/10.5066/P9H5QEAC

Muir, J. B., & Tsai, V. C. (2020). Geometric and level set tomography using ensemble

Kalman inversion. *Geophysical Journal International*, *220*(2), 967–980. https://doi.org/10.1093/gji/ggz472

Muir, J. B., Clayton, R. W., Tsai, V. C., & Brissaud, Q. (2021). Parsimonious velocity inversion applied to the Los Angeles Basin, CA. https://doi.org/10.31223/X5F03K

Nakata, N., Chang, J. P., Lawrence, J. F., & Boué, P. (2015). Body wave extraction and tomography at Long Beach, California, with ambient-noise interferometry. *Journal of Geophysical Research: Solid Earth*, *120*(2), 1159–1173. https://doi.org/10.1002/2015JB011870

Paitz, P., Edme, P., Gräff, D., Walter, F., Doetsch, J., Chalari, A., et al. (2020). Empirical Investigations of the Instrument Response for Distributed Acoustic Sensing (DAS) across 17 Octaves. *Bulletin of the Seismological Society of America*, (Xx). https://doi.org/10.1785/0120200185

Rajaure, S., Asimaki, D., Thompson, E. M., Hough, S., Martin, S., Ampuero, J. P., et al. (2017). Characterizing the Kathmandu Valley sediment response through strong motion recordings of the 2015 Gorkha earthquake sequence. *Tectonophysics*, *714–715*, 146–157. https://doi.org/10.1016/j.tecto.2016.09.030

Schmandt, B., & Clayton, R. W. (2013). Analysis of teleseismic P waves with a 5200-station array in Long Beach, California: Evidence for an abrupt boundary to Inner Borderland rifting. *Journal of Geophysical Research: Solid Earth*, *118*(10), 5320–5338. https://doi.org/10.1002/jgrb.50370

Singh, S. K., Mena, E., & Castro, R. (1988). Some aspects of source characteristics of the 19 September 1985 Michoacan earthquake and ground motion amplification in and near Mexico City from strong motion data. *Bulletin - Seismological Society of America*.

Spica, Z. J., Perton, M., Martin, E. R., Beroza, G. C., & Biondi, B. (2020). Urban Seismic Site Characterization by Fiber-Optic Seismology. *Journal of Geophysical Research: Solid Earth*, *125*(3), 1–29. https://doi.org/10.1029/2019JB018656

Thompson, E. M., Wald, D. J., & Worden, C. B. (2014). A VS30 Map for California with geologic and topographic constraints. *Bulletin of the Seismological Society of America*. https://doi.org/10.1785/0120130312

Wang, H. F., Zeng, X., Miller, D. E., Fratta, D., Feigl, K. L., Thurber, C. H., & Mellors, R. J. (2018). Ground motion response to an ML 4.3 earthquake using co-located distributed acoustic sensing and seismometer arrays. *Geophysical Journal International*, *213*(3), 2020–2036. https://doi.org/10.1093/GJI/GGY102

White, M. C. A., Fang, H., Catchings, R. D., Goldman, M. R., Steidl, J. H., & Ben-Zion, Y. (2021). Detailed traveltime tomography and seismic catalogue around the 2019 Mw7.1 Ridgecrest, California, earthquake using dense rapid-response seismic data. *Geophysical Journal International*, *227*(1), 204–227. https://doi.org/10.1093/gji/ggab224

Wills, C. J., Petersen, M., Bryant, W. A., Reichle, M., Saucedo, G. J., Tan, S., et al. (2000). A site-conditions map for California based on geology and shear-wave velocity. *Bulletin of the Seismological Society of America*, *90*(6 SUPPL.), 187–208. https://doi.org/10.1785/0120000503

Wirth, E. A., Vidale, J. E., Frankel, A. D., Pratt, T. L., Marafi, N. A., Thompson, M., & Stephenson, W. J. (2019). Source-Dependent Amplification of Earthquake Ground Motions in Deep Sedimentary Basins. *Geophysical Research Letters*, *46*(12), 6443–

6450. https://doi.org/10.1029/2019GL082474

Yong, A., Hough, S. E., Iwahashi, J., & Braverman, A. (2012). A terrain-based site-conditions map of california with implications for the contiguous united states. *Bulletin of the Seismological Society of America*, *102*(1), 114–128. https://doi.org/10.1785/0120100262

Yu, C., Zhan, Z., Lindsey, N. J., Ajo-Franklin, J. B., & Robertson, M. (2019). The Potential of DAS in Teleseismic Studies: Insights From the Goldstone Experiment. *Geophysical Research Letters*, *46*(3), 1320–1328. https://doi.org/10.1029/2018GL081195

Zhan, Z. (2019). Distributed acoustic sensing turns fiber-optic cables into sensitive seismic antennas. *Seismological Research Letters*, *91*(1), 1–15. https://doi.org/10.1785/0220190112

Chapter 4

FAULT ZONE IMAGING WITH DISTRIBUTED ACOUSTIC SENSING: SURFACE-TO-SURFACE WAVE SCATTERING

Yang, Y., Zhan, Z., Shen, Z., & Atterholt, J. (2022). Fault Zone Imaging With Distributed Acoustic Sensing: Surface-To-Surface Wave Scattering. *Journal of Geophysical Research: Solid Earth*, 127(6), e2022JB024329. https://doi.org/10.1029/2022JB024329

Abstract

Fault zone complexities contain important information about factors controlling earthquake dynamic rupture. High-resolution fault zone imaging requires high-quality data from dense arrays and new seismic imaging techniques that can utilize large portions of recorded waveforms. Recently, the emerging Distributed Acoustic Sensing (DAS) technique has enabled near-surface imaging by utilizing existing telecommunication infrastructure and anthropogenic noise sources. With dense sensors at several meters' spacing, the unaliased wavefield can provide unprecedented details for fault zones. In this work, we use a DAS array converted from a 10-km underground fiber-optic cable across Ridgecrest City, California. We report clear acausal and coda signals in ambient noise cross-correlations caused by surface-to-surface wave scattering. We use these scattering-related waves to locate and characterize potential faults. The mapped fault locations are generally consistent with those in the USGS Quaternary Fault database of the United States but are more accurate than the extrapolated ones. We also use waveform modeling to infer that a 35-m wide, 90-m deep fault with 30% velocity reduction can best fit the observed scattered coda waves for one of the identified fault zones. These findings demonstrate the potential of DAS for passive imaging of fine-scale faults in an urban environment.

4.1 Introduction

Faults are characterized as damaged material that accommodate localized deformation of rocks (Ben-Zion, 2008). The deformation of fault zone rocks is associated with earthquake generation and rupture process (Perrin et al., 2016; Thakur et al., 2020). The fault material with reduced seismic velocity and altered rheological properties can also amplify ground shaking and influence the migration of hydrocarbons and fluids (Caine et al., 1996; Spudich & Olsen, 2001). Thus, mapping the location and properties of faults is critical for understanding earthquake process and assessing seismic hazard. One common method of mapping faults is the observation of exhumed faults in the field (e.g., Collettini et al., 2009; Faulkner et al., 2003; Mitchell & Faulkner, 2009), which utilizes slices through the fault outcrops. Fault zone drilling projects can extend the examination of fault structure to greater depths and be used to monitor long-term changes in physical properties (e.g., Hickman et al., 2004; Hung et al., 2009). These methods provide precise measurements at single points of observation but require considerable labor and resources. Seismological methods can help develop a more complete picture of subsurface fault characteristics. Earthquake locations and focal mechanisms shed light on fault locations and structural complexities (Ross et al., 2017; Wang & Zhan, 2020). Seismic tomography can produce images of seismic velocity and attenuation near a fault zone (e.g., Allam et al., 2014; Liu et al., 2021; Y. Wang et al., 2019). Fault zone trapped waves recorded by the sensors within the fault zones can be used to model fault zone geometries and properties in detail (e.g., Lewis et al., 2007; Li et al., 2004; Li & Malin, 2008).

The methods above give detailed information on large faults that are visible at the surface or faults with abundant seismicity. Small, buried faults that are not readily visible in the terrain and have little cataloged seismicity may be difficult to discern, yet can contribute to the hidden hazards in urban settings. With the deployment of dense arrays, improved spatial coherence at high frequencies allows noise-based tomography to capture finer details of the subsurface (AlTheyab et al., 2016; Castellanos & Clayton, 2021). Distributed acoustic sensing (DAS) enables repurposing pre-existing telecommunication fiber-optic cables into permanent, cost-effective, dense arrays of strainmeters in urban areas (Lindsey & Martin, 2021; Zhan, 2019). Its working principle is to use optical interferometry on laser photons backscattered from the fiber's intrinsic imperfections to measure strain or strain rate along the fiber. With several meters’ channel spacing, DAS can record unaliased high-frequency wavefields and capture the waves that attenuate too rapidly to be detected by conventional networks. In practice, DAS-recorded ambient noise wavefields have been used successfully for near-surface imaging and fault zone identification (e.g., Cheng et al., 2021; Yang et al., 2021).

In this study we use a DAS array rapidly deployed after the 2019 Ridgecrest M7.1 earthquake (Li et al., 2021). The Ridgecrest earthquake ruptured the Little Lake and the Airport Lake fault zones, and produced numerous aftershocks (Ross et al., 2019). The Little Lake fault zone (LLFZ) is part of the Eastern California shear zone, which is composed of a network of dextral, normal, and dextral-oblique faults (Amos et al., 2013). The DAS array at Ridgecrest City was converted from a underground dark fiber in the city of Ridgecrest, which crossed the southern end of the LLFZ (Figure 4.1). The three mapped fault traces across the DAS array, unlike the northern part of the LLFZ, are not well constrained by the current USGS fault maps and are only inferred with large uncertainty (Figure 4.1). While the primary goal of this DAS array was to study the aftershocks (Li et al., 2021), the unprecedented spatial resolution also offers an opportunity to improve our knowledge of the fault locations and properties.

In this work, we first report evident spurious arrivals (acausal signals that may appear in noise cross-correlation but do not exist in true Green's function) and coda waves in noise cross-correlations related to surface wave scattering. We then use waveform modeling to confirm that the cause of the scattering waves can be faults. With the travel times of the spurious arrivals, we map the fault locations and compare them with current fault maps in this region. With the amplitudes of the coda waves, we constrain the geometry and property of one of the identified faults.

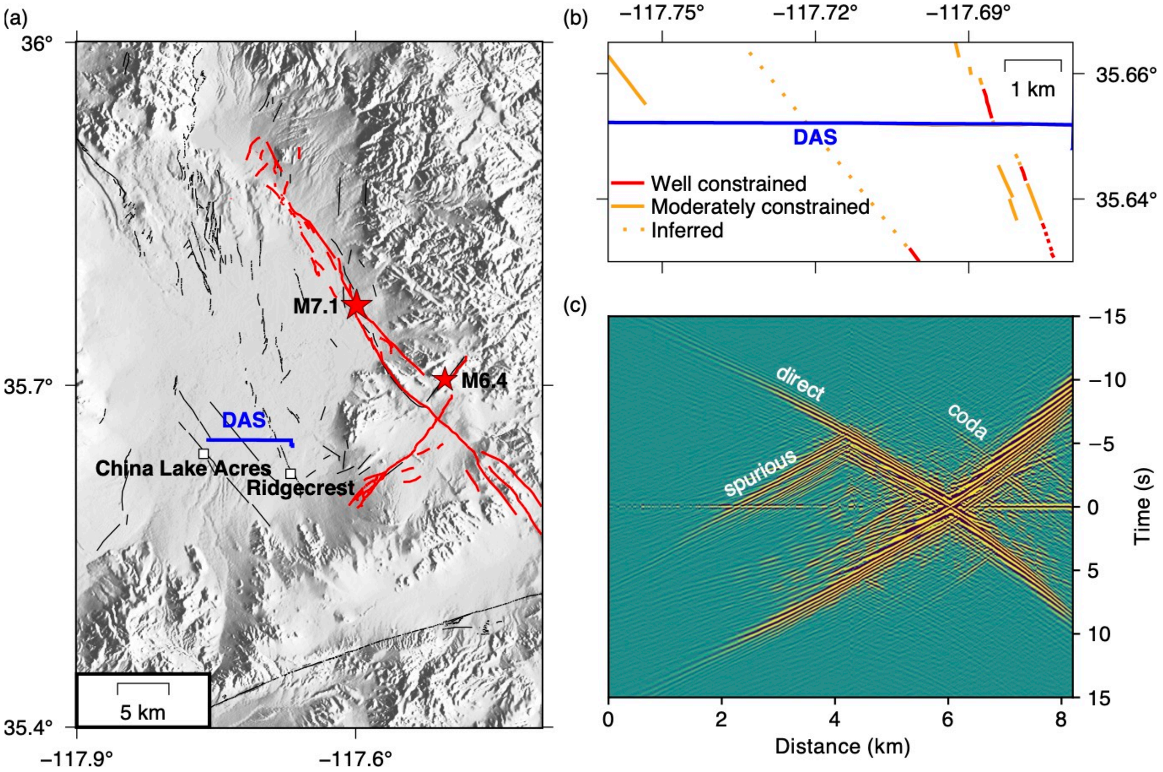

Figure 4.1: Study region and noise cross-correlation example. (a) Map view of the Ridgecrest DAS array. The ground trace of the Ridgecrest DAS array is shown in blue. The M7.1 mainshock and the M6.4 foreshock are marked with the red stars. The fault zones are marked with black lines (Jennings, 1975). The surface rupture of 2019 Ridgecrest M7.1 earthquake is marked in red lines (Brandenberg et al., 2019); (b) A zoomed-in view of the DAS array and the Little Lake fault zone across the array; (c) Example wavefield of ambient noise cross-correlation. The channel at 6-km distance is used as a virtual source. In addition to the direct Rayleigh waves, we observe scattered surface coda waves and spurious arrivals appeared as acausal signals.

4.2 Surface wave scattering

4.2.1 Observation in noise cross-correlations

We repurpose a 10-km telecommunications cable across Ridgecrest City to a DAS array of 1250 channels with 8-meter spacing. In this work we focus on the segment along the W Inyokern Road which is roughly an 8-km linear array. We use continuous data from July to

October 2019 to compute ambient noise cross-correlation. The processing generally follows Bensen et al., (2007), but is modified for higher frequencies. For example, the data are band-pass filtered in [0.1, 10] Hz, and the temporal normalization and spectral whitening are applied to each 1-hour data segment. The detailed noise cross-correlation processing steps have been described in Yang et al., (2021).

An example wavefield of cross-correlations using a channel at 6 km distance as the virtual source to all the channels is shown in Figure 4.1c. In addition to the direct surface waves, we can also observe secondary signals exhibiting either acausal energy (arriving at correlation times earlier than the direct wave) or coda energy (arriving at correlation times later than the direct wave). The acausal and coda energy always emerges from several fixed locations when we move the virtual source along the linear array.

4.2.2 Interpretation with synthetics

Secondary signals have been observed in noise cross-correlations and attributed to a persistent active source or passive scattering from material heterogeneities in the shallow crust (Chang et al., 2016; Ma et al., 2013; Nakata, 2016; Retailleau & Beroza, 2021; Zeng & Ni, 2010; Zhan et al., 2010). The cause of the secondary arrivals in our case of a linear DAS array can be simplified as a 1D scenario. Under this 1D scenario, both the seismic structure and the scatterer extend infinitely in the direction perpendicular to the array. We make this assumption for the following reasons: 1) The dominant contribution to the empirical Green's function comes from the constructive interference of waves generated by the stationary points along the receiver line (Snieder, 2004); 2) The primary noise source is the traffic noise with weekly periodicity (Yang et al., 2021); the colinear geometry of the DAS array and highway means that the vast majority of vehicle-generated surface waves are along the DAS array; 3) The directional sensitivity of DAS emphasizes longitudinal Rayleigh waves along the station pairs more than conventional seismometers (Martin et al., 2018). Based on these considerations, our observed scattering may lack the resolution of a 3D scatterer structure, however, we can still locate and characterize the average scatterer structure close to the DAS array.

The origins of the direct and secondary phases are illustrated in Figure 4.2. For the direct waves, the arrival times are the surface-wave travel times from one receiver to the other (Figure 4.2a, e). For the coda waves, the later arrival times are caused by the cross-correlation between waves traveling from the noise source to one receiver and waves traveling from the noise source to the other receiver but reflected by a passive scatterer. The coda waves' arrival times are the summation of the travel times from the scatterer to both receivers (Figure 4.2b, e). Both direct and coda waves are part of the true Green's functions and their travel times are symmetrical on the positive and negative lag times. It is more appropriate to refer to acausal energy as 'spurious arrivals', as it is not part of the true Green's functions between the receivers. For the 1D scenario here, the spurious arrivals appear when there exists a persistent noise source or a passive scatterer between the receivers (Figure 4.2c, d; Ma et al., 2013; Nakata, 2016). The earlier spurious arrival times in the cross-correlations are the difference between the travel times of the waves from the active source/scatterer to the two receivers (Figure 4.2c, d, e), and are not symmetrical between the positive and negative sides. Note that the intersection of the scattering waves (including spurious arrivals and coda waves) and the direct waves is the location of the active source/passive scatterer. The direct and scattering waves arrive at the same time because the virtual receiver is overlapping with the active source/passive scatterer. Both active sources and passive scatterers can generate spurious arrivals, whereas coda waves can be ascribed only to passive scatterers. Given the clearly observed coda waves in our noise cross-correlations, we believe that scattering from passive scatterers must be the primary cause, if not the only one. Additionally, the aftershocks recorded by the DAS array also display clear body-to-surface converted waves, further confirming the presence of passive scatterers (Atterholt et al., 2022).

We find the location of the scatterers generally coincide with the fault traces across the array, for example, the faults in the middle and the east in Figure 4.1b are close to the interception of direct and scattered waves in Figure 4.1c. To verify that the presence of a fault can result in the observed scattering-related phases, we simulate noise cross-correlations using a fully elastic GPU-based two-dimensional finite difference code (Li et al., 2014). Our background velocity model is based on a recent tomography study along this DAS array (Yang et al.,

2021) and superimposed by a 20-m wide, 40-m deep, rectangular fault with 40% velocity reduction at the distance of 4 km. We place two in-plane noise sources 40 km away from each end of the array. Receivers have the same layout as the DAS array. The simulated wavefield is accurate up to 10 Hz with the grid spacing of 4 m and the time increment of 0. 8 ms. We then cross-correlate the synthetic seismogram recorded at the receiver at 1.6 km with the synthetic seismograms from all the other receivers. Both spurious arrivals and coda waves are visible in the synthetic noise cross-correlation (Figure 4.2e), confirming that the observed scattering waves can be caused by faults.

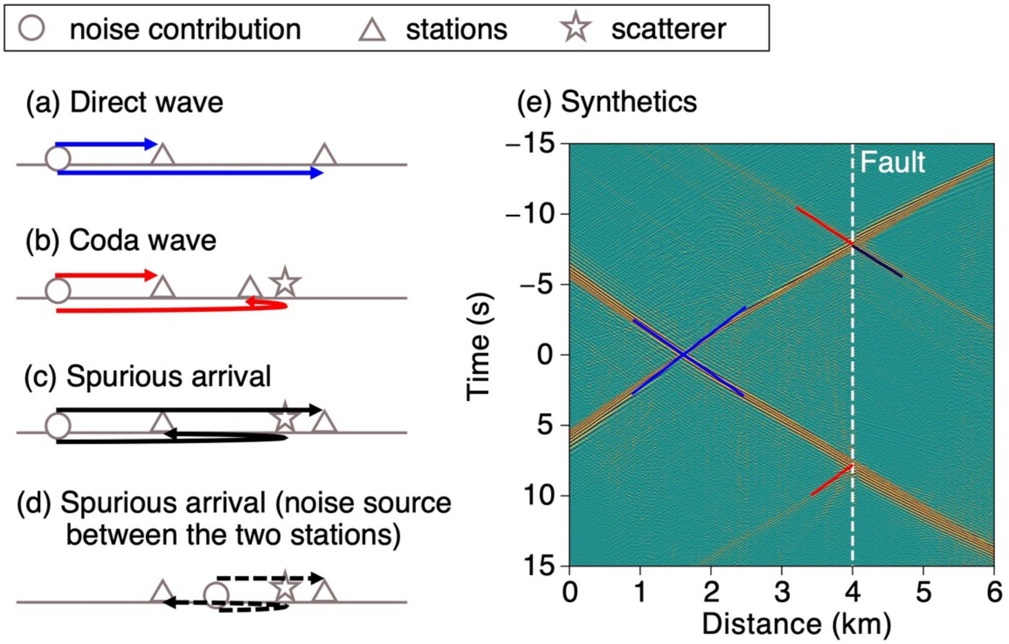

Figure 4.2: Explanation for the cause of the observed scattering waves. (a)-(d) Schematic cartoon showing the generation of the direct waves, coda, and spurious arrivals appeared as acausal signals in the cross-correlation. (e) Synthetic noise cross-correlation using waveform modeling. The noise source is put 40 km away from the array and the fault is at 4 km distance. The virtual source is at 1.6 km distance. The blue, red, and black lines

represent the phases caused by the situations in blue, red, and black lines in Figure 4. 2(a)-(d), respectively.

4.3 Locate the faults with the spurious arrivals

4.3.1 Group velocity inversion for travel-time prediction

Previous regional studies of passive noise scatterers focus on longer periods and usually assume a homogeneous background velocity model to locate the scatterers (Ma et al., 2013; Zeng & Ni, 2010). The lateral variation of the shallow subsurface structure in our case, on the other hand, could have a substantial effect on the mapping resolution. Yang et al., (2021) showed that the shear velocity in the top 30 meters along the Ridgecrest DAS profile has a lateral variation up to ~30% over only 8-km distance. This is illustrated well by the bending in the arrival times of the direct wave group as shown in Figure 4.1c. Therefore, we invert for the group velocity model along the profile. For each channel pair, we apply frequency-time analysis on the envelop of the cross-correlations and get the group velocity dispersion in the period [0.1, 1] s (or the frequency band [1, 10] Hz) averaged over the distance between the channel pair. The approximately one thousand channels provide half million channel pairs for a dense coverage of the profile. We invert for the group velocity dispersion at the 8-m spacing grids along the profile using linear inversion with second-order Tikhonov regularization. The group velocity model shows a slow section in the east end of the profile (Figure 4.3a), which is consistent with the microbasin imaged in the shear wave velocity model using phase velocity (Yang et al., 2021).

Given the group velocity model and assuming all surface waves' ray paths are in-plane, we can predict the frequency-dependent (1-10 Hz) arrival times of direct, spurious, and coda waves for any trial scatterer location. For a channel as virtual source at distance $\boldsymbol{x}_{\mathbf{src}}$, and a receiver channel at distance $\boldsymbol{x}_{\mathbf{rec}}$, the arrival times of the direct waves at frequency $\boldsymbol{f}$ will be

$$\boldsymbol{t}_{\mathbf{direct}}(\boldsymbol{f}) = \pm \int_{x_{\mathrm{src}}}^{x_{\mathrm{rec}}} \frac{\mathbf{1}}{\boldsymbol{v}(\boldsymbol{x}, \boldsymbol{f})} \boldsymbol{dx}, \tag{4.1}$$

where $\boldsymbol{v}(\boldsymbol{x}, \boldsymbol{f})$ denotes the group velocity at the distance $\boldsymbol{x}$ and the frequency $\boldsymbol{f}$, respectively. As described in Section 2, if a fault located at distance $\boldsymbol{x}_{\mathbf{scat}}$ can scatter the seismic waves from the ambient noise, we will observe spurious arrivals or coda waves. If the fault is between the source and receiver channels, there will be spurious arrivals arriving at

$$\boldsymbol{t}_{\mathbf{spurious}}(\boldsymbol{f}) = \left|\int_{x_{\mathrm{scat}}}^{x_{\mathrm{rec}}} \frac{\mathbf{1}}{\boldsymbol{v}(\boldsymbol{x}, \boldsymbol{f})} \boldsymbol{dx}\right| - \left|\int_{x_{\mathrm{src}}}^{x_{\mathrm{scat}}} \frac{\mathbf{1}}{\boldsymbol{v}(\boldsymbol{x}, \boldsymbol{f})} \boldsymbol{dx}\right|. \tag{4.2}$$

If the fault is located on the same side as the source and receiver channels, there will be coda waves arriving at

$$\boldsymbol{t}_{\mathbf{coda}}(\boldsymbol{f}) = \pm \left(\left|\int_{x_{\mathrm{scat}}}^{x_{\mathrm{rec}}} \frac{\mathbf{1}}{\boldsymbol{v}(\boldsymbol{x}, \boldsymbol{f})} \boldsymbol{dx}\right| + \left|\int_{x_{\mathrm{src}}}^{x_{\mathrm{scat}}} \frac{\mathbf{1}}{\boldsymbol{v}(\boldsymbol{x}, \boldsymbol{f})} \boldsymbol{dx}\right|\right). \tag{4.3}$$

In this section we will only use the spurious arrivals for fault localization as they are typically stronger than the coda waves and hence more suitable for stacking. An example of predicted travel times is shown in Figure 4.3b. We calculate the arrival times for direct waves and spurious arrivals at 4 Hz, assuming a fault at 4 km. We can see the spurious arrival times are well predicted, as is the bending feature of the direct waves at the 7-8 km distance.

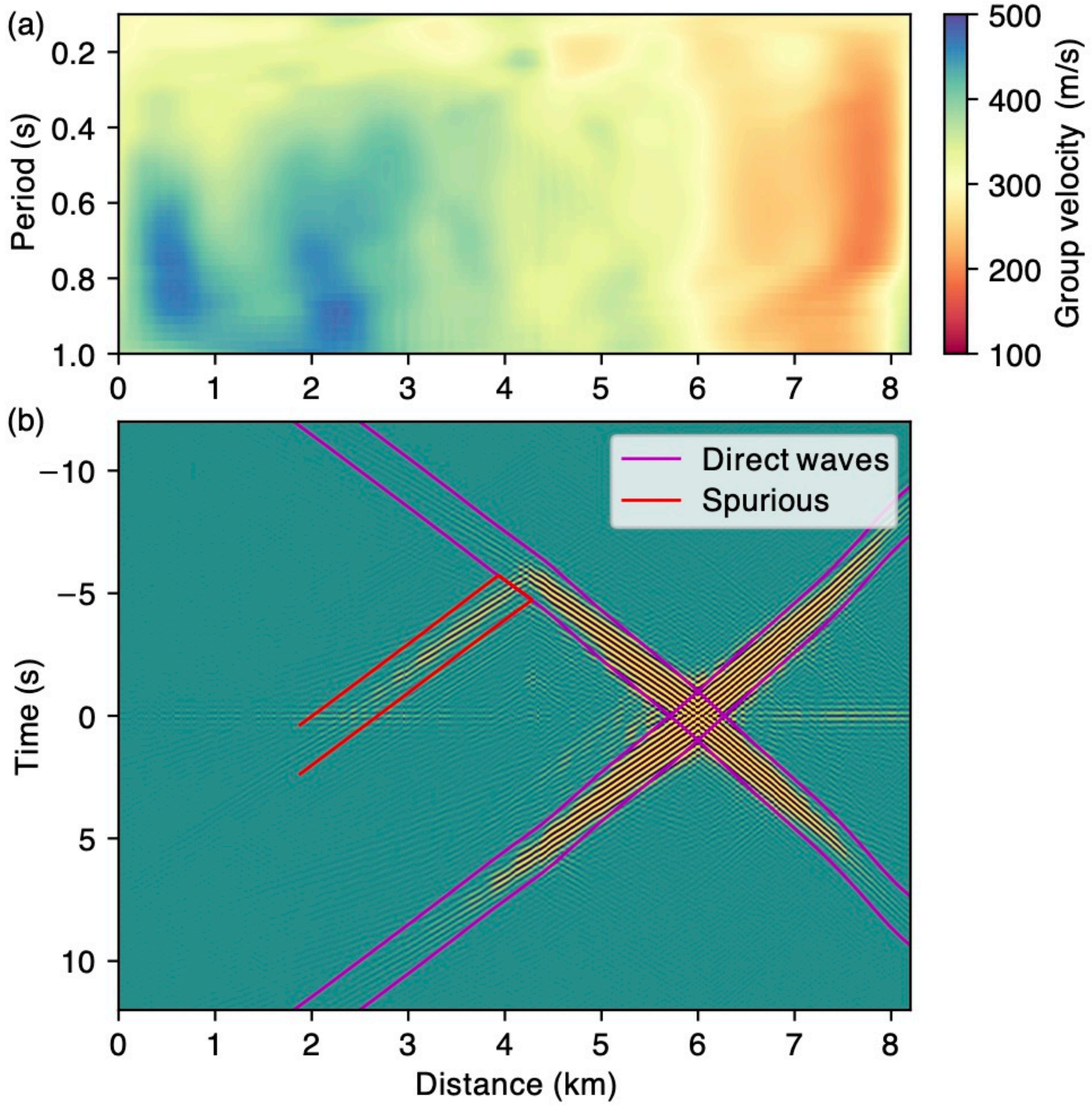

Figure 4.3: Group velocity model and an example of predicted travel times. (a) Group velocity dispersion along the DAS array in the period of [0.1, 1] s inverted from direct surface wave arrival times; (b) Cross-correlation with the virtual source at 6 km, filtered in a narrow frequency band around 4 Hz. The purple and red lines mark the 2-sec time windows around arrival times of direct waves and spurious arrivals, respectively. The

arrival times are calculated by the group velocity model in (a) assuming a scatterer at 4.3 km.

4.3.2 Fault mapping results

We perform a grid search for the scatterer with an 8-m grid spacing. For each trial scatterer location, we calculate the arrival times of the spurious arrivals using equation (4.2). We stack the envelope amplitudes of the cross-correlation over a four-period time window centered on the predicted arrival times and get the maximum stacked amplitude. The stacking is done for narrow frequency bands between 1 Hz and 10 Hz, using frequency-dependent group velocities. All channels can be considered as virtual sources while only the receivers within 1 km distance from the assumed scatterer are used for stacking. We take the median of the maximum stacked amplitude from all virtual sources and create a 'scattering amplitude' profile as shown in a. We detect multiple stripes with high scattering amplitudes in the grid search result, for example, at 1 km, 4.3 km, and 7.3 km. To be more quantitative, we find the local maxima of the scattering amplitudes as indicative of the presence of fault scatterers. We calculate the peak prominence (how much a peak deviates from the surrounding baseline of the signal) for the scattering amplitudes at each frequency. If the peak prominence exceeds a certain threshold, we consider the peak to be a fault candidate.

From the scattering amplitude profile, we can identify several scattering peaks marked with 'A', 'B', 'C', 'D', and the most obvious one throughout all frequencies marked with 'X' (Figure 4.4b). Notable is the closeness of the discovered faults A-D to the USGS-mapped Quaternary faults a-d (Figure 4.4c, Jennings, 1975). In particular, the two closely spaced fault branches 'c', and 'd' in the east that are classified as 'well constrained' are closely located with the two peaks 'C' and 'D' (Figure 4.4b) in our data, with different frequency dependences. The fault in the west ('a' in Figure 4.4c) classified as 'moderately constrained' seems associated with the peak marked with 'A' in Figure 4.4b. For the middle zone where the location is inferred rather than directly observed as stated in the USGS database, we identified two scattering peaks ('B' and 'X' in Figure 4.4b), one at closer location with fault ‘b’ (Figure 4.4c) and the other one about 1 km to the east. In the earthquake body-to-surface wave scattering, the located fault here is also offset to the east, consistent with the more obvious scattering peak ‘X’ in our mapping (Atterholt et al., 2022). Based on the observation and comparison, we believe that the scatterers are indeed related with faults even though their precise positions deviate when there is a lack of constraint in the USGS database.

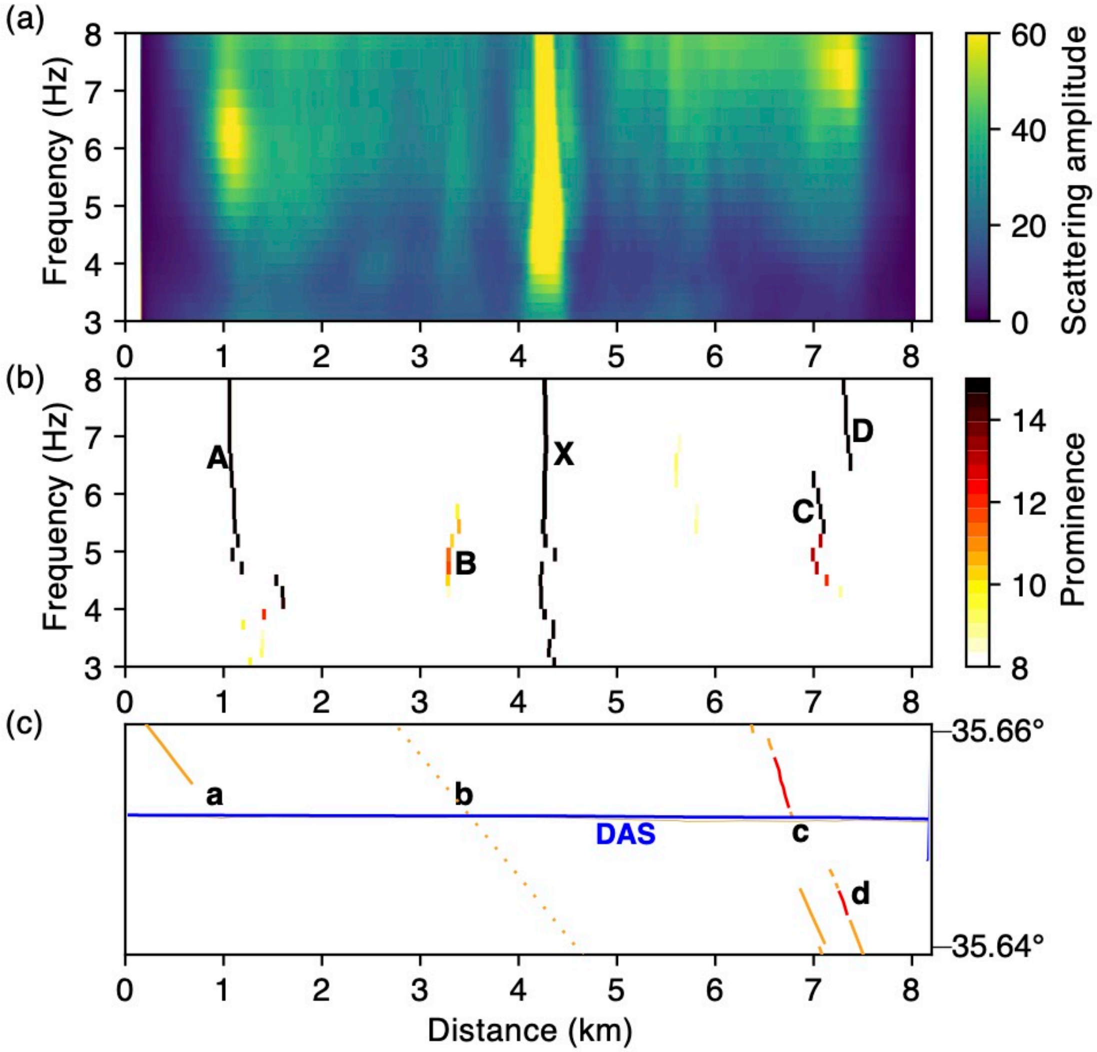

Figure 4.4: Fault mapping results using spurious arrivals. (a) Grid search results for the scatterer location using the stacked amplitudes along the predicted spurious arrival times;

(b) Peak prominence of the scattering amplitudes in (a), which is calculated individually for each frequency; (c) The DAS array with the USGS mapped fault traces. The legend is the same as that seen in Figure 4.1b. The fault traces are closely aligned with some of the detected scatterers in (b).

4.4 Resolving fault zone property with coda waves

With fault locations being accurately mapped, we aim to further investigate the fault zone properties. However, the strength of the stacked spurious arrival amplitudes in Section 3 does not necessarily represent fault zone properties. As shown in Figure 4.2d, spurious arrivals can be caused not only by far-field noise sources within stationary zones, but also by noise sources between receiver pairs. In the case of the Ridgecrest DAS array, which is located alongside a highway with traffic as the dominant source of noise, the variation of amplitude among the scatterers might be due to noise source attributes rather than the scatterer strength. Therefore, the spurious arrivals' amplitudes are affected largely by their noise sources and are difficult to quantify because they don't share the same noise source as the direct waves (Figure 4.2d; see section 5.1 for more detailed discussion). In contrast, the coda waves are part of the true Green's function between the two sensors and share the same contributions from noise sources within the stationary zones as the direct waves. In this section, we develop a framework to use the coda waves in noise interferometry to resolve fault zone characteristics.

4.4.1 Reflection/transmission coefficient ratio

Given a virtual source, the direct wave amplitude in the cross-correlation of the channel on the opposite side of the fault from the source channel can be written as

$$A_{\mathrm{direct}}(f) = A_{\mathrm{CCproc}}(f) A_{\mathrm{src}}(f) A_{\mathrm{path}}(x, f) T(f), \tag{4.4}$$

where f is the frequency, A_{CCproc} is the amplitude response due to cross-correlation processing, A_{src} is the source effect on the amplitude, A_{path} is the path attenuation effect, x is the location of the receiver channel, and T is the transmission coefficient related to the fault properties. Similarly, the coda wave amplitude in the cross-correlation of the channel on the same side as the fault from the source channel can be expressed as

$$A_{\mathrm{coda}}(f) = A_{\mathrm{CCproc}}(f) A_{\mathrm{src}}(f) A'_{\mathrm{path}}(x, f) R(f), \tag{4.5}$$

where R is the reflection coefficient related to the fault properties. Although it has long been debated whether the absolute amplitude in cross-correlations is usable, taking the amplitude ratio can cancel out the A_{CCproc} term caused by the common processing in the cross-correlation calculation. In addition, if we carefully select two receiver channels that are symmetrical and close enough to the located fault, the path-related attenuation term A_{path} and A'_{path} should be almost identical. The ray paths of the direct and coda waves are shown in Figure 4.5a. Now, if we divide coda wave amplitudes by direct wave amplitudes recorded on two symmetrical channels, we have

$$\frac{A_{\mathrm{coda}}(f)}{A_{\mathrm{direct}}(f)} = \frac{R(f)}{T(f)}. \tag{4.6}$$

The concept is that $\frac{A_{\mathrm{coda}}(f)}{A_{\mathrm{direct}}(f)}$ represents the fault properties and should be independent of source or receiver location. In this equation, we don't take fault zone attenuation and site effect into consideration, because these effects are negligible in our case of a small, shallow fault without strong material contrast on its two sides. However, for future applications on major fault zones, these factors should be calculated using the velocity model and incorporated in the equation.

4.4.2 R/T dispersion measurements and modeling results

We take the identified fault 'X' at around 4 km (Figure 4.4) as an example to resolve its property with the reflection/transmission coefficient ratio method. Given the locations of virtual source, receivers, and faults, we can predict the travel times of direct and coda waves using equations (4.1) and (4.3). We cut a window with a frequency-dependent length around the predicted travel times and measure the peak envelop amplitude. Then the reflection/transmission coefficient R/T is determined with equation (4.6). As shown in Figure

4.5, we select a virtual source and filter the cross-correlations in narrow frequency bands. For each pair of channels with the same distance to the fault, we can get the associated R/T ratio. We avoid the channels closest to the fault because coda waves overlap with direct waves. When we shift the channel pair further away from the fault, the measured R/T remains steady (Figure 4.5c, e). We can also shift virtual sources and repeat the process. The measurements confirm our statement in Section 4.1 that R/T is independent of source location and receiver-to-fault distance. We can see a distinct increase of R/T from 0.12 at 2.5 Hz to 0.16 at 4.5 Hz, indicating clear frequency dependency (Figure 4.5b-e). Using all available virtual sources and symmetrical channel pairs within 1.2 km from the fault, we can construct the R/T dispersion curve with uncertainty Figure 4.6d). The dispersion curve is between 1.5 and 6 Hz because coda waves are difficult to observe outside of this frequency range.

To better understand what the observed R/T dispersion means for fault properties, we simulate the R/T dispersion curves for different fault models using waveform modeling. Many fault parameters, such as fault zone width, depth extent, dipping angle, velocity, attenuation, and country-rock velocities, can influence seismic observations (Lewis & Ben-Zion, 2010; Li et al., 2004; Thurber, 2003). With only the R/T dispersion curve, there will certainly be large trade-offs among the many model parameters and it's impossible to solve all of them properly. In this work, we intend to have a simple quantitative model that can explain the observed main features adequately well. Therefore, we simplify a fault zone as a rectangular shape with three most common parameters: fault zone width w, depth extent h, and shear velocity reduction Δv (Figure 4.5a).

We use a high-resolution shear velocity model along the DAS array as background velocity and embed the rectangular fault in the mapped locations (Yang et al., 2021). The P-wave and density models are calculated with empirical relations in the crust (Brocher, 2005). We perform a rough grid search for the three parameters. For each set of the parameters, we use the fully elastic two-dimensional finite difference code with a grid spacing of 4 m and a time increment of 0. 8 ms to ensure accurate simulations up to 10 Hz (Li et al., 2014). Since the coda waves in cross-correlations correspond to the fault-reflected waves in the true Green's function, we directly put the source at the virtual source location without calculating cross-correlations to expedite the grid search process. For the simulated wavefield, we apply the same procedure that we apply to the data to track the travel times of direct and reflected waves and then calculate the R/T dispersion using the peak envelop amplitudes. We use grid search on the set of parameters to do a least squares fitting between observed and synthetic R/T dispersion. Our grid search results show that the data is best fitted by a 35-m wide, 90-m deep fault with 30% reduction in shear velocity (Figure 4.6). When we set each of the three parameters to the value of the best-fitted model and examine the two-dimensional grid search results, we find that the fault width and velocity reduction are both well resolved whereas the depth extent is the least resolved (Figure 4.6a~c). Theoretically, our frequency band may limit the depth resolution. The sensitivity kernel computed from the velocity model along the DAS array suggests the lowest frequency of 1.5 Hz is most sensitive to the top 100-200 meters. The lower bound of frequency is limited by the noise source property and DAS array aperture. We anticipate that future DAS arrays with longer interrogation range will improve the sensitivity to greater depth.

The resolved fault zone parameters hold important information for fault dynamics. We refer to the characterized low-velocity zone as the fault damage zone. According to field studies on outcrops over different regions, damage zone width can vary from tens of meters to kilometers and is thought to have a scaling law with fault displacement. Even though different regressed scaling relations including linear, logarithm and power laws can span over three orders of magnitude, the damage zone width generally have a positive correlation with fault displacement (Choi et al., 2016; Faulkner et al., 2011; Fossen & Hesthammer, 2000). Our resolved 35-meter wide damage zone could imply a medium-size fault with a fault displacement-damage zone width ratio close to 1 (Torabi & Berg, 2011). On the other hand, our estimated 30% shear wave reduction of the fault damage zone is surprisingly comparable to that of those major faults (20%~60%) studied by fault zone trapped waves (e.g., Lewis & Ben-Zion, 2010; Li et al., 2004). The velocity reduction together with damage zone width and depth can guide numerical modeling of earthquake dynamic ruptures and even long-term earthquake behaviors such as the earthquake cycle duration and potential maximum magnitudes (Huang et al., 2014; Thakur et al., 2020; Weng et al., 2016).

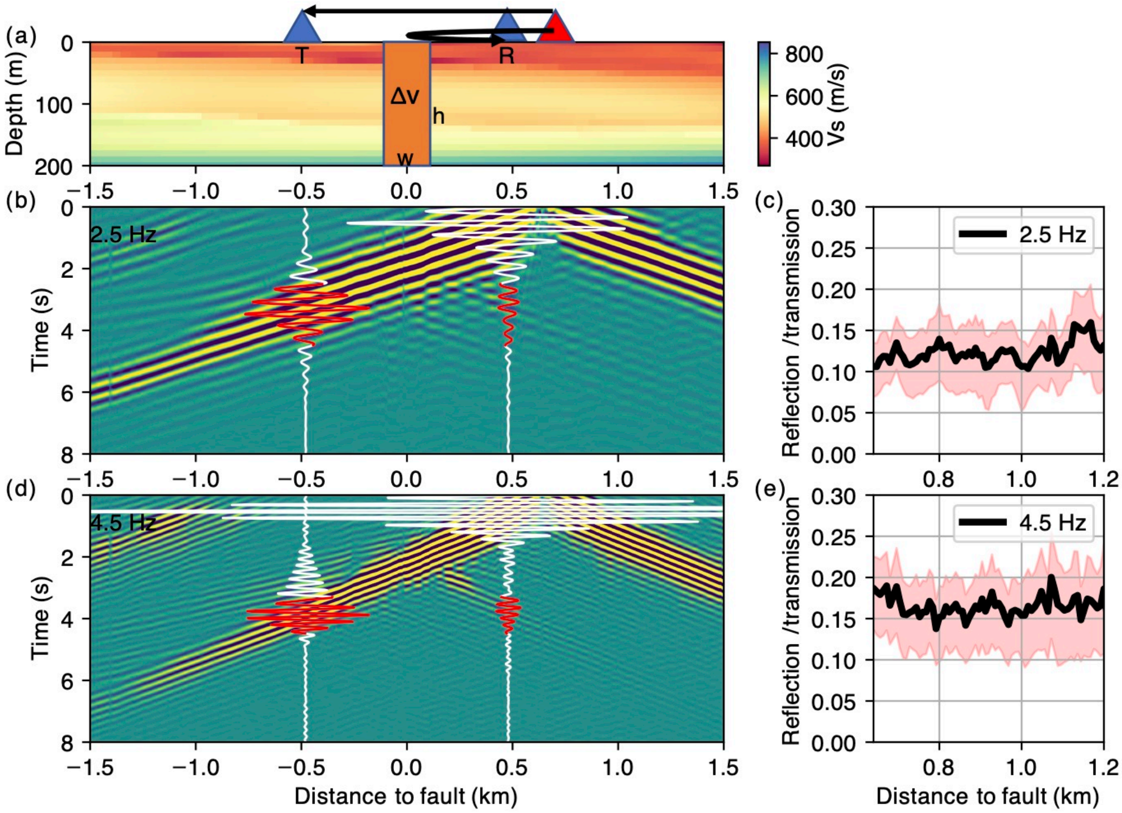

Figure 4.5: The illustration of reflection/transmission coefficient ratio and the observed frequency dependency. (a) A two-dimensional background shear velocity model with a simplified rectangular fault in the center. The red triangle represents the channel as virtual source. The blue triangles represent two symmetrical receiver channels regarding the fault. R: reflected wave amplitude, which can be measured by the coda wave amplitude; T: transmitted wave amplitude, which can be measured by the direct wave amplitude; Δv: velocity reduction; w: fault width; h: fault depth; (b) 2.5 Hz cross-correlation record section, the waveforms of the two symmetrical channels are plotted in white lines, with the red portion of the waveform used to measure R and T. (c) R/T measurements at symmetric channel pairs at different distances from the fault. The uncertainty is determined by using

100 different virtual sources; (d) (e) are similar to (b) (c) respectively but for the frequency of 4.5 Hz.

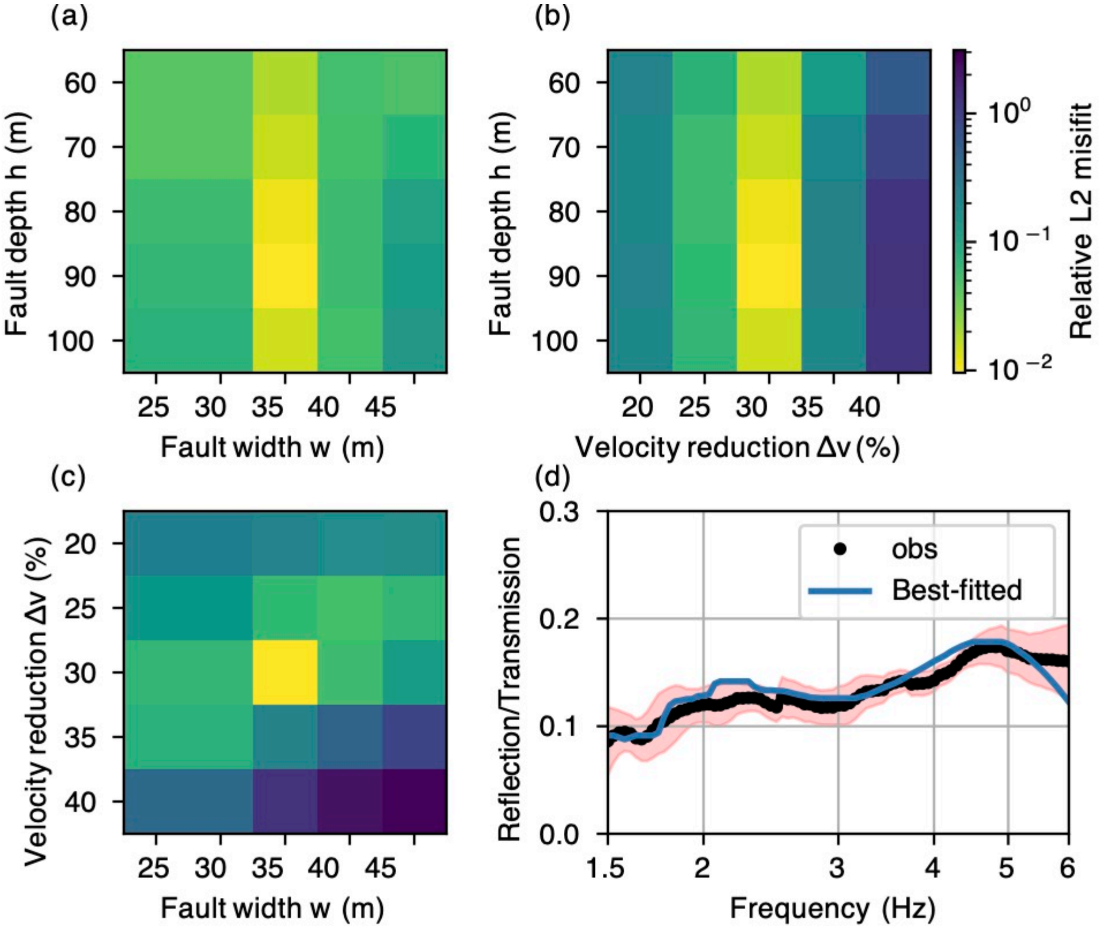

Figure 4.6: Grid search results of fitting the observed R/T data using waveform modeling. (a)(b)(c) are two-dimensional slices showing the misfit variation with fixed velocity reduction, fault width, and fault depth, respectively. The parameters are fixed at the value of the best-fitted model. (d) The R/T dispersion curve measured by the observed data (black) and the synthetic data using the best-fitted model (blue). The data uncertainty in the red shaded area is calculated by the two times the standard deviation of the measurements from all available virtual sources and symmetrical channel pairs.

4.5 Discussion

4.5.1 Understanding the amplitude of spurious arrivals

For a passive scatterer, both spurious arrivals and coda waves are generated by the scattered seismic waves, which is expected to have less coherence and thus weaker amplitudes in the cross-correlations compared to the direct waves. In our observation, all the coda waves have less than 20% amplitude of the direct waves. Some spurious arrivals are stronger than coda waves but remain weaker than direct waves, e.g., at 5.3 km and 7 km (Figure 4.3b). Some spurious arrivals have exceptionally high amplitudes that are comparable to, if not higher than, the amplitudes of direct wave, e.g., at 4.3 km (Figure 4.1c, Figure 4.3b). It was also observed in recent studies of the Wasatch fault in Salt Lake City, Utah, and the Tanlu fault zone in Eastern China that spurious arrivals arising exactly at the fault have amplitudes comparable to direct waves (Gkogkas et al., 2021; Gu et al., 2021).

Here we show that the high amplitudes of spurious arrivals do not necessarily indicate a particularly strong fault or the presence of active source at the located fault. Instead, the cause could be near-field noise sources. As shown in Figure 4.2d, noise sources between the cross-correlated channel pairs can contribute to spurious arrivals but not to direct waves. This is most certainly the case in our instance because the primary noise source is traffic everywhere along the cable. The less attenuation of the seismic energy from near-field sources may add to the high coherence and subsequent strong spurious arrivals in the cross-correlations. We perform a synthetic test using the two-dimensional finite difference simulation. For this conceptual test, we use a one-dimensional velocity model averaged from the tomography model along this DAS array and add a rectangular fault. The fault parameters are the same as the one used in Section 2.2. We put 20 far-field sources 40 km away from each end of the array and 15 near-field sources evenly distributed from 2 km to 5 km distance (Figure 4.7a). The synthetic seismogram is then cross correlated between the receiver at 6.2 km and all other receivers. The simulated cross-correlation wavefield confirms that the within-array noise sources can produce spurious arrivals stronger than direct waves, even though no noise source is placed right at the fault (Figure 4.7b). This explains why we must use the weaker coda waves to characterize the fault zone structures, rather than the spurious arrivals.

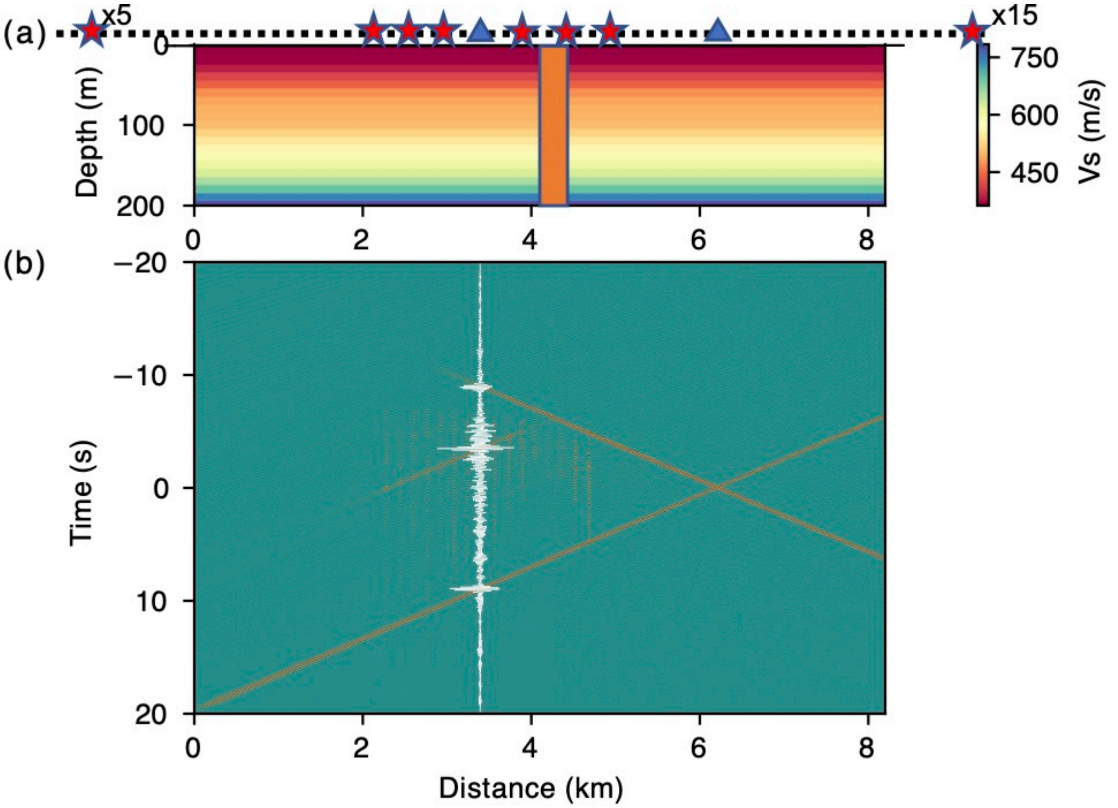

Figure 4.7: Synthetic noise cross-correlation using waveform modeling. (a) The velocity model used in simulation. Red stars denote the noise sources. In addition to the far-field noise sources in the stationary points, we put several noise sources inside the array. Blue triangles show the two channels, between which the cross-correlation is plotted as the white waveform in (b). The orange rectangle represents the fault. (b) The cross-correlation wavefield. The blue triangle on the right in (a) is the virtual source.

4.5.2 Implications for fault imaging at shallow depth

Shallow structures in the top hundreds of meters in general have low seismic velocities, high attenuation, high Vp/Vs ratios, and heterogeneities across very small distances that are challenging to study (e.g., Liu et al., 2015; Qin et al., 2020). Noise interferometry with high-resolution, high-frequency seismic experiments can help enhance our visions on the shallow structure and associated seismic hazards (Castellanos & Clayton, 2021; Yang et al., 2021). Shallow fault complexities such as the splayed features and localized fault-related shallow sources can further contribute to seismic hazards (e.g., Gradon et al., 2021; Huang & Liu, 2017). Our study using high-frequency surface wave scattering in DAS noise interferometry can capture the faulting structure at the top 100 m and discern different faults at sub-kilometer scales (Figure 4.4). We also show the accuracy of the mapped fault locations by comparing to the USGS Quaternary fault map and the results from earthquake body-to-surface wave scattering. We then use coda wave amplitudes to give the best-fitting model of the identified shallow fault. The resulted fault geometry is close to that characterized by earthquake body-to-surface wave scattering, which is a good verification of this method (Atterholt et al., 2022). The two methods using scattering from different types of waves have complementary sensitivity kernels. For example, body-to-surface wave scattering can discern fault depth of burial at very shallow depth by using high-frequency waves while the reflection/transmission coefficient ratio in this work is particularly sensitive to fault zone velocity reduction. Although we do not know whether these located shallow faults are branches that are connected at depth, the mapped shallow locations indicate possible paths that the earthquake rupture can propagate to the surface.

DAS is particularly useful for studying logistically difficult regions, including marine, volcanic, and glacial regions (Lindsey et al., 2019; Nishimura et al., 2021; Walter et al., 2020). This method of passive imaging with DAS can be beneficial for fault detection and imaging for the cases that surface evidence or seismicity catalog is not accessible.

4.6 Conclusions

In this work we apply noise interferometry on a 10-km DAS array with 8 meters' spacing in Ridgecrest, California. The dense nature of DAS allows for the recovery of unprecedented wavefield details. We report clear surface wave scattering in noise cross-correlation functions including scattered coda waves and spurious arrivals that do not exist in true Green's functions. We use waveform modeling to show that the observed scattered waves can be caused by faults with velocity reduction. We use travel times of the spurious arrivals to map the fault locations. We locate several strong fault scatterers that are generally consistent with the USGS fault map but with refined locations. We further use amplitudes of the coda waves to characterize the geometry and velocity reduction of the mapped faults. We identify a 35-m wide, 90-m deep fault with 30% velocity reduction for one of the identified fault zones. Our results suggest a viable application of DAS for refining prior fault maps or imaging hidden faults at top 100 meters at high lateral resolution in urban areas.

References

Allam, A. A., Ben-Zion, Y., Kurzon, I., & Vernon, F. (2014). Seismic velocity structure in the Hot Springs and Trifurcation areas of the San Jacinto fault zone, California, from double-difference tomography. *Geophysical Journal International*, *198*(2), 978–999. https://doi.org/10.1093/gji/ggu176

AlTheyab, A., Lin, F. C., & Schuster, G. T. (2016). Imaging near-surface heterogeneities by natural migration of backscattered surface waves. *Geophysical Journal International*, *204*(2), 1332–1341. https://doi.org/10.1093/gji/ggv511

Amos, C. B., Brownlee, S. J., Rood, D. H., Burch Fisher, G., Bürgmann, R., Renne, P. R., & Jayko, A. S. (2013). Chronology of tectonic, geomorphic, and volcanic interactions and the tempo of fault slip near Little Lake, California. *Bulletin of the Geological Society of America*, *125*(7–8), 1187–1202. https://doi.org/10.1130/B30803.1

Atterholt, J., Zhan, Z., & Yang, Y. (2022). Fault zone imaging with distributed acoustic sensing: body-to-surface wave scattering. https://doi.org/10.1002/ESSOAR.10510749.1

Ben-Zion, Y. (2008). Collective Behavior of Earthquakes and Faults. *Reviews of Geophysics*, *46*, 1–70. https://doi.org/10.1029/2008RG000260.1.INTRODUCTION

Bensen, G. D., Ritzwoller, M. H., Barmin, M. P., Levshin, A. L., Lin, F., Moschetti, M. P., et al. (2007). Processing seismic ambient noise data to obtain reliable broad-band surface wave dispersion measurements. *Geophysical Journal International*, *169*(3), 1239–1260. https://doi.org/10.1111/j.1365-246X.2007.03374.x

Brandenberg, S. J., Wang, P., Nweke, C. C., Hudson, K., Mazzoni, S., Bozorgnia, Y., et al. (2019). Preliminary Report on Engineering and Geological Effects of the July 2019 Ridgecrest Earthquake Sequence, Report of the NSF-Sponsored Geotechnical Extreme Event Reconnaissance Association, (July), 1–77. https://doi.org/10.18118/G6H66K

Brocher, T. M. (2005). Empirical Relations between Elastic Wavespeeds and Density in the Earth's Crust. *Bulletin of the Seismological Society of America*, *95*(6), 2081–2092. https://doi.org/10.1785/0120050077

Caine, J. S., Evans, J. P., & Forster, C. B. (1996). Fault zone architecture and permeability structure. *Geology*, *24*(11), 1025–1028. https://doi.org/10.1130/0091-7613(1996)024<1025:FZAAPS>2.3.CO;2

Castellanos, J. C., & Clayton, R. W. (2021). The Fine-Scale Structure of Long Beach, California, and Its Impact on Ground Motion Acceleration. *Journal of Geophysical Research: Solid Earth*, *126*(12). https://doi.org/10.1029/2021jb022462

Chang, J. P., de Ridder, S. A. L., & Biondi, B. L. (2016). High-frequency Rayleigh-wave tomography using traffic noise from Long Beach, California. *Geophysics*, *81*(2), B1–B11. https://doi.org/10.1190/GEO2015-0415.1

Cheng, F., Chi, B., Lindsey, N. J., Dawe, T. C., & Ajo-Franklin, J. B. (2021). Utilizing distributed acoustic sensing and ocean bottom fiber optic cables for submarine structural characterization. *Scientific Reports*, *11*(1), 1–14. https://doi.org/10.1038/s41598-021-84845-y

Choi, J. H., Edwards, P., Ko, K., & Kim, Y. S. (2016). Definition and classification of fault damage zones: A review and a new methodological approach. *Earth-Science Reviews*, *152*, 70–87. https://doi.org/10.1016/j.earscirev.2015.11.006

Collettini, C., Niemeijer, A., Viti, C., & Marone, C. (2009). Fault zone fabric and fault weakness. *Nature*, *462*(7275), 907–910. https://doi.org/10.1038/nature08585

Faulkner, D. R., Lewis, A. C., & Rutter, E. H. (2003). On the internal structure and mechanics of large strike-slip fault zones: Field observations of the Carboneras fault in southeastern Spain. *Tectonophysics*, *367*(3–4), 235–251. https://doi.org/10.1016/S0040-1951(03)00134-3

Faulkner, D. R., Mitchell, T. M., Jensen, E., & Cembrano, J. (2011). Scaling of fault damage zones with displacement and the implications for fault growth processes. *Journal of Geophysical Research: Solid Earth*, *116*(5), 1–11. https://doi.org/10.1029/2010JB007788

Fossen, H., & Hesthammer, J. (2000). <JSG 2000 Fossen Hesthammer.pdf>, *22*, 851–863.

Gkogkas, K., Lin, F. C., Allam, A. A., & Wang, Y. (2021). Shallow damage zone structure of the wasatch fault in Salt Lake City from ambient-noise double beamforming with a temporary linear array. *Seismological Research Letters*, *92*(4), 2453–2463. https://doi.org/10.1785/0220200404

Gradon, C., Roux, P., Moreau, L., Lecointre, A., & Ben Zion, Y. (2021). Characterization with dense array data of seismic sources in the shallow part of the San Jacinto fault zone. *Geophysical Journal International*, *224*(2), 1133–1140. https://doi.org/10.1093/gji/ggaa411

Gu, N., Zhang, H., Nakata, N., & Gao, J. (2021). Fault detection by reflected surface waves based on ambient noise interferometry. *Earthquake Research Advances*, *1*(4), 100035. https://doi.org/10.1016/j.eqrea.2021.100035

Hickman, S., Zoback, M., & Ellsworth, W. (2004). Introduction to special section: Preparing for the San Andreas Fault Observatory at Depth. *Geophysical Research Letters*, *31*(12), 10–13. https://doi.org/10.1029/2004GL020688

Huang, L., & Liu, C. Y. (2017). Three Types of Flower Structures in a Divergent-Wrench Fault Zone. *Journal of Geophysical Research: Solid Earth*, *122*(12), 10,478-10,497. https://doi.org/10.1002/2017JB014675

Huang, Y., Ampuero, J., & Helmberger, D. V. (2014). Earthquake ruptures modulated by waves in damaged fault zones. *Journal of Geophysical Research: Solid Earth*, *119*(4), 3133–3154. https://doi.org/10.1002/2013JB010724

Hung, J. H., Ma, K. F., Wang, C. Y., Ito, H., Lin, W., & Yeh, E. C. (2009). Subsurface structure, physical properties, fault-zone characteristics and stress state in scientific drill holes of Taiwan Chelungpu Fault Drilling Project. *Tectonophysics*, *466*(3–4), 307–321. https://doi.org/10.1016/j.tecto.2007.11.014

Jennings, C. W. (1975). *Fault map of California with locations of volcanoes, thermal springs, and thermal wells: California Division of Mines and Geology California Geologic Data Map 1, scale 1:750,000.*

Lewis, M. A., & Ben-Zion, Y. (2010). Diversity of fault zone damage and trapping structures in the Parkfield section of the San Andreas Fault from comprehensive analysis of near fault seismograms. *Geophysical Journal International*, *183*(3), 1579–1595. https://doi.org/10.1111/j.1365-246X.2010.04816.x

Lewis, M. A., Ben-Zion, Y., & McGuire, J. J. (2007). Imaging the deep structure of the San Andreas Fault south of Hollister with joint analysis of fault zone head and direct P arrivals. *Geophysical Journal International*, *169*(3), 1028–1042. https://doi.org/10.1111/j.1365-246X.2006.03319.x

Lewis, Michael A., & Ben-Zion, Y. (2010). Diversity of fault zone damage and trapping structures in the Parkfield section of the San Andreas Fault from comprehensive analysis of near fault seismograms. *Geophysical Journal International*, *183*(3), 1579–1595. https://doi.org/10.1111/j.1365-246X.2010.04816.x

Li, D., Helmberger, D., Clayton, R. W., & Sun, D. (2014). Global synthetic seismograms using a 2-D finite-difference method. *Geophysical Journal International*, *197*(2), 1166–1183. https://doi.org/10.1093/gji/ggu050

Li, Y., & Malin, P. E. (2008). San Andreas Fault damage at SAFOD viewed with fault-guided waves. *Geophysical Research Letters*, *35*(8), 1–6. https://doi.org/10.1029/2007GL032924

Li, Y., Vidale, J. E., & Cochran, E. S. (2004). Low-velocity damaged structure of the San Andreas Fault at Parkfield from fault zone trapped waves. *Geophysical Research Letters*, *31*(12), 1–5. https://doi.org/10.1029/2003GL019044

Li, Z., Shen, Z., Yang, Y., Williams, E., Wang, X., & Zhan, Z. (2021). Rapid Response to the 2019 Ridgecrest Earthquake With Distributed Acoustic Sensing. *AGU Advances*, *2*(2). https://doi.org/10.1029/2021av000395

Lindsey, N. J., & Martin, E. R. (2021). Fiber-Optic Seismology. *Annual Review of Earth and Planetary Sciences*, *49*(1), 309–336. https://doi.org/10.1146/annurev-earth-072420-065213

Lindsey, N. J., Craig Dawe, T., & Ajo-Franklin, J. B. (2019). Illuminating seafloor faults and ocean dynamics with dark fiber distributed acoustic sensing. *Science*, *366*(6469), 1103–1107. https://doi.org/10.1126/science.aay5881

Liu, X., Ben-Zion, Y., & Zigone, D. (2015). Extracting seismic attenuation coefficients from cross-correlations of ambient noise at linear triplets of stations. *Geophysical Journal International*, *203*(2), 1149–1163. https://doi.org/10.1093/gji/ggv357

Liu, X., Beroza, G. C., Yang, L., & Ellsworth, W. L. (2021). Ambient noise Love wave attenuation tomography for the LASSIE array across the Los Angeles basin. *Science Advances*, *7*(22), 2–8. https://doi.org/10.1126/sciadv.abe1030

Ma, Y., Clayton, R. W., Tsai, V. C., & Zhan, Z. (2013). Locating a scatterer in the active volcanic area of Southern Peru from ambient noise cross-correlation. *Geophysical Journal International*, *192*(3), 1332–1341. https://doi.org/10.1093/gji/ggs103

Martin, E. R., Lindsey, N. J., Ajo-Franklin, J. B., & Biondi, B. (2018). Introduction to Interferometry of Fiber Optic Strain Measurements. *EarthArXiv*, *2*, 1–33.

Mitchell, T. M., & Faulkner, D. R. (2009). The nature and origin of off-fault damage surrounding strike-slip fault zones with a wide range of displacements: A field study from the Atacama fault system, northern Chile. *Journal of Structural Geology*, *31*(8), 802–816. https://doi.org/10.1016/j.jsg.2009.05.002

Nakata, N. (2016). Near-surface S-wave velocities estimated from traffic-induced Love waves using seismic interferometry with double beamforming. *Interpretation*, *4*(4), SQ23–SQ31. https://doi.org/10.1190/INT-2016-0013.1

Nishimura, T., Emoto, K., Nakahara, H., Miura, S., Yamamoto, M., Sugimura, S., et al. (2021). Source location of volcanic earthquakes and subsurface characterization using fiber-optic cable and distributed acoustic sensing system. *Scientific Reports*, *11*(1), 1–12. https://doi.org/10.1038/s41598-021-85621-8

Perrin, C., Manighetti, I., Ampuero, J.-P., Cappa, F., & Gaudemer, Y. (2016). Location of largest earthquake slip and fast rupture controlled by along-strike change in fault structural maturity due to fault growth. *Journal of Geophysical Research: Solid Earth*, *121*(5), 3666–3685. https://doi.org/10.1002/2015JB012671

Qin, L., Ben-Zion, Y., Bonilla, L. F., & Steidl, J. H. (2020). Imaging and Monitoring Temporal Changes of Shallow Seismic Velocities at the Garner Valley Near Anza, California, Following the M7.2 2010 El Mayor-Cucapah Earthquake. *Journal of Geophysical Research: Solid Earth*, *125*(1), 1–17. https://doi.org/10.1029/2019JB018070

Qiu, H., Allam, A. A., Lin, F. C., & Ben-Zion, Y. (2020). Analysis of Fault Zone Resonance Modes Recorded by a Dense Seismic Array Across the San Jacinto Fault Zone at Blackburn Saddle. *Journal of Geophysical Research: Solid Earth*, *125*(10), 1–21. https://doi.org/10.1029/2020JB019756

Retailleau, L., & Beroza, G. C. (2021). Towards structural imaging using seismic ambient field correlation artefacts. *Geophysical Journal International*, *225*(2), 1453–1465. https://doi.org/10.1093/gji/ggab038

Ross, Z. E., Hauksson, E., & Ben-Zion, Y. (2017). Abundant off-fault seismicity and orthogonal structures in the San Jacinto fault zone. *Science Advances*, *3*(3). https://doi.org/10.1126/sciadv.1601946

Ross, Z. E., Idini, B., Jia, Z., Stephenson, O. L., Zhong, M., Wang, X., et al. (2019). 2019 Ridgecrest earthquake sequence. *Science*, *3665*(October), 346–351.

Snieder, R. (2004). Extracting the Green's function from the correlation of coda waves: A derivation based on stationary phase. *Physical Review E - Statistical Physics, Plasmas, Fluids, and Related Interdisciplinary Topics*. https://doi.org/10.1103/PhysRevE.69.046610

Spudich, P., & Olsen, K. B. (2001). Fault zone amplified waves as a possible seismic hazard along the Calaveras Fault in central California. *Geophysical Research Letters*, *28*(13), 2533–2536. https://doi.org/10.1029/2000GL011902

Thakur, P., Huang, Y., & Kaneko, Y. (2020). Effects of Low-Velocity Fault Damage Zones on Long-Term Earthquake Behaviors on Mature Strike-Slip Faults. *Journal of Geophysical Research: Solid Earth*, *125*(8), 1–20. https://doi.org/10.1029/2020JB019587

Thurber, C. (2003). Earthquake locations and three-dimensional fault zone structure along the creeping section of the San Andreas fault near Parkfield, CA: Preparing for SAFOD. *Geophysical Research Letters*, *30*(3), 10–13. https://doi.org/10.1029/2002gl016004

Torabi, A., & Berg, S. S. (2011). Scaling of fault attributes: A review. *Marine and Petroleum Geology*, *28*(8), 1444–1460. https://doi.org/10.1016/j.marpetgeo.2011.04.003

Walter, F., Gräff, D., Lindner, F., Paitz, P., Köpfli, M., Chmiel, M., & Fichtner, A. (2020). Distributed acoustic sensing of microseismic sources and wave propagation in glaciated terrain. *Nature Communications*, *11*(1). https://doi.org/10.1038/s41467-020-15824-6

Wang, X., & Zhan, Z. (2020). Seismotectonics and Fault Geometries of the 2019 Ridgecrest Sequence: Insight From Aftershock Moment Tensor Catalog Using 3-D Green's Functions. *Journal of Geophysical Research: Solid Earth*, *125*(5), 1–15. https://doi.org/10.1029/2020JB019577

Wang, Y., Allam, A., & Lin, F. C. (2019). Imaging the Fault Damage Zone of the San Jacinto Fault Near Anza With Ambient Noise Tomography Using a Dense Nodal Array. *Geophysical Research Letters*, *46*(22), 12938–12948. https://doi.org/10.1029/2019GL084835

Weng, H., Yang, H., Zhang, Z., & Chen, X. (2016). Earthquake rupture extents and coseismic slips promoted by damaged fault zones. *Journal of Geophysical Research: Solid Earth*, *121*(6), 4446–4457. https://doi.org/10.1002/2015JB012713

Yang, Y., Atterholt, J. W., Shen, Z., Muir, J. B., Williams, E. F., & Zhan, Z. (2021). Sub-kilometer correlation between near-surface structure and ground motion measured with distributed acoustic sensing. *Geophysical Research Letters*. https://doi.org/10.1029/2021gl096503

Zeng, X., & Ni, S. (2010). A persistent localized microseismic source near the Kyushu Island, Japan. *Geophysical Research Letters*, *37*(24), 8–13. https://doi.org/10.1029/2010GL045774

Zhan, Z. (2019). Distributed acoustic sensing turns fiber-optic cables into sensitive seismic antennas. *Seismological Research Letters*, *91*(1), 1–15. https://doi.org/10.1785/0220190112

Zhan, Z., Ni, S., Helmberger, D. V., & Clayton, R. W. (2010). Retrieval of Moho-reflected shear wave arrivals from ambient seismic noise. *Geophysical Journal International*, *182*(1), 408–420. https://doi.org/10.1111/j.1365-246X.2010.04625.x

U.S. Geological Survey and New Mexico Bureau of Mines and Mineral Resources, Quaternary fault and fold database for the United States, accessed August 1, 2019, at: https://www.usgs.gov/natural-hazards/earthquake-hazards/faults

C h a p t e r 5

FIBER-OPTIC SEISMIC SENSING OF VADOSE ZONE SOIL MOISTURE DYNAMICS

Shen, Z.*, **Yang, Y.***, Fu, X., Adams, K. H., Biondi, E., & Zhan, Z. (under revision). Fiber-optic seismic sensing of vadose zone soil moisture dynamics. *Nature Communications.*

Abstract

Vadose zone soil moisture—water stored in the unsaturated region between the surface and the groundwater table—is often considered a pivotal intermediary water reservoir in semi-arid regions. In face of climate variability, understanding its dynamics in response to changes in meteorologic forcing patterns is essential to enhance the resiliency of our ecological and agricultural system. However, the inability to observe high-resolution vadose zone soil moisture dynamics over large spatiotemporal scales hinders quantitative characterization. Here, utilizing pre-existing fiber-optic cables as seismic sensors, we demonstrate a fiber-optic seismic sensing principle to robustly capture vadose zone soil moisture dynamics. Our observations in Ridgecrest, California reveal sub-seasonal precipitation replenishments and a prolonged drought in the vadose zone, consistent with a zero-dimensional hydrological model. Our results suggest a significant water loss of 0.25 m/year through evapotranspiration at our field side, validated by eddy-covariance based measurements in nearby region. Yet discrepancies between our observations and modeling in more detailed dynamics highlight the necessity for complementary in-situ observations for further validation. Given the escalated regional drought risk under climate change, our findings underscore the promise of fiber-optic seismic sensing as a large-scale and long-term observational tool to facilitate water resources management in semi-arid regions.

5.1 Main text

The vadose zone plays a vital role in sustaining natural ecosystems (Berdugo et al., 2020; Fan et al., 2017; Rietkerk et al., 2004; Scanlon et al., 2007), altering water and nutrient cycles (Jackson et al., 2005; Or & Lehmann, 2019; Zhou et al., 2019), and informing agricultural water resource management (Nielsen et al., 2009; Reynolds et al., 2007). Acting as an intermediary between surface soil moisture and deep groundwater, it is thought to function as a backup reservoir of water in semiarid regions, which is crucial for strengthening the resilience of our ecological and agricultural systems (Evaristo et al., 2015; Padrón et al., 2020; Rietkerk et al., 2004). To the first order, water stored in the vadose zone can be readily replenished by precipitation and lost to the atmosphere via evapotranspiration or deep drainage to recharge groundwater (Figure 5.1a). While this conceptual model has long been indoctrinated in hydrology, it is challenging to quantitatively monitor the long-term, large-scale vadose zone soil moisture dynamics at depth. Modern microwave remote sensing missions, such as the SMAP (Soil Moisture Active Passive, Entekhabi et al., 2010) and SMOS (Soil Moisture and Ocean Salinity, Kerr et al., 2001), and GNSS (Global Navigation Satellite System) based techniques (Edokossi et al., 2020; Larson et al., 2010) provide good estimates of global soil moisture only down to ~5 centimeters at 10-40 km spatial resolution every few days and can further extend to the 1-m root zone using data assimilation (Babaeian et al., 2019). Satellite-based gravimetric measurements are sensitive to greater depths but rely on aforementioned microwave missions to disaggregate between surface soil moisture and deep groundwater (Rowlands et al., 2005). In-situ instruments such as lysimeters allow for direct measurements of the water content change in unsaturated soil, which are commonly used as a tool to calibrate satellite-derived soil moisture (Pütz et al., 2018). Yet these point-wise measurements do not provide a large-scale view of vadose zone dynamics. Other hydro-geophysical means, including time-domain reflectometer, ground penetrating radar, and electromagnetic system, can characterize detailed vadose zone soil structures (Behroozmand et al., 2019; Huisman et al., 2003; Klotzsche et al., 2018; Pellerin, 2002) but the operational cost of long-term monitoring is often prohibitive for extensive deployment (Babaeian et al., 2019; Hermans et al., 2023).

Recently, time-lapse seismology has shown great promise to characterize subsurface hydrological processes using the seismic velocity change (dv/v) as an indicator of water saturation (Campillo & Paul, 2003; Timothy Clements & Denolle, 2018; Mao et al., 2022). Water content in the subsurface perturbs seismic velocity, and thus can be inferred by repeatedly measuring the arrival time variation of seismic surface waves propagating between two seismic stations on a regular basis. In addition, the dispersive nature of surface waves with long periods sampling greater depths enables a glimpse into the depth-dependence of the subsurface water cycle. However, due to the sparsity of regional seismic networks in tens of kilometers spacing, time-lapse seismology typically has limited spatial resolution and uses long-period surface waves (i.e., 1-10 seconds) that are sensitive to groundwater rather than vadose zone soil moisture (Timothy Clements & Denolle, 2018; Mao et al., 2022). Therefore, resolving the water dynamics in the vadose zone is a task better suited for a denser continuous seismic network.

Distributed acoustic sensing (DAS) offers an affordable and scalable solution for long-term monitoring through ultra-dense seismic arrays (Zhan, 2020). By converting Rayleigh-backscattered laser signals due to intrinsic fiber impurities to longitudinal strain or strain rates, DAS repurposes pre-existing telecommunication fiber-optic cables into thousands of seismic sensors over tens of kilometers. With meter-scale channel spacing, DAS continuously records high-frequency wavefields and boosts the spatiotemporal resolution of time-lapse seismology at shallow depths (Rodríguez Tribaldos & Ajo-Franklin, 2021). Here, we demonstrate that the vadose zone soil moisture can be fiber-optically sensed using a DAS array in Ridgecrest, California.

Located to the north of Mojave Desert, the city of Ridgecrest is nestled in the Indian Wells valley basin (Figure 5.1b), which is a typical semi-arid region receiving an annual precipitation of ~0.05 m (Table 5.S1). Due to the severe droughts in the past few years, groundwater in this region has been critically overdrawn to meet the agricultural and municipal demand. While this historic drought is reflected in the declining water levels in regional aquifers and the drying surface moisture (McColl et al., 2017), its impact on water stored in the shallow subsurface remains unclear. On July 10, 2019, a pre-existing telecommunication fiber optic cable along U.S. Route 395 Business, a major road in Ridgecrest was transformed to a l0-km long DAS array with 1250 channels spacing 8 meters (Figure 5.1b). The Ridgecrest DAS array was initially deployed as a rapid response to the

2019 M7.1 Ridgecrest earthquake (Li et al., 2021) and has been continuously running for two and a half years (Jul. 2019-Mar. 2022) with a few small data gaps.

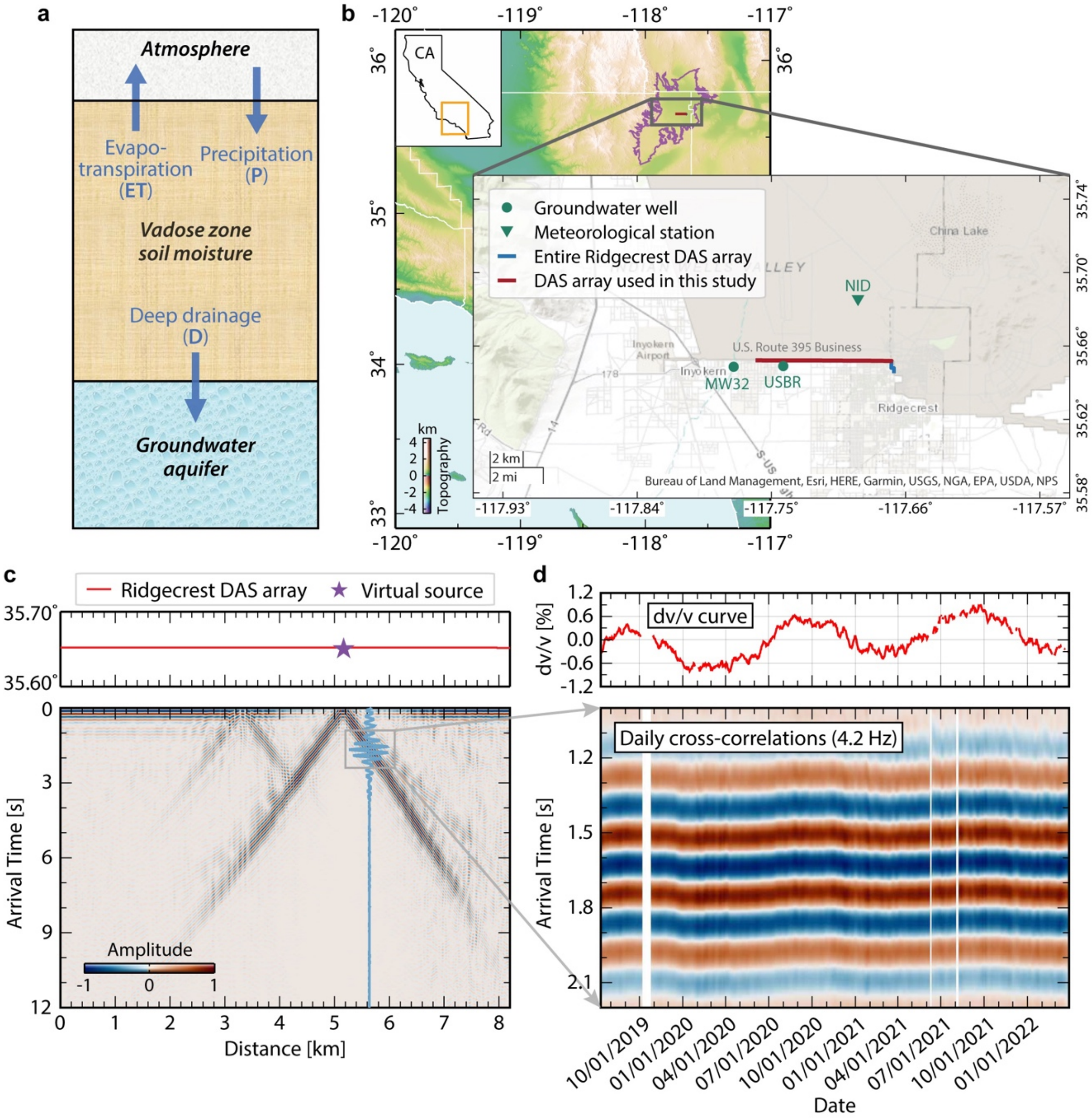

Figure 5.1: Conceptual model for the vadose zone water dynamics and time-lapse seismology example on Ridgecrest DAS array. (a) Water stored in the vadose zone can be readily replenished by precipitation (P) and lost due to evapotranspiration (ET) to the atmosphere or deep drainage (D) to recharge deeper aquifers. (b) Map view of Ridgecrest DAS array. The purple line is the boundary of Indian wells valley. In the inserted panel, the green triangle

and circles denote nearby meteorological station and groundwater wells, respectively. The blue line and overlying red line represent the entire DAS cable and an 8-km DAS segment used in this study, respectively. (c) Record section of weekly stacked seismic waveforms at 4.2 Hz from a virtual source (purple star) at a cable distance of 5.2 km. The blue waveform shows the seismogram received 60-channels away from the virtual source. (d) dv/v measurements (top panel) for the channel pair in (c). Bottom panel presents the temporal variation of direct surface waves. Vertical white strips are data gaps.

The fine channel spacing of DAS enables the use of direct high-frequency surface waves for vadose zone monitoring. As an example, Figure 5.1c clearly shows 4.2-Hz Rayleigh waves propagating along the array for ~2 km, derived with one week of ambient noise data (see Methods for details). For a channel pair separated by 480 m, repeated retrieval of surface waves weekly presents distinct signals of high signal-to-noise ratios with temporal variations of direct arrivals (Figure 5.1d). Taking the 2.5-year averaged waveform as a reference, we calculate the relative seismic velocity change (dv/v) with time as the opposite of the relative time shift of surface wave arrivals. The resulting dv/v curve shows a clear seasonality with lows in the winter and highs in the summer, along with an upward trend over the 2.5 years of observational period (Figure 5.1d). Specifically, the annual highs of dv/v elevated from 0.4% in 2019 to 0.6% in 2021 and further to 0.8% in 2022 (Figure 5.1d).

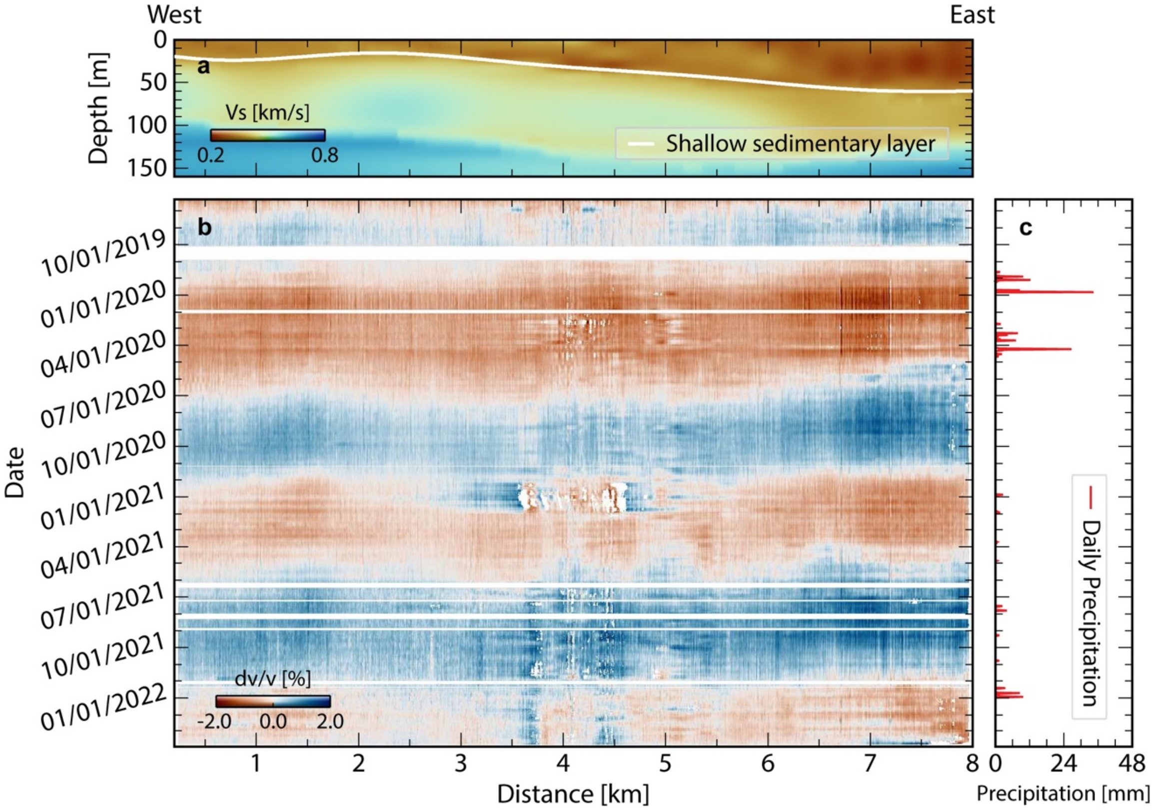

Figure 5.2: Subsurface dv/v spatiotemporal evolution. (a) Shear wave tomography beneath the Ridgecrest DAS array (Yang, Atterholt, et al., 2022). The white line delineates the shallow sedimentary layer. (b) 4.2 Hz dv/v results across the Ridgecrest DAS array. The white regions are either data gaps or low quality dv/v measurements. Note the correlation between lateral variations of sediment thickness and dv/v measurements. (c) Precipitation data from meteorological station. Note the correlation between precipitation in (c) and horizontal dv/v anomalies in (b).

Repeating and integrating the measurements for all channel pairs, the 8-km-long DAS array reveals the spatiotemporal evolution of subsurface dv/v in unprecedented details (Figure 5.2; see Methods for details). We observe an evident spatial variation in dv/v amplitude with ±1.5% at the east end gradually decaying westward to ±0.5% at 2-3 km, followed by a slight increase at 0-2 km (Figure 5.2b). This lateral spatial variation correlates well with the tapering of the shallow sediment thickness westward from 60 m to less than 20 m (Figure

5.2a). A similar correlation between larger dv/v and thicker sediment has been reported previously (Timothy Clements & Denolle, 2018; Mao et al., 2022) but is observed on a much finer scale here. Moreover, we observe temporal variations of dv/v across multiple time scales. First, rapid dv/v amplitude drops are observed throughout the DAS array in response to sub-seasonal meteorological forcing (e.g., rainfalls in April 2020; Figure 5.2c), leaving distinct horizontal footprints on the dv/v map (Figure 5.2b). Second, our 4.2 Hz dv/v measurements exhibit a strong seasonality and a long-term increasing trend along the cable (i.e., lighter red and deeper blue in Figure 5.2b). In fact, rather than just a single frequency band, the cable-wide-averaged dv/v curves present consistent multiscale temporal variations across a broad frequency band (2.5-7.1 Hz; Figure 5.3b), corresponding to a sensitivity depth extending down to 150 m (Figure 5.3a, Figure 5.S1). The dv/v amplitude monotonically increases with frequency, indicating a primary dv/v contribution from the top 20 m (Figure 5.3a).

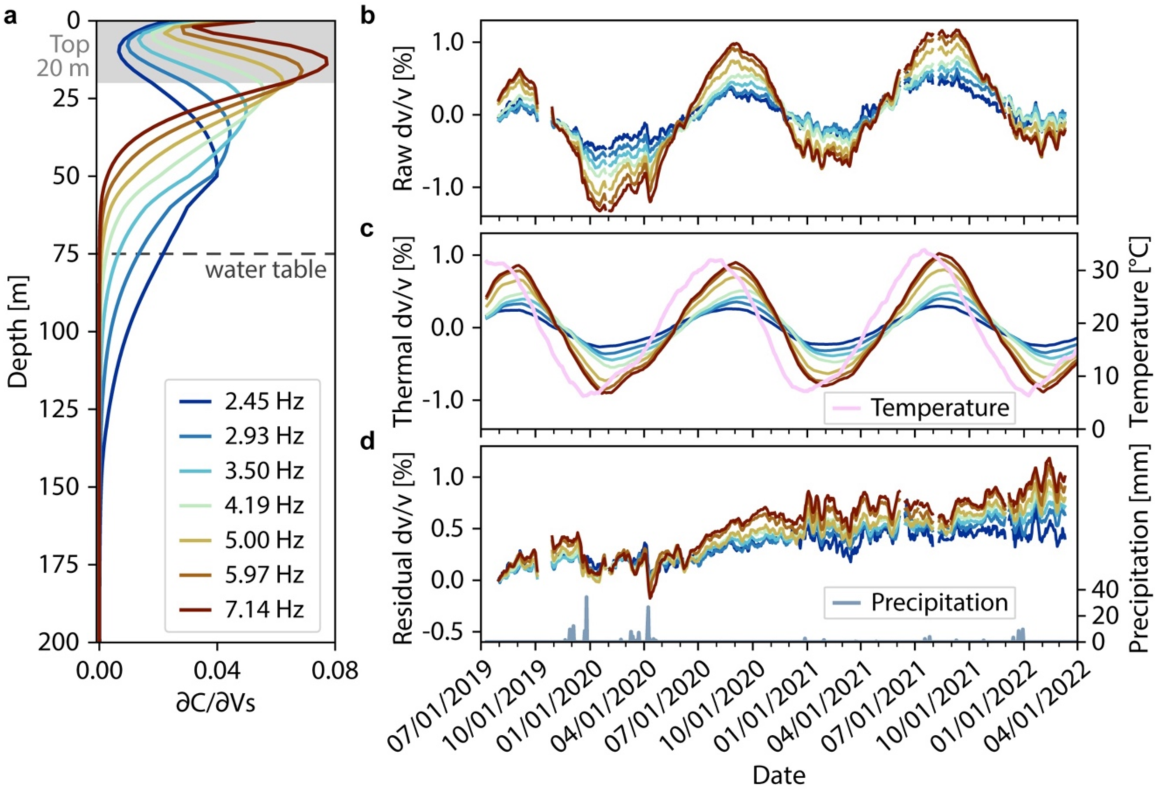

Figure 5.3: Subsurface dv/v analysis at varying frequencies. (a) Surface wave sensitivity kernels for different frequencies varying from 2.45 to 7.14 Hz. The black dashed line indicates the groundwater table, and the shaded area denotes the top 20 m. (b) Cable-wide-averaged dv/v curves for varying frequencies. (c) Thermal dv/v fitted by the surface temperature curve in purple. (d) dv/v measurements (set to 0 on day 1 for visualization) after the thermoelastic correction. The blue line denotes precipitation.

Among the observed dv/v variations over multiple time scales, the seasonal variation is the predominant one. Previous studies attribute seasonality in long-period seismic signals to groundwater level changes, but their reported dv/v amplitudes are one order of magnitude smaller than this study (Timothy Clements & Denolle, 2018; Mao et al., 2022). Such amplitude discrepancy arises from the choice of frequency band and inter-station distance. In fact, previous studies using high-frequency seismic waves yield the same order of magnitude variation in dv/v amplitudes (T. Clements & Denolle, 2023; Illien et al., 2021). Nonetheless, the groundwater table at our field site is approximately at depths of 75-90 m (Figure 5.S2), far below the observable depth (top 20 m) of our strongest signals, therefore ruling out groundwater fluctuation as the main cause to our observed dv/v seasonality. On the other hand, surface temperature follows a seasonal pattern (Figure 5.3c), and the associated thermoelastic effect can extend considerably deep (Ben-Zion & Leary, 1986; Berger, 1975; Tsai, 2011). Indeed, the surface temperature variation has been shown to correlate with the seasonality of dv/v amplitude comparable to our observations (T. Clements & Denolle, 2023; Richter et al., 2014), suggesting thermal fluctuation as the main cause for the observed seasonality here. We correct the thermoelastic component of dv/v by scaling and shifting the surface temperature curve to best fit seasonal dv/v variations (Figure 5.3c, see Methods for details). The estimated phase lags between temperature and our dv/v observations ranges from 10 to 60 days with longer delay time at greater depths, yielding a reasonable estimate of soil thermal diffusivity (T. Clements & Denolle, 2023; Tsai, 2011) (see Methods for details; Figure 5.S3).

With the thermoelastic component corrected, the remaining cable-wide-averaged dv/v curves preserve sub-seasonal variations aligned with meteorological forcing and a frequency-dependent long-term trend (Figure 5.3d). Specifically, we observe that intense rainfall sequences in January and April 2020 have led to dramatic dv/v drops of up to 1% within days, followed by a gradual recovery to elevated levels months later (Figure 5.3d). Qualitatively, this can be explained as a direct result of soil moisture changes in response to meteorological forcing. As rainfalls recharge the vadose zone, increases in water saturation in soil perturb the elastic properties of porous soil (Brutsaert, 1964; Lo et al., 2005), and consequently reduce the seismic velocity (Roumelioti et al., 2020). In contrast, outside of the wet season, vadose zone dynamics are dominated by water loss through evapotranspiration, resulting in a reduction in soil moisture and a recovery of the seismic velocity (Illien et al., 2021). The soil drying process is especially prominent during the historic drought beginning in the summer of 2020 (Williams et al., 2022), where we observe a sharp climb of dv/v (Figure 5.3d). Overall, the long-term dv/v increase is consistently observed across a broad frequency band with a more pronounced effect at higher frequencies, implying that shallow soil moisture dynamics is the dominant driver to the observed seismic signals (Figure 5.3a).

To further quantify the soil moisture dynamics (i.e., time series of soil moisture budget) using dv/v observations, we resort to an existing rock physics model (Mindlin, 2021; Solazzi et al., 2021) tailored for unconsolidated unsaturated porous soil medium (see Methods for details). The forward model calculates dv/v as a function of soil moisture profile and a given lithology model, which enables us to invert for water content changes in the top 20 m that can best fit dv/v measurements across all frequencies (see Methods for details; Figures 5.S4a and 5.S5). As the inversion requires an assumed lithology model, we examine two endmember lithology (Solazzi et al., 2021)—Esperance sand and Missouri clay—to establish upper and lower bounds for the inferred vadose zone water content changes. Despite amplitude differences, results from the two endmembers consistently mirror our observed dv/v patterns, capturing episodic replenishments from precipitation and a long-term trend of water loss from 2019 to 2022 (Figure 5.4a).

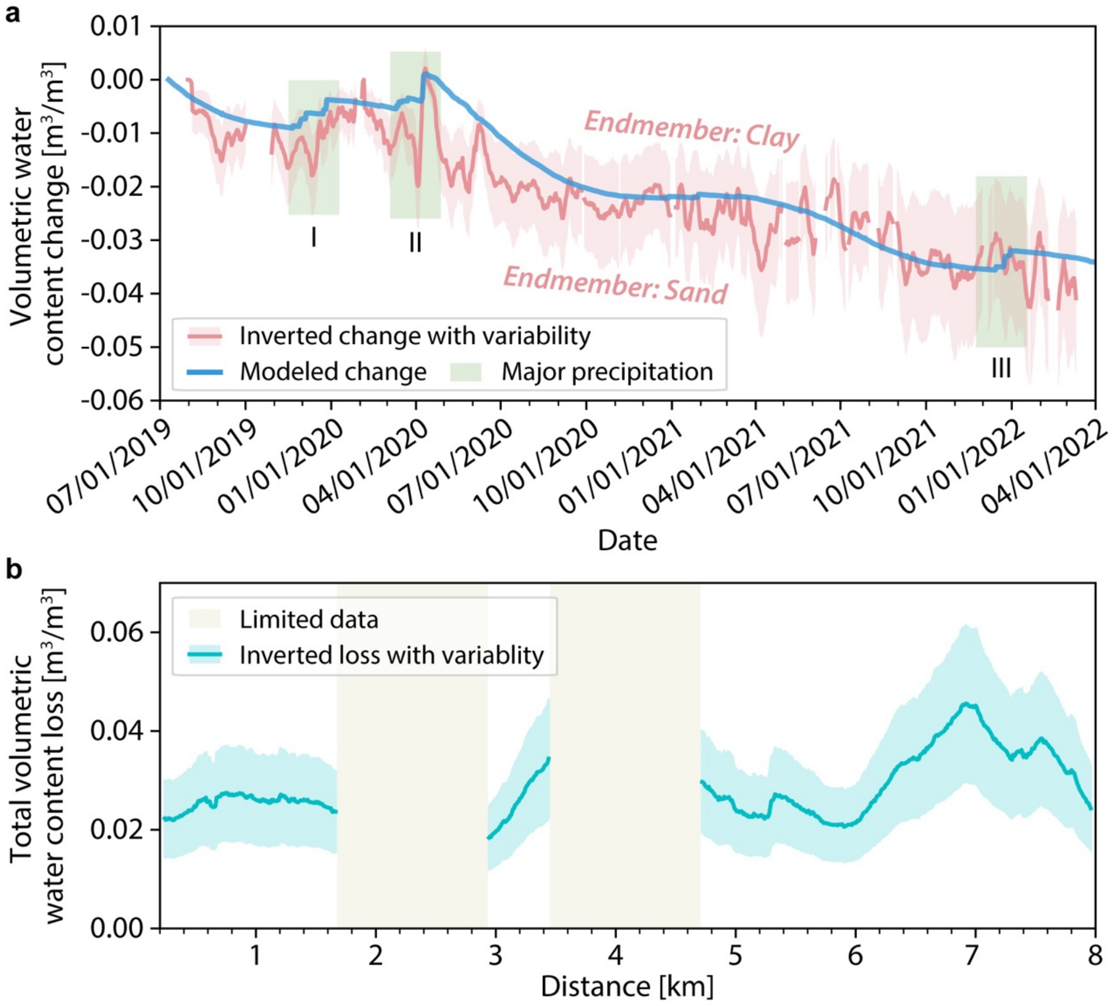

Figure 5.4: Vadose zone soil moisture loss. (a) Modeled and inverted volumetric water content changes in the top 20 m at a cable distance of 7.2 km. The red shaded area is bounded by inversion results derived from two end-member lithology models, and the red curve represents the mean variation. The three green shaded areas highlight the major precipitation periods during our study period. (b) Lateral variation of total vadose zone soil moisture loss during the 2.5-year study period. The blue shaded region indicates the variability in total soil moisture loss, bounded by the two end-member lithology models, with the blue line representing the mean variation. The light-gray shaded gaps indicate cable sections lacking sufficient high-quality data for robust estimates.

For independent validation, we further use a zero-dimensional hydrological model forced with meteorological and SMAP data products to simulate subsurface volumetric water content changes at our field site (Reichle et al., 2019; Stahl & McColl, 2022) (Figure 5.1a; see Methods for details; Figure 5.S4b). Taking the eastern side of the DAS cable as an example, our modeled soil moisture changes closely track the dv/v inverted trend within the bounds of the two endmember cases and exhibit remarkable consistency with the mean curve (Figure 5.4a). This robust quantitative consistency between our observation and modeling demonstrates the efficacy of fiber-optic seismic sensing in capturing vadose zone soil moisture dynamics. Our result unveils a significant water loss rate of 0.25 m/yr through evapotranspiration, surpassing the annual precipitation in Ridgecrest (Table 5.S1). In fact, the inferred value is consistent with the eddy-covariance based measurement of evapotranspiration of 0.2 m/yr in the nearby southwestern Mojave Desert covered by similar vegetations (see Methods for details). Furthermore, leveraging our dv/v data across the entire cable, we invert the lateral variations in total soil moisture loss over the 2.5-year observational period (see Methods for details; Figure 5.4b). Despite variations in the assumed lithology models, the eastern end (i.e., 6-8 km) appears to experience a greater loss in vadose zone soil moisture compared to the western end (Figure 5.4b), suggesting a high sensitivity of evapotranspiration rate to localized environmental forcing. Achieving such high-resolution spatial variations is challenging with satellite-based remote sensing techniques, but feasible with our fiber-optic seismic sensing. Extrapolating the spatially averaged water content change in our field site to the entire Mojave Desert region, a first-order estimate yields an annual water loss of ~30 km^3, comparable to the total capacity of Hoover Dam.

Despite the overall agreement between our modeled and inverted water content changes, quantitative discrepancies still exist in finer details. Unlike the rapid replenishment from the two rainfall sequences in 2020, our inverted declining trend of soil moisture is not perturbed by the precipitation sequence in December 2021, differing from the hydrological model (Figure 5.4a). This discrepancy may arise from oversimplification of the hydrological model, which does not consider surface runoff. Moreover, the modeled soil moisture loss rate between April and October 2020 is slower than our observed rate (Figure 5.4a), likely due to an underestimation of evapotranspiration in our hydrological model. To this extent, our dv/v observations could impose tight constraints to parameterized hydrological models at the regional scale.

With the Ridgecrest DAS array, we demonstrate the viability of fiber-optic seismic sensing for high-resolution vadose zone soil moisture dynamics. For practical applications of fiber-optic seismic sensing in various environments, the noise source distribution, poor cable coupling, and unclear subsurface lithology would lead to uncertainties in the fiber-optically estimated vadose zone water content changes. Combined with continued seismic sensing, future work involving direct in-situ measurements for different soil types and regional scale modeling will increase the robustness of the inverted vadose zone soil moisture dynamics. Given the escalated regional drought risk under climate change, our findings highlight the promise of fiber-optic seismic sensing as a large-scale, long-term, and cost-effective observational tool to enhance our climate resilience in semi-arid regions.

5.2 Methods

5.2.1 Time-lapse seismology

5.2.1.1 Temporal resolution

To compute ambient noise cross-correlations, we preprocess daily seismograms by removing mean and linear trend, bandpass filtering between 1-10 Hz, downsampling to 50 Hz, time domain normalization and spectral whitening (Bensen et al., 2007). The 24-hour seismic data are then cut into 40-s segments for each channel. For any given channel pair, all the segments are cross-correlated, normalized, and stacked to present the daily cross-correlation. The 2.5-year continuous raw data recorded by our Ridgecrest DAS array yields a total volume of 80 TB for ambient noise cross-correlations. We implement GPU-based parallel processing to effectively accelerate the massive computation. Once the daily cross-correlations are computed, we smooth them over a seven-day moving window to reduce periodic traffic source effect. The causal and acausal branches of cross-correlations show great symmetry (Figure 5.S6), suggesting the distribution of noise sources is overall even. We also observe clear scattered surface waves at ~4 km, which has been suggested as the seismic signatures of a geologically inferred fault (Yang, Zhan, et al., 2022). To further enhance the signal-to-noise ratio (SNR), we average the causal and acausal branches for all the cross-correlations.

We use the direct surface wave to assess seismic velocity changes (dv/v) rather than coda waves (Obermann et al., 2013, 2016; Pacheco & Snieder, 2006), because its sensitivity kernel is more deterministic. To quantify the seismic velocity change (dv/v), we apply a cross-spectrum method to compute the time shifts of 1-s surface wave windows between daily and reference cross-correlations (Clarke et al., 2011). Here, we use the cross-spectrum method for its extensive use and effective uncertainty quantification. Benefitting from our high-quality cross-correlations, the resulting dv/v uncertainties are generally small, with the majority falling below 0.04% (Figure 5.S7). Nonetheless, notable large dv/v uncertainties are observed near the 4-km mark along the cable (vertical stripes in Figure 5.S7), which is attributed to scattered surface waves affecting the signal quality of retrieved direct surface waves (Figure 5.S6). Other methods, such as a straightforward time-domain cross-correlation and wavelet-based approaches, have also demonstrated great performance in previous dv/v studies (Mordret et al., 2020; Yuan et al., 2021). The use of these methods for DAS data under various signal-to-noise levels remains further investigation to reduce the uncertainty. The reference waveform is obtained by averaging over all the daily cross-correlations and the 1-s window is chosen as 0.5 s before and after the peak of the reference surface wave. Our dv/v results are opposite to the time shift measurements and are only accepted for waveform coherency larger than 0.5 and dv/v uncertainty smaller than 0.1%.

5.2.1.2 Spatial resolution

Rolling along the 8-km segment, we repeat the above procedures for all source-receiver pairs that are 480 m (60 channels) apart and pinpoint the dv/v results to their center locations, resulting in a time-lapse dv/v map of the Ridgecrest DAS array. An inter-channel distance of 480 m satisfies the three-wavelength criterion for high-frequency (>2 Hz) Rayleigh waves, and is thus sufficient to develop robust waveforms for direct arrivals.

We use Rayleigh waves at a broad frequency band of 1–10 Hz and 7 sub-bands centered at 2.45 Hz, 2.93 Hz, 3.50 Hz, 4.19 Hz, 5.00 Hz, 5.97 Hz, and 7.14 Hz for dv/v, which allows us to constrain temporal changes at depths. Although our shear wave velocity model achieves high resolution in the top 150 m, the velocity uncertainty at very shallow depths remains high. Future attempts incorporating high-quality higher-frequency ballistic waves would enhance the depth resolution of our tomography model. Thus, we calculate Rayleigh wave sensitivity kernels based on the 1D shear velocity model averaged along the cable. The observed dv/v increases with frequency, reflecting an exponentially decaying sensitivity of surface waves with depth (Mordret et al., 2020; Obermann et al., 2013) and suggesting that the major contribution comes from the top 20 meters (Figure 5.S1).

5.2.2 Correction for thermoelastic effects

We follow the framework proposed by Richter et al., (2014), which has a straightforward functional form:

$$\left(\frac{\mathrm{d}v}{v}\right)_{\mathrm{thermo}} = a\delta T(t-\tau), \tag{5.1}$$

where $\delta T(t)$ is the demeaned daily surface air temperature at time t. Our objective is to determine the amplitude a and phase shift τ by optimization techniques. To focus on the annual pattern related to temperature, we use a sliding window average method to remove the transient signals. For each frequency, we use grid search to find the best length of the sliding window between 0 and 90 days that can maximize the correlation coefficient between the smoothed dv/v and surface temperature. We then use grid search to find the best-fitted parameters (a, τ) that minimizes the difference between the observed dv/v and the functional form $a\delta T(t-\tau)$. By removing thermoelastic effects from the dv/v, we tease out a more accurate representation of the subsurface velocity changes that are related to soil moisture fluctuations.

The thermoelastic induced dv/v changes also show depth dependent pattern. With increasing frequency, the maximum correlation coefficient is larger and the fitted τ is smaller (Figure 5.S3), implying greater thermoelastic effects and more synchronization with temperature fluctuations at shallower depths. The observed amplitude of thermoelastic dv/v has comparable amplitude with previous studies (T. Clements & Denolle, 2023; Meier et al., 2010). We can further use the time delay between dv/v and temperature to calculate the thermal diffusivity following the thermoelastic modeling (Prawirodirdjo et al., 2006) with a thermal thickness of 2 meter. Consequently, this yields an average value of $1.49 \times 10^{-6} \mathrm{m}^2/\mathrm{s}$., consistent with previous inferred values (T. Clements & Denolle, 2023; Prawirodirdjo et al., 2006; Tsai, 2011).

5.2.3 Estimating vadose zone water loss from dv/v observations

5.2.3.1 Quantitative relation between vadose zone soil moisture and dv/v

We built on and modified the quantitative relations between vadose zone soil moisture and dv/v proposed by Solazzi et al., (2021). Here we briefly summarize the Solazzi model that enables a direct prediction of dv/v from a given vadose zone soil moisture change, which follows dv/v(*t*) = f(vadose zone *soil moisture change, lithology model, t*) (Figure 5.S4a). Assuming that the vadose zone consists of *n* unconsolidated soil layers of isotropic soil property with a water saturation s_j and a thickness of h_j where j denotes the jth layer, the P and S wave velocity of the jth layer are given as:

$$V_{P,j} = \sqrt{\frac{K_j + \frac{4}{3}\mu_j}{\rho_j}};\ V_{S,j} = \sqrt{\frac{\mu_j}{\rho_j}}, \tag{5.2}$$

where K_j, μ_j and ρ_j represent the effective bulk modulus, effective shear modulus and effective bulk density in the jth layer, respectively. To account for the saturating water effect, we adopt the classic Biot-Gassmann equations to compute the effective elastic moduli and bulk density.

$$K_j = K_{d,j} + \frac{\left(1 - \frac{K_{d,j}}{K_{Se,j}}\right)^2}{\frac{\phi_j}{K_{f,j}} + \frac{1-\phi_j}{K_{Se,j}} - \frac{K_{d,j}}{K_{Se,j}^2}} \tag{5.3}$$

$$\mu_j = \mu_{d,j} \tag{5.4}$$

$$\rho_j = (1-\phi_j)\rho_{Se,j} + \phi_j\left[s_j\rho_w + (1-s_j)\rho_a\right], \tag{5.5}$$

where $K_{f,j}$, $K_{Se,j}$, and $K_{d,j}$ denote the fluid bulk modulus, effective bulk modulus of solid grains and drained bulk moduli of the porous medium in the *j*th layer, respectively. ϕ_j and $\mu_{d,j}$ are the porosity and drained shear moduli of the *j*th layer, respectively. $\rho_{Se,j}$, ρ_w and ρ_a represent the density of solid grains, water, and air, respectively. For low-frequency seismic waves, the fluid bulk modulus $K_{f,j}$ can be approximated as:

$$K_{f,j} = \left(\frac{s_j}{K_w} + \frac{1-s_j}{K_a}\right)^{-1}, \tag{5.6}$$

where K_w and K_a are the bulk moduli of water and air, respectively. Based on the classic Hertz-Mindlin theory (Mindlin, 2021), we compute the drained elastic moduli $K_{d,j}$ and $\mu_{d,j}$ given as:

$$K_{d,j} = \left[\frac{N^2\left(1-\phi_j\right)^2\mu_{Se,j}^2}{18\pi^2\left(1-\nu_{Se,j}\right)^2}P_{e,j}\right]^{\frac{1}{3}} \tag{5.7}$$

$$\mu_{d,j} = \frac{2+3f-(1+3f)\nu_{Se,j}}{5(2-\nu_{Se,j})}\left[\frac{3N^2(1-\phi_j)^2\mu_{Se,j}^2}{2\pi^2(1-\nu_{Se,j})^2}P_{e,j}\right]^{\frac{1}{3}}, \tag{5.8}$$

where N and f are the average number of contacts per particle and the fraction of non-slipping particles. $P_{e,j}$ denotes the effective pressure. Solazzi et al., (2021) implemented a water saturation- and depth-dependent $P_{e,j}$ to investigate the capillary suction effect on the seismic velocity and suggested that the surface-wave dispersion in coarse-grained soil textures are not sensitive to capillary effects, which are consistent with both laboratory (Cho & Santamarina, 2001; Dong & Lu, 2016)and field observations (Fratta et al., 2005). In particular, during the pendular stage, capillary force can perturb small strain stiffness but may not significantly affect large strain stiffness (Cho & Santamarina, 2001). Since our study region predominately consists of coarse-grained sand soil, we opt out of including the capillary effect in the calculation of $P_{e,j}$. $\nu_{Se,j}$ and $\mu_{Se,j}$ are Poisson's ratio and the effective shear modulus of the solid grains in the *j*th layer, respectively. Assuming the soil at *j*th layer consists of *m* types of constituents, we employ the Hill's equation to compute $\nu_{Se,j}$, $\mu_{Se,j}$ and $\rho_{Se,j}$.

$$\nu_{Se,j} = \frac{3K_{Se,j} - 2\mu_{Se,j}}{2(3K_{Se,j} + \mu_{Se,j})} \tag{5.9}$$

$$\mu_{Se,j} = \frac{1}{2}\left[\sum_{i=1}^{m} \gamma_{i,j}\mu_{i,j} + \frac{1}{\sum_{i=1}^{m}\frac{\gamma_{i,j}}{\mu_{i,j}}}\right] \tag{5.10}$$

$$\rho_{Se,j} = \sum_{i=1}^{m} \gamma_{i,j}\rho_{i,j}, \tag{5.11}$$

where $\gamma_{i,j}$ and $\rho_{i,j}$ are the volumetric fraction and density of the *i*th constituent in the *j*th layer. $K_{Se,j}$ denotes the effective bulk modulus of the corresponding grains in the *j*th layer, which is given as:

$$K_{Se,j} = \frac{1}{2}\left[\sum_{i=1}^{m} \gamma_{i,j}K_{i,j} + \frac{1}{\sum_{i=1}^{m}\frac{\gamma_{i,j}}{K_{i,j}}}\right]. \tag{5.12}$$

Following Solazzi et al., (2021), we selected parameters for Esperance sand and Missouri clay to represent two end-member lithology models (Table 5.S2). These models serve as the upper and lower bounds for our estimated volumetric water content. We also calculated the average of these two models, which we compared with the outputs from the hydrological model.

5.2.3.2 Estimating the vadose zone soil moisture loss

Based on the forward modeling from water saturation to dv/v, we conduct a grid search approach for the daily vadose zone soil moisture change (Δs) to best fit our daily frequency-dependent dv/v observations (Figure 5.S4a). Typically, the number of vadose zone soil layers

n is greater than our dv/v observations (i.e., dv/v data at 7 center frequencies), making the inverse problem underdetermined. To simplify the problem, we assume that the daily vadose zone water content change primarily comes from the surface and follows an exponential decay with depth.

$$\Delta s(z) = \Delta s_0 e^{-\frac{z}{\lambda}}, \tag{5.13}$$

where Δs_0 is the magnitude and λ is an exponential decay parameter. To justify, our chosen mathematical form aligns with theoretical principles, as it mirrors the exponential profile typically observed in grass roots (Wang et al., 2007), which strongly governs the exponential decay in evapotranspiration with increasing depth. In this manner, the simplified vadose zone water content profile significantly reduces the model space to be searched and enables a straightforward comparison with our hydrological modeling. Given a specific lithology model, we calculate the elastic moduli before and after changes in water content. This model allows us to determine the depth-dependent seismic velocity changes before and after these water content alterations, and consequently, to compute the frequency-dependent dv/v. We fix λ = 1m based on the average root depth in this region and perform a grid-search for Δs_0 ranging from -0.1m^3/m^3 to 0.1m^3/m^3 with an interval of 0.001m^3/m^3 to minimize the mean-square misfit between predicted and observed dv/v across different frequencies for a 400-meter cable segment at the eastern end (i.e., 7.2-7.6 km). For instance, given a lithology model averaged from the two endmembers (red line in Figure 5.4; Table 5.S2), a soil moisture increase of 0.0275 m^3/m^3 in the top 20-m vadose zone effectively explains the observed trend in dv/v, which monotonically varies from -0.23% at 2.45 Hz to 1.24% at 7.14 Hz following the April 2020 precipitation event (Figure 5.S5).

Repeating the inversion of daily volumetric water content changes for all DAS channels, we can estimate the total vadose zone soil moisture loss across the 8-km cable over the 2.5 years of our observational period. To ensure robust estimates, we apply the following two criteria for data quality control: (a). For a given channel and a specific date, the square root of the resolved mean square misfit must be less than 0.1%; (b). For a given channel, the number of inverted daily soil moisture changes must exceed 70% of the total days of our observation period to robustly determine total soil moisture loss. To account for lithology model uncertainties, we use the two end-member models as estimate bounds to represent the variability of the total soil moisture loss. The resulting lateral variations of total vadose zone soil moisture loss are shown in Figure 5.4b, with two gaps at 2-3 km and round 4-km mark. The gaps are due to insufficient high-quality data that can meet our criteria. For example, the dv/v uncertainty is generally large around the 4-km mark (Figure 5.S7).

5.2.4 Hydrological modeling

We use a physics-based 0-D bucket model to describe the water mass balance in the top 20 m subsurface (Figure 5.S4b). Specifically, the inputs include precipitation and temperature data from the local weather station NID (Figure 5.1), and surface soil moisture from SMAP. Following Stahl & McColl (2022), the water balance of a vertically averaged, horizontally homogeneous control volume of soil extending from the land surface down to a depth Δz [m] (Figure 5.1a) can be modeled as:

$$\Delta z\left(\theta_{fc} - \theta_w\right)\frac{ds}{dt} = P(t) - E(s,t) - Q(s,t). \tag{5.14}$$

Here, s is the volume fraction of water within the pore volume of the soil, and θ represents soil moisture (the ratio of the volume of water to the unit volume of soil [m^3 m^{-3}]), the subscripts fc and w represent field capacity and wilting point soil moisture, respectively. t is time [s], $P(t)$ is hourly rate of precipitation representing water entering the model domain [m/h], $E(s,t)$ is the hourly rate of evapotranspiration representing water leaving the model domain into the atmosphere [m/h], and $Q(s,t)$ is the rate of deep drainage (vertical transport of water to deeper soil layers) and runoff (horizontal transport) [m/h]. θ_{fc} can be approximated as the porosity of soil, ϕ. Given the semi-arid climate of our field site and considering that groundwater is largely disconnected from the control volume at this site (i.e. estimated groundwater depth >75 m below the surface), we assume Q is zero so that no water leaves from the bottom of the bucket (at 20 m depth). This assumption, however, limits our ability to capture water loss due to lateral runoff, and thus may lead to overestimation of water mass during storm seasons. We model E as the product of actual water saturation as measured by SMAP and potential evapotranspiration (PET, m/h). Thus, after the above simplification, we arrive at the following ordinary differential equation:

$$\Delta z \cdot \phi \cdot \frac{ds}{dt} = P(t) - PET(t) \cdot \frac{SMAP(t)}{\phi}. \tag{5.15}$$

We use the temperature based Thornthwaite equation (Thornthwaite, 1948) to estimate PET:

$$PET(t) = 1.6 \left(\frac{10T(t)}{I}\right)^{a}, \tag{5.16}$$

where $a = 6.75 \cdot 10^{-7} \cdot I^3 - 7.71 \cdot 10^{-5} \cdot I^2 + 0.01792 \cdot I + 0.49239$, and the heat index $I = 83$ calculated from the temperature in summer. $T(t)$ is the atmospheric temperature data (in degree Celcius) from the NID station.

We use the Forward Euler method with a time step size of $\Delta t = 3$ hours, and the following parameters: $\Delta z = 20$ m, $\theta_{fc} \approx \phi = 0.25$ for the top 20 m depth, $\theta_w = 0.01$, to integrate the discretized version of Equation (5.2):

$$s_{n+1} = s_n + \frac{\Delta t}{\Delta z\left(\theta_{fc} - \theta_w\right)}\left[P(t) - PET(t)\frac{SMAP(t)}{\phi}\right], \tag{5.17}$$

where s_n represents saturation at time step *n*. The choice of $\Delta z = 20$ m is based on the seismic data analysis that indicates the strongest sensitivity to meteorologic forcing at the highest frequency. The choice of $\phi = 0.25$, representing the average porosity over 20 m, takes into account the compaction effect at depth. We find that initial saturation does not change the temporal trend of predicted moisture. The time step size of 3 hours is determined by the available data frequency for precipitation, SMAP and temperature. Overall, the model is most truthful in its predicted temporal dynamics of moisture but bears uncertainty in the amplitude of soil moisture, requiring future in-situ field validation.

5.2.5 Eddy-covariance measurements of evapotranspiration

We inferred a vadose zone water loss of 0.25 m/yr, which is consistent with USGS published eddy-covariance based evapotranspiration measurement of 0.2 m/yr at a sparse shrub site (hereafter refer to as shrub site) in the southwestern Mojave Desert. Even though the evapotranspiration measurement (April 2018-March 2019) does not overlap with our observational period (July 2019-April 2022), the shrub site features vegetation coverage similar to that of our Ridgecrest filed site under comparable climate conditions (annual precipitation of 0.068 m/yr at shrub site vs. 0.05 m/yr in Ridgecrest). This similarity in vegetation coverage and climates assures similar estimations of subsurface water loss through both transpiration and evaporation processes. Future benchmarks would involve in-situ field measurements and their incorporation into hydrological modeling to improve parameter estimation.

Supplementary Material

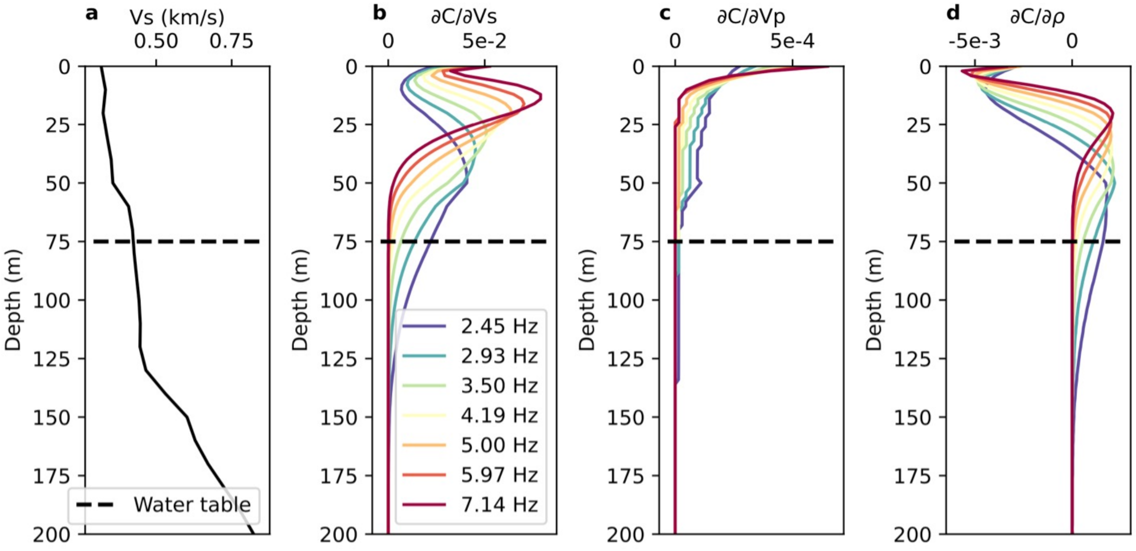

Figure 5.S1: Shear velocity model and surface wave sensitivity kernels. (a) Shear velocity model averaged along the cable. The sensitivity kernels of frequency-dependent surface wave velocity with respect to depth-dependent (b) shear velocity, (c) compressional velocity, and (d) density. Black dashed lines represent the local groundwater level. For all the

sensitivity kernels, the measured dv/v that monotonically increases with frequency should be sensitive to the vadose zone above 20-m depth rather than groundwater.

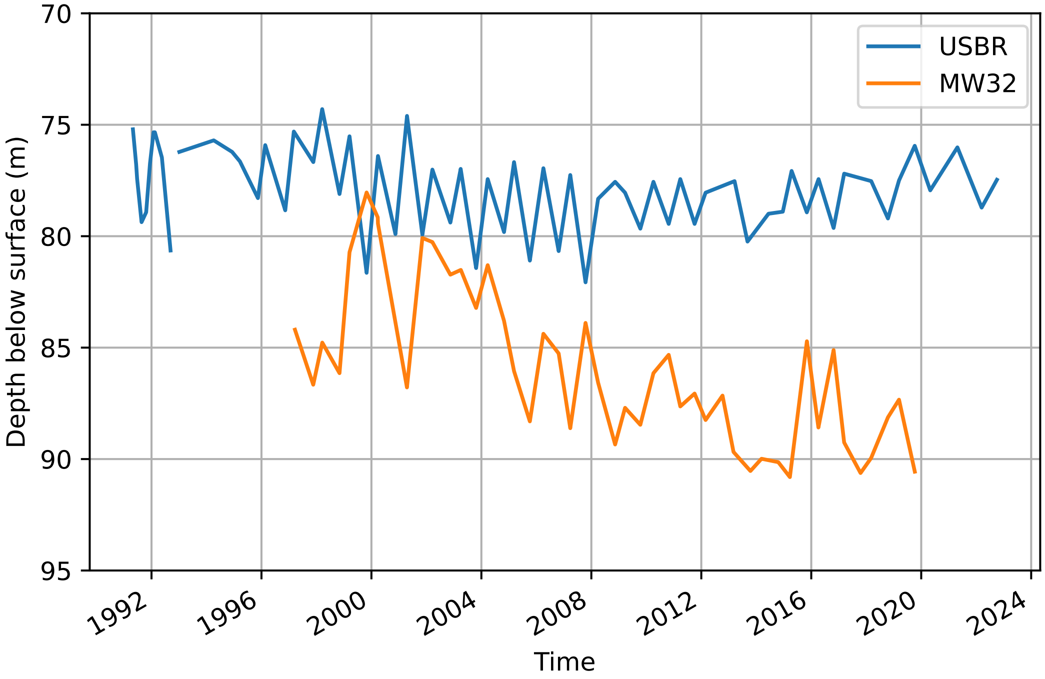

Figure 5.S2: Groundwater level data in the past twenty years measured at nearby groundwater monitoring wells USBR and MW32. The locations of the two wells are indicated in Figure 5.1.

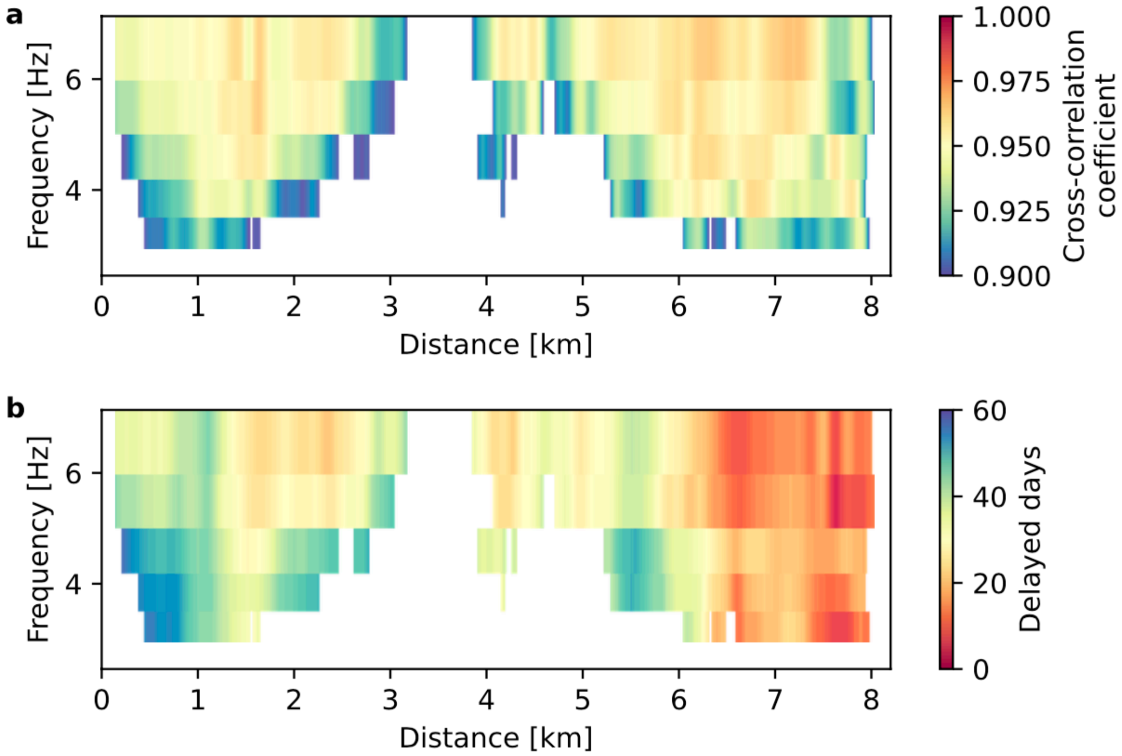

Figure 5.S3: Fitting dv/v with 60-day smoothed surface temperature for all the channels and frequencies. (a) maximum correlation coefficient. (b) best fitted time delay. The correlation coefficient between dv/v and temperature increases with frequency, whereas the phase-lag decreases with frequency.

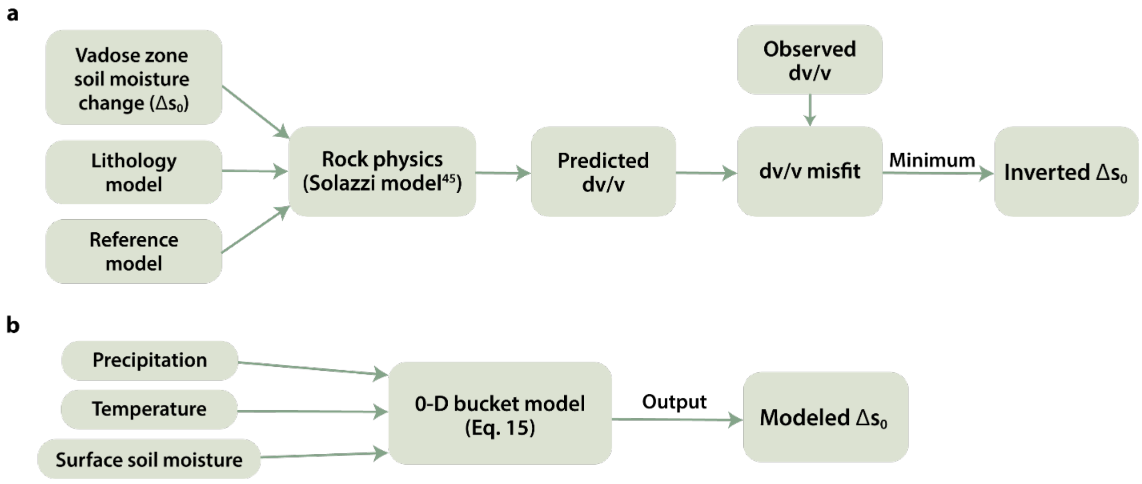

Figure 5.S4: Flowchart describing major steps in obtaining inverted and modeled vadose zone soil moisture changes. (a) Major steps obtaining inverted daily soil moisture changes from dv/v observations. (b) Major steps in our hydrological modeling.

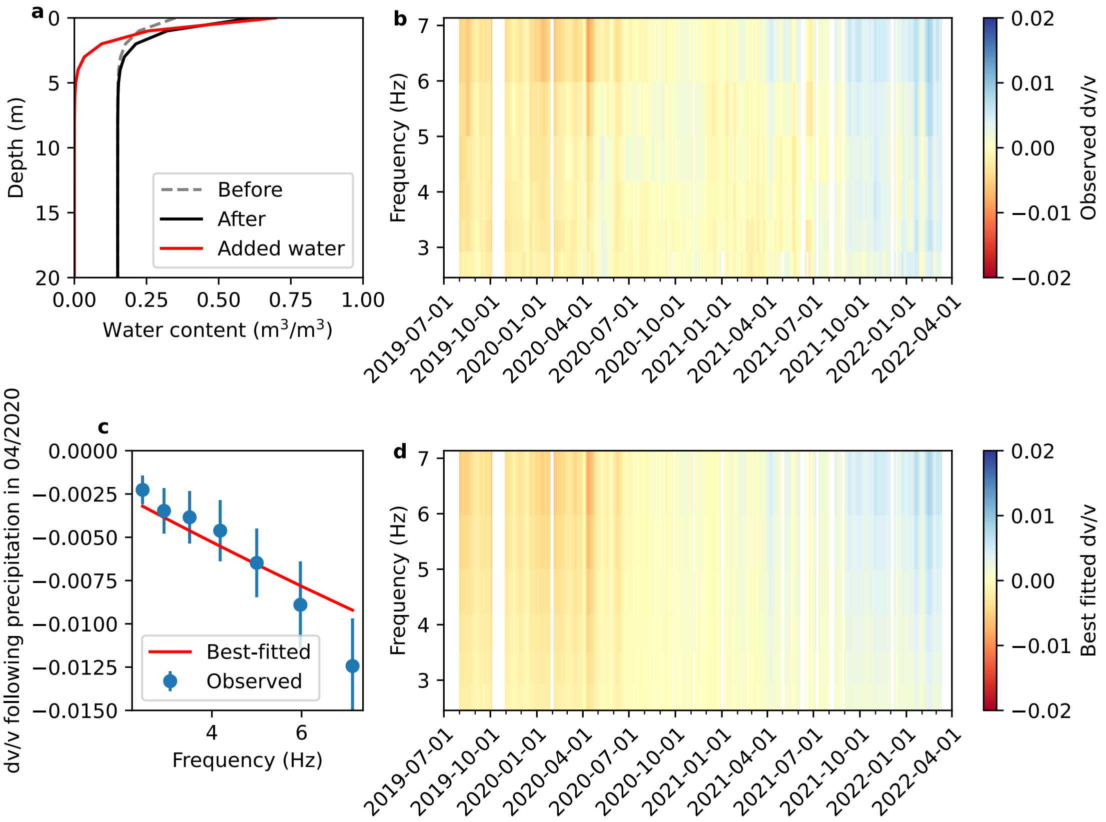

Figure 5.S5: Inversion from dv/v to average water content changes in the vadose zone. (a) This panel displays the reference (gray dashed line), added (red line), and resultant (black line) depth profiles of water content within the top 20 meters of the vadose zone. (b) Over a 2.5-year period and across 7 frequency bands, the dv/v measured by DAS is averaged for a cable segment between 7.2 and 7.6 km along the cable. (c) The observed dv/v values for the day after the significant precipitation event in April 2020 are plotted as blue dots with error bars. The red line represents the synthetic dv/v computed using the water profile from panel (a). (d) Synthetic dv/v computed from the best-fitted inversion model, which is shown in the red curve of Figure 5.4.

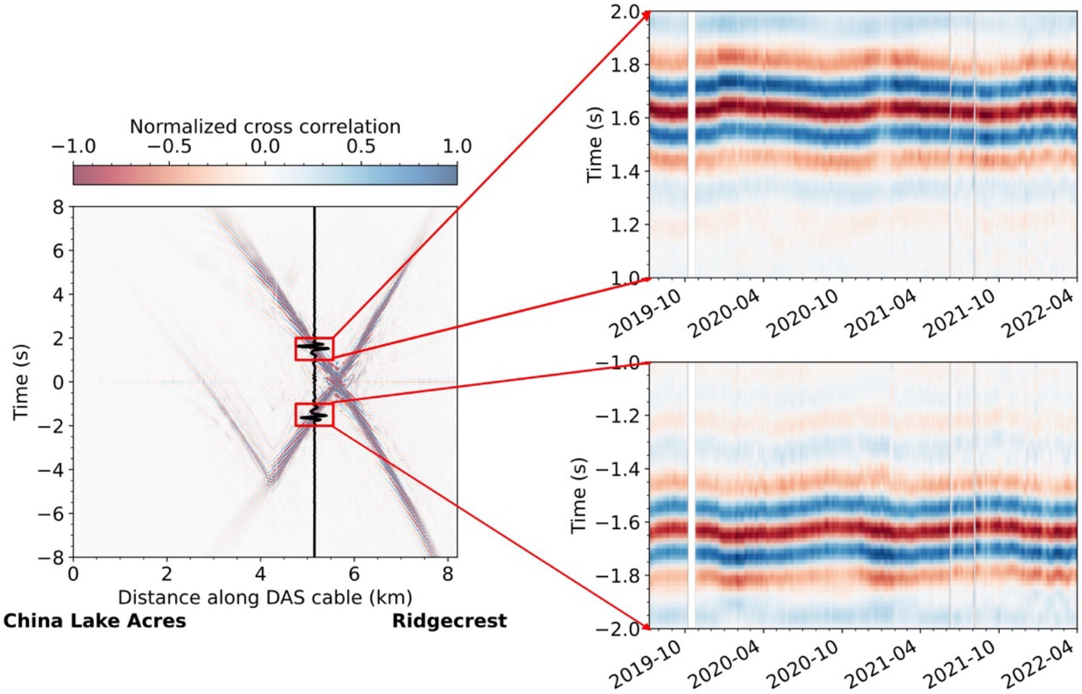

Figure 5.S6: Example of direct Rayleigh waves on cross-correlation waveform. The symmetry of the Rayleigh waves indicates that the source distribution is generally uniform in space, and the resulting dv/v is attributed to the medium rather than noise source variations.

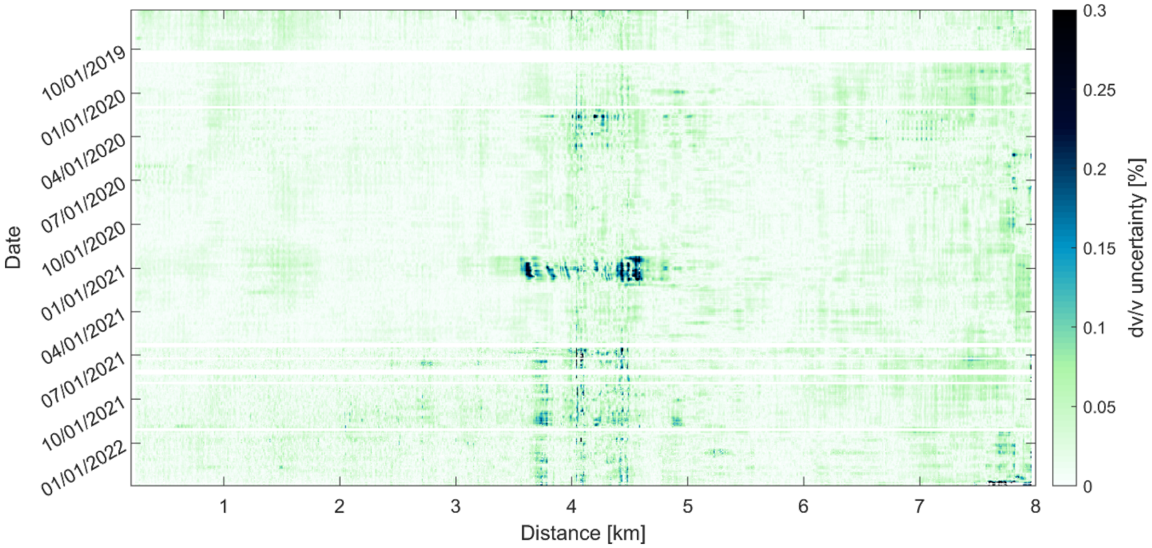

Figure 5.S7: dv/v measurement uncertainty for the central frequency of 4.2 Hz. Note the relatively large uncertainty near 4 km (vertical stripes) due to the scattered surface waves in Figure 5.S6.

Table 5.S1: Monthly Total Precipitation (mm) for meteorological station NID

Year	Jan	Feb	Mar	Apr	May	Jun	Jul	Aug	Sep	Oct	Nov	Dec
2019	0	0	44.20	7.37	0	0	0	0	0	0	13.21	0
2020	0	1.78	23.11	48.00	0	0	0	0	0	0	0	0
2021	2.03	0	0	0	0	0	6.86	0	1.27	1.27	0	27.18
2022	0	0	0	0	0	2.79	0	8.13	0	0	0	8.13

*Shaded area represents our dv/v data coverage.

Table 5.S2. Properties and components of endmember soils.

Soil Type	ϕ	S_{wr}	N	f	Quartz (%)	Kaolinite (%)
Esperance sand	0.25	0.15	6	0.1	70	30
Missouri clay	0.25	0.23	8	0.3	10	90

References

Babaeian, E., Sadeghi, M., Jones, S. B., Montzka, C., Vereecken, H., & Tuller, M. (2019). Ground, Proximal, and Satellite Remote Sensing of Soil Moisture. *Reviews of Geophysics*, *57*(2), 530–616. https://doi.org/10.1029/2018RG000618

Behroozmand, A. A., Auken, E., & Knight, R. (2019). Assessment of Managed Aquifer Recharge Sites Using a New Geophysical Imaging Method. *Vadose Zone Journal*, *18*(1), 180184. https://doi.org/10.2136/vzj2018.10.0184

Bensen, G. D., Ritzwoller, M. H., Barmin, M. P., Levshin, A. L., Lin, F., Moschetti, M. P., et al. (2007). Processing seismic ambient noise data to obtain reliable broad-band surface wave dispersion measurements. *Geophysical Journal International*, *169*(3), 1239–1260. https://doi.org/10.1111/j.1365-246X.2007.03374.x

Ben-Zion, Y., & Leary, P. (1986). Thermoelastic strain in a half-space covered by unconsolidated material. *Bulletin of the Seismological Society of America*, *76*(5), 1447–1460. https://doi.org/10.1785/BSSA0760051447

Berdugo, M., Delgado-Baquerizo, M., Soliveres, S., Hernández-Clemente, R., Zhao, Y., Gaitán, J. J., et al. (2020). Global ecosystem thresholds driven by aridity. *Science*, *367*(6479), 787–790. https://doi.org/10.1126/science.aay5958

Berger, J. (1975). A note on thermoelastic strains and tilts. *Journal of Geophysical Research (1896-1977)*, *80*(2), 274–277. https://doi.org/10.1029/JB080i002p00274

Brutsaert, W. (1964). The propagation of elastic waves in unconsolidated unsaturated granular mediums. *Journal of Geophysical Research*, *69*(2), 243–257. https://doi.org/10.1029/JZ069i002p00243

Campillo, M., & Paul, A. (2003). Long-Range Correlations in the Diffuse Seismic Coda. *Science*, *299*(5606), 547–549. https://doi.org/10.1126/science.1078551

Cho, G. C., & Santamarina, J. C. (2001). Unsaturated Particulate Materials—Particle-Level Studies. *Journal of Geotechnical and Geoenvironmental Engineering*, *127*(1), 84–96. https://doi.org/10.1061/(ASCE)1090-0241(2001)127:1(84)

Clarke, D., Zaccarelli, L., Shapiro, N. M., & Brenguier, F. (2011). Assessment of resolution and accuracy of the Moving Window Cross Spectral technique for monitoring crustal temporal variations using ambient seismic noise. *Geophysical Journal International*, *186*(2), 867–882. https://doi.org/10.1111/j.1365-246X.2011.05074.x

Clements, T., & Denolle, M. A. (2023). The Seismic Signature of California's Earthquakes, Droughts, and Floods. *Journal of Geophysical Research: Solid Earth*, *128*(1), e2022JB025553. https://doi.org/10.1029/2022JB025553

Clements, Timothy, & Denolle, M. A. (2018). Tracking Groundwater Levels Using the Ambient Seismic Field. *Geophysical Research Letters*, *45*(13), 6459–6465. https://doi.org/10.1029/2018GL077706

Dong, Y., & Lu, N. (2016). Dependencies of Shear Wave Velocity and Shear Modulus of Soil on Saturation. *Journal of Engineering Mechanics*, *142*(11), 04016083. https://doi.org/10.1061/(ASCE)EM.1943-7889.0001147

Edokossi, K., Calabia, A., Jin, S., & Molina, I. (2020). GNSS-Reflectometry and Remote Sensing of Soil Moisture: A Review of Measurement Techniques, Methods, and Applications. *Remote Sensing*, *12*(4), 614. https://doi.org/10.3390/rs12040614

Entekhabi, D., Njoku, E. G., O'Neill, P. E., Kellogg, K. H., Crow, W. T., Edelstein, W. N., et al. (2010). The Soil Moisture Active Passive (SMAP) Mission. *Proceedings of the IEEE*, *98*(5), 704–716. https://doi.org/10.1109/JPROC.2010.2043918

Evaristo, J., Jasechko, S., & McDonnell, J. J. (2015). Global separation of plant transpiration from groundwater and streamflow. *Nature*, *525*(7567), 91–94. https://doi.org/10.1038/nature14983

Fan, Y., Miguez-Macho, G., Jobbágy, E. G., Jackson, R. B., & Otero-Casal, C. (2017). Hydrologic regulation of plant rooting depth. *Proceedings of the National Academy of Sciences*, *114*(40), 10572–10577. https://doi.org/10.1073/pnas.1712381114

Fratta, D., Alshibli, K., Tanner, W., & Roussel, L. (2005). Combined TDR and P-Wave Velocity Measurements for the Determination of In Situ Soil Density—Experimental Study. *Geotechnical Testing Journal*, *28*(6), 553–563. https://doi.org/10.1520/GTJ12293

Hermans, T., Goderniaux, P., Jougnot, D., Fleckenstein, J. H., Brunner, P., Nguyen, F., et al. (2023). Advancing measurements and representations of subsurface heterogeneity and dynamic processes: towards 4D hydrogeology. *Hydrology and Earth System Sciences*, *27*(1), 255–287. https://doi.org/10.5194/hess-27-255-2023

Huisman, J. A., Hubbard, S. S., Redman, J. D., & Annan, A. P. (2003). Measuring Soil Water Content with Ground Penetrating Radar: A Review. *Vadose Zone Journal*, *2*(4), 476–491. https://doi.org/10.2136/vzj2003.4760

Illien, L., Andermann, C., Sens-Schönfelder, C., Cook, K. L., Baidya, K. P., Adhikari, L. B., & Hovius, N. (2021). Subsurface Moisture Regulates Himalayan Groundwater Storage and Discharge. *AGU Advances*, *2*(2), e2021AV000398. https://doi.org/10.1029/2021AV000398

Jackson, R. B., Jobbágy, E. G., Avissar, R., Roy, S. B., Barrett, D. J., Cook, C. W., et al. (2005). Trading Water for Carbon with Biological Carbon Sequestration. *Science*, *310*(5756), 1944–1947. https://doi.org/10.1126/science.1119282

Kerr, Y. H., Waldteufel, P., Wigneron, J.-P., Martinuzzi, J., Font, J., & Berger, M. (2001). Soil moisture retrieval from space: the Soil Moisture and Ocean Salinity (SMOS) mission. *IEEE Transactions on Geoscience and Remote Sensing*, *39*(8), 1729–1735. https://doi.org/10.1109/36.942551

Klotzsche, A., Jonard, F., Looms, M. c., van der Kruk, J., & Huisman, J. a. (2018). Measuring Soil Water Content with Ground Penetrating Radar: A Decade of Progress. *Vadose Zone Journal*, *17*(1), 180052. https://doi.org/10.2136/vzj2018.03.0052

Larson, K. M., Braun, J. J., Small, E. E., Zavorotny, V. U., Gutmann, E. D., & Bilich, A. L. (2010). GPS Multipath and Its Relation to Near-Surface Soil Moisture Content. *IEEE Journal of Selected Topics in Applied Earth Observations and Remote Sensing*, *3*(1), 91–99. https://doi.org/10.1109/JSTARS.2009.2033612

Li, Z., Shen, Z., Yang, Y., Williams, E., Wang, X., & Zhan, Z. (2021). Rapid Response to the 2019 Ridgecrest Earthquake With Distributed Acoustic Sensing. *AGU Advances*, *2*(2). https://doi.org/10.1029/2021av000395

Lo, W.-C., Sposito, G., & Majer, E. (2005). Wave propagation through elastic porous media containing two immiscible fluids. *Water Resources Research*, *41*(2). https://doi.org/10.1029/2004WR003162

Mao, S., Lecointre, A., van der Hilst, R. D., & Campillo, M. (2022). Space-time monitoring of groundwater fluctuations with passive seismic interferometry. *Nature Communications*, *13*(1), 4643. https://doi.org/10.1038/s41467-022-32194-3

McColl, K. A., Alemohammad, S. H., Akbar, R., Konings, A. G., Yueh, S., & Entekhabi, D. (2017). The global distribution and dynamics of surface soil moisture. *Nature Geoscience*, *10*(2), 100–104. https://doi.org/10.1038/ngeo2868

Meier, U., Shapiro, N. M., & Brenguier, F. (2010). Detecting seasonal variations in seismic velocities within Los Angeles basin from correlations of ambient seismic noise. *Geophysical Journal International*, *181*(2), 985–996. https://doi.org/10.1111/j.1365-246X.2010.04550.x

Mindlin, R. D. (2021). Compliance of Elastic Bodies in Contact. *Journal of Applied Mechanics*, *16*(3), 259–268. https://doi.org/10.1115/1.4009973

Mordret, A., Courbis, R., Brenguier, F., Chmiel, M., Garambois, S., Mao, S., et al. (2020). Noise-based ballistic wave passive seismic monitoring – Part 2: surface waves. *Geophysical Journal International*, *221*(1), 692–705. https://doi.org/10.1093/gji/ggaa016

Nielsen, D. C., Vigil, M. F., & Benjamin, J. G. (2009). The variable response of dryland corn yield to soil water content at planting. *Agricultural Water Management*, *96*(2), 330–336. https://doi.org/10.1016/j.agwat.2008.08.011

Obermann, A., Planès, T., Larose, E., Sens-Schönfelder, C., & Campillo, M. (2013). Depth sensitivity of seismic coda waves to velocity perturbations in an elastic heterogeneous medium. *Geophysical Journal International*, *194*(1), 372–382. https://doi.org/10.1093/gji/ggt043

Obermann, A., Planès, T., Hadziioannou, C., & Campillo, M. (2016). Lapse-time-dependent coda-wave depth sensitivity to local velocity perturbations in 3-D heterogeneous elastic media. *Geophysical Journal International*, *207*(1), 59–66. https://doi.org/10.1093/gji/ggw264

Or, D., & Lehmann, P. (2019). Surface Evaporative Capacitance: How Soil Type and Rainfall Characteristics Affect Global-Scale Surface Evaporation. *Water Resources Research*, *55*(1), 519–539. https://doi.org/10.1029/2018WR024050

Pacheco, C., & Snieder, R. (2006). Time-lapse traveltime change of singly scattered acoustic waves. *Geophysical Journal International*, *165*(2), 485–500. https://doi.org/10.1111/j.1365-246X.2006.02856.x

Padrón, R. S., Gudmundsson, L., Decharme, B., Ducharne, A., Lawrence, D. M., Mao, J., et al. (2020). Observed changes in dry-season water availability attributed to human-induced climate change. *Nature Geoscience*, *13*(7), 477–481. https://doi.org/10.1038/s41561-020-0594-1

Pellerin, L. (2002). Applications Of Electrical And Electromagnetic Methods For Environmental And Geotechnical Investigations. *Surveys in Geophysics*, *23*(2), 101–132. https://doi.org/10.1023/A:1015044200567

Prawirodirdjo, L., Ben-Zion, Y., & Bock, Y. (2006). Observation and modeling of thermoelastic strain in Southern California Integrated GPS Network daily position time series. *Journal of Geophysical Research: Solid Earth*, *111*(B2). https://doi.org/10.1029/2005JB003716

Pütz, T., Fank, J., & Flury, M. (2018). Lysimeters in Vadose Zone Research. *Vadose Zone Journal*, *17*(1), 180035. https://doi.org/10.2136/vzj2018.02.0035

Reichle, R. H., Liu, Q., Koster, R. D., Crow, W. T., De Lannoy, G. J. M., Kimball, J. S., et al. (2019). Version 4 of the SMAP Level-4 Soil Moisture Algorithm and Data Product. *Journal of Advances in Modeling Earth Systems*, *11*(10), 3106–3130. https://doi.org/10.1029/2019MS001729

Reynolds, J. F., Smith, D. M. S., Lambin, E. F., B. L. Turner, I. I., Mortimore, M., Batterbury, S. P. J., et al. (2007). Global Desertification: Building a Science for Dryland Development. *Science*. https://doi.org/10.1126/science.1131634

Richter, T., Sens-Schönfelder, C., Kind, R., & Asch, G. (2014). Comprehensive observation and modeling of earthquake and temperature-related seismic velocity changes in northern Chile with passive image interferometry. *Journal of Geophysical Research: Solid Earth*, *119*(6), 4747–4765. https://doi.org/10.1002/2013JB010695

Rietkerk, M., Dekker, S. C., de Ruiter, P. C., & van de Koppel, J. (2004). Self-Organized Patchiness and Catastrophic Shifts in Ecosystems. *Science*, *305*(5692), 1926–1929. https://doi.org/10.1126/science.1101867

Rodríguez Tribaldos, V., & Ajo-Franklin, J. B. (2021). Aquifer Monitoring Using Ambient Seismic Noise Recorded With Distributed Acoustic Sensing (DAS) Deployed on Dark Fiber. *Journal of Geophysical Research: Solid Earth*, *126*(4), 1–20. https://doi.org/10.1029/2020JB021004

Roumelioti, Z., Hollender, F., & Guéguen, P. (2020). Rainfall-Induced Variation of Seismic Waves Velocity in Soil and Implications for Soil Response: What the ARGONET (Cephalonia, Greece) Vertical Array Data Reveal. *Bulletin of the Seismological Society of America*, *110*(2), 441–451. https://doi.org/10.1785/0120190183

Rowlands, D. D., Luthcke, S. B., Klosko, S. M., Lemoine, F. G. R., Chinn, D. S., McCarthy, J. J., et al. (2005). Resolving mass flux at high spatial and temporal resolution using

GRACE intersatellite measurements. *Geophysical Research Letters*, *32*(4). https://doi.org/10.1029/2004GL021908

Scanlon, T. M., Caylor, K. K., Levin, S. A., & Rodriguez-Iturbe, I. (2007). Positive feedbacks promote power-law clustering of Kalahari vegetation. *Nature*, *449*(7159), 209–212. https://doi.org/10.1038/nature06060

Solazzi, S. G., Bodet, L., Holliger, K., & Jougnot, D. (2021). Surface-Wave Dispersion in Partially Saturated Soils: The Role of Capillary Forces. *Journal of Geophysical Research: Solid Earth*, *126*(12), e2021JB022074. https://doi.org/10.1029/2021JB022074

Stahl, M. O., & McColl, K. A. (2022). The Seasonal Cycle of Surface Soil Moisture. *Journal of Climate*, *35*(15), 4997–5012. https://doi.org/10.1175/JCLI-D-21-0780.1

Thornthwaite, C. W. (1948). An Approach toward a Rational Classification of Climate. *Geographical Review*, *38*(1), 55–94. https://doi.org/10.2307/210739

Tsai, V. C. (2011). A model for seasonal changes in GPS positions and seismic wave speeds due to thermoelastic and hydrologic variations. *Journal of Geophysical Research*, *116*(B4), B04404. https://doi.org/10.1029/2010JB008156

Wang, L., D’Odorico, P., Ringrose, S., Coetzee, S., & Macko, S. A. (2007). Biogeochemistry of Kalahari sands. *Journal of Arid Environments*, *71*(3), 259–279. https://doi.org/10.1016/j.jaridenv.2007.03.016

Williams, A. P., Cook, B. I., & Smerdon, J. E. (2022). Rapid intensification of the emerging southwestern North American megadrought in 2020–2021. *Nature Climate Change*, *12*(3), 232–234. https://doi.org/10.1038/s41558-022-01290-z

Yang, Y., Zhan, Z., Shen, Z., & Atterholt, J. (2022). Fault Zone Imaging With Distributed Acoustic Sensing: Surface-To-Surface Wave Scattering. *Journal of Geophysical Research: Solid Earth*, *127*(6), e2022JB024329. https://doi.org/10.1029/2022JB024329

Yang, Y., Atterholt, J. W., Shen, Z., Muir, J. B., Williams, E. F., & Zhan, Z. (2022). Sub-Kilometer Correlation Between Near-Surface Structure and Ground Motion Measured With Distributed Acoustic Sensing. *Geophysical Research Letters*, *49*(1), e2021GL096503. https://doi.org/10.1029/2021GL096503

Yuan, C., Bryan, J., & Denolle, M. (2021). Numerical comparison of time-, frequency- and wavelet-domain methods for coda wave interferometry. *Geophysical Journal International*, *226*(2), 828–846. https://doi.org/10.1093/gji/ggab140

Zhan, Z. (2020). Distributed Acoustic Sensing Turns Fiber-Optic Cables into Sensitive Seismic Antennas. *Seismological Research Letters*, *91*(1), 1–15. https://doi.org/10.1785/0220190112

Zhou, S., Williams, A. P., Berg, A. M., Cook, B. I., Zhang, Y., Hagemann, S., et al. (2019). Land–atmosphere feedbacks exacerbate concurrent soil drought and atmospheric aridity. *Proceedings of the National Academy of Sciences*, *116*(38), 18848–18853. https://doi.org/10.1073/pnas.1904955116

Chapter 6

CHARACTERIZING SOUTH POLE FIRN STRUCTURE WITH FIBER OPTIC SENSING

Yang, Y., Zhan, Z., Karrenbach, M. H., Reid-McLaughlin, A., Biondi, E., Wiens, D. A., & Aster, R. C. (under revision). Characterizing South Pole Firn Structure with Fiber Optic Sensing. *Geophysical Research Letters*.

Abstract

The firn layer covers 98% of Antarctica's ice sheets and is key to protecting underlying glacial ice from the external environment. Accurate measurement of firn properties is essential for assessing cryosphere mass balance and climate change impacts. Characterizing firn structure through core sampling is typically expensive and logistically challenging. Seismic surveys relying on translating seismic velocities into firn densities offer an efficient alternative or complement to in-situ measurements. This study employs Distributed Acoustic Sensing technology to transform an existing fiber-optic cable near the South Pole into a multichannel, low-maintenance, continuously interrogated seismic array. The data resolve 16 seismic wave firn propagation modes at frequencies up to 100 Hz that constrain P and S wave velocities as functions of depth. Leveraging nearby SPICEcore firn density data, we find prior empirical density-velocity relationships underestimate firn air content by over 15%. We present a new empirical relationship for the South Pole region.

6.1 Introduction

The Antarctic Ice Sheet (AIS), Earth's largest surface freshwater reservoir, plays an important role as an indicator of climate change and contributor to sea-level change (Shepherd et al., 2018). Firn is a transitional layer from fresh snow to deeper glacial ice (e.g., Gow, 1969), covers 98% of the AIS (Winther et al., 2001), and critically protects it against environmental perturbations (e.g., MacAyeal, 2018; The Firn Symposium team et al., 2024). In warmer ice sheet systems, such as Greenland or the Antarctic Peninsula, firn provides pore space for heat insulation and surface meltwater retention and refreezes into impermeable ice lenses, thus mitigating mass loss through runoff and moderating sea-level change (Dunmire et al., 2024; Harper et al., 2012; Kuipers Munneke et al., 2015; Medley et al., 2022; Noël et al., 2022). Moreover, the firn layer influences the accurate assessment of key factors relevant to climate change, such as satellite altimetry of surface elevation changes and subsequent calculations of AIS mass variations (Arthern & Wingham, 1998; Noël et al., 2018; van Wessem et al., 2018). Variable mass, density, and thickness of the firn layer, influenced by diverse conditions across Antarctica can introduce significant uncertainty when spatially limited measurements are extrapolated to large regions (Boening et al., 2012; van den Broeke, 2008; Ligtenberg et al., 2011).

In situ observations of firn structure can be obtained from snow depth profiles, which sample the upper few meters for density, temperature, and core stratigraphy (e.g., Herron & Langway, 1980; Järvinen et al., 2013; Ligtenberg et al., 2011). Limitations of this methodology may include inherent sparsity of drilling or snow pit sites, associated logistical costs, and possible shortfalls in capturing deeper firn layer complexities due to limited sampling depth. Complementing in-situ measurements, non-destructive geophysical methods, such as seismic and radar techniques, can noninvasively characterize firn properties (Abbasi et al., 2010; Arthern et al., 2013; Chaput et al., 2022; Diez et al., 2016; Hollmann et al., 2021; Jones et al., 2023; Weihaupt, 1963). More recently, distributed acoustic sensing (DAS) of optical fibers has emerged as a tool for glacial seismology applications, offering logistical tractability in challenging environments (Booth et al., 2020; Fichtner et al., 2023; Walter et al., 2020; Zhou et al., 2022). DAS transforms a fiber-optic cable into a dense array of uniaxial strainmeters, providing dense spatial and temporal wavefield resolution across distances up to 100 km (Fan et al., 2023; Lindsey & Martin, 2021; Zhan, 2020). The firn layer's unusual seismic properties, characterized by low near-surface velocities, high degree of lateral homogeneity, and strong near-surface velocity gradient, hosts multiple wave propagation states such as high mode surface wave overtones and leaking modes (Chaput et al., 2022; Kennett, 2023). Utilizing DAS's high-density seismic wavefield sampling, these modes can be characterized and used to refine estimates of firn seismic velocities and structure.

In this work, we leverage an 8-km preexisting buried data communication fiber-optic cable near the South Pole, converting it into a dense seismic array with 1-m spatial sampling. Our goal is to advance understanding of the seismic velocity characteristics of firn, specifically applied here to the dry and cold firn layer of the polar plateau region, which is generally characteristic of much of East Antarctica but less extensively investigated than other firn environments.

6.2 South Pole DAS experiment and observations

In January 2023, we utilized a preexisting data fiber-optic cable to create a dense fiber-oriented horizontal strainmeter array with DAS technology. The cable extends between the Amundsen-Scott South Pole Station and the Global Seismographic Network (GSN; Ringler et al., 2022) station QSPA, located at the South Pole Remote Earth Science and Seismological Observatory (SPRESSO) approximately 8 km from the pole (Figure 6.1; Anthony et al., 2021). The cable, buried about ten meters below the surface, provided a stable temperature and low air circulation environment that facilitated very high signal-to-noise data collection. The fact that the cable is buried 10 meters below the surface affects the relative amplitudes of the observed modes but does not affect estimates of phase velocity, nor does it compromise sensitivity to the top 10 meters of firn (Figures 6.S1, S2). An OptaSense QuantX interrogator (Figure 6.1b), recording at 1000 Hz sampling rate, produced seismic records from every 1 m along the cable using an 8.2 m gauge (spatial smoothing) length. Along-fiber strain rate data from the DAS system were complemented by twelve co-located Fairfield ZLand 3-component geophone nodes spaced about 600 m apart with their transverse components oriented perpendicular to the optical fiber.

Active seismic energy was generated with a propelled energy generator (PEG-40 kg) source. This system is lightweight, highly portable, and engineered for easy mounting onto a Kässbohrer Geländefahrzeug AG PistenBully snow tractor. Repeated impulsive shots were performed for subsequent stacking at two locations aligned with the cable direction, which produced signals with useful frequency content to about 100 Hz. The first set of shots was within the array near its southern terminus (close to DAS Channel 1000), where we executed

1066 shots. To mitigate potential bias in firn structure introduced by human vehicle and other activity near the South Pole Station, we executed another 960 shots at a more remote and quiet location beyond the QSPA seismic station, 10 km away from the South Pole station. This latter site experiences minimal human disturbance. The consistency between these two surveys enhances confidence that the seismic conditions described here are indicative of regional conditions in the South Pole and relevant to other regions of interior Antarctica.

We aligned shot onset times and stacked the DAS recorded data (Figure 6.1c). A 2D *f-k* transform was applied to convert these time-space data into the frequency-wavenumber domain. This allowed us to calculate along-fiber phase velocity through dividing the radian frequency by the wavenumber, leading to a detailed frequency-phase velocity (*f-v*) image that revealed dispersion curves for at least 16 distinct wave propagation modes (Figure 6.2a). These included Rayleigh wave modes with a cutoff velocity around 2000 m/s, a leaking mode exceeding 2000 m/s, and pseudoacoustic modes indicative of surface-reflected P waves trapped in the strong near-surface firn layer seismic velocity gradient (e.g., Albert, 1998) with velocities ranging between 2000 and 4000 m/s. The detailed resolution of multiple firn seismic modes resembles the observations of Fichtner et al., (2023) using airplane landings as a seismic source in Greenland. In our case, the quiet environment at the South Pole, a uniformly buried and well-coupled fiber, together with the strong energy stacked from the active surveys allows for still higher signal-to-noise recording and the detection of additional modes.

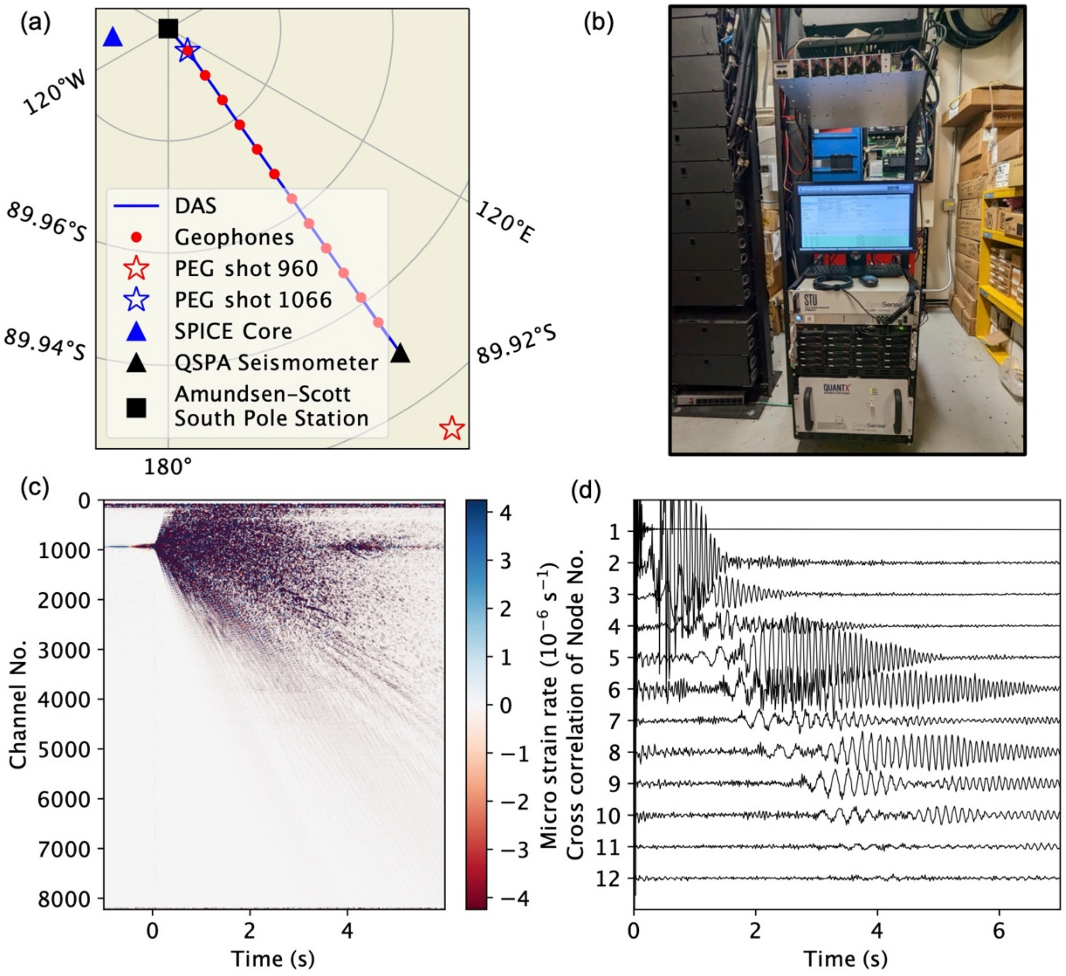

Figure 6.1: Field setting and observations. (a) The South Pole Quiet Sector, showing the locations of the DAS cable, QSPA site, Ice Core, active shots, and geophone-equipped seismic stations. (b) Interrogator and acquisition monitor installed in the Amundsen-Scott South Pole Station. (c) Time-domain wavefield imaged in the DAS data, stacked over 1066 shots applied near Channel 1000, as shown in (a). (d) Cross correlation functions of transverse geophone components, using the geophone closest to Channel 1000 as a virtual source.

6.3 Discrepancies between seismic observations and velocities derived from ice core data

Multiple well resolved seismic wave propagation modes allow us to invert for the vertical seismic firn structure, and to assess these results relative to prior empirical relationships between seismic velocities and density. The South Pole Ice Core (SPICEcore) project, drilled 2.7 km from the Amundsen–Scott South Pole Station in 2014 –2016, provided in situ firn density measurements (Winski et al., 2019). The SPICEcore site was selected to ensure proximity to South Pole Station, avoidance of previous station infrastructure and science sectors, and minimal influence from past and present station emissions (Casey et al., 2014). Given its proximity to our study (Figure 6.1a) and the homogeneous snow and glacial conditions near the South Pole (Watanabe et al., 2003), it provides a reliable firn density data set for this study.

The work by Kohnen & Bentley (1973) at New Byrd Station provided an early look into seismic velocity-density relationships. The empirical relation between P-wave velocities and density was derived from seismic data and firn density profiles from multiple ice cores (Kohnen, 1972)

$$\rho(z) = \frac{\rho_{ice}}{1 + \left(\frac{V_{P,ice} - V_P(z)}{2250\ \mathrm{m/s}}\right)^{1.22}}, \tag{6.1}$$

where z is depth, $\rho(z)$ is the density in the unit of kg/m^3, $V_P(z)$ is P-wave velocity in units of m/s, and $V_{P,ice}$ is P-wave velocity in the sub-firn ice. The empirical relation between firn density and S-wave velocities was derived on the Alpine glacier Colle Gnifetti (Diez et al., 2014)

$$\rho(z) = \frac{\rho_{ice}}{1 + \left(\frac{V_{S,ice} - V_S(z)}{950\ \mathrm{m/s}}\right)^{1.17}}, \tag{6.2}$$

where $V_S(z)$ is S-wave velocity in the unit of m/s, and $V_{S,ice}$ is S-wave velocity in the sub-firn ice. Using these two equations, we apply $\rho(z)$ from the SPICEcore, $\rho_{ice} = 920\ \mathrm{kg/m^3}$, $V_{P,ice} = 3810\ \mathrm{m/s}$, and $V_{S,ice} = 1860\ \mathrm{m/s}$ from a seismic reflection study close to South Pole (Peters et al., 2008) to predict $V_P(z)$ and $V_S(z)$.

Using the empirical $V_P(z)$ and $V_S(z)$ we employed the method of Kennett (2023) to compute the complete seismic response in *f*-*v* space (Figure 6.2b) and observed significant discrepancies between observed and predicted wave propagation mode dispersion curves. First, the observed cutoff velocity for the Rayleigh and pseudoacoustic modes is substantially higher than predicted, indicating that sub-firn glacial seismic velocities at the South Pole exceed the values from (6.1) and (6.2). Second, discrepancies at high frequencies indicate reduced seismic velocity in the upper firn layers relative to those predicted by (6.1) and (6.2).

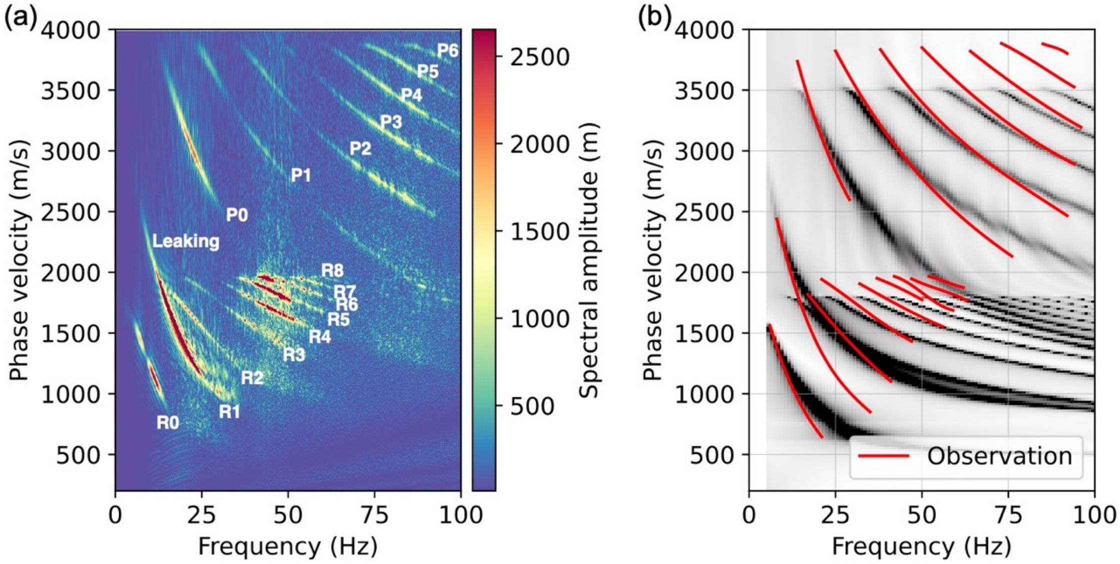

Figure 6.2: Comparison of observed and synthetic frequency-velocity (*f*-*v*) Images. (a) The *f*-*v* image computed from the wavefield stacked over 960 active shots that were performed 2 km from the QSPA station (Figure 6.1a). Identified pseudoacoustic and Rayleigh wave modes are marked in white text. (b) Synthetic *f*-*v* image derived from SPICEcore (Casey et al., 2014) firn-core density-based seismic velocities using equations (6.1) and (6.2), with red dispersion curves from (a).

6.4 Characterizing firn structure with multimode seismic inversion

6.4.1 Seismic velocity model parameterization

We used the observed multimode dispersion curves to obtain new empirical relation suitable for the firn of the South Pole region. The observational constraints include (normal) Rayleigh modes, leaking modes, and pseudoacoustic modes (Figure 6.2a). Normal Rayleigh modes are principally sensitive to V_S , (e.g., Pan et al., 2019) while leaking modes and pseudoacoustic modes are sensitive to both V_S and V_P (Kennett, 2023; Li et al., 2022; Shi et al., 2022). The prominent presence of multiple leaking and pseudoacoustic modes in our observations thus enables us to robustly invert for both V_S and V_P. This contrasts with Rayleigh/Love wave surface wave inversions for 1-D models parametrized solely using V_S in which V_P is empirically inferred from V_S due to limited sensitivity. We use a model parameterization with the functional form of (6.1) and (6.2) that integrates SPICEcore density data and leverages the relationship between seismic velocities within the dry firn layer and specific coefficients tied to density

$$\rho(z) = \frac{\rho_{ice}}{1 + \left(\frac{V_{x,ice} - V_x(z)}{A_x}\right)^{k_x}}, \tag{6.3}$$

where x can represent either P or S waves, A_P, A_S are the scaling velocities, and k_P, k_S are exponents determining depth dependence. The upper bounds of the Rayleigh and pseudoacoustic phase velocities approximate $V_{S,ice}$ and $V_{P,ice}$, respectively, enabling us to constrain these values directly from the phase velocity-frequency spectra. This reduces the number of free parameters to four and is applied to fit all observed modes.

6.4.2 Inversion framework and misfit optimization

Surface wave inversions for seismic structure are most commonly performed by minimizing least-square residuals between fundamental modes group or phase velocities. Even with advancements incorporating multimode or leaking modes, modal identification can be challenging and is essential prior to applying these methods (e.g., Fichtner et al., 2023; Li et al., 2022). Our method employs an image-based misfit function, which calculates the normalized cross-correlation between two images. We first employ the method introduced by Kennett (2023), to forward model the seismic response in *f*-v space. This circumvents the intricate task of root searching within the complex frequency-wavenumber domain (e.g., Pan et al., 2013) inherent in other methods. Maintaining consistent discretization in velocity and frequency, fitting the synthetic *f*-v image to observed *f*-v image eliminates the need to individually identify modes. We estimate the unknown parameters in (6.3) utilizing the ensemble Markov chain Monte Carlo (MCMC) method. We employ the emcee Python package (Foreman-Mackey et al., 2013) for its capability to navigate nonlinear and highly correlated likelihood surfaces typical in forward modeling. The method's convergence is less consistent in expansive model spaces and our streamlined model with only four parameters ensures efficient exploration without excessive computational demands.

Figure 6.3a illustrates the posterior distributions of our four model parameters from the MCMC simulation. The maximum a posteriori parameters provide a South Pole empirical relation specific to our observations as termed in Equation (6.3): $A_P = 2283\ \mathrm{m/s}, A_S = 1068\ \mathrm{m/s}, k_P = 1.028, k_S = 1.036$, with $V_{P,ice} = 3870\ \mathrm{m/s}$, and $V_{S,ice} = 1970\ \mathrm{m/s}$. Figure 6.3b shows the corresponding maximum a posteriori V_P and V_S model. We present in Figure 6.S3 the posterior distribution of the inverted Vp and Vs models. The corresponding *f*-v image is shown in Figure 6.3c overlain with the observed dispersion curves. The close match between model and the high-resolution DAS recordings demonstrates the effectiveness of the inversion approach and parameterization using just four free parameters. Results confirm deviations from (6.1) and (6.2), with the South Pole region requiring higher seismic velocities in sub-firn ice, larger scaling velocities, and smaller exponents for V_P and V_S.

6.4.3 Analysis of radial anisotropy in South Pole firn

Inverted stacked active seismic survey pseudoacoustic and Rayleigh mode data enable us to resolve the (vertical) radially polarized seismic velocity. Radial anisotropy, in which horizontal elastic parameters differ from those in the vertical direction, has been widely documented in glacial firn (Diez et al., 2016; Pearce et al., 2023; Schlegel et al., 2019; Zhang et al., 2022). Theoretically, Rayleigh waves are sensitive to the vertically polarized V_S (V_{SV}) while Love waves are sensitive to the horizontally polarized V_S (V_{SH}). To investigate potential radial anisotropy, we employ ambient noise interferometry for the transverse geophone components to extract Love wave group velocities. We process 10 days of geophone data following the conventional workflow for ambient noise interferometry (Bensen et al., 2007). The 2–30 Hz cross-correlation data revealed Love wave signals (Figure 6.1d) for which we conducted a time-frequency analysis to calculate group velocity dispersion (Figure 6.3d).

Interestingly, the Love wave group velocity was remarkably well fitted using our Rayleigh wave-derived V_{SV} model (Figure 6.3d), indicating a low degree of radial anisotropy. Studies reporting 10–15% radial anisotropy ($\frac{V_{SH}}{V_{SV}} - 1$) in the upper 50–60 m of the firn column include Diez et al. (2016) and Pearce et al. (2023). Previous studies typically account for at least 5% radial anisotropy when converting DAS-measured V_{SV} to V_{SH} (Fichtner et al., 2023). In this study, however, adding even 5% radial anisotropy to compute the V_{SH} and the dispersion curves results in a large discrepancy in fitting the Love wave modes, as demonstrated in Figure 6.3d, confirming that South Pole firn exhibits very weak radial anisotropy.

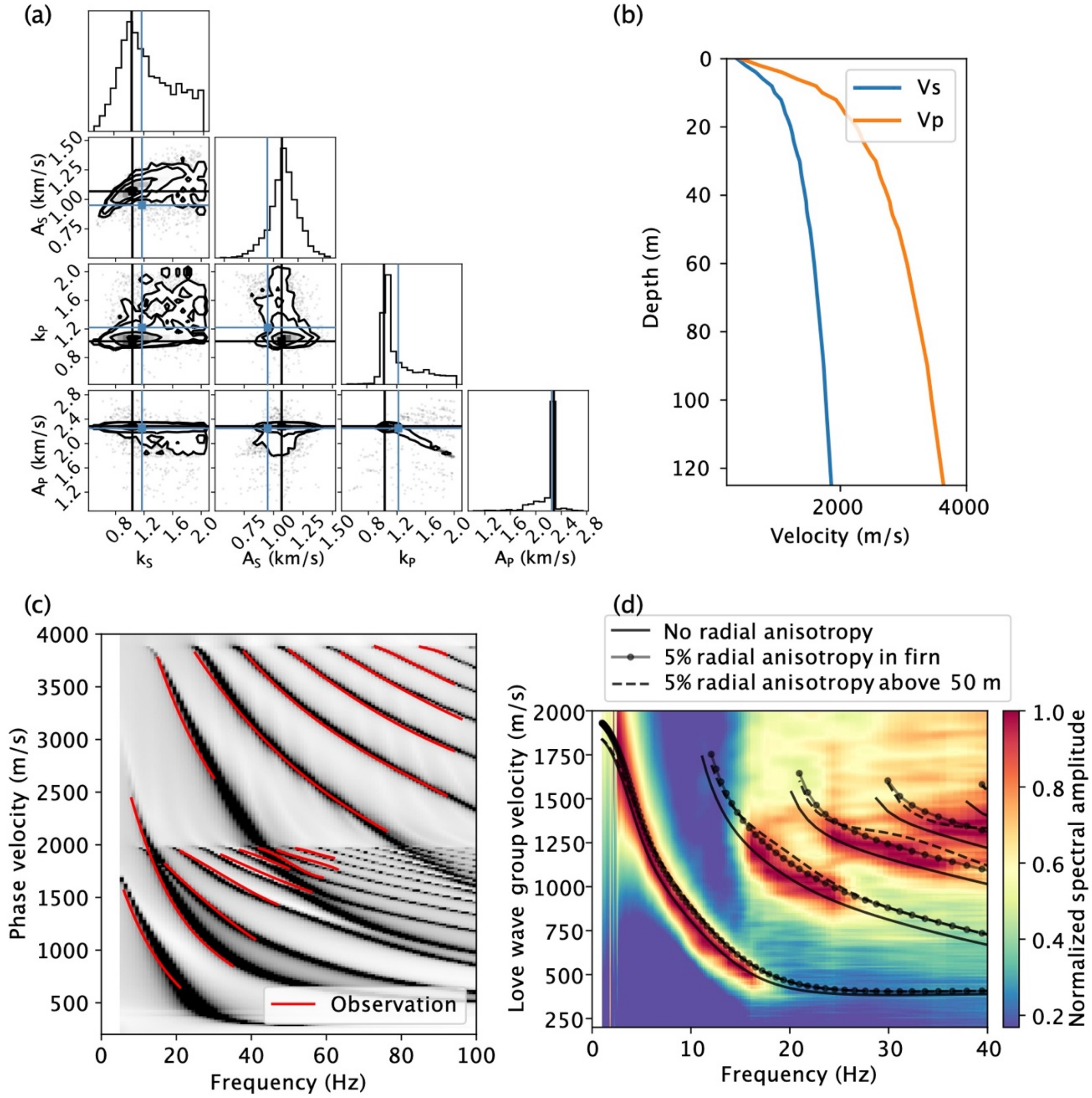

Figure 6.3: Inverted firn structure and model fitting for the parameters in equation (6.3). (a) The posterior distributions of the parameters from our inversion model. The diagonal subplots display marginal distributions as histograms for each parameter and the off-diagonal subplots reveal 2D marginal distributions between parameter pairs with contours displaying confidence intervals calculated from the sampled posterior distribution. The blue lines within the plot mark the reference values from empirical relations in Equations (6.1) and (6.2). The black lines indicate the maximum a posteriori parameters. (b) The maximum a posteriori seismic velocity model. (c) Synthetic *f-v* image using the best- fitting seismic velocity model

(b), along with red dispersion curves from Figure 6.2a. (d) Observed *f*-*v* image for Love wave group velocities, computed using ambient noise data from fiber co-located geophones (Figure 6.1d). Solid black synthetic dispersion curves correspond to the (isotropic) model in (b) and dashed and dotted dispersion curves correspond to Love waves with introduced radial anisotropy.

6.5 Discussion and conclusions

6.5.1 The South Pole empirical relation and its implication for AIS mass change estimate

Firn density carries information for ice sheet modeling, relevant to meltwater capacity (Medley et al., 2022), solid-ice discharge over the grounding line (Rignot et al., 2019), altimetric mass-balance uncertainty (Smith et al., 2023), and paleoclimate reconstruction (Craig et al., 1988). Therefore, it is essential to use validated relationships to translate seismic velocities (V_P or V_S) to the density. Currently, most V_P-density empirical relationships in use have been derived from analyses of multiple boreholes spanning glacial regions worldwide (Kohnen, 1972). In contrast, V_S-density relationships have been specifically derived for the alpine Colle Gnifetti glacier (Diez et al., 2014). These site or region-specific models introduce potential biases when applied to interior Antarctica with contrasting climatic and geophysical characteristics relative to, for example, the warmer, more dynamic environments of interior Greenland and the lower-elevation sectors of West Antarctica. Empirical models based on data from these latter regions underestimate seismic velocity in the dry, cold firn at Kohnen Station in interior Dronning Maud Land (Schlegel et al., 2019) and in this study.

Figure 6.4a and 4b display relationships between density and Vp, and density and Vs, respectively. Even under the same density (air content), site-specific conditions such as temperature and snow accumulation rates affect the mechanical properties of firn, as evidenced by the difference in seismic velocities. This variation can significantly bias the conversion from seismic velocity to density. In Figure 6.4c, we plot the depth profiles of density derived from these different empirical relations and juxtapose these against core density observations. The V_P-density relation (6.1) overestimates density by about 5%, and the V_S-density relation (6.2) overestimates it by about 8% in the Polar Plateau/East Antarctic context.

From density, we can calculate firn air content (FAC), which is an indicator of the meltwater storage capacity of the firn. Importantly, FAC variability significantly impacts surface height variations observed in satellite altimetry, with over 60% of this variability attributable to FAC changes (Veldhuijsen et al., 2023). FAC can be calculated from firn density and depth (Ligtenberg et al., 2014) as

$$\mathrm{FAC} = \frac{1}{\rho_i} \int_{z_s}^{z(\rho_i)} (\rho_i - \rho(z))\mathrm{d}z, \tag{6.4}$$

where $\rho(z)$ is the depth-dependent density, ρ_i is glacial ice density, and z_s and $z(\rho_i)$ are the surface and the depth at which the ice density is reached, respectively. Calculation using the three different empirical relations (Diez et al., 2014; Kohnen, 1972) suggests that the V_P-density relationship (6.1) underestimates FAC by about 11%, and the V_S-density model (6.2) underestimates it by about 17% for East Antarctica. These findings highlight the need for further region-specific empirical relationships that can better capture regional variations necessary for accurate firn density estimations and AIS mass balance estimation.

Results presented here represent a new model for the South Pole, and assessing its broader applicability for interior Antarctica requires additional data collection. Fiber-optic cables are particularly efficient and effective for characterizing seismic wave dispersion and can be readily deployed to acquire more comprehensive data to support or refine these initial findings.

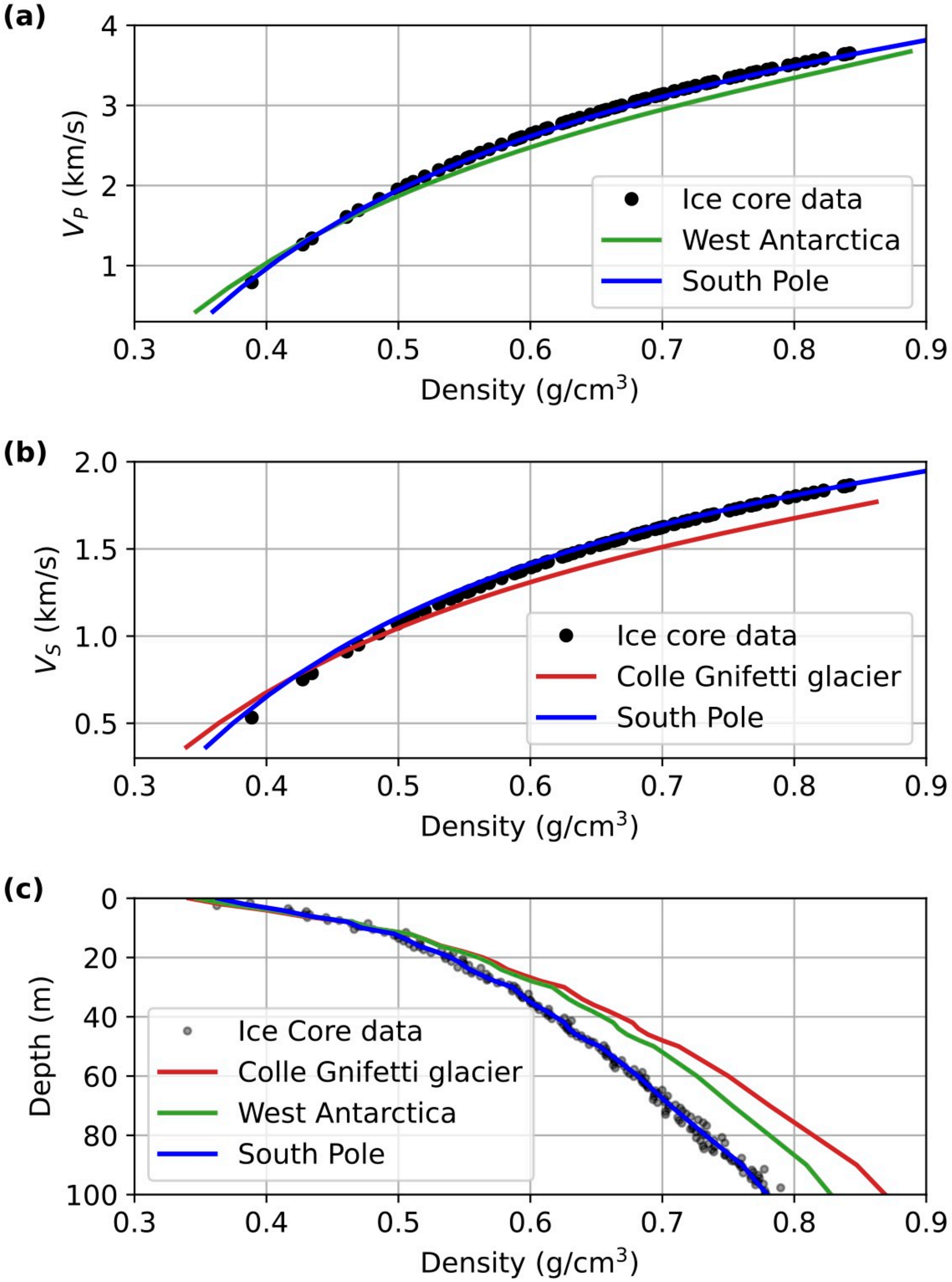
(a)
V_P (km/s)
4
3
2
1
0.3
0.4
0.5
0.6
0.7
0.8
0.9
Density (g/cm^3)
Ice core data
West Antarctica
South Pole
(b)
V_S (km/s)
2.0
1.5
1.0
0.5
0.3
0.4
0.5
0.6
0.7
0.8
0.9
Density (g/cm^3)
Ice core data
Colle Gnifetti glacier
South Pole
(c)
Depth (m)
0
20
40
60
80
100
0.3
0.4
0.5
0.6
0.7
0.8
0.9
Density (g/cm^3)
Ice Core data
Colle Gnifetti glacier
West Antarctica
South Pole

Figure 6.4: Comparison of empirical relations with the DAS-inverted South Pole seismic velocity model (blue). (a) V_P-density relations; green curve represents empirical relation derived for West Antarctica sites (Equation 6.1 of Kohnen, 1972); (b) V_S-density relation; red curve represent empirical relation derived for Greenland sites (Equation 6.2 of Diez et al., 2014); (c) Firn density profiles converted from our seismic velocity model using the three empirical relations. Black dots in all panels indicate data points from the SPICEcore project.

6.5.2 Weak radial anisotropy in South Polar firn

Firn layer seismic and structural anisotropy, both azimuthal and radial, has been a subject of extensive study. Azimuthal anisotropy, characterized by velocity variations with horizontal direction, is typically observed in firn under the influence of ice flow and surface strain rates, with reported values ranging from 0–4% (Diez et al., 2016; Chaput et al., 2022; Hollmann et al., 2021; Zhou et al., 2022). Radial anisotropy, denoting velocity differences between horizontal and vertical polarizations, generally exhibits a larger amplitude. It has been attributed to effective anisotropy from thin layering, intrinsic anisotropy from the preferred orientation of ice crystals, and to structural anisotropy introduced by features such as aligned crevasses and micro-cracks, which are particularly pronounced in the upper 50 m of the firn layer (Diez et al., 2016; Pearce et al., 2023; Zhang et al., 2022). Observed radial anisotropy is commonly substantial (around 10–15%).

Our findings near South Pole, a high altitude (2835 m) plateau characterized by a slowly moving ice sheet (10 m/year), low precipitation (5 cm/year), and cold temperatures (-49.3°C annual average), deviate from observations at other firn locations. We detected negligible radial anisotropy through ambient noise interferometry using the co-located geophones (Figure 6.3C). A similar observation made at Kohnen Station showed minimal radial anisotropy at depths below 10 m (Schlegel et al., 2019). The absence of radial anisotropy at the South Pole site further underscores the diversity in firn layering characteristics in different Antarctic regions and reiterates the value of localized studies in glacial seismology.

6.5.3 Potential for long-term fiber-seismic monitoring to glacial firn stability and hydrology

Firn contains significant pore space that can store or transmit meltwater. In the northernmost sectors of Antarctica, the vast majority of surface meltwater is retained and commonly refrozen within the firn, contributing to its stability (Medley et al., 2022), but surface melt is historically scarce to absent in interior Antarctica (Trusel et al., 2012). In Greenland, half of the total surface melt is absorbed by the firn pore spaces (Fettweis et al., 2020). The potential impacts of meltwater on Antarctic mass balance and ice shelf stability—through increased runoff, bed injection, and ice-shelf fracture—underscore the importance of monitoring firn conditions (Bell et al., 2018).

To accurately track the fate of meltwater in the firn system, various observational tools have been employed to monitor near-surface firn properties, ranging from in-situ temperature measurements and dielectric techniques (Miller et al., 2020; Sihvola & Tiuri, 1986), to seismic and radar observations (Chaput et al., 2018; Killingbeck et al., 2020), to remote sensing via synthetic aperture radars and microwave scatterometers (Alley et al., 2018; Fahnestock et al., 1993). The deployment of surface instrumentation on glaciers faces significant challenges due to the harsh and dynamic environment, where seasonal variations in surface morphology due to ablation, crevassing, or melting can compromise data collection or reliability (e.g., MacAyeal, 2018) DAS offers an attractive solution for glacial firn hydrology monitoring (Manos et al., 2024). By utilizing a fiber optic cable, DAS can provide sensitivity in wide areas across multiple glacial features without the typical constraints of traditional seismic sensing methods, such as the need for independent power and other infrastructure at sensing points.

6.6 Conclusions

Distributed Acoustic Sensing (DAS) applied to an 8-km fiber-optic cable near the South Pole and the detection and inversion of sixteen seismic propagation modes at frequencies up to 100 Hz enables us to constrain the P- and S-wave velocities of the firn layer. We derive a new empirical relation between density and P- and S-wave velocities for the low precipitation and cold South Pole firn regime that may be applicable to extensive regions of the Antarctic Plateau and interior Antarctica with comparable environmental conditions. This refined model represents an improvement over previous empirical relationships for this site, effectively reducing the underestimation of firn air content by over 15%. This study, more generally, highlights the effectiveness and future potential of fiber-optic sensing technology in glacial seismology.

Supplementary Material

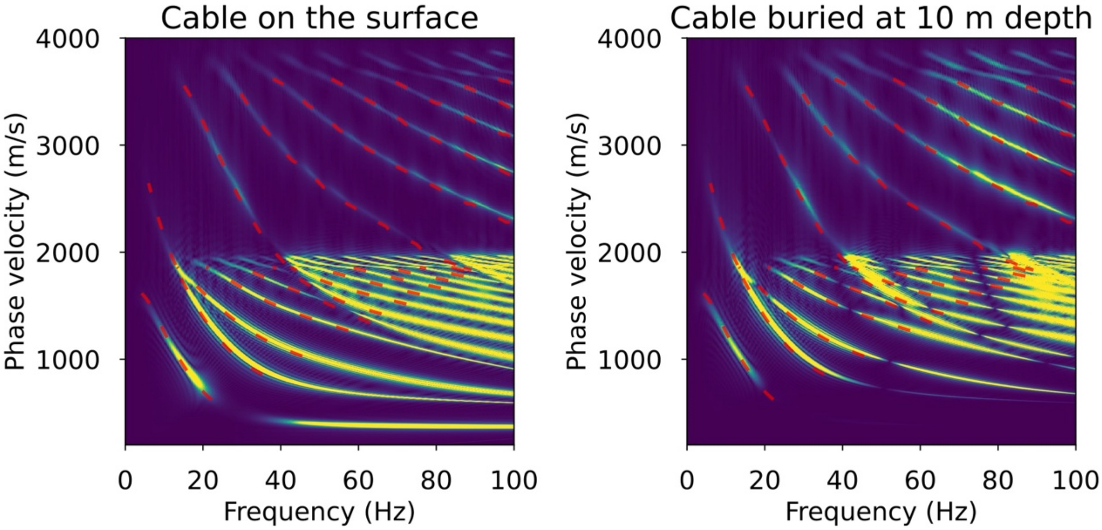

Figure 6.S1: Synthetic tests for two cable scenarios. Left panel: DAS cable on the surface. Right panel: DAS cable buried at a depth of 10 meters. The observed modes from our data are indicated by red dashed lines. Although the depth of the cable alters the amplitudes of the seismic propagation modes, it has no effect on the phase velocity measurements.

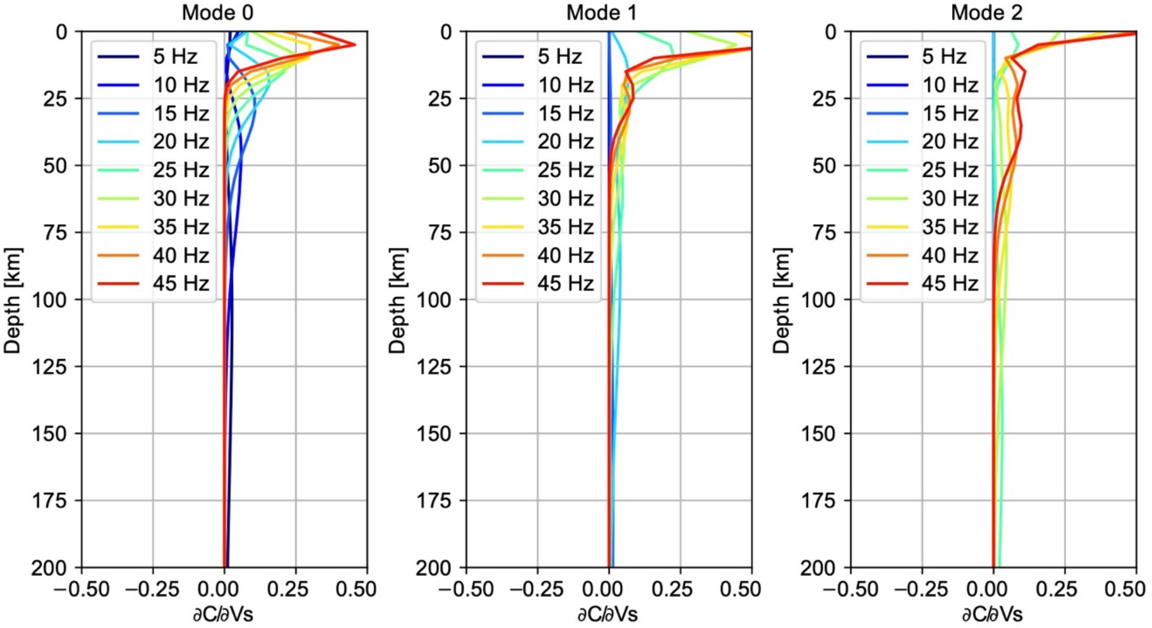

Figure 6.S2: Sensitivity of Rayleigh wave modes to shear wave velocity at various depths. From left to right, the panels display the sensitivity of the 0th, 1st, and 2nd Rayleigh modes to shear wave velocities. Although the fundamental mode of our observed Rayleigh waves is truncated at approximately 25 Hz and the first overtone at about 40 Hz, the sensitivity kernel plot reveals that these modes, particularly the first and second overtones around 40 Hz, are highly sensitive to changes in shear velocity within the top 10 meters of the firn structure.

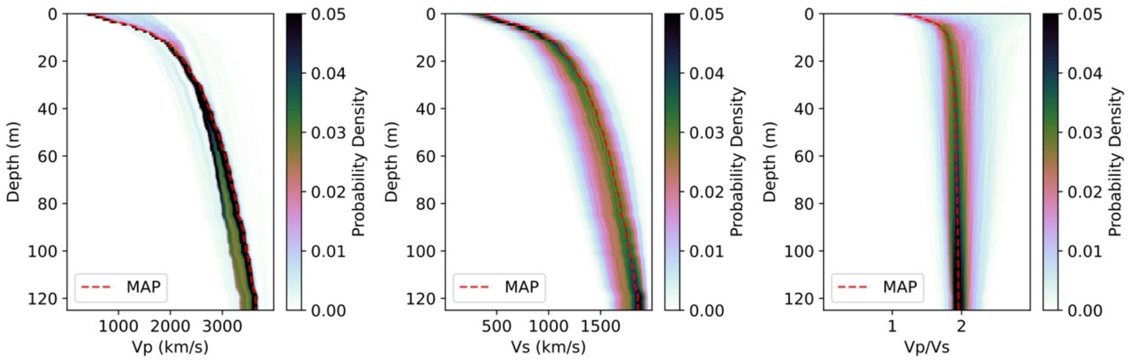

Figure 6.S3: A color density plot of the posterior probability distribution of the inverted Vp and Vs models, along with Vp/Vs results. The red dashed lines show the maximum a posteriori (MAP) model with depth.

References

Abbasi, R., Abdou, Y., Ackermann, M., Adams, J., Aguilar, J. A., Ahlers, M., et al. (2010). Measurement of sound speed vs. depth in South Pole ice for neutrino astronomy. *Astroparticle Physics*, *33*(5–6), 277–286. https://doi.org/10.1016/j.astropartphys.2010.01.012

Albert, D. G. (1998). Theoretical modeling of seismic noise propagation in firn at the South Pole, Antarctica. *Geophysical Research Letters*, *25*(23), 4257–4260. https://doi.org/10.1029/1998GL900155

Alley, K. E., Scambos, T. A., Miller, J. Z., Long, D. G., & MacFerrin, M. (2018). Quantifying vulnerability of Antarctic ice shelves to hydrofracture using microwave scattering properties. *Remote Sensing of Environment*, *210*, 297–306. https://doi.org/10.1016/j.rse.2018.03.025

Anthony, R. E., Aster, R. C., Wiens, D., Nyblade, A., Anandakrishnan, S., Huerta, A., et al. (2015). The Seismic Noise Environment of Antarctica. *Seismological Research Letters*, *86*(1), 89–100. https://doi.org/10.1785/0220140109

Anthony, Robert E., Ringler, A. T., DuVernois, M., Anderson, K. R., & Wilson, D. C. (2021). Six Decades of Seismology at South Pole, Antarctica: Current Limitations and Future Opportunities to Facilitate New Geophysical Observations. *Seismological Research Letters*, *92*(5), 2718–2735. https://doi.org/10.1785/0220200448

Arthern, R. J., & Wingham, D. J. (1998). The Natural Fluctuations of Firn Densification and Their Effect on the Geodetic Determination of Ice Sheet Mass Balance. *Climatic Change*, *40*(3), 605–624. https://doi.org/10.1023/A:1005320713306

Arthern, R. J., J. Corr, H. F., Gillet-Chaulet, F., Hawley, R. L., & Morris, E. M. (2013). Inversion for the density-depth profile of polar firn using a stepped-frequency radar. *Journal of Geophysical Research: Earth Surface*, *118*(3), 1257–1263. https://doi.org/10.1002/jgrf.20089

Bell, R. E., Banwell, A. F., Trusel, L. D., & Kingslake, J. (2018). Antarctic surface hydrology and impacts on ice-sheet mass balance. *Nature Climate Change*, *8*(12), 1044–1052. https://doi.org/10.1038/s41558-018-0326-3

Bensen, G. D., Ritzwoller, M. H., Barmin, M. P., Levshin, A. L., Lin, F., Moschetti, M. P., et al. (2007). Processing seismic ambient noise data to obtain reliable broad-band surface wave dispersion measurements. *Geophysical Journal International*, *169*(3), 1239–1260. https://doi.org/10.1111/j.1365-246X.2007.03374.x

Boening, C., Lebsock, M., Landerer, F., & Stephens, G. (2012). Snowfall-driven mass change on the East Antarctic ice sheet. *Geophysical Research Letters*, *39*(21). https://doi.org/10.1029/2012GL053316

Booth, A. D., Christoffersen, P., Schoonman, C., Clarke, A., Hubbard, B., Law, R., et al. (2020). Distributed Acoustic Sensing of Seismic Properties in a Borehole Drilled on a Fast-Flowing Greenlandic Outlet Glacier. *Geophysical Research Letters*, *47*(13), e2020GL088148. https://doi.org/10.1029/2020GL088148

van den Broeke, M. (2008). Depth and Density of the Antarctic Firn Layer. *Arctic, Antarctic, and Alpine Research*, *40*(2), 432–438. https://doi.org/10.1657/1523-0430(07-021)[BROEKE]2.0.CO;2

Casey, K. A., Fudge, T. J., Neumann, T. A., Steig, E. J., Cavitte, M. G. P., & Blankenship, D. D. (2014). The 1500 m South Pole ice core: recovering a 40 ka environmental record. *Annals of Glaciology*, *55*(68), 137–146. https://doi.org/10.3189/2014AoG68A016

Chaput, J., Aster, R. C., McGrath, D., Baker, M., Anthony, R. E., Gerstoft, P., et al. (2018). Near-Surface Environmentally Forced Changes in the Ross Ice Shelf Observed With Ambient Seismic Noise. *Geophysical Research Letters*, *45*(20), 11,187-11,196. https://doi.org/10.1029/2018GL079665

Chaput, J., Aster, R., Karplus, M., & Nakata, N. (2022). Ambient high-frequency seismic surface waves in the firn column of central west Antarctica. *Journal of Glaciology*, *68*(270), 785–798. https://doi.org/10.1017/jog.2021.135

Chaput, Julien, Aster, R., Karplus, M., Nakata, N., & Gerstoft, P. (2022). Near-surface seismic anisotropy in Antarctic glacial snow and ice revealed by high-frequency ambient noise. *Journal of Glaciology*, 1–17. https://doi.org/10.1017/jog.2022.98

Craig, H., Horibe, Y., & Sowers, T. (1988). Gravitational Separation of Gases and Isotopes in Polar Ice Caps. *Science*, *242*(4886), 1675–1678. https://doi.org/10.1126/science.242.4886.1675

Diez, A., Eisen, O., Weikusat, I., Eichler, J., Hofstede, C., Bohleber, P., et al. (2014). Influence of ice crystal anisotropy on seismic velocity analysis. *Annals of Glaciology*, *55*(67), 97–106. https://doi.org/10.3189/2014AoG67A002

Diez, A., Bromirski, P. D., Gerstoft, P., Stephen, R. A., Anthony, R. E., Aster, R. C., et al. (2016). Ice shelf structure derived from dispersion curve analysis of ambient seismic noise, Ross Ice Shelf, Antarctica. *Geophysical Journal International*, *205*(2), 785–795. https://doi.org/10.1093/gji/ggw036

Dunmire, D., Wever, N., Banwell, A. F., & Lenaerts, J. T. M. (2024). Antarctic-wide ice-shelf firn emulation reveals robust future firn air depletion signal for the Antarctic Peninsula. *Communications Earth & Environment*, *5*(1), 1–13. https://doi.org/10.1038/s43247-024-01255-4

Fahnestock, M., Bindschadler, R., Kwok, R., & Jezek, K. (1993). Greenland Ice Sheet Surface Properties and Ice Dynamics from ERS-1 SAR Imagery. *Science*, *262*(5139), 1530–1534. https://doi.org/10.1126/science.262.5139.1530

Fan, C., Li, H., Zhang, K., Liu, H., Sun, Y., Liu, H., et al. (2023). 300 km ultralong fiber optic DAS system based on optimally designed bidirectional EDFA relays. *Photonics Research*, *11*(6), 968–977. https://doi.org/10.1364/PRJ.485701

Fettweis, X., Hofer, S., Krebs-Kanzow, U., Amory, C., Aoki, T., Berends, C. J., et al. (2020). GrSMBMIP: intercomparison of the modelled 1980–2012 surface mass balance over the Greenland Ice Sheet. *The Cryosphere*, *14*(11), 3935–3958. https://doi.org/10.5194/tc-14-3935-2020

Fichtner, A., Hofstede, C., N. Kennett, B. L., Nymand, N. F., Lauritzen, M. L., Zigone, D., & Eisen, O. (2023). Fiber-Optic Airplane Seismology on the Northeast Greenland Ice Stream. *The Seismic Record*, *3*(2), 125–133. https://doi.org/10.1785/0320230004

Foreman-Mackey, D., Hogg, D. W., Lang, D., & Goodman, J. (2013). emcee: The MCMC Hammer. *Publications of the Astronomical Society of the Pacific*, *125*(925), 306–312. https://doi.org/10.1086/670067

Gow, A. J. (1969). On the Rates of Growth of Grains and Crystals in South Polar Firn. *Journal of Glaciology*, *8*(53), 241–252. https://doi.org/10.3189/S0022143000031233

Harper, J., Humphrey, N., Pfeffer, W. T., Brown, J., & Fettweis, X. (2012). Greenland ice-sheet contribution to sea-level rise buffered by meltwater storage in firn. *Nature*, *491*(7423), 240–243. https://doi.org/10.1038/nature11566

Herron, M. M., & Langway, C. C. (1980). Firn Densification: An Empirical Model. *Journal of Glaciology*, *25*(93), 373–385. https://doi.org/10.3189/S0022143000015239

Hollmann, H., Treverrow, A., Peters, L. E., Reading, A. M., & Kulessa, B. (2021). Seismic observations of a complex firn structure across the Amery Ice Shelf, East Antarctica. *Journal of Glaciology*, *67*(265), 777–787. https://doi.org/10.1017/jog.2021.21

Järvinen, O., Leppäranta, M., & Vehviläinen, J. (2013). One-year records from automatic snow stations in western Dronning Maud Land, Antarctica. *Antarctic Science*, *25*(5), 711–728. https://doi.org/10.1017/S0954102013000187

Jones, G. A., Ferreira, A. M. G., Kulessa, B., Schimmel, M., Berbellini, A., & Morelli, A. (2023). Constraints on the Cryohydrological Warming of Firn and Ice in Greenland From Rayleigh Wave Ellipticity Data. *Geophysical Research Letters*, *50*(15), e2023GL103673. https://doi.org/10.1029/2023GL103673

Kennett, B. (2023). Interacting Seismic Waveguides: Multimode Surface Waves and Leaking Modes. *Seismica*, *2*(1). https://doi.org/10.26443/seismica.v2i1.282

Killingbeck, S. F., Schmerr, N. C., Montgomery, L. N., Booth, A. D., Livermore, P. W., Guandique, J., et al. (2020). Integrated Borehole, Radar, and Seismic Velocity Analysis Reveals Dynamic Spatial Variations Within a Firn Aquifer in Southeast Greenland. *Geophysical Research Letters*, *47*(18), e2020GL089335. https://doi.org/10.1029/2020GL089335

Kohnen, H. (1972). Über die Beziehung zwischen seismischen Geschwindigkeiten und der Dichte in Firn und Eis (On the Relation between Seismic Velocities and Density in Firn and Ice). *Geophysik*, *38*(5), 925–935.

Kohnen, H., & Bentley, C. R. (1973). Seismic Refraction and Reflection Measurements at “Byrd” Station, Antarctica. *Journal of Glaciology*, *12*(64), 101–111. https://doi.org/10.3189/S0022143000022747

Kuipers Munneke, P., Ligtenberg, S. R. M., Noël, B. P. Y., Howat, I. M., Box, J. E., Mosley-Thompson, E., et al. (2015). Elevation change of the Greenland Ice Sheet due to surface mass balance and firn processes, 1960–2014. *The Cryosphere*, *9*(6), 2009–2025. https://doi.org/10.5194/tc-9-2009-2015

Li, Z., Shi, C., Ren, H., & Chen, X. (2022). Multiple Leaking Mode Dispersion Observations and Applications From Ambient Noise Cross-Correlation in Oklahoma. *Geophysical Research Letters*, *49*(1), e2021GL096032. https://doi.org/10.1029/2021GL096032

Ligtenberg, S. R. M., Helsen, M. M., & van den Broeke, M. R. (2011). An improved semi-empirical model for the densification of Antarctic firn. *The Cryosphere*, *5*(4), 809–819. https://doi.org/10.5194/tc-5-809-2011

Ligtenberg, S. R. M., Kuipers Munneke, P., & van den Broeke, M. R. (2014). Present and future variations in Antarctic firn air content. *The Cryosphere*, *8*(5), 1711–1723. https://doi.org/10.5194/tc-8-1711-2014

Lindsey, N. J., & Martin, E. R. (2021). Fiber-Optic Seismology. *Annual Review of Earth and Planetary Sciences*, *49*(1), 309–336. https://doi.org/10.1146/annurev-earth-072420-065213

Manos, J.-M., Gräff, D., Martin, E., Paitz, P., Walter, F., Fichtner, A., & Lipovsky, B. P. (2024). DAS to Discharge: Using Distributed Acoustic Sensing (DAS) to infer glacier runoff. Retrieved from https://eartharxiv.org/repository/view/6680/

Medley, B., Neumann, T. A., Zwally, H. J., Smith, B. E., & Stevens, C. M. (2022). Simulations of firn processes over the Greenland and Antarctic ice sheets: 1980–2021. *The Cryosphere*, *16*(10), 3971–4011. https://doi.org/10.5194/tc-16-3971-2022

Miller, O., Solomon, D. K., Miège, C., Koenig, L., Forster, R., Schmerr, N., et al. (2020). Hydrology of a Perennial Firn Aquifer in Southeast Greenland: An Overview Driven by Field Data. *Water Resources Research*, *56*(8), e2019WR026348. https://doi.org/10.1029/2019WR026348

Noël, B., van de Berg, W. J., van Wessem, J. M., van Meijgaard, E., van As, D., Lenaerts, J. T. M., et al. (2018). Modelling the climate and surface mass balance of polar ice sheets using RACMO2 – Part 1: Greenland (1958–2016). *The Cryosphere*, *12*(3), 811–831. https://doi.org/10.5194/tc-12-811-2018

Noël, B., Lenaerts, J. T. M., Lipscomb, W. H., Thayer-Calder, K., & van den Broeke, M. R. (2022). Peak refreezing in the Greenland firn layer under future warming scenarios. *Nature Communications*, *13*(1), 6870. https://doi.org/10.1038/s41467-022-34524-x

Pan, L., Chen, X., Wang, J., Yang, Z., & Zhang, D. (2019). Sensitivity analysis of dispersion curves of Rayleigh waves with fundamental and higher modes. *Geophysical Journal International*, *216*(2), 1276–1303. https://doi.org/10.1093/gji/ggy479

Pan, Y., Xia, J., & Zeng, C. (2013). Verification of correctness of using real part of complex root as Rayleigh-wave phase velocity with synthetic data. *Journal of Applied Geophysics*, *88*, 94–100. https://doi.org/10.1016/j.jappgeo.2012.09.012

Pearce, E., Zigone, D., Hofstede, C., Fichtner, A., Rimpot, J., Olander Rasmussen, S., et al. (2023). *Firn Seismic Anisotropy in the North East Greenland Ice Stream from Ambient Noise Surface Waves* (preprint). Ice sheets/Greenland. https://doi.org/10.5194/egusphere-2023-2192

Peters, L. E., Anandakrishnan, S., Holland, C. W., Horgan, H. J., Blankenship, D. D., & Voigt, D. E. (2008). Seismic detection of a subglacial lake near the South Pole, Antarctica. *Geophysical Research Letters*, *35*(23). https://doi.org/10.1029/2008GL035704

Rignot, E., Mouginot, J., Scheuchl, B., van den Broeke, M., van Wessem, M. J., & Morlighem, M. (2019). Four decades of Antarctic Ice Sheet mass balance from 1979–2017. *Proceedings of the National Academy of Sciences*, *116*(4), 1095–1103. https://doi.org/10.1073/pnas.1812883116

Ringler, A. T., Anthony, R. E., Aster, R. C., Ammon, C. J., Arrowsmith, S., Benz, H., et al. (2022). Achievements and Prospects of Global Broadband Seismographic Networks After 30 Years of Continuous Geophysical Observations. *Reviews of Geophysics*, *60*(3), e2021RG000749. https://doi.org/10.1029/2021RG000749

Schlegel, R., Diez, A., Löwe, H., Mayer, C., Lambrecht, A., Freitag, J., et al. (2019). Comparison of elastic moduli from seismic diving-wave and ice-core microstructure analysis in Antarctic polar firn. *Annals of Glaciology*, *60*(79), 220–230. https://doi.org/10.1017/aog.2019.10

Shepherd, A., Ivins, E., Rignot, E., Smith, B., van den Broeke, M., Velicogna, I., et al. (2018). Mass balance of the Antarctic Ice Sheet from 1992 to 2017. *Nature*, *558*(7709), 219–222. https://doi.org/10.1038/s41586-018-0179-y

Shi, C., Ren, H., Li, Z., & Chen, X. (2022). Calculation of normal and leaky modes for horizontal stratified models based on a semi-analytical spectral element method. *Geophysical Journal International*, *230*(3), 1928–1947. https://doi.org/10.1093/gji/ggac163

Sihvola, A., & Tiuri, M. (1986). Snow Fork for Field Determination of the Density and Wetness Profiles of a Snow Pack. *IEEE Transactions on Geoscience and Remote Sensing*, *GE-24*(5), 717–721. https://doi.org/10.1109/TGRS.1986.289619

Smith, B. E., Medley, B., Fettweis, X., Sutterley, T., Alexander, P., Porter, D., & Tedesco, M. (2023). Evaluating Greenland surface-mass-balance and firn-densification data using ICESat-2 altimetry. *The Cryosphere*, *17*(2), 789–808. https://doi.org/10.5194/tc-17-789-2023

Trusel, L. D., Frey, K. E., & Das, S. B. (2012). Antarctic surface melting dynamics: Enhanced perspectives from radar scatterometer data. *Journal of Geophysical Research: Earth Surface*, *117*(F2). https://doi.org/10.1029/2011JF002126

Veldhuijsen, S. B. M., van de Berg, W. J., Brils, M., Kuipers Munneke, P., & van den Broeke, M. R. (2023). Characteristics of the 1979–2020 Antarctic firn layer simulated with IMAU-FDM v1.2A. *The Cryosphere*, *17*(4), 1675–1696. https://doi.org/10.5194/tc-17-1675-2023

Walter, F., Gräff, D., Lindner, F., Paitz, P., Köpfli, M., Chmiel, M., & Fichtner, A. (2020). Distributed acoustic sensing of microseismic sources and wave propagation in glaciated terrain. *Nature Communications*, *11*(1). https://doi.org/10.1038/s41467-020-15824-6

Watanabe, O., Jouzel, J., Johnsen, S., Parrenin, F., Shoji, H., & Yoshida, N. (2003). Homogeneous climate variability across East Antarctica over the past three glacial cycles. *Nature*, *422*(6931), 509–512. https://doi.org/10.1038/nature01525

Weihaupt, J. G. (1963). Seismic and gravity studies at the South Pole. *Geophysics*, *28*(4), 582–592. https://doi.org/10.1190/1.1439232

van Wessem, J. M., van de Berg, W. J., Noël, B. P. Y., van Meijgaard, E., Amory, C., Birnbaum, G., et al. (2018). Modelling the climate and surface mass balance of polar ice sheets using RACMO2 – Part 2: Antarctica (1979–2016). *The Cryosphere*, *12*(4), 1479–1498. https://doi.org/10.5194/tc-12-1479-2018

Winski, D. A., Fudge, T. J., Ferris, D. G., Osterberg, E. C., Fegyveresi, J. M., Cole-Dai, J., et al. (2019). The SP19 chronology for the South Pole Ice Core – Part 1: volcanic matching and annual layer counting. *Climate of the Past*, *15*(5), 1793–1808. https://doi.org/10.5194/cp-15-1793-2019

Winther, J.-G., Jespersen, M. N., & Liston, G. E. (2001). Blue-ice areas in Antarctica derived from NOAA AVHRR satellite data. *Journal of Glaciology*, *47*(157), 325–334. https://doi.org/10.3189/172756501781832386

Zhan, Z. (2020). Distributed Acoustic Sensing Turns Fiber-Optic Cables into Sensitive Seismic Antennas. *Seismological Research Letters*, *91*(1), 1–15. https://doi.org/10.1785/0220190112

Zhang, Z., Nakata, N., Karplus, M., Kaip, G., & Yi, J. (2022). Shallow Ice-Sheet Composite Structure Revealed by Seismic Imaging Near the West Antarctic Ice Sheet (WAIS) Divide Camp. *Journal of Geophysical Research: Earth Surface*, *127*(12), e2022JF006777. https://doi.org/10.1029/2022JF006777

Zhou, W., Butcher, A., Brisbourne, A. M., Kufner, S.-K., Kendall, J.-M., & Stork, A. L. (2022). Seismic Noise Interferometry and Distributed Acoustic Sensing (DAS): Inverting for the Firn Layer S-Velocity Structure on Rutford Ice Stream, Antarctica. *Journal of Geophysical Research: Earth Surface*, *127*(12), e2022JF006917. https://doi.org/10.1029/2022JF006917

Chapter 7

MAPPING LOS ANGELES BASIN DEPTH WITH S-TO-P CONVERTED PHASES

Abstract

We use two dense arrays: the Community Seismic Network, a dense network of low-cost accelerometers in schools across LA region, and a 2022 basin-wide node survey, consisting of 290 geophones deployed for a month, to map the Los Angeles (LA) basin depth. The maximum depth of is estimated to be 9 km, based on S-waves generated by earthquakes below the basin that covert to P-waves at the sediment/bedrock interface. This estimate depends on the velocities within and below the basin, and the depth presented here uses the SCEC CVMS4.26 model. This depth is the primary factor controlling the resonance properties of the LA Basin, which is important for seismic hazard assessment, and allows for the estimation of the basin stretching factor.

7.1 Introduction

The Los Angeles (LA) basin was formed by the capture and subsequent rotation of the Transverse Ranges by the Pacific plate 20 Ma. This created an accommodation space that became the LA basin and several other smaller basins. The basin has been modified by cycles of extension and compression events (Ingersoll & Rumelhart, 1999; Wright, 1991; Yerkes, 1965) and has been influenced by the presence of a complicate faulting including the Newport-Inglewood fault (Hough & Graves, 2020; Shaw & Suppe, 1996). Sedimentary basins can trap and amplify earthquake ground shaking (Denolle et al., 2014; Olsen, 2000), and given its location beneath the densely populated metropolitan area of Los Angeles, it is crucial to accurately characterize the structure of the LA basin for seismic hazard assessment. The resonant period of the basin, which is directly related to its depth, is particularly important for the structural health and stability of buildings in the area. Despite its importance, the depth of the LA basin remains poorly constrained. Current estimates of the depth are based on gravity studies with poorly constrained densities (McCulloh, 1960). There is no basin-wide direct estimate of the basin depth.

The depth of the basin is also important for determining stretching factor for the basin, which in turn controls the level of thermal subsidence that has occurred (Ma & Clayton, 2016; McKenzie, 1978; Turcotte & McAdoo, 1979). The basin is close to being in isostatic equilibrium, with the free-air gravity across the basin measured at -10 mgals. Note, the gravitational response of the LA basin without isostatic compensation would be approximately -300 mgals (Turcotte & McAdoo, 1979). As the upwelling of the mantle as part of the Airy isostatic compensation cools there will be thermal subsidence in the basin, which Turcotte and McAdoo estimates to be in the range of about 1/3 of the current basin depth.

The depth of the LA basin has been studied using various geophysical methods, including gravity measurements, seismic tomography, and receiver functions. Gravity measurements have been used to infer the density distribution within the basin, providing insights into its composition and structure. According to McCulloh (1960), the maximum depth of the LA basin is estimated to be 9.1 km. However, this estimate carries considerable uncertainty due to the poorly known density distribution with depth (Wright, 1991). Seismic tomography studies at multiple scales have revealed complex subsurface velocity structure of the LA basin, but these results are often insensitive to sharp discontinuities (Castellanos & Clayton, 2021; Jia & Clayton, 2021; Lee et al., 2014; Lin et al., 2013; Nakata et al., 2015). Seismic receiver function studies have been instrumental in identifying seismic discontinuities, contributing significantly to our understanding of the basin's overall shape and depth (Ma & Clayton, 2016). However, these studies are typically limited to linear arrays that permit the identification of the scattered phases. Similar to the receiver function methods, S-to-p converted phases from local earthquakes have been used to map basin depth (Chopra et al., 2010; Langston, 2003; Mandal, 2007), but their identification is challenging, especially in urban settings with sparse arrays. Consequently, a comprehensive and detailed picture of the basin's depth and structure remains elusive, primarily due to limitations in spatial coverage of seismic arrays.

The Community Seismic Network (CSN) represents significant progress in this context by providing low-cost, dense data coverage for detailed seismic hazard studies of the LA basin (Clayton et al., 2015). The CSN has been used to detect and analyze seismic events in real-time, improve models of ground motion and site amplification, and refine seismic velocity model based on ground motions (Clayton et al., 2019; Kohler et al., 2013; Muir et al., 2022). In June-July 2022, a collaborative effort by the University of Utah, Caltech, and UC Riverside, deployed a ~300-node survey throughout the LA Basin, significantly expanding upon the 40 stations of the permanent Southern California Seismic Network (SCSN). This dense array, known as the Los Angeles Basin 2022 (LAB2022) project, has enabled high-resolution mapping of the LA basin using multiple seismological techniques. In this paper, we aim to leverage the two dense arrays, CSN and LAB2022, along with the SCSN, to map the LA basin's depth using S-to-p converted phases.

7.2 Observation and synthetics of S-to-p converted phases

7.2.1 Dense seismic arrays and local earthquakes

A total of 729 stations were utilized in this study, including 41 broadband stations from SCSN, 289 nodes from LAB2022, and 399 accelerometers from CSN (Figure 7.1a). The CSN network consists of strong-motion accelerometers with an average interstation distance of 0.8 km, located in the Los Angeles area of California (Clayton et al., 2015). The noise floor of these accelerometers is higher than the ambient noise level and consequently cannot be used for ambient noise interferometry. However, they can still record clear waveforms for local earthquakes of magnitude 3.5 or greater. LAB2022 includes two linear arrays with about 48 nodes each and approximately 200 additional stations distributed across the basin, providing dense coverage (Figure 7.1a). This dense coverage is essential for capturing and identifying detailed seismic waveforms that help in mapping subsurface structures with high resolution.

The first event with visible intermediate phase between P and S phases was the M3.5 Compton event in October 2019 (Figure 7.1b). The hypocenter depth of the event from the SCSN catalog is 23.6 km, which is very close to the Moho depth in this region. After reviewing all M3.5+ events recorded by the CSN, we identified four events with clearly visible intermediate phases. During the one-month deployment period of LAB2022, five events with magnitudes around 2 and depths approaching or exceeding 10 km exhibited clear intermediate phases. Detailed event information is provided in Table 7.1.

Table 7.1: Information of the events used in this study

Time	Magnitude	Longitude	Latitude	Depth (m)	Event ID
2024-06-02T16:56:15.760	3.36	-118.178000	34.084330	10400.0	40611087
2022-06-26T16:36:35.590	2.17	-118.534167	33.837167	12890.0	40291816
2022-06-26T09:45:05.100	2.28	-118.348667	33.987667	10960.0	40291656
2022-06-25T12:42:23.120	1.97	-117.977833	33.683833	11860.0	40291224
2022-06-25T10:27:05.840	1.99	-118.543833	33.920000	10740.0	40291160
2022-06-22T03:06:10.310	2.03	-118.063667	33.693667	15900.0	40288808
2021-04-05T11:44:01.950	4.00	-118.333333	33.940500	19340.0	39838928
2021-01-20T16:31:58.950	3.52	-118.271667	33.918667	19760.0	39762912
2019-10-18T07:19:51.180	3.54	-118.218500	33.891333	23630.0	38905415

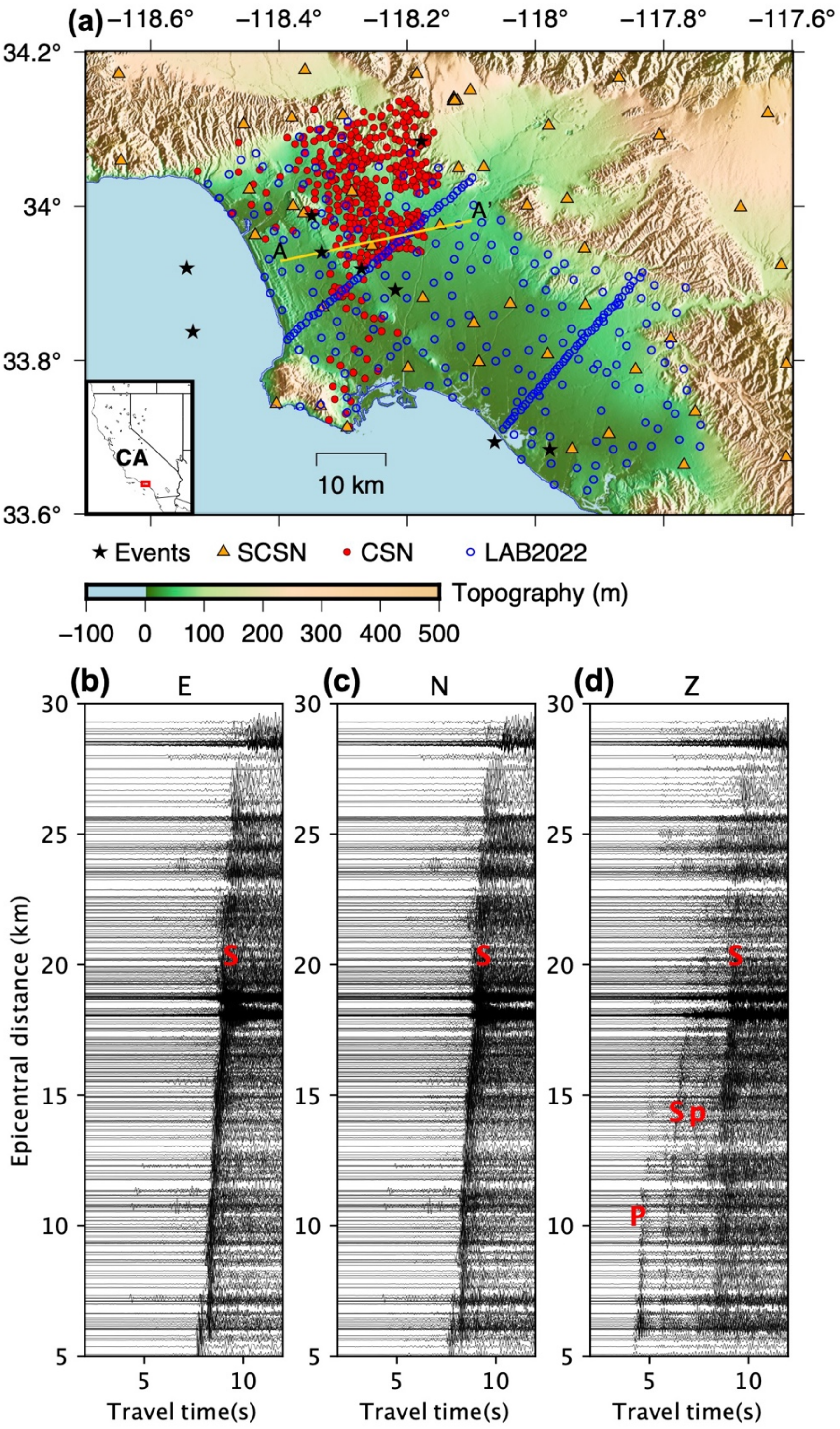

Figure 7.1: (a) Map of station and event epicenters used in this study. The red dots are the CSN array, the blue circles are the LAS2022 node array, and the orange triangles are the

SCSN stations. (b) Example waveform observed in the October 2019 Compton event, showing clear intermediate phase on the vertical component only.

7.2.2 Observation and synthetics of the local earthquakes

Clear arrivals between the P and S phases are visible only on the vertical component (Figure 7.1d). We use PhaseNet to pick the P and S arrival times of these events based on three-component data (Zhu & Beroza, 2019). PhaseNet is a neural network-based picker that improves the accuracy and consistency of phase picking, which is essential for reliable phase identification and subsequent analysis. PhaseNet is trained to only pick the P and S waves, and hence we manually pick the arrival times of the intermediate phases (Figure 7.2c). Since the intermediate phase is only visible in the vertical component, we considered several candidates for this phase ending with the P wave to the surface: basin and surface reflected P wave (PpPp), basin converted P wave (Sp), and Moho reflected P wave (PmP).

Further verification was conducted using 2D full waveform modeling with the community velocity model CVM-SCEC 4.26 (Figure 7.2ab) (Lee et al., 2014; Li et al., 2014; Small et al., 2017). This 3D model incorporates detailed geological and geophysical data specific to the LA basin, making it a best model for simulating seismic wave propagation. A full wavefield movie included in the supplementary material shows that the observed intermediate phase corresponds to an S-to-P wave conversion at the basin interface. Comparing the observed waveforms and phase picks with the synthetic seismograms, we found good alignment of the P and S arrivals. However, the S-to-P observed arrival time is consistently earlier (Figure 7.2c), suggesting that the phase is converted at a deeper interface, indicating that the basin might be deeper than currently modeled by the community velocity model. This discrepancy highlights the need for updating the model with more accurate basin depths.

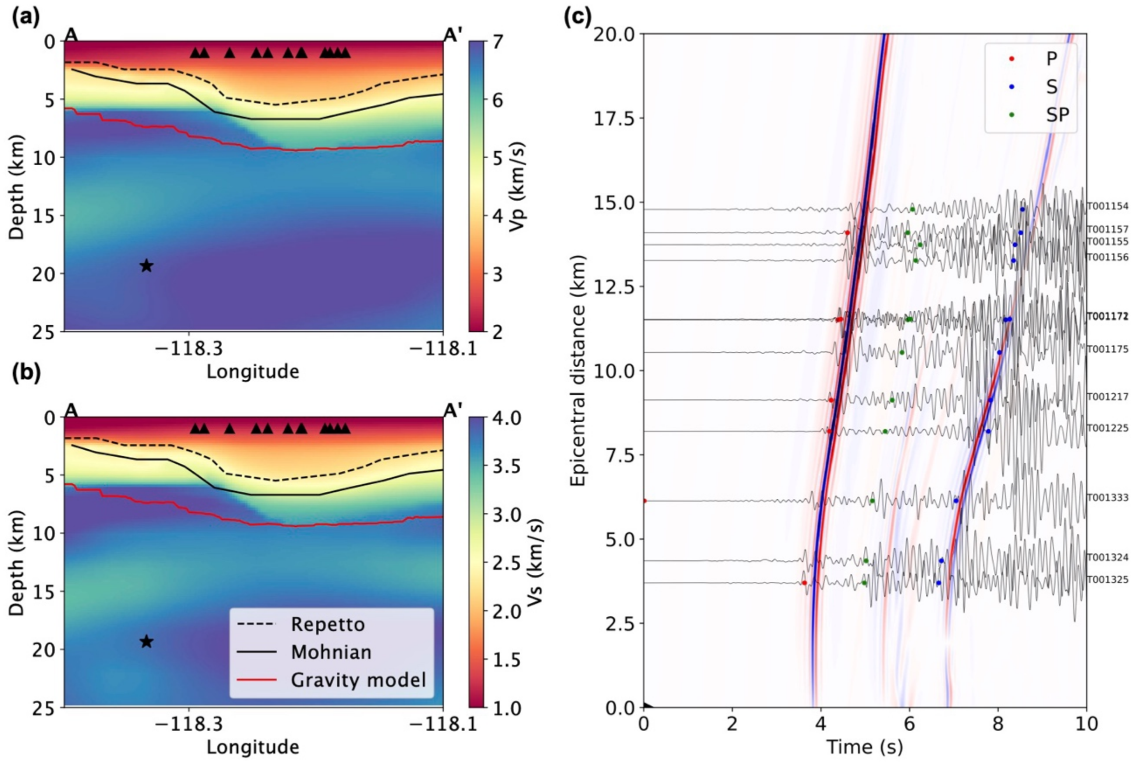

Figure 7.2: Wavefield simulation and observation. (a) The P-velocity model along the profile AA’ (Figure 7.1a) sliced from CVM-SCEC. The event hypocenter and the stations within 1 km from the profile are plotted as a star and triangles, respectively. The two interfaces within the LA basin, Repetto and Mohnian interfaces, are plotted with dashed and solid lines, respectively. (b) Similar to (a), but for the S-velocity model. (c) The background image shows the vertical component wavefield simulation on the surface receivers, with clearly visible P, S-to-P, and S phases. The black waveform shows the observed data. The red and blue dots are P and S arrival picks from PhaseNet. The green dots are manual picks of S-to-P phases.

7.3 Mapping LA basin depth

With phase picks of P, S, and S-to-p converted arrivals, we can use the differential travel times of these phases to map the LA basin depth. We apply three methodologies, ranging from simple to complex, to estimate the basin depth.

7.3.1 Conventional mapping method

The first approach is the conventional method for mapping basin depth using converted phases, which assumes a vertically incident S-to-p phase (Bao et al., 2021; Chopra et al., 2010; Mandal, 2007; Stone et al., 2021):

$$H = \frac{T_{Ss-Sp}}{\frac{1}{V_S} - \frac{1}{V_P}}, \tag{7.1}$$

where V_P, V_S represent the velocities of P and S waves respectively, T_{Ss-Sp} is the differential travel time between the S-to-p converted wave and the S wave, and H represents the basin depth (Figure 7.3a). With a known reference model of V_P and V_S, we can estimate the basin depth using the measured differential travel times. This simplified approach, which is commonly used in receiver functions, is generally effective for mapping relatively shallow basins with depths of 1 to 2 km and with earthquakes far away, where the assumption of a vertically incident S-to-p wave holds. This method has been validated in several studies (Bao et al., 2021; Chopra et al., 2010; Mandal, 2007; Stone et al., 2021), demonstrating its effectiveness in various geological settings.

7.3.2 Modified conventional method for deeper events

In the LA Basin, where the epicentral distances are comparable with the event depth, we modify the vertically incident assumption. With the community velocity model (CVMS), the depth-averaged V_P in the basin is only slightly larger than the V_S in the lower crust, suggesting that the ray path is generally straight from the hypocenter to the station (Figure 7.3b). The basin depth at the conversion point can be calculated as:

$$H = \frac{T_{Ss-Sp}}{\frac{1}{V_S} - \frac{1}{V_P}} \cdot \frac{h}{\sqrt{h^2 + d^2}}, \tag{7.2}$$

where h is the hypocenter depth, and d is the epicentral distance. This adjustment makes the conversion point moving towards the epicenter (Figure 7.3b).

7.3.3 Detailed ray-tracing analysis

The next level of complexity is to use ray-tracing to more precisely calculate the exact ray paths of S-to-p and S waves. This method allows us to model the travel paths of seismic waves through a heterogeneous medium, taking into account variations in seismic velocities. We use the PyKonal package, which leverages a fast marching algorithm to efficiently solve the Eikonal equation (White et al., 2020). For each event-station pair, we calculate the S wave travel time from the event location (Figure 7.3c) and the P wave travel time from the station location (Figure 7.3d). By overlaying these travel time plots, we can identify the S-to-p travel times converted at various points within the event-station plane (Figure 7.3e). Note that we performed 2D ray-tracing in the event-station plane rather than 3D ray-tracing. This approach significantly reduces computational demands and narrows the range of candidate conversion points to search over. This simplification is valid because most of the ray paths lie within the event-station plane, and the difference between 2D ray-tracing and 3D ray-tracing is minimal (Figure 7.S1). To pinpoint the actual conversion points, we apply Snell's law, ensuring that the horizontal slowness is conserved along the ray path. By calculating the horizontal slowness at each grid point along the ray path, we can accurately identify the most plausible conversion points (Figure 7.3f).

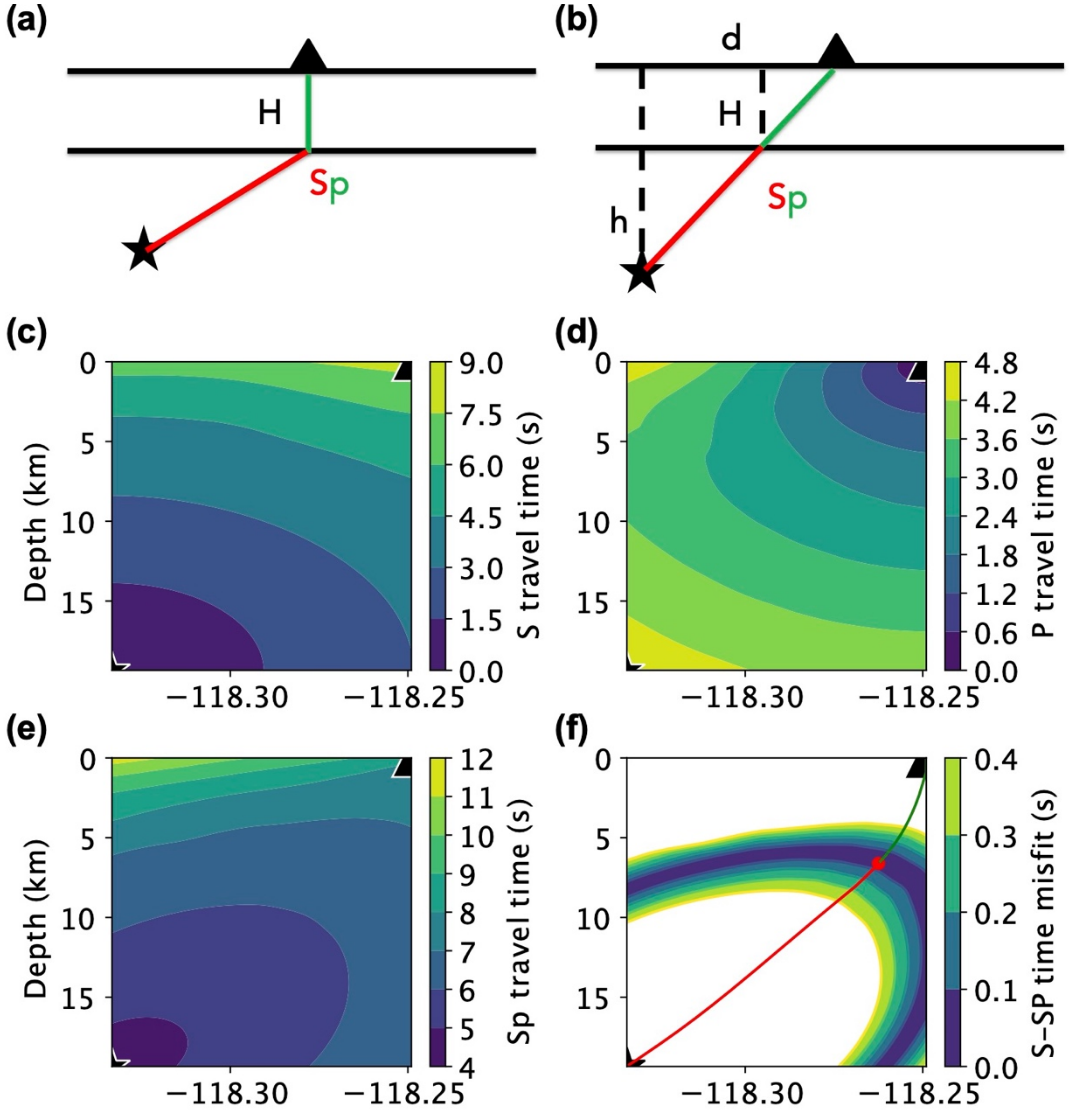

Figure 7.3: Illustration of three different mapping schemes. (a) Mapping basin depth assuming the S-to-p path is vertically incident in the basin. (b) Mapping basin depth assuming the S-to-p path follows a straight trajectory from source to receiver. (c) S-wave travel times from the source computed using ray tracing. (d) P-wave travel times from the receiver computed using ray tracing. (e) S-to-p converted arrival times from source to receiver, derived by adding the travel times from (c) and (d). (f) The area where travel times differ by more than 0.4 s from the observed S-to-p travel time is masked. The final ray path is determined by conserving horizontal slowness.

7.4 Results

We mapped the LA basin depth using all three methods described above. For the first two methods, we need to use the average V_P and V_S in the basin. We use the model from Muir et al. (2022), in which the basin depth and the velocity model are both defined. The time averaged V_P and V_S in the basin are 3.602 km/s and 1.880 km/s, respectively. The basin depth mapped using the vertically incident S-to-p phase method (Figure 7.4a) fails to produce a clearly visible basin depth pattern, with the mapped depth consistently exceeding 8 km, especially in the Orange County Coastal Plain, which is unreasonable. The uncertainty, computed as the standard deviation of all measurements within each grid, is presented in Figure 7.4b. This method shows high uncertainty across the entire basin, with an average standard deviation of 3.14 km.

The basin depth mapped using the straight trajectory method is shown in Figure 7.4c. This approach provides a more reasonable and detailed basin pattern, improving both depth estimation and spatial resolution compared to the conventional method. The uncertainty for this method is shown in Figure 7.4d, with an average standard deviation of only 0.59 km. This reduced uncertainty makes the modified straight trajectory method a simpler yet more reliable option for mapping LA basin depth.

The basin depth using the detailed ray-tracing method is presented in Figure 7.4e. This method shows a basin pattern generally consistent with the one in Figure 7.4c, but the use of a detailed velocity model allows for refined mapping for each individual event-station pair, resulting in a slightly deeper depth. The uncertainty for the detailed ray-tracing method is shown in Figure 7.4f, with an average standard deviation of 0.56 km, making it a slightly more robust result. Here, we averaged the velocity model in the event-station plane to reduce the effect of local heterogeneities in the 3D velocity model, which is not perfect. Using the 3D velocity model directly increases the average uncertainty to 0.72 km (Figure 7.S2).

The second and third methods produce more reasonable basin patterns and lower uncertainties than the conventional method. The deepest part of the LA basin in the Central

Basin has an average depth of 9.2 km, with a sharp increase in depth observed across the Newport-Inglewood fault.

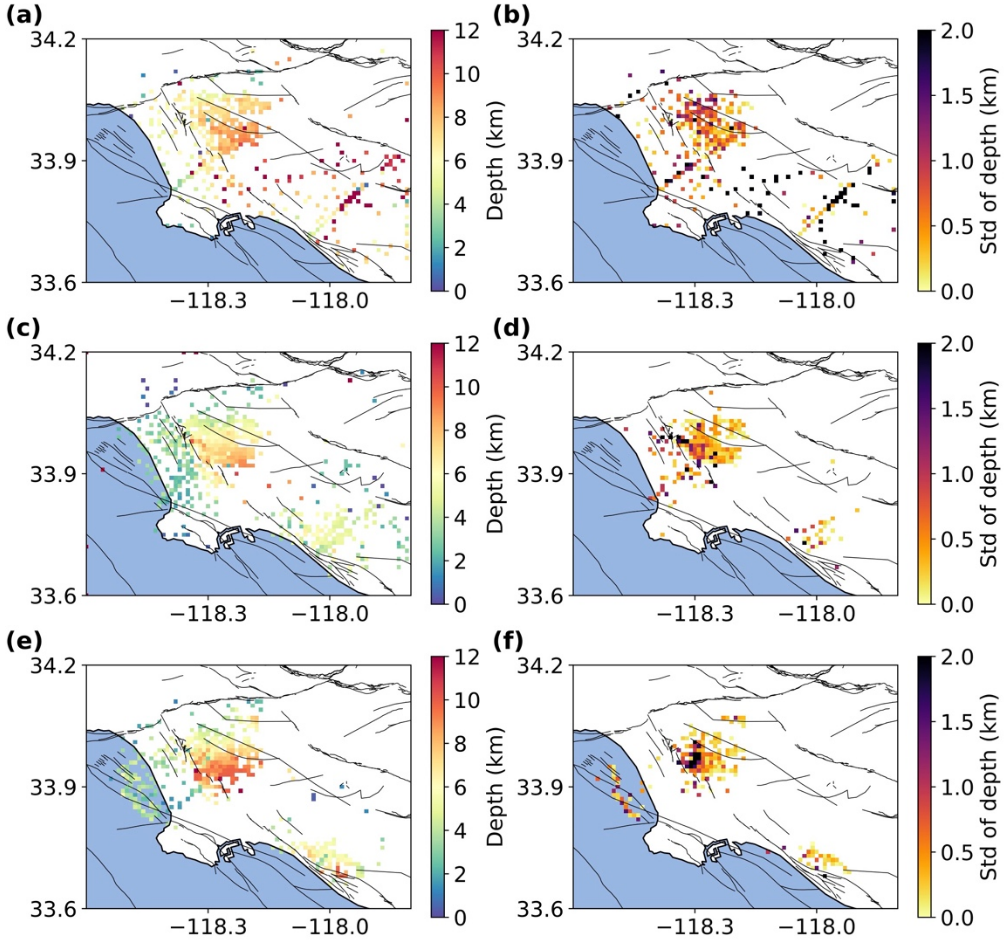

Figure 7.4: LA basin mapping results. The results are mapped onto a mesh and averaged across all available station-event pairs. (a) Mapped depth using the method illustrated in Figure 7.3a. (b) The uncertainty, computed as the standard deviation of all measurements within each grid (if more than one measurement is available). (c) Mapped depth using the method illustrated in Figure 7.3b. (d) Uncertainty corresponding to (c), computed as the standard deviation of all measurements within each grid. (e) Mapped depth using the detailed ray-tracing method illustrated in Figures 7.3c-f. (f) Uncertainty corresponding to (e), computed as the standard deviation of all measurements within each grid.

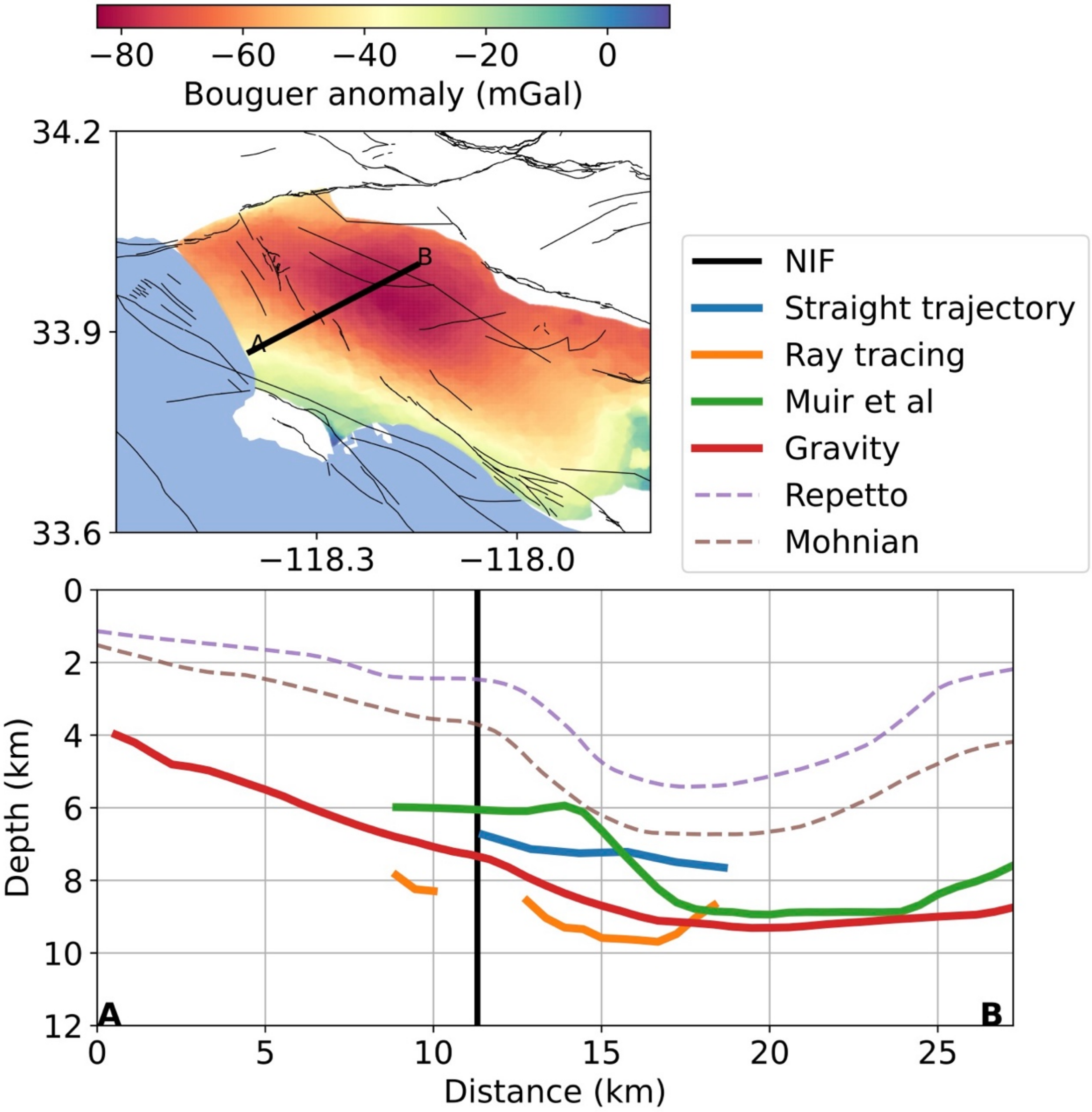

Figure 7.5: Comparison among cross-sections of different basin depth models. The upper panel shows the Bouguer gravity anomaly in the LA basin and the location of cross-section AB across the NIF. In the lower panel, the Repetto and Mohnian interfaces are plotted with dashed lines. The intersection of the NIF with the cross-section is indicated by the vertical black line. The red line represents the gravity-derived basin depth. The green line shows the basin depth from Muir et al. (2022). The basin depth mapped using the straight trajectory and ray tracing methods are shown by the blue and orange lines, respectively.

7.5 Discussion and conclusion

7.5.1 Interpretation of results

Having an accurate estimate of the depth and shape is important for two reasons. The first is that the resonance properties for earthquake strong motions primary depends on the local depth of the basin. As shown in Filippitzis et al. (2021), the amplification of the basin at longer periods is about a factor of 5 larger than the adjacent bedrock (at 5-sec period for example). It is therefore important for the design of tall buildings in Los Angeles that this amplification factor be known.

The basin depths are also important for investigating the tectonics of the area. The free-air gravity over the LA Basin is approximately -10 mgals, which when compared to a -300 mgal that is due to the basin itself, indicates that the basin very close to isostatically compensated. Assuming an Airy mechanism, this means that the Moho in this area is upwarped by an amount approximately equal to the basin depth. The was directly observed by Ma & Clayton (2016) on a line across the southern LA Basin. Assuming an average Moho depth in the Los Angeles region, it means that the crust beneath LA is thinned to as little as 6 km. This thinning is created by (at least) two factors: the first is the stretching due to the opening of the accommodation space in the wake of the rotation of the Transverse Ranges, and the second if the thermal subsidence that occurs when the upwelling mantle that provides the isostatic compensation cools. Ma & Clayton (2016) directly observe and estimate the basin depth and the Moho depth, and hence they can estimate the stretching factor of the to be approximately 2. This means that the thermal contraction component of the basin depth is about 3 km.

The results on the depth of the basin presented here depend on the depth averaged velocities. These depths will change if the underlying model is changed. The second method (straight ray method) provides a simple mechanism to convert the depth to the new velocity function, and to compare various depth estimates.

7.5.2 Methodological insights

We design new methods tailored for mapping LA basin depth with S-to-p phases of local earthquakes recorded by dense arrays. The modified straight trajectory method is a viable alternative for quickly estimating basin depth. However, the detailed ray-tracing method provides the highest accuracy and lowest uncertainty, making it the preferred approach. The primary source of uncertainty is the velocity model used in ray tracing. Updating the velocity model will improve the accuracy of basin depth mapping.

Thanks to the dense coverage provided by the permanently monitoring CSN, we will continue to receive additional data for mapping, improving the resolution and coverage of the LA basin depth mapping. With more data, it will be important to develop automatic algorithms for S-to-p phase picking. Our current manual picks can serve as labels for training these algorithms.

7.5.3 Conclusions

The depth of the LA basin has been accurately mapped using two dense seismic arrays: the CSN and the LAB2022. These arrays provided robust data, allowing us to utilize differential travel times between direct S waves and S-to-p converted phases from local earthquakes. Our mapping offers independent constraints that enhance previous seismic tomography and gravity surveys. The results indicate that a substantial part of the central LA Basin has a depth of over 9 km. This improved depth mapping enhances our understanding of the basin's geological structure and contributes to better seismic hazard assessments.

Supplementary Material

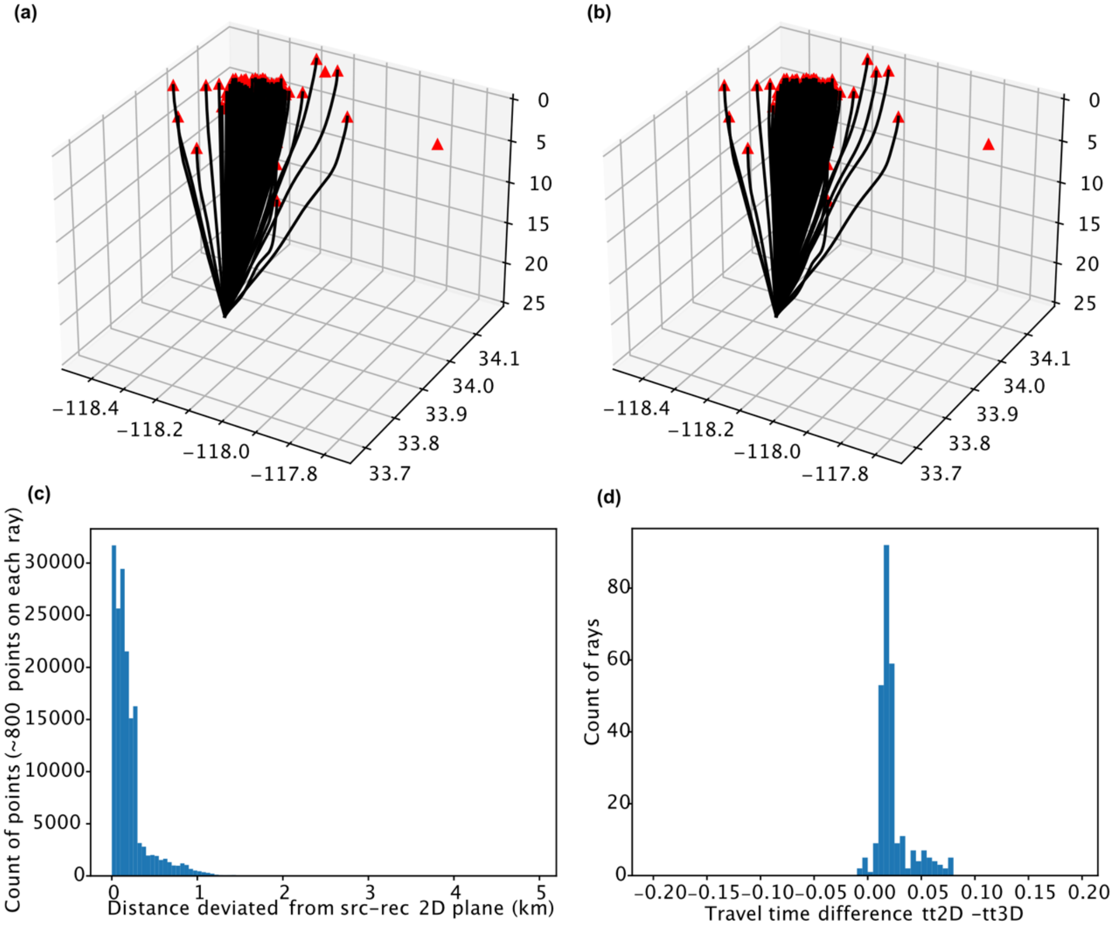

Figure 7.S1: Difference between 3D and 2D ray-tracing in the event-station plane using the October 2019 Compton event as an example. (a) S wave ray path using 2D ray-tracing in the event-station plane. (b) S wave ray path using 3D ray-tracing. (c) Difference in the total distance of the ray paths in (a) and (b). Most distances are consistent with differences close to 0 km. (d) Difference in travel times between (a) and (b). Although 2D ray-tracing gives slightly longer arrival times, the overall differences are minimal.

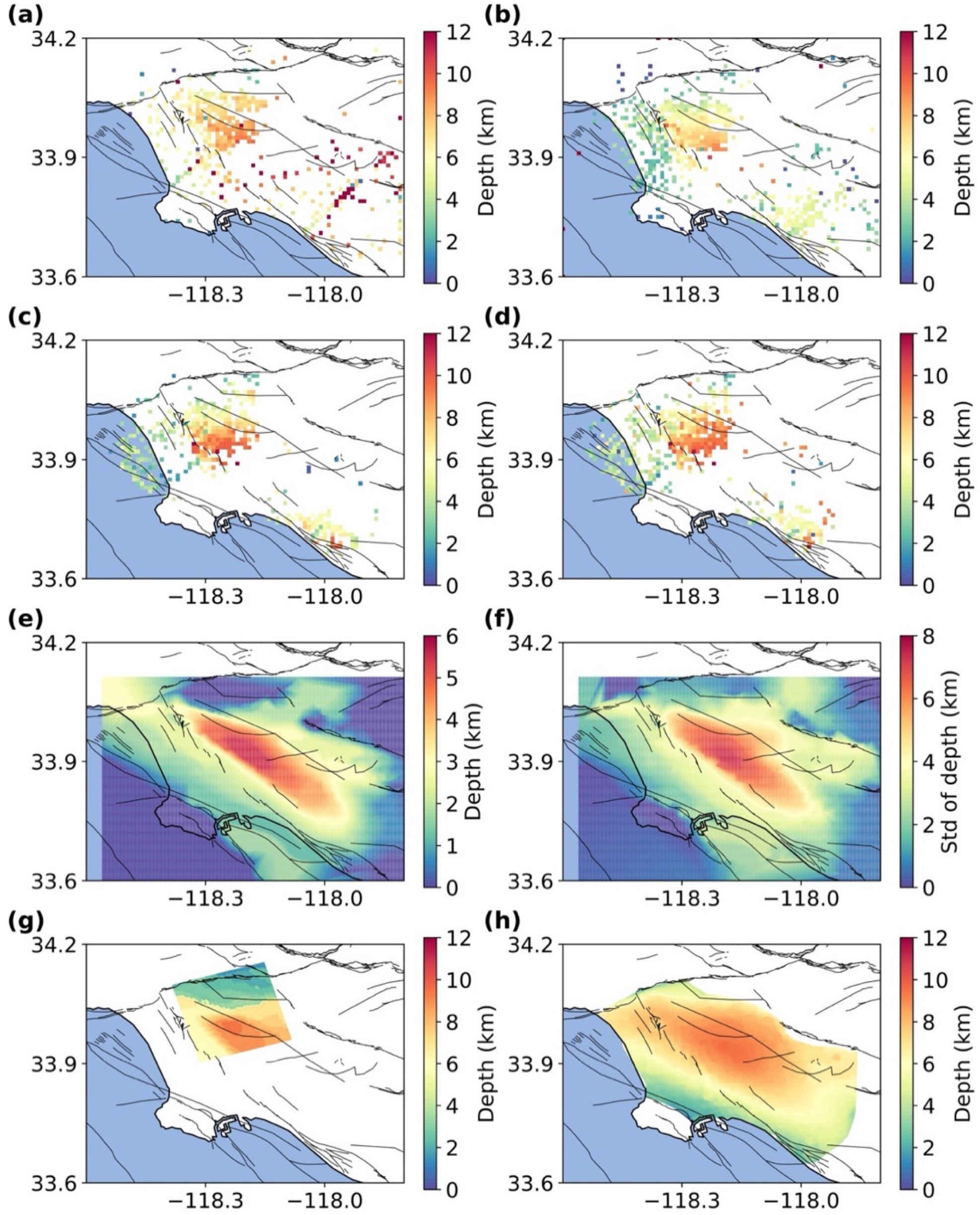

Figure 7.S2: Comparison among different basin depth models. (a) Mapped depth using the method illustrated in Figure 7.3a. (b) Mapped depth using the method illustrated in Figure 7.3b. (c) Mapped depth using the detailed ray-tracing method illustrated in Figures 7.3c-f, with the 2D velocity model averaged to a 1D velocity model in each event-station plane. (d) Mapped depth using the detailed ray-tracing method illustrated in Figures 7.3c-f, with the original 2D velocity model. (e) Depth of the Repetto interface from Wright (1991). (f) Depth of the Mohnian interface from Wright (1991). (g) Basin depth from Muir et al.

(2022). (h) Basin depth model from gravity studies converted with a constant density profile.

References

Bao, F., Li, Z., Shi, Y., Tian, B., Chong, J., & Rong, W. (2021). Sediment Structures Constrained by Converted Waves From Local Earthquakes Recorded by a Dense Seismic Array in the Tangshan Earthquake Region. *Pure and Applied Geophysics*, *178*(2), 379–397. https://doi.org/10.1007/s00024-021-02667-5

Castellanos, J. C., & Clayton, R. W. (2021). The Fine-Scale Structure of Long Beach, California, and Its Impact on Ground Motion Acceleration. *Journal of Geophysical Research: Solid Earth*, *126*(12). https://doi.org/10.1029/2021jb022462

Chopra, S., Rao, K. M., & Rastogi, B. K. (2010). Estimation of Sedimentary Thickness in Kachchh Basin, Gujarat Using SP Converted Phase. *Pure and Applied Geophysics*, *167*(10), 1247–1257. https://doi.org/10.1007/s00024-009-0022-3

Clayton, R. W., Heaton, T., Kohler, M., Chandy, M., Guy, R., & Bunn, J. (2015). Community Seismic Network: A Dense Array to Sense Earthquake Strong Motion. *Seismological Research Letters*, *86*(5), 1354–1363. https://doi.org/10.1785/0220150094

Clayton, R. W., Kohler, M., Guy, R., Bunn, J., Heaton, T., & Chandy, M. (2019). CSN-LAUSD Network: A Dense Accelerometer Network in Los Angeles Schools. *Seismological Research Letters*.

Denolle, M. A., Dunham, E. M., Prieto, G. A., & Beroza, G. C. (2014). Strong ground motion prediction using virtual earthquakes. *Science*. https://doi.org/10.1126/science.1245678

Filippitzis, F., Kohler, M. D., Heaton, T. H., Graves, R. W., Clayton, R. W., Guy, R. G., et al. (2021). Ground motions in urban Los Angeles from the 2019 Ridgecrest earthquake sequence. *Earthquake Spectra*, *37*(4), 2493–2522. https://doi.org/10.1177/87552930211003916

Hough, S. E., & Graves, R. W. (2020). The 1933 Long Beach Earthquake (California, USA): Ground Motions and Rupture Scenario. *Scientific Reports*, *10*(1), 10017. https://doi.org/10.1038/s41598-020-66299-w

Ingersoll, R. V., & Rumelhart, P. E. (1999). Three-stage evolution of the Los Angeles basin, southern California. *Geology*, *27*(7), 593. https://doi.org/10.1130/0091-7613(1999)027<0593:TSEOTL>2.3.CO;2

Jia, Z., & Clayton, R. W. (2021). Determination of Near Surface Shear-Wave Velocities in the Central Los Angeles Basin With Dense Arrays. *Journal of Geophysical Research: Solid Earth*, *126*(5), e2020JB021369. https://doi.org/10.1029/2020JB021369

Kohler, M. D., Heaton, T. H., & Cheng, M.-H. (2013). The Community Seismic Network and Quake-Catcher Network: Enabling structural health monitoring through instrumentation by community participants. In *Sensors and Smart Structures Technologies for Civil, Mechanical, and Aerospace Systems 2013* (Vol. 8692, pp. 1049–1056). SPIE.

Langston, C. A. (2003). Local Earthquake Wave Propagation through Mississippi Embayment Sediments, Part I: Body-Wave Phases and Local Site Responses. *Bulletin of the Seismological Society of America*, *93*(6), 2664–2684. https://doi.org/10.1785/0120030046

Lee, E. J., Chen, P., Jordan, T. H., Maechling, P. B., Denolle, M. A. M., & Beroza, G. C. (2014). Full-3-D tomography for crustal structure in Southern California based on the scattering-integral and the adjoint-wavefield methods. *Journal of Geophysical Research: Solid Earth*, *119*(8), 6421–6451. https://doi.org/10.1002/2014JB011346

Li, D., Helmberger, D., Clayton, R. W., & Sun, D. (2014). Global synthetic seismograms using a 2-D finite-difference method. *Geophysical Journal International*, *197*(2), 1166–1183. https://doi.org/10.1093/gji/ggu050

Lin, F. C., Li, D., Clayton, R. W., & Hollis, D. (2013). High-resolution 3D shallow crustal structure in Long Beach, California: Application of ambient noise tomography on a dense seismic array. *Geophysics*, *78*(4). https://doi.org/10.1190/geo2012-0453.1

Ma, Y., & Clayton, R. W. (2016). Structure of the Los Angeles Basin from ambient noise and receiver functions. *Geophysical Journal International*. https://doi.org/10.1093/gji/ggw236

Mandal, P. (2007). Sediment Thicknesses and Qs vs. Qp Relations in the Kachchh Rift Basin, Gujarat, India Using Sp Converted Phases. *Pure and Applied Geophysics*, *164*(1), 135–160. https://doi.org/10.1007/s00024-006-0158-3

McCulloh, T. H. (1960). Gravity variations and the geology of the Los Angeles basin of California. *US Geol. Surv. Profess. Pap. 400-B*, 320–325.

McKenzie, D. (1978). Some remarks on the development of sedimentary basins. *Earth and Planetary Science Letters*, *40*(1), 25–32. https://doi.org/10.1016/0012-821X(78)90071-7

Muir, J. B., Clayton, R. W., Tsai, V. C., & Brissaud, Q. (2022). Parsimonious Velocity Inversion Applied to the Los Angeles Basin, CA. *Journal of Geophysical Research: Solid Earth*, *127*(2). https://doi.org/10.1029/2021JB023103

Nakata, N., Chang, J. P., Lawrence, J. F., & Boué, P. (2015). Body wave extraction and tomography at Long Beach, California, with ambient-noise interferometry. *Journal of Geophysical Research: Solid Earth*, *120*(2), 1159–1173. https://doi.org/10.1002/2015JB011870

Olsen, K. B. (2000). Site Amplification in the Los Angeles Basin from Three-Dimensional Modeling of Ground Motion. *Bulletin of the Seismological Society of America*, *90*(6B), S77–S94. https://doi.org/10.1785/0120000506

Shaw, J. H., & Suppe, J. (1996). Earthquake hazards of active blind-thrust faults under the central Los Angeles basin, California. *Journal of Geophysical Research: Solid Earth*, *101*(B4), 8623–8642. https://doi.org/10.1029/95JB03453

Small, P., Gill, D., Maechling, P. J., Taborda, R., Callaghan, S., Jordan, T. H., et al. (2017). The SCEC unified community velocity model software framework. *Seismological Research Letters*, *88*(6), 1539–1552. https://doi.org/10.1785/0220170082

Stone, I., Wirth, E. A., & Frankel, A. D. (2021). Structure and QP–QS Relations in the Seattle and Tualatin Basins from Converted Seismic Phases. *Bulletin of the Seismological Society of America*, *111*(3), 1221–1233. https://doi.org/10.1785/0120200390

Turcotte, D. L., & McAdoo, D. C. (1979). Thermal subsidence and petroleum generation in the southwestern block of the Los Angeles Basin, California. *Journal of Geophysical Research: Solid Earth*, *84*(B7), 3460–3464. https://doi.org/10.1029/JB084iB07p03460

White, M. C. A., Fang, H., Nakata, N., & Ben-Zion, Y. (2020). PyKonal: A Python Package for Solving the Eikonal Equation in Spherical and Cartesian Coordinates Using the Fast Marching Method. *Seismological Research Letters*, *91*(4), 2378–2389. https://doi.org/10.1785/0220190318

Wright, T. L. (1991). Structural geology and tectonic evolution of the Los Angeles Basin, California. *Active Margin Basins*, 35–134.

Yerkes, R. F. (1965). *Geology of the Los Angeles basin, California: an introduction*. US Government Printing Office.

Zhu, W., & Beroza, G. C. (2019). PhaseNet: A deep-neural-network-based seismic arrival-time picking method. *Geophysical Journal International*, *216*(1), 261–273. https://doi.org/10.1093/gji/ggy423

Chapter 8

SHALLOW SEISMICITY IN THE LONG BEACH - SEAL BEACH, CA AREA

Yang, Y., & Clayton, R. W. (2023). Shallow Seismicity in the Long Beach–Seal Beach, California Area. *Seismological Research Letters*. https://doi.org/10.1785/0220220358

Abstract

Seismicity can help to locate fault zones that are often difficult to characterize in densely populated urban areas. In this study we use three dense nodal arrays consisting of thousands of sensors to detect and locate seismic events in the Long Beach - Seal Beach area of California. Small events can be detected at sufficient signal-to-noise levels during the night, when urban noise is relatively low. We detect and locate more than a thousand events with magnitudes below 2. Most of the located events are clustered at very shallow depth, 0-2 km. The results support previous suggestions that the shallow Newport-Inglewood fault is a wide splayed fault in this area. The seismicity pattern also compares well with some newly identified faults from reflection seismic surveys. The shallow events, which elude detection by the regional seismic network, underscore the complex nature of the faults and their seismic hazard.

8.1 Introduction

According to modern assessment (e.g., Field *et al.*, 2015), seismic hazard in the Los Angeles and the Long Beach area, California, is largely controlled by the Newport-Inglewood fault (NIF; Taber, 1920). Several studies have concluded that the damaging 1933 Long Beach earthquake (Wood et al., 1933) occurred on the NIF, rupturing from southeast to northwest (E. Hauksson & Gross, 1991; Hough & Graves, 2020), with the significant damage concentrated in the Long Beach and south Los Angeles areas (Wood *et al.*, 1933; Hough and Graves, 2020). The NIF is predominantly a strike-slip fault with an estimated 60-km cumulative offset, but it does not have significant seismicity associated with it (Egill Hauksson, 1987). There are a large number of major oil fields along the NIF

(Eaton, 1933), and cross-sections derived as part of hydrocarbon exploration show that the NIF starts to splay at depths shallower 5 km (Gish & Boljen, 2021). Detailed characterization of hazard in this densely populated urban area has been hindered by the paucity of modern seismicity and the complexity of shallow fault structures.

The current Southern California Seismic Network (SCSN) catalog has located a total of 546 events from 1932 to 2008 with a nominal magnitude of completeness of $M > 1.8$ (Hutton et al., 2010) and a total of 199 events from 2008 to 2018 using template matching methods with a nominal magnitude of completeness of $M > 0.3$ (Ross *et al.*, 2019, Figure 8.1). This zone is also unusual for southern California in that it has a number of deep events (below 15 km). There are 49 such events in the SCSN catalog in the past 20 years. Some of these events are actually below the Moho, according to studies by Inbal *et al.* (2015, 2016) using part of the same arrays' data used in this study. Detecting and locating these deep events required preprocessing to reduce the surface noise, which consisted of downward continuation of the recorded wavefield to a depth of 5 km (Inbal et al., 2016). This brings the deep events closer to the array and reduces the surface noise (primarily surface waves) considerably. This was confirmed by Yang *et al.* (2021), who showed that the deep events are not evident with standard processing. The downward continuation step precludes detection of earthquakes shallower than 5 km depth. In this study we develop methodology to detect and locate shallow events.

The paucity of cataloged seismicity may be due to the sparse SCSN network (interstation spacing of 10 km or ~0.01 stations/km^2) in the Long Beach area. In this study we use three temporary, dense-array surveys deployed in the area for oil exploration (Figure 8.1). These arrays comprise short-period vertical sensors that have a spatial density of ~100 sensors/km^2, which facilitates the detection of small local earthquakes. The study area is, however, a very noisy urban region, and this makes it a challenge to detect weak seismicity. In this paper, we exploit the density of the array to detect the coherent signals of the shallow seismicity. Modern methods such as template matching (Ross et al., 2019; Shelly et al., 2007) and machine learning approaches (Mousavi et al., 2020; Ross et al., 2018; Zhu &

Beroza, 2019) cannot be used directly because of the lack of templates or a training set for the nodal arrays and the seismicity in this area. Therefore, we use a standard STA/LTA method and a spatial clustering filter to exploit station density. One of the challenges of this study is that shallow detection is often associated with anthropological activities, and for this reason we focus on the nighttime events when the urban area is considerably quieter seismically, as shown in Figure 8.2.

Table 8.1: The general information about the three arrays.

ID	Dates	# of nodes	Name
LB3D	2011/01/05 - 2011/06/15	5441	Long Beach
ELB	2012/01/10 - 2012/04/13	2484	East Long Beach
SB3D	2018/01/22 - 2018/02/15 (Span of complete array)	5228	Seal Beach

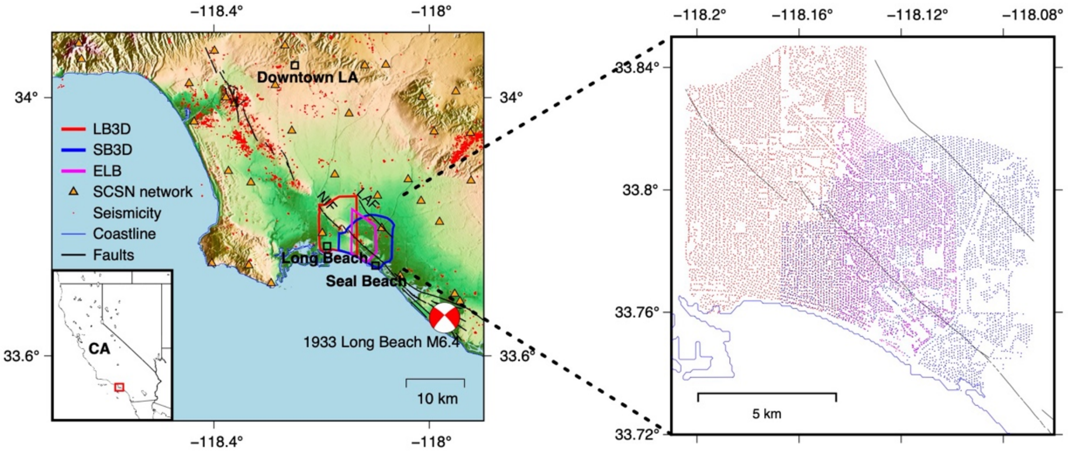

Figure 8.1: Map of the study area. The red dots show seismicity from the template matching-based catalog (Ross et al., 2019), the beachball is the focal mechanism for the 1933 M6.4 Long Beach earthquake (Hauksson & Gross, 1991), and the black lines are the known faults from USGS Quaternary Fault and Fold Database. The orange triangles represent the SCSN stations. The red, blue, and magenta lines outline the Long Beach (LB3D), the Seal Beach (SB3D), and the extended Long Beach (ELB) arrays, respectively.

The zoomed-in view of the three nodal arrays is shown on the right, with dots showing the location of the sensors.

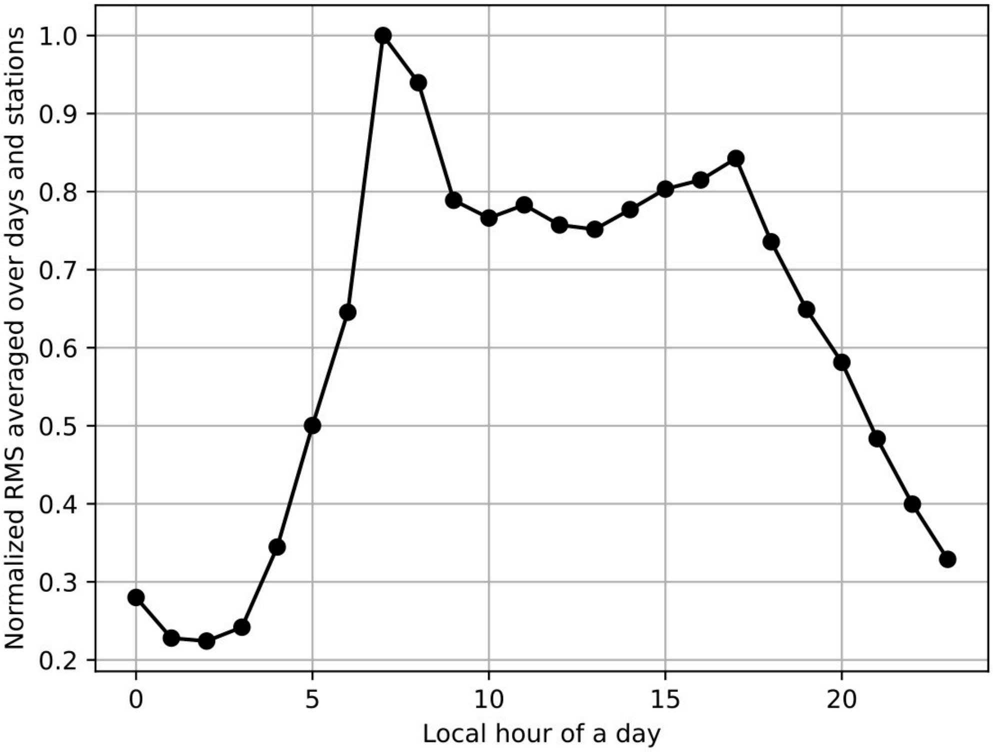

Figure 8.2: The noise amplitude variation with local hours. The curve is averaged over all the nodes in the SB3D array and for all the dates, which clearly reveals day-night anthropogenic noise variation and rush hours.

8.2 Data and methods

Data used in this study come from three separate surveys that occurred at different times and were deployed for different lengths of time. The survey information is shown in Table 1. The arrays have an average sensor spacing of approximately 100 m. The instruments are Fairfield Z-land nodes each consisting of a vertical short-period velocity sensor with a lower-frequency corner of 10 Hz. Previous studies with these data have shown that these instruments have sensitivity to frequencies as low as approximately 0.1 Hz (Castellanos et al., 2020; Lin et al., 2013). The data were recorded continuously at 500 Hz sampling rates and were then down-sampled to 250 Hz.

The Long Beach-Seal Beach study area has a high level of cultural noise that varies significantly over the span of a day. Figure 8.2 shows the hourly root-mean-square (RMS) energy averaged over the stations of the Seal Beach array and the duration of the survey. There is a factor of approximately two difference in noise levels between daytime and nighttime hours. Because the focus of our study is on elucidation of shallow fault structures rather than catalog completeness, we restrict our analysis to nighttime hours (9 pm to 5 am Pacific time) to maximize the signal-to-noise ratio. We excluded Sunday nights from the analysis with the Long Beach array because the seismic-survey contractor used that time period to run the vibrator sources at full power near the Long Beach Airport. The bandpass filter of 2-8 Hz is designed to remove the vibrator sweep frequencies, which is 8-80 Hz. In normal operations, the vibrators are only operated during the daytime at highly reduced power (Snover et al., 2020). Some machine-learning denoisers are proposed recently to remove the urban noise (Yang et al., 2022), but these methods are based on trace-by-trace method and may degrade the spatial correlated pattern of the earthquakes recorded in a dense nodal array (Figure 8.S1).

In this study, the P waves are picked with a short-time-average over long-time-average (STA/LTA)-based picker (Bungum et al., 1971; White et al., 2019; Withers et al., 1998). The window lengths of 0.25 and 10.0 s are used for the STA and LTA, respectively. The STA/LTA algorithm registers a detection when the ratio of the two averages (each calculated as the root mean square signal amplitude) exceeds an onset threshold of 5 and remains above a secondary threshold of 2 for at least 2 s.

The second step is to associate the single station-based picks into events. The STA/LTA method can be triggered by spurious signals that originate from shallow noise sources in the vicinity of the geophones. Therefore, we associate the picks in both time and space to mitigate the false detections. It takes a maximum of 2 seconds for P-waves to traverse the arrays, and hence, a quick way to associate events is to count the number of single-station picks within a 2-second sliding window. If, at any moment, the number of picks is larger than two standard deviations from the mean of a day, a potential event is declared (Figure 8.3).

After the association, candidate events are further screened by a spatial coherence filter. The local anthropogenic noise may trigger nearby sensors but not usually the sensors away from the triggered one. For a pick at sensor to be kept in the associated event we require that 20% of sensors within 1 km of that sensor to also have picks (Figure 8.3f). After the spatial clustering, the number of events decreases from more than 600,000 to about 50,000. This process eliminates most of the uncorrelated random picks.

Identified events are located by a cascade of methods designed to improve locations. For the initial location, the events are individually located using the algorithm NonLinLoc (Lomax et al., 2009), which is a probabilistic, global-search approach. During the grid search, it is assumed that both the velocity model and picks can produce 0.5-s errors. This input prior-uncertainty is quite large and could be improved using a path-dependent error. After that, a double-difference relocation is performed to refine the relative location. The differential times of all the event pairs are calculated with cross-correlation of the waveforms in a window around the P wave arrival times (0.5 s before and 2 s after). The differential travel times obtained by cross-correlating waveforms are input into GrowClust (Trugman & Shearer, 2017), which is a cluster-based double-difference relocation algorithm. A minimum of 8 differential travel times and a minimum cross-correlation coefficient of 0.7 are required to relocate each event pair. For both absolute and relative location, a 1-D velocity model averaged from the SCEC-CVMS model in this region is used (Small et al., 2017). The event is kept if either is relocated by GrowClust or has an uncertainty (estimated by NonLinLoc) less than 2 km. After relocation, the number of events decreases from 50,000 to 3363 (including day and night). We use bootstrapping to estimate the error of the relocation results (Trugman & Shearer, 2017). The resulting average horizontal error is 0.12 km and the average vertical error is 0.16 km.

The local magnitude of the events can be estimated with a simple regression based on the largest amplitudes and hypocentral distances recorded at the sensors as used in a Wood-Anderson seismograph (Richter, 1935):

$$M_L = \log_{10} A + a \log_{10} \Delta + b, \tag{8.1}$$

where A is the peak amplitude of the P-wave waveform recorded at a station with epicentral distance Δ. For calibration, we use a total of 11 events that are already recorded in the SCSN catalog and are located closest to the nodal array. Given the accurate magnitudes M_L from the SCSN catalog, and the peak amplitudes A and the epicentral distances Δ based on the recordings of our nodes, we can optimize the empirical parameters a and b in the equation with linear regression. We have the resulted best-fitted a = 0.4958 and b =1.8517. With the fixed parameters a and b, we calculate the magnitude for the events that are not in the SCSN catalog but detected and located by the nodal arrays. For each event, we determine its magnitude using the median of the magnitudes calculated by all the nodes following equation (8.1).

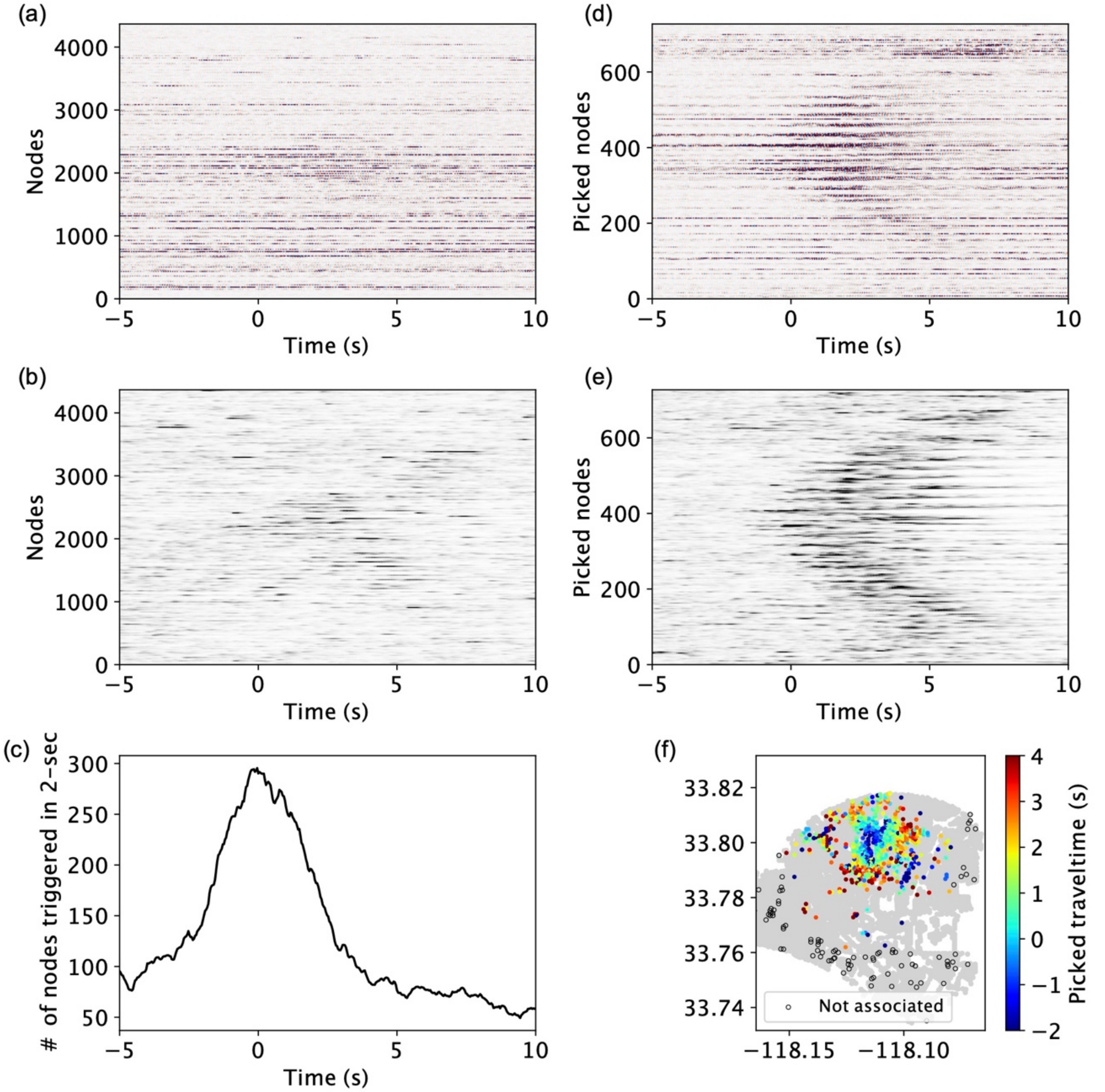

Figure 8.3: The scheme of detection and association. (a) 15-sec continuous waveforms around a detected event for all the sensors in SB3D array; (b) STA/LTA of the data in (a); (c) the number of the single-station picks in a 2-sec sliding window for the picks in (b). (d) similar as (a), but only for all the picked sensors; (e) similar as (b), but only for all the picked sensors; (f) the spatial distribution of all the picked sensors for this event, with

colors showing the picked arrival times. Black circles represent the sensors that were picked during this event but did not pass the following spatial clustering for association.

8.3 Results

The nearby SCSN cataloged events are all detected and located with better-resolved hypocenters (Figure 8.4). They are not, however, included in our relocated catalog, because they are outside the array area and the relocation requires multiple events with coherent waveforms. The SCSN cataloged events are relatively large (~M2) and don't have repeating counterparts within several months. We detected, located, and relocated a total of 1262 nighttime events during a non-continuous period of 8 months in the Long Beach area. The magnitudes of these events range between 0.40 and 1.34 with a mean value of 0.81. The distribution of the located seismicity is shown in Figure 8.5. The main feature of the seismicity is that the bulk of it is shallower than 2 km depth, with several large clusters along the NIF and around the Seal Beach Pier. Figure 8.5 shows two vertical cross-sections of the located events, one of which has a high-resolution seismic reflection profile produced by 3D Seismic Solutions Inc shown in the background. The diffuse seismicity and the complicated seismic section show that at shallow depths, the NIF is a wide splay zone with a width >1 km. A new fault between the Los Alamitos fault (LAF) and the NIF, and also north of the Garden Grove Fault (GGF) newly detected by oil-company analysis is evident in the cross-section (Figure 8.5).

The hourly distributions of seismicity in all areas typically show a bell-shape distribution with a significant increase in the number of earthquakes at night due to the decrease in anthropogenic noise (Figure 8.2). Although we only present nighttime events in this work, we also processed daytime data for comparison. Our results show that the number of events detected per hour in the nighttime is indeed higher than that in the day time. The clusters of the events that appear during the daytime are mostly located around the Long Beach airport but do not appear to correspond to other areas of the city where we expect to have anthropological noise such as freeways and rail lines, industrial areas, port area, oil fields (Figure 8.S2). The calculated magnitudes for the daytime detections are substantially larger than that of nighttime events, which is due to the large amplitudes from the strong cultural noise right on the surface. The events number-magnitude distribution also differs between the daytime and nighttime events (Figure 8.6). We use the maximum curvature method to calculate the Mc (Wiemer & Wyss, 2000), where Mc is set as the maximum of the first derivative of the discrete G-R law plot. Then, we use all the events above Mc to compute the b-value and its uncertainty with the maximum likelihood estimate method (Aki, 1965). The daytime distribution is poorly fit with a power law whereas the nighttime distribution has a regressed b-value of nearly 2 (Figure 8.6). Currently we do not include daytime detections in our results since we don't have a procedure for distinguishing between earthquake and anthropogenic noise sources.

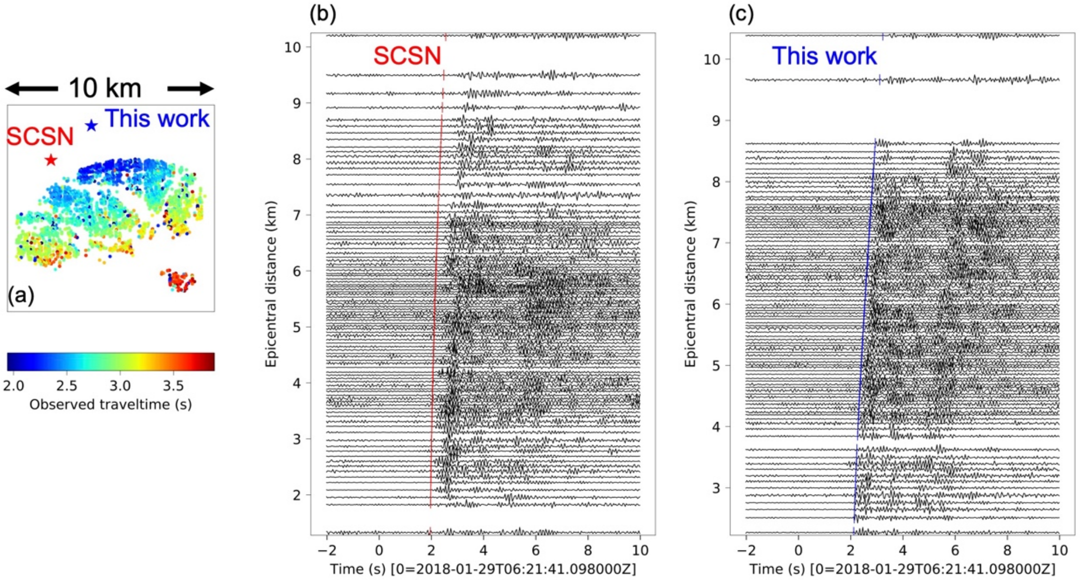

Figure 8.4: Comparison between the earthquake location in SCSN catalog and this study. (a) Epicenters of SCSN catalog in red and our located results in blue. The dots represent the sensors with color indicating the picked travel times; (b) waveform sorted by the hypocenter in the red star in (a) with predicted P wave arrival time shown in red bars; (c) similar as (b), but for the hypocenter in blue in (a).

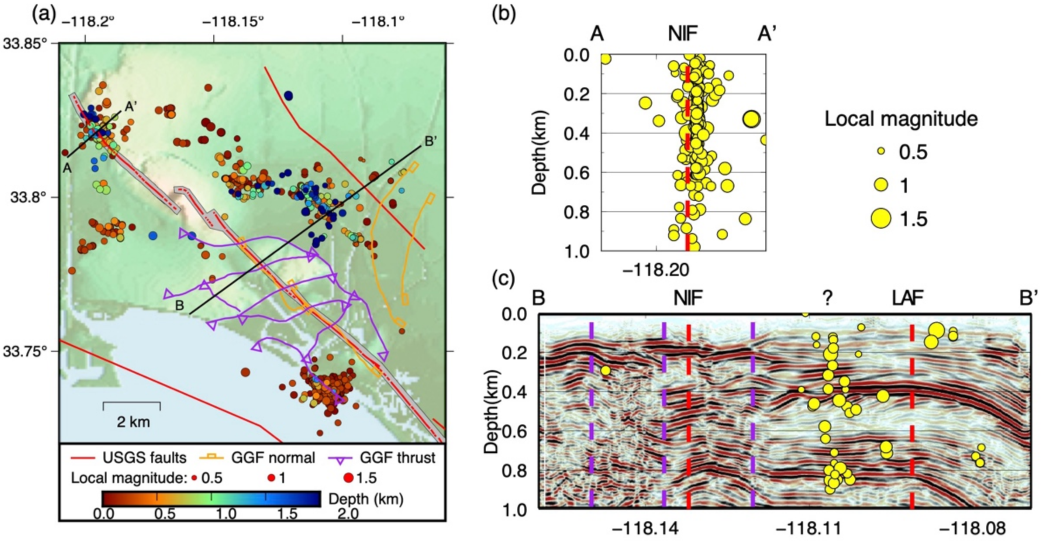

Figure 8.5: Distribution of the relocated nighttime events in the Long Beach area shown as circles. (a) the horizontal view. The circles are the events with their colors showing the depth and their sizes showing the magnitude. The red lines show the fault traces in USGS database (U.S. Geological Survey and California Geological Survey, 1993). The purple and the orange lines represent the recently mapped thrust and normal faults of the Garden Grove fault zone (GGF), respectively (Gish & Boljen, 2021). The black lines mark the location of the two cross-sections shown in (b) and (c). The gray shaded area depicts the ~ 250 m wide Alquist-Priolo zone as previously estimated (California Division of Mines and Geology (CDMG), 1976). (b) Seismicity on the depth profile AA’ with the red dashed line showing the location where the NIF crosses the profile. (c) Seismicity on the depth profile BB’ with the red dashed line showing the locations where the NIF and LAF cross the profile. The purple dashed lines show the locations where the GGF traces are across the profile.

The background shows the high-resolution seismic reflection profile produced by 3DSeismicSolutions Inc.

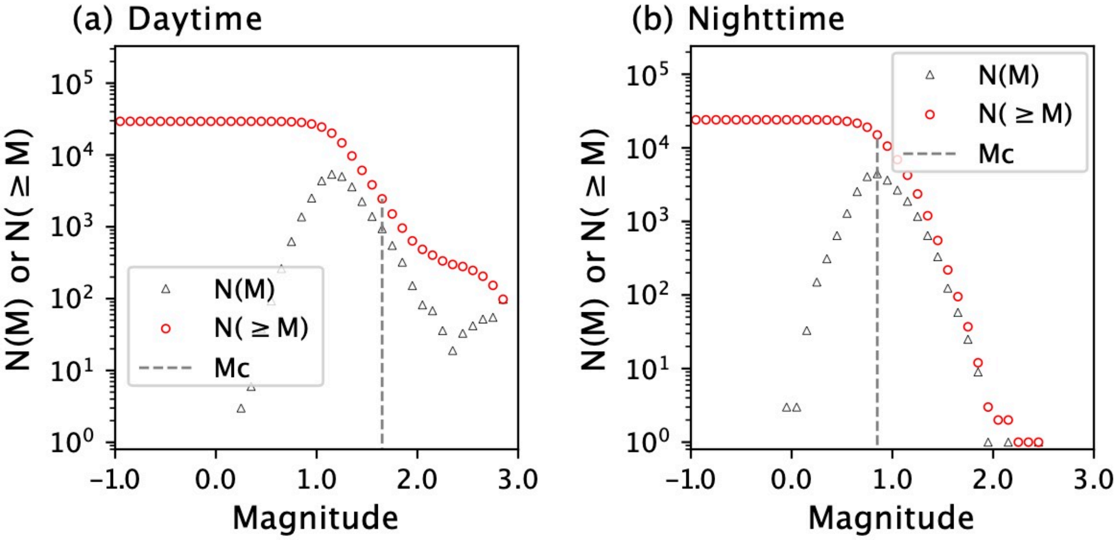

Figure 8.6: Magnitude distribution for daytime and nighttime events. (a) magnitude distribution for daytime events. (b) magnitude distribution for nighttime events. Here all the events including those that were not relocated are plotted. The nighttime distribution is more consistent with a power law while the daytime events clearly are not.

8.4 Discussion

8.4.1 Active faults beneath Long Beach

The study area, comprising parts of Long Beach and Seal Beach, is crossed by the southern portion of the NIF, which appears on the USGS Fault Map to be a strike-slip fault with a single main strand. Detailed subsurface mapping of the oil fields along the NIF has revealed a variety of complex structural patterns, and many of these cannot easily be reconciled with a pure strike-slip origin (Wright, 1991). The formation of the splay features is likely related to the tectonic environment of the LA basin, in which the regional stress field transitioned from extension to compression (Harding, 1973; Williams et al., 1989). Previous results support the idea that the NIF changes character along strike (Wright, 1991). In Long Beach, the NIF is a relatively simple fault with a pair of strands. In Seal Beach, the NIF is a wide flower structure with several splays currently active. Inbal *et al.* (2015) located the seismicity in Long Beach with the depths gradually increasing to the northeast of the NIF, indicating a dipping structure. The seismicity and the seismic reflection profile confirm that the NIF is actually dispersed across a zone that is at least 1 km wide at the surface (Figure 8.5).

The active source portion of the Seal Beach array was processed by 3D Seismic Solutions Inc to produce 3D reflection images of the subsurface (Gish & Boljen, 2021). The top one second of these images (about 1 km in depth) are shown in Figure 8.5. Their analysis has identified a previously unknown fault with significant offset, in the area between the NIF and LAF faults, which they have named the Garden Grove Fault (GGF). At least part of the unmapped GGF is active, as shown in Figure 8.7. The seismicity pattern along the NW-SW trend is at a 10-degree angle to the shoreline as does the mapped fault. The seismicity ceases near the San Gabriel River where the fault is cut through by another orthogonal fault (Figure 8.7). The southern end of both the fault and the seismicity is determined by the extent of the Seal Beach survey. The part of GGF without seismicity may be inactive during the very limited deployment duration. It is also possible that the events' frequency content is above the highest frequency we used in this paper.

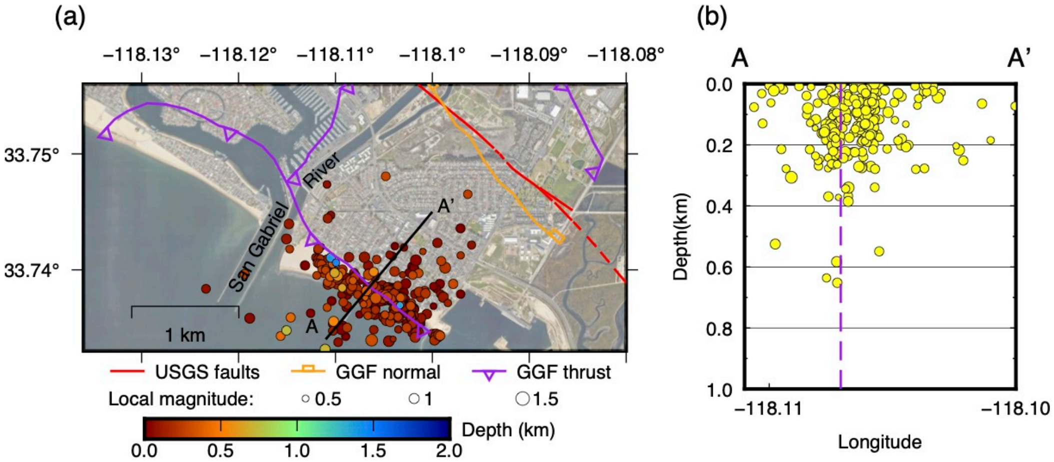

Figure 8.7: A zoomed-in view of the cluster of shallow Seismicity in the southeast corner of the study region. (a) The seismicity identifies a fault along the coast that is also identified in the interpretation of the seismic data by the company 3DSeismicSolutions. This fault is intersected or truncated on the NW by another fault. Note that this seismicity is about 2-3

km away from the Seal Beach oilfield. The symbols of the faults are the same as those in Figure 8.5. (b) Seismicity along the depth profile AA'. The magnitude scale is the same as that in (a). The purple dashed line showing the location where the fault mapped by reflection surveys intersects with the profile.

8.4.2 Shallow seismicity

One notable feature is that most of the events detected in this study are clustered at very shallow depth (<2 km). Although the earthquakes in the SCSN catalog and the template matching-based QTM catalog using regional stations (Ross et al., 2019) are deeper than 6 km, previous studies using the Long Beach and Extended Long Beach arrays present similar results showing the seismicity is clustered in the top 5 km (Li et al., 2018; Yang et al., 2021). We did not detect any deep events but as shown by Inbal *et al.* (2016), detecting deep earthquakes in a noisy urban environment requires spatial filtering to reduce surface noise. Applying such a filter in this study would attenuate the detected shallow seismicity.

Tectonic seismicity in Southern California is rarely observed shallower than 2 km (Sanders, 1990). A lack of near-source station coverage or the use of generalized regional velocity models have typically been considered as the causes of the large uncertainty in the earthquake depth in published catalogs. A sequence of unusually shallow earthquakes (< 3 km) has been reported in 1993 inside the Rock Valley fault zone, NV (Smith et al., 1993). The convincing evidence is the extremely short S minus P times recorded in their near-source three-component receiver. The nodal arrays in our study, however, only have single vertical component. We attempted to use the array data to determine focal mechanisms for identified earthquakes but were unsuccessful because spatial patterns were too noisy to be interpretable. We suspect this is due to paths being almost horizontal leaving the source (for shallow events) and hence encountering strong near surface heterogeneity and scattering. An example is shown in Figure 8.S3.

Relatively little is known about very shallow seismogenesis. Long (2019) summarizes the studies on shallow seismicity swarms in the southeastern U.S. and proposes a positive feedback mechanism to account for the mechanics of shallow seismicity. The key is a low-stress environment rather than an increase in tectonic stress. In a low-stress environment, fractures can be open or filled with fluid and can be held open further by their asperities. During faulting, the reduction in fracture volume increases the fluid pressure, enhancing the capability of fluids to trigger more earthquakes. This mechanism works only at shallow depths and low stress where fractures and faults can hold fluids. In this fluid-rich environment, shallow seismicity may have different properties from the seismicity at greater depth. The focal mechanisms of shallow induced seismicity are associated with joint directions (Zoback & Hickman, 1982), and the spectral decay of shallow seismicity is more rapid (Marion & Long, 1980). Many studies have also pointed that the shallow earthquakes generally have higher than normal b-values (Goebel et al., 2017; Li et al., 2015; Meng et al., 2018; Mori & Abercrombie, 1997; Rivière et al., 2018; C. H. Scholz, 1968; Spada et al., 2013), which is consistent with the mechanism that they nucleate at lower differential stress (Christopher H. Scholz, 2015). A key question for hazard assessment is: does shallow seismicity increase seismic hazard? Although we expect that large earthquakes will likely nucleate and release energy at 6-10 km depth, shallow seismicity suggests that there are many possible paths for a rupture to propagate to the surface. The regulatory zones surrounding the surface traces of active faults in California are named Alquist-Priolo zone, which has a minimum extent of fifty feet from the fault. Our results suggest the zone of high hazard at the surface may therefore be much wider than the Alquist-Priolo zone indicates (Figure 8.5).

8.5 Conclusions

We use three dense urban exploration seismic networks in Long Beach, CA to detect and locate local seismicity. Besides the documented events from outside the arrays in SCSN catalog, a large number of shallow events inside the array are detected. The location results support the previous conclusion that the Newport-Inglewood fault is a wide splayed fault in this area. The seismicity pattern also compares well with some newly identified faults from reflection seismic surveys. The shallow events call for attention on the potential shallow seismicity-related hazard.

Supplementary Material

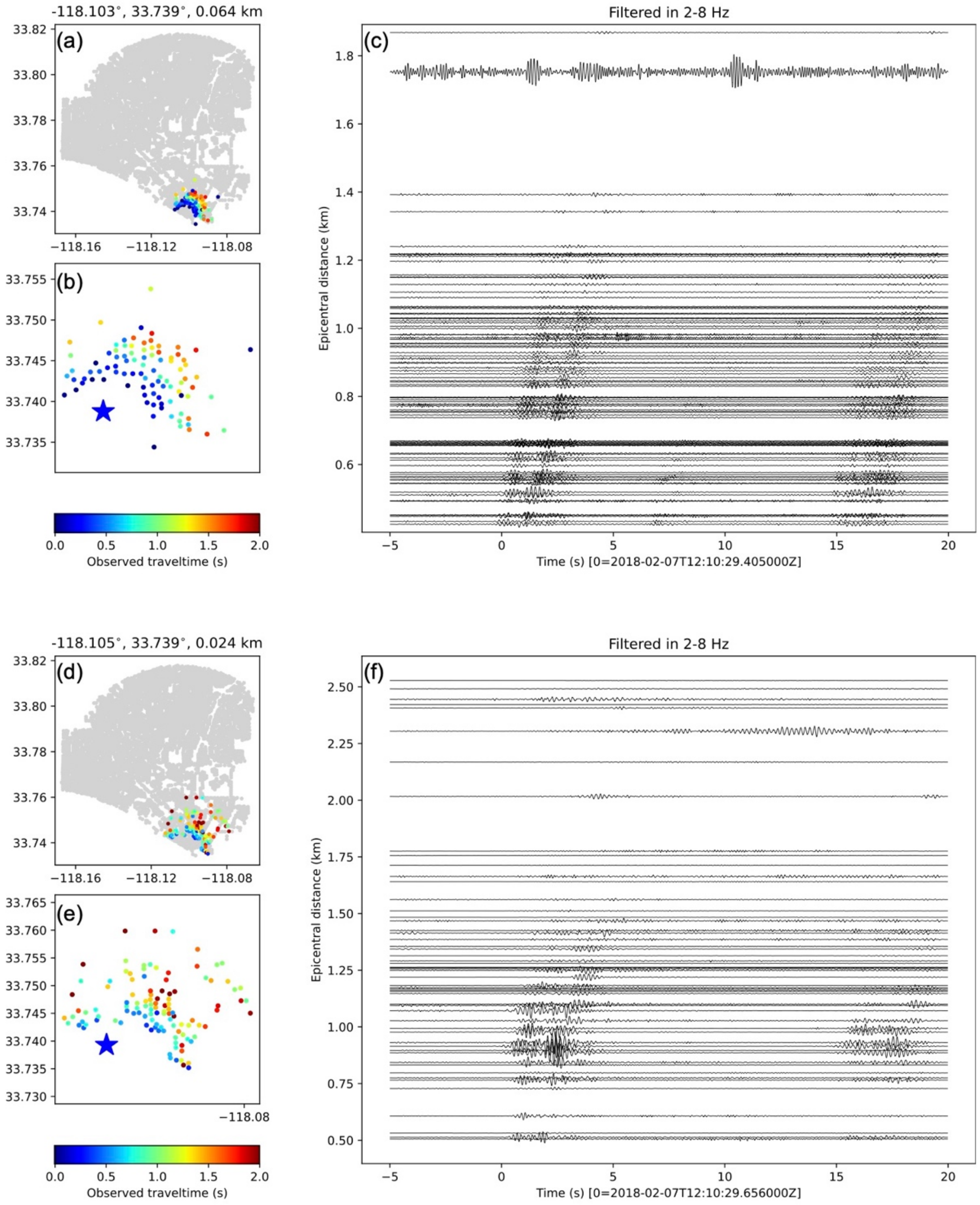

Figure 8.S1: Comparison showing the effect of the urban denoiser. (a)-(c): Our detection and location scheme directly applied to the raw data. (d)-(f) Our detection and location scheme directly applied to the data after the urban denoiser of Yang et al (2022). It is clear that the detected event passes the denoiser, but the coherent earthquake arrivals have been suppressed.

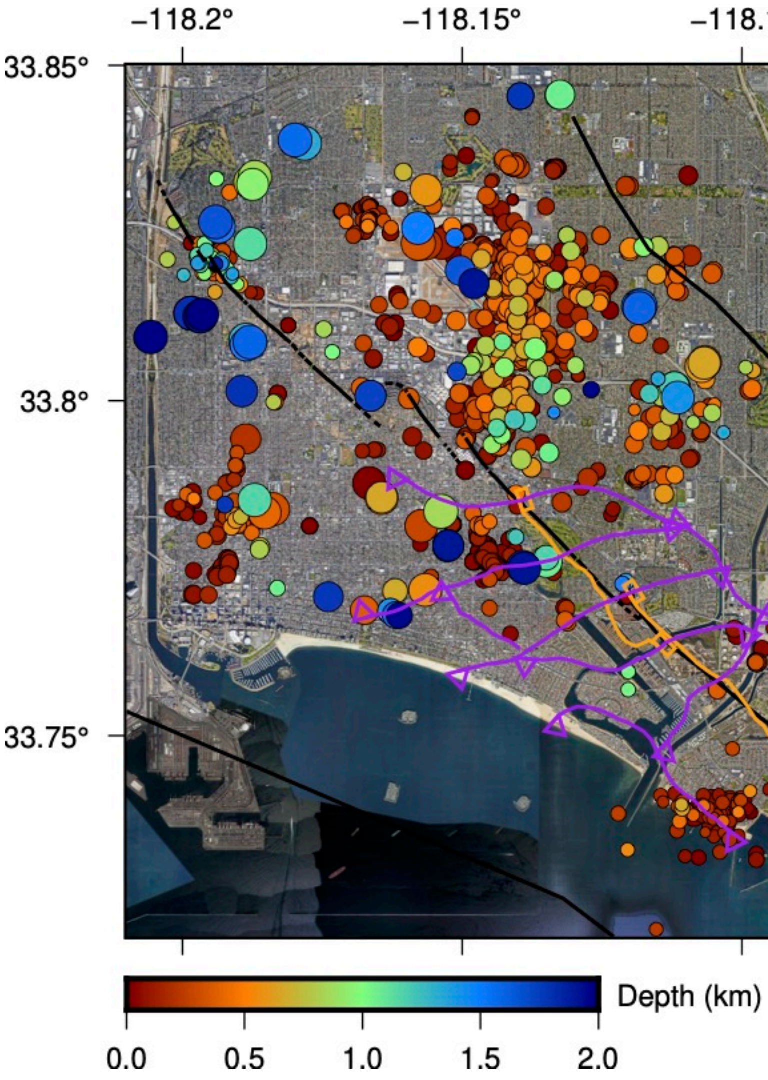

Figure 8.S2: Map of the cataloged daytime events in the Long Beach area, with color showing depth and size showing magnitude. Note that the magnitude scale here is the same as that in Figure 8.4. The substantially larger events are due to strong cultural noise right on the surface.

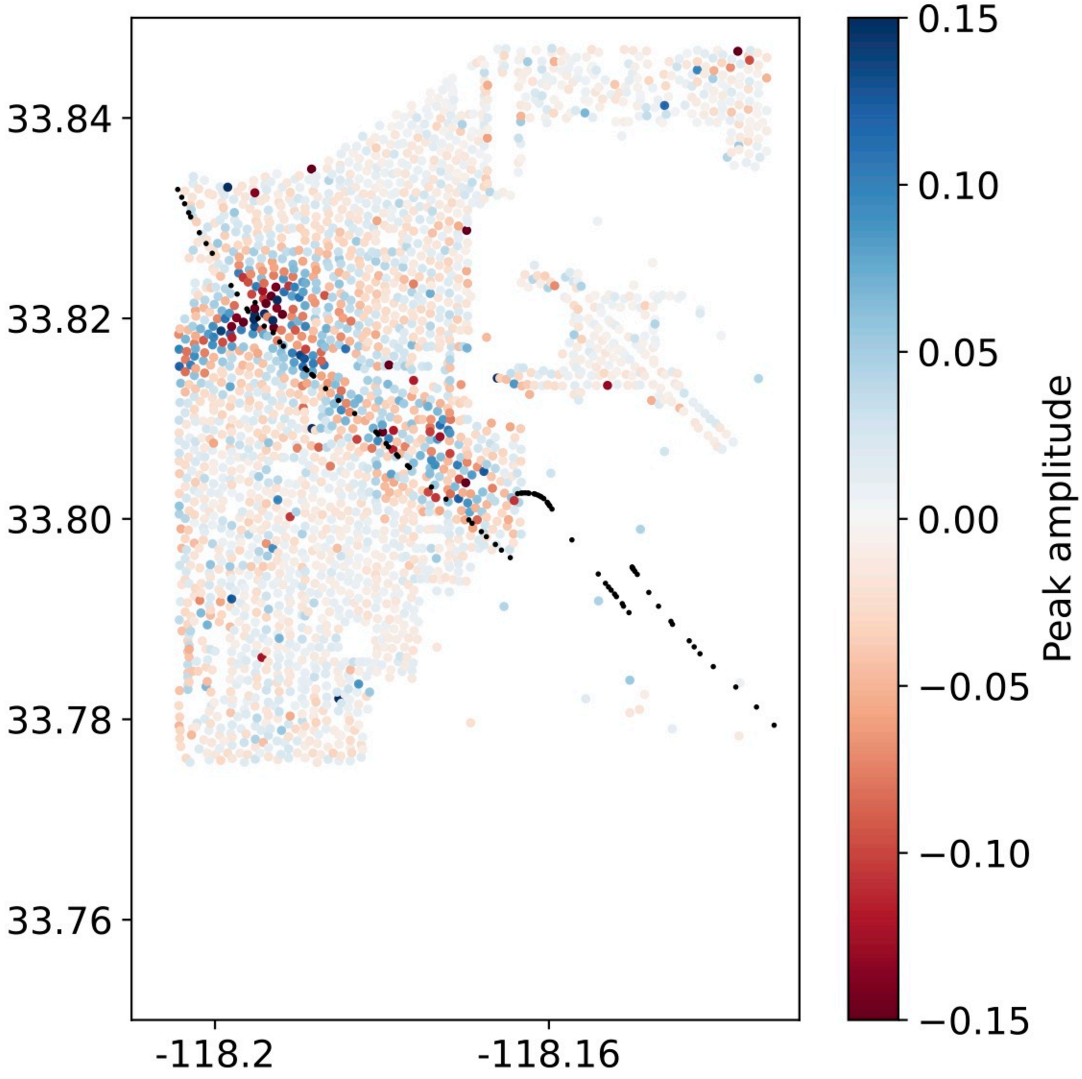

Figure 8.S3: Attempts to determine the focal mechanism. The figure shows the peak amplitude for a magnitude=0.71 event on the NIF. The amplitude pattern flows the apparent surface heterogeneity due to the NIF zone. No clear focal mechanism pattern can be seen.

References

Aki, K. (1965). Maximum likelihood estimate of b in the formula logN=a-bM and its confidence limits. *Bulletin of the Earthquake Research Institute University of Tokyo*, *43*, 237–239.

Bungum, H., Husebye, E. S., & Ringdal, F. (1971). The NORSAR Array and Preliminary Results of Data Analysis. *Geophysical Journal International*, *25*(1–3), 115–126. https://doi.org/10.1111/j.1365-246X.1971.tb02334.x

California Division of Mines and Geology (CDMG),. (1976). Active Fault Mapping and Evaluation Program—Ten Year Program to Implement Alquist-Priolo Special Studies Zones Act, California Division of Mines and Geology Special Publication. California Division of Mines and Geology Special Publication.

Castellanos, J. C., Clayton, R. W., & Juarez, A. (2020). Using a Time-Based Subarray Method to Extract and Invert Noise-Derived Body Waves at Long Beach, California. *Journal of Geophysical Research: Solid Earth*, *125*(5). https://doi.org/10.1029/2019JB018855

Eaton, J. E. (1933). Long Beach, California, Earthquake of March 10, 1933: GEOLOGICAL NOTES. *AAPG Bulletin*, *17*(6), 732–738. https://doi.org/10.1306/3D932B6C-16B1-11D7-8645000102C1865D

Field, E. H., Biasi, G. P., Bird, P., Dawson, T. E., Felzer, K. R., Jackson, D. D., et al. (2015). Long-Term Time-Dependent Probabilities for the Third Uniform California Earthquake Rupture Forecast (UCERF3). *Bulletin of the Seismological Society of America*, *105*(2A), 511–543. https://doi.org/10.1785/0120140093

Gish, D., & Boljen, S. (2021). Newly identified fault in Seal Beach, CA, quietly rattles beneath the city. *Temblor*. https://doi.org/10.32858/temblor.219

Goebel, T. H. W., Kwiatek, G., Becker, T. W., Brodsky, E. E., & Dresen, G. (2017). What allows seismic events to grow big?: Insights from b-value and fault roughness analysis in laboratory stick-slip experiments. *Geology*, *45*(9), 815–818. https://doi.org/10.1130/G39147.1

Harding, T. P. (1973). Newport-Inglewood Trend, California--An Example of Wrenching Style of Deformation. *AAPG Bulletin*, *57*(January), 97–116. https://doi.org/10.1306/819A424C-16C5-11D7-8645000102C1865D

Hauksson, E., & Gross, S. (1991). Source parameters of the 1933 Long Beach earthquake. *Bulletin - Seismological Society of America*, *81*(1), 81–98.

Hauksson, Egill. (1987). Seismotectonics of the Newport-Inglewood fault zone in the Los Angeles basin, southern California. *Bulletin of the Seismological Society of America*, *77*(2), 539–561.

Hough, S. E., & Graves, R. W. (2020). The 1933 Long Beach Earthquake (California, USA): Ground Motions and Rupture Scenario. *Scientific Reports*, *10*(1), 10017. https://doi.org/10.1038/s41598-020-66299-w

Hutton, K., Woessner, J., & Hauksson, E. (2010). Earthquake Monitoring in Southern California for Seventy-Seven Years (1932-2008). *Bulletin of the Seismological Society of America*, *100*(2), 423–446. https://doi.org/10.1785/0120090130

Inbal, A., Clayton, R. W., & Ampuero, J.-P. (2015). Imaging widespread seismicity at midlower crustal depths beneath Long Beach, CA, with a dense seismic array: Evidence for a depth-dependent earthquake size distribution. *Geophysical Research Letters*, *42*(15), 6314–6323. https://doi.org/10.1002/2015GL064942

Inbal, A., Ampuero, J.-P., & Clayton, R. W. (2016). Localized seismic deformation in the upper mantle revealed by dense seismic arrays. *Science*, *354*(6308), 88–92. https://doi.org/10.1126/science.aaf1370

Li, Z., Peng, Z., Meng, X., Inbal, A., Xie, Y., Hollis, D., & Ampuero, J. P. (2015). Matched filter detection of microseismicity in long beach with a 5200-station dense array. *SEG Technical Program Expanded Abstracts*, *34*(December), 2615–2619. https://doi.org/10.1190/segam2015-5924260.1

Li, Z., Peng, Z., Hollis, D., Zhu, L., & McClellan, J. (2018). High-resolution seismic event detection using local similarity for Large-N arrays. *Scientific Reports*, *8*(1), 1–10. https://doi.org/10.1038/s41598-018-19728-w

Lin, F. C., Li, D., Clayton, R. W., & Hollis, D. (2013). High-resolution 3D shallow crustal structure in Long Beach, California: Application of ambient noise tomography on a dense seismic array. *Geophysics*, *78*(4). https://doi.org/10.1190/geo2012-0453.1

Lomax, A., Michelini, A., & Curtis, A. (2009). Earthquake Location, Direct, Global-Search Methods. In *Encyclopedia of Complexity and Systems Science* (pp. 1–33). New York, NY: Springer New York.

Long, L. T. (2019). The mechanics of natural and induced shallow seismicity: A review and speculation based on studies of eastern U.S. Earthquakes. *Bulletin of the Seismological Society of America*, *109*(1), 336–347. https://doi.org/10.1785/0120180134

Marion, G. E., & Long, L. T. (1980). Microearthquake spectra in the southeastern United States. *Bulletin of the Seismological Society of America*, *70*(4), 1037–1054. https://doi.org/10.1785/BSSA0700041037

Meng, X., Yang, H., & Peng, Z. (2018). Foreshocks, b Value Map, and Aftershock Triggering for the 2011 Mw 5.7 Virginia Earthquake. *Journal of Geophysical Research: Solid Earth*, *123*(6), 5082–5098. https://doi.org/10.1029/2017JB015136

Mori, J., & Abercrombie, R. E. (1997). Depth dependence of earthquake frequency-magnitude distributions in California: Implications for rupture initiation. *Journal of Geophysical Research: Solid Earth*, *102*(B7), 15081–15090. https://doi.org/10.1029/97jb01356

Mousavi, S. M., Ellsworth, W. L., Zhu, W., Chuang, L. Y., & Beroza, G. C. (2020). Earthquake transformer—an attentive deep-learning model for simultaneous earthquake detection and phase picking. *Nature Communications*, *11*(1), 1–12. https://doi.org/10.1038/s41467-020-17591-w

Richter, C. F. (1935). An instrumental earthquake magnitude scale*. *Bulletin of the Seismological Society of America*, *25*(1), 1–32. https://doi.org/10.1785/BSSA0250010001

Rivière, J., Lv, Z., Johnson, P. A., & Marone, C. (2018). Evolution of b-value during the seismic cycle: Insights from laboratory experiments on simulated faults. *Earth and Planetary Science Letters*, *482*, 407–413. https://doi.org/10.1016/j.epsl.2017.11.036

Ross, Z. E., Meier, M. A., Hauksson, E., & Heaton, T. H. (2018). Generalized seismic phase detection with deep learning. *Bulletin of the Seismological Society of America*, *108*(5), 2894–2901. https://doi.org/10.1785/0120180080

Ross, Z. E., Trugman, D. T., Hauksson, E., & Shearer, P. M. (2019). Searching for hidden earthquakes in Southern California. *Science*, *771*(May), 767–771. https://doi.org/10.1126/science.aaw6888

Sanders, C. O. (1990). Earthquake depths and the relation to strain accumulation and stress near strike-slip faults in southern California. *Journal of Geophysical Research: Solid Earth*, *95*(B4), 4751–4762. https://doi.org/10.1029/JB095iB04p04751

Scholz, C. H. (1968). The frequency-magnitude relation of microfracturing in rock and its relation to earthquakes. *Bulletin of the Seismological Society of America*, *58*(1), 399–415. https://doi.org/10.1785/BSSA0580010399

Scholz, Christopher H. (2015). On the stress dependence of the earthquake b value. *Geophysical Research Letters*, *42*(5), 1399–1402. https://doi.org/10.1002/2014GL062863

Shelly, D. R., Beroza, G. C., & Ide, S. (2007). Non-volcanic tremor and low-frequency earthquake swarms. *Nature*, *446*(7133), 305–307. https://doi.org/10.1038/nature05666

Small, P., Gill, D., Maechling, P. J., Taborda, R., Callaghan, S., Jordan, T. H., et al. (2017). The SCEC unified community velocity model software framework. *Seismological Research Letters*, *88*(6), 1539–1552. https://doi.org/10.1785/0220170082

Smith, K., Shields, G., & Brune, J. (1993). Shallow Earthquakes, Rock Valley Fault Zone, Southern Nevada Test Site 1 A Sequence of Very Shallow Earthquakes in the Rock Valley Fault Zone, Southern Nevada Test Site.

Snover, D., Johnson, C. W., Bianco, M. J., & Gerstoft, P. (2020). Deep Clustering to Identify Sources of Urban Seismic Noise in Long Beach, California. *Seismological Research Letters*, (March). https://doi.org/10.1785/0220200164

Spada, M., Tormann, T., Wiemer, S., & Enescu, B. (2013). Generic dependence of the frequency-size distribution of earthquakes on depth and its relation to the strength profile of the crust. *Geophysical Research Letters*, *40*(4), 709–714. https://doi.org/10.1029/2012GL054198

Taber, S. (1920). The Inglewood earthquake in Southern California, June 21, 1920. *Bulletin of the Seismological Society of America*, *10*(3), 129–145. https://doi.org/10.1785/BSSA0100030129

Trugman, D. T., & Shearer, P. M. (2017). GrowClust: A Hierarchical clustering algorithm for relative earthquake relocation, with application to the Spanish Springs and Sheldon, Nevada, earthquake sequences. *Seismological Research Letters*, *88*(2), 379–391. https://doi.org/10.1785/0220160188

U.S. Geological Survey and California Geological Survey. (1993). Quaternary fault and fold database for the United States. Retrieved from https://www.usgs.gov/natural-hazards/earthquake-hazards/faults

White, M. C. A., Ben-Zion, Y., & Vernon, F. L. (2019). A Detailed Earthquake Catalog for the San Jacinto Fault-Zone Region in Southern California. *Journal of Geophysical Research: Solid Earth*, *124*(7), 6908–6930. https://doi.org/10.1029/2019JB017641

Wiemer, S., & Wyss, M. (2000). Minimum Magnitude of Completeness in Earthquake Catalogs: Examples from Alaska, the Western United States, and Japan. *Bulletin of the Seismological Society of America*, *90*(4), 859–869. https://doi.org/10.1785/0119990114

Williams, G. D., Powell, C. M., & Cooper, M. A. (1989). Geometry and kinematics of inversion tectonics. *Geological Society, London, Special Publications*, *44*(1), 3–15. https://doi.org/10.1144/GSL.SP.1989.044.01.02

Withers, M., Aster, R., Young, C., Beiriger, J., Harris, M., Moore, S., & Trujillo, J. (1998). A comparison of select trigger algorithms for automated global seismic phase and event detection. *Bulletin of the Seismological Society of America*, *88*(1), 95–106.

Wood, H. O., Buwalda, J. P., & Martel, R. R. (1933). The Long Beach Earthquake. *Science*, *78*(2016), 147–149.

Wright, T. L. (1991). Structural geology and tectonic evolution of the Los Angeles Basin, California. *Active Margin Basins*, 35–134.

Yang, L., Liu, X., & Beroza, G. C. (2021). Revisiting evidence for widespread seismicity in the upper mantle under Los Angeles. *Science Advances*, *7*(4). https://doi.org/10.1126/sciadv.abf2862

Yang, L., Liu, X., Zhu, W., Zhao, L., & Beroza, G. C. (2022). Toward improved urban earthquake monitoring through deep-learning-based noise suppression. *Science Advances*, *8*(15), eabl3564. https://doi.org/10.1126/sciadv.abl3564

Zhu, W., & Beroza, G. C. (2019). PhaseNet: A deep-neural-network-based seismic arrival-time picking method. *Geophysical Journal International*, *216*(1), 261–273. https://doi.org/10.1093/gji/ggy423

Zoback, M. D., & Hickman, S. (1982). In situ study of the physical mechanisms controlling induced seismicity at Monticello Reservoir, South Carolina. *Journal of Geophysical Research*, *87*(B8), 6959–6974. https://doi.org/10.1029/JB087iB08p06959

C h a p t e r 9

SEISMIC WAVE PROPAGATION AND INVERSION WITH NEURAL OPERATORS

Yang, Y.*, Gao, A. F.*, Castellanos, J. C.*, Ross, Z. E., Azizzadenesheli, K., & Clayton, R. W. (2021). Seismic Wave Propagation and Inversion with Neural Operators. *The Seismic Record*, 1(3), 126–134. https://doi.org/10.1785/0320210026

Abstract

Seismic wave propagation forms the basis for most aspects of seismological research, yet solving the wave equation is a major computational burden that inhibits the progress of research. This is exacerbated by the fact that new simulations must be performed whenever the velocity structure or source location is perturbed. Here, we explore a prototype framework for learning general solutions using a recently developed machine learning paradigm called Neural Operator. A trained Neural Operator can compute a solution in negligible time for any velocity structure or source location. We develop a scheme to train Neural Operators on an ensemble of simulations performed with random velocity models and source locations. As Neural Operators are grid-free, it is possible to evaluate solutions on higher resolution velocity models than trained on, providing additional computational efficiency. We illustrate the method with the 2D acoustic wave equation and demonstrate the method's applicability to seismic tomography, using reverse-mode automatic differentiation to compute gradients of the wavefield with respect to the velocity structure. The developed procedure is nearly an order of magnitude faster than using conventional numerical methods for full waveform inversion.

9.1 Introduction

The simulation of seismic wave propagation through Earth's interior underlies most aspects of seismological research, from the simulation of strong ground shaking due to large earthquakes (Graves & Pitarka, 2016; Rodgers et al., 2019), to imaging the subsurface velocity structure (Fichtner et al., 2009; Gebraad et al., 2020; Lee et al., 2014; Tape et al., 2009; Virieux & Operto, 2009), to derivation of earthquake source properties (Duputel et al., 2015; Wang & Zhan, 2020; Ye et al., 2016). The compute costs associated with these wavefield simulations are substantial, and for reasons of computational efficiency, 1D models are often used, even when better 3D velocity models are available. As a result, seismic wave simulations are often the limiting factor in the pace of geophysical research.

Recently, deep learning approaches have been explored with the goal of solving various geophysical partial differential equations (Moseley et al., 2020, 2021; Smith et al., 2021). Beyond the goal of accelerating compute capabilities, such physics-informed neural networks may offer other advantages such as grid-independence, low memory overhead, differentiability, and on-demand solutions. These properties can then result in deep learning being used to solve geophysical inverse problems (Smith et al., 2022; Xiao et al., 2021; Zhu et al., 2021), as a wider selection of algorithms and frameworks are then available for use, such as approximate Bayesian inference techniques like variational inference.

One of the major challenges associated with wave propagation is that a new simulation must be performed whenever the properties of the source or velocity structure are perturbed in some way. This alone substantially increases the necessary compute costs, making some problems prohibitively expensive even if they are mathematically or physically tractable. For the most part, these limitations have been accepted as an inevitable part of seismology, but now physics-informed machine learning approaches have started to offer some pathways for moving beyond this issue. For example, Smith et al. (2021) use a deep neural network to solve the Eikonal equation for any source-receiver pair by taking these locations as input. This then can be exploited for hypocenter inversion by allowing for gradients of the travel time field to be computed with respect to the source location (Smith et al., 2022). However, these models are relatively inefficient to train and even then are only able to learn approximate solution operators to the differential equations.

The aforementioned limitations may seem surprising, but result from a basic attribute of neural networks that in fact makes them ill-suited for solving differential equations. Specifically, neural networks are designed for learning maps between two finite dimensional spaces, while learning a general solution operator for a differential equation requires the ability to map between two infinite dimensional spaces (i.e. function spaces). A paradigm for learning maps between function spaces was recently developed (Jonthan D Smith et al., 2022), and has been termed Neural Operator. The general idea behind these models is that they have shared parameters over all possible functions describing the initial conditions, which allows them operate on functions, even when the inputs are a numerically discretized representation of them.

Here, we explore the potential of Neural Operators in improving seismic wave propagation and inversion. We develop a prototype framework for training Neural Operators on the 2D acoustic wave equation and show that this approach provides a suite of tantalizing new advantages over conventional numerical methods for seismic wave propagation. This study provides a proof of concept of this technology and its application to seismology.

9.2 Preliminaries

For a given function A and a Green's function G, let U denote the solution to a linear PDE, i.e., the solution operator,

$$U(x) = (\mathcal{L}\, A)(x) = \int G(x, y)A(y)dy, \tag{9.1}$$

in which $\mathcal{L}$ is the corresponding linear operator. For example, suppose that the PDE to be solved is the acoustic wave equation; then A could describe the velocity structure as well as the initial conditions. Neural operator generalizes this formulation to the nonlinear setting where a set of linear operators are sequentially applied to construct a general nonlinear solution operator. In its basic form, an l-layered neural operator is constructed as follows:

$$U(x) = \mathcal{L}_l(\sigma(\mathcal{L}_{l-1} \dots \sigma(\mathcal{L}_1 V) \dots))(x), \tag{9.2}$$

in which $\mathcal{L}_i$ is such that for any function V, we have,

$$(\mathcal{L}_i V)(x) = W_i(x) + \int K_i(x, y)V(y)dy. \tag{9.3}$$

Under this framework, $W_i(x)$ and $K_i(x, y)$ constitute the learnable components of the Neural Operator and allow for a solution to be produced for any prescribed function A. In a limited sense, Neural Operators can be viewed as generalized Green's functions.

9.3 Methods

We designed a framework that applies Neural Operators to the 2D acoustic wave equation. The basic idea for this procedure is outlined schematically in Figure 9.1. A specific type of Neural Operator, called a Fourier Neural Operator (FNO; Li et al., 2020a) receives a velocity model specified on an arbitrary, possibly irregular mesh, along with the coordinates of a point source. One of the main features of FNO is that the major calculations are performed in the frequency domain, which allows the convolutions in equation (9.3) to be rapidly computed. The output of the FNO is the complete wavefield solution, which can be queried anywhere within the medium, regardless of whether the points lie on the input mesh.

The most basic component of the FNO is a Fourier block (Figure 9.1), which first transforms an input function (V) to the Fourier domain. In the first layer of the network, V is equal to the initial conditions, A. Then, a kernel K_i) is computed specifically for this function and is truncated at low order, before performing the integration via multiplication. Finally, the result is transformed back and a non-linear activation function is applied, which concludes the Fourier block. For this study, the architecture of the FNO contains 4 sequential Fourier blocks and applies a ReLU activation to the output of each (Figure 9.1). We note that the truncation of the Fourier modes is performed on the function values after lifting them to a higher dimensional space, rather than the raw input function, so that this does not lead to compression. We refer the interested readers to (Li et al., 2020a) for more mathematical details about the FNO.

We constructed a training dataset of simulations to learn from by first generating random velocity models. We set up a 64×64 grid with 0.16 km spacing to define the velocity model. Then, we created 5,000 random velocity models by sampling random fields having a von

Karman covariance function with the following parameters: Hurst exponent $\kappa = 0.5$, correlation length $\boldsymbol{a} = [a_x, a_y] = [0.16\ \text{km}, 0.16\ \text{km}]$, and $\varepsilon = 0.1, \mu = 3\ \text{km/s}$, and $\sigma = 0.15\ \text{km}$. Then, for each of these velocity models, we apply a Ricker wavelet source at a random point, and solve the acoustic wave equation using a spectral-element method (SEM; Afanasiev et al., 2019). It should be noted that there is a source grid used since this is a requirement of the spectral-element method. As Gaussian random fields can represent all continuous functions, the purpose of these steps is to create a suite of simulations that span a range of possible conditions. We show later that they can even well-approximate strongly discontinuous velocity models. An example velocity model and simulation is shown in Figure 9.1. Applying the aforementioned procedure results in a training dataset of 5,000 data samples, each of which is a different simulation.

Given the simulation dataset, we can proceed to train a FNO model in a supervised capacity, where the goal is to learn a model that can reliably output a solution to the wave equation for arbitrary input conditions. The training is performed using batch gradient descent, where the parameters of the FNO are updated to minimize the error against the "true" spectral-element solutions. A mean-square error loss function is used. We use a batch size of 30 simulations and train the model for a maximum of 300 epochs. We use all but 200 of the simulations for training, and set aside the remainder for cross-validation of the model. The time required to train the model from scratch is approximately 18 hours using 6 NVIDIA Tesla V100 GPUs.

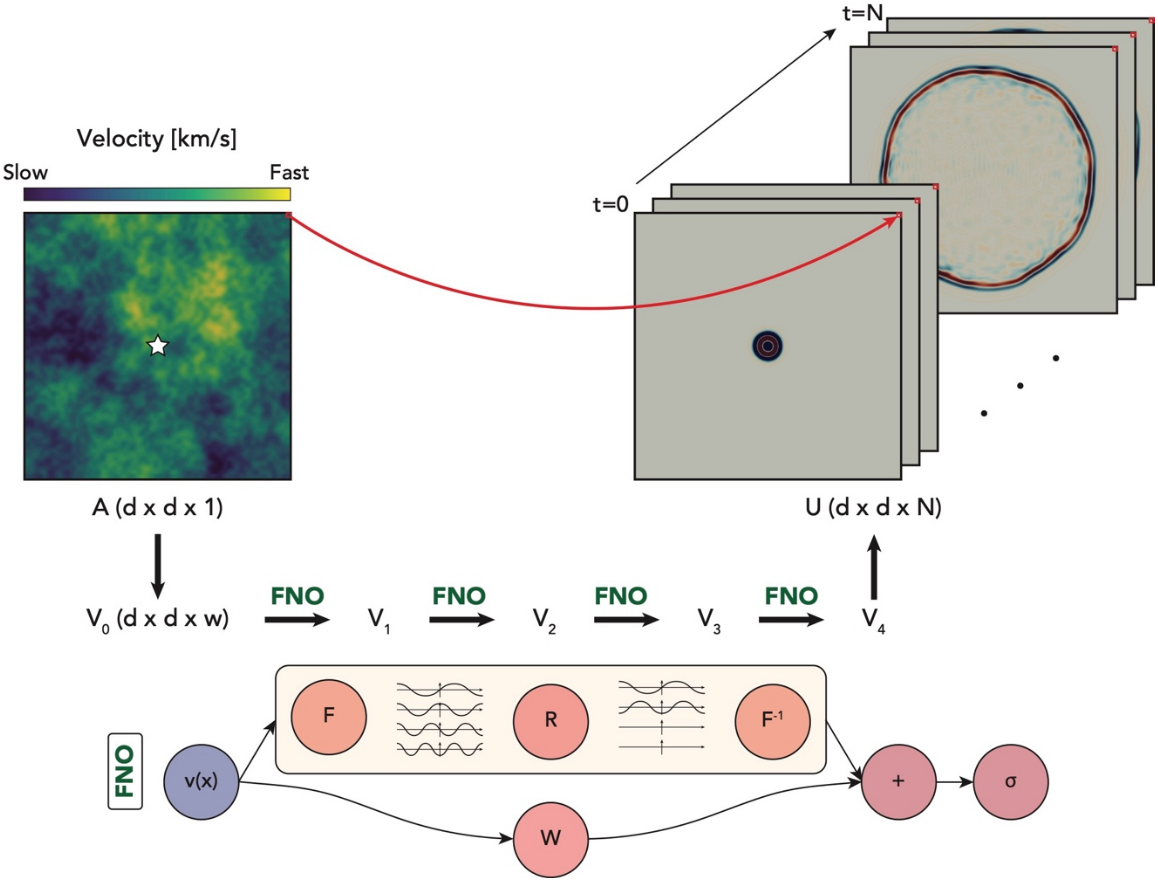

Figure 9.1: Our approach applying FNO to the 2D acoustic wave equation. The inputs to the FNO model are the velocity model with dimensions $d \times d \times 1$ and the source location, indicated by the white star. The input velocity model is lifted to a higher dimensional space with size $d \times d \times w$ using a neural network. Then, we apply four Fourier operator layers, and finally project back to the target wavefield dimensions of $d \times d \times N$ using a neural network. The bottom panel shows details of the Fourier layer architecture: we define v to be the input. On top: We apply a Fourier transform F to v, then apply a linear transformation R to the lower Fourier modes, filtering out higher modes. Then we apply an inverse Fourier transform F^{-1}. On the bottom: we apply a local linear transform W to v.}

9.4 Experiments

9.4.1 Initial wavefield demonstration

Figure 9.2 shows two example wavefields corresponding to two different velocity models, each with a different source. The spectral element solution is shown alongside the wavefield predicted by the FNO for the 8 different receivers (blue triangles). For these examples, the input velocity model is 64×64. The relative ℓ_2 loss of the FNO wavefields are 0.180 and 0.363. These examples are representative of the entire validation dataset, which has a loss of 0.273 relative to the spectral element solutions.

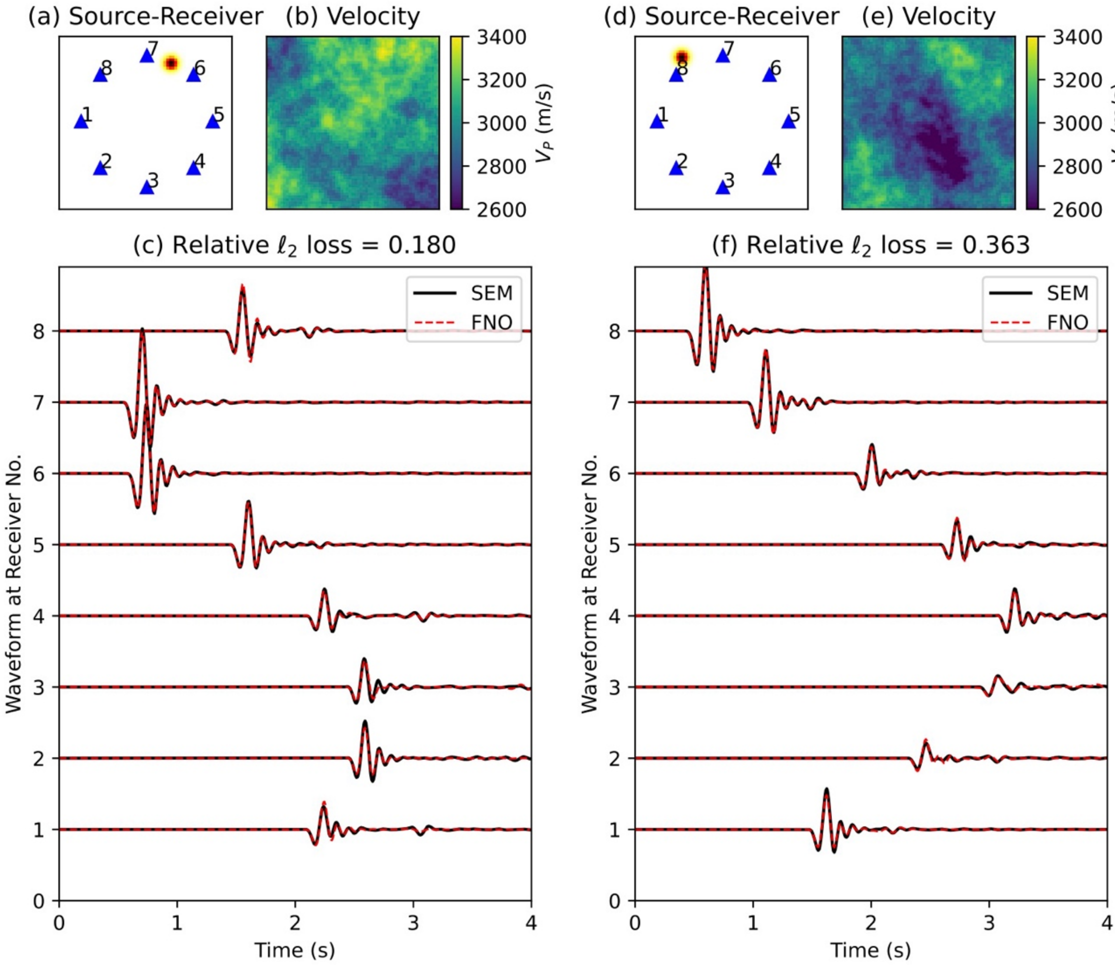

Figure 9.2: Examples of two validation wavefield simulations from the trained FNO model. (a) the source-receiver locations with receivers in blue and source in red; (b) the velocity structure; (c) waveforms simulated with SEM (black) and FNO (red). (d-f) same as (a-c), but for a different velocity model. The relative ℓ_2 loss of the two examples are 0.180 and

0.363, respectively, which are representative of the entire validation data set with an average ℓ_2 loss of 0.273. We demonstrate that the FNO simulation results are able to capture both the major arrivals as well as some reflections.

9.4.2 The number of simulations needed for training

Once fully trained, the FNO can evaluate a new solution in a fraction of a second, and thus the time to train the FNO will be the vast majority of the needed compute time. A primary concern about the computational demands of the FNO approach is therefore the number of simulations needed for training. Here, we examine how the number of training simulations influences the accuracy of the solution. We create a series of tests in which the number of training simulations is varied from 800 at the fewest, to 4800 at the most. The results are shown in Figure 9.3, where we show the FNO wavefield predictions for each dataset. Even with 1200 training samples, there is no indication that there is overfitting since the training waveform error is similar across different models (Figure 9.3a,b). Training using just 1200 simulations is able to predict the major arrival. Increasing number of training samples provides a better fit of the reflections (e.g. 3.2 sec in Figure 9.3c).

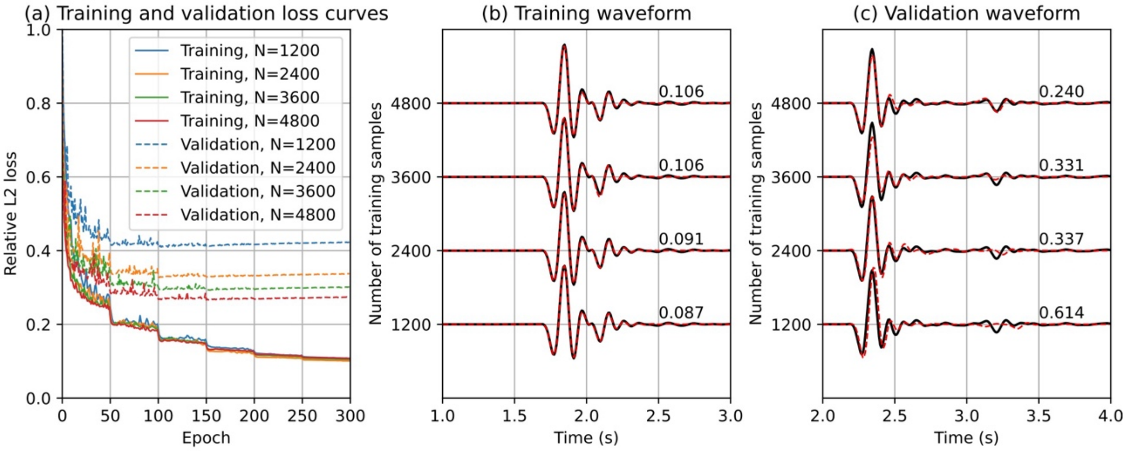

Figure 9.3: Model performance as a function of the number of training samples. (a) Training and validation loss curves as a function of different numbers of training samples. (b) Example waveform fitting of a single training example from models trained with varying number of training examples. (c) Example waveform fitting of a single validation example from models trained with varying number of training examples. The numbers to the right of each

waveform shows the relative ℓ_2 misfit. This shows that the model trained on 4800 samples is able to capture the reflections, whereas the model trained on smaller number of samples does not generalize to reflections in the validation example.

9.4.3 Generalization to arbitrary velocity models

The FNO was trained only on velocity models drawn from Gaussian random fields, and while this family of functions is broad, it does not include some types of functions that exist in the Earth, such as discontinuous functions. This rises the question of whether the FNO can still generalize well to these cases. Figure 9.4a-c shows an example of a predicted wavefield for a velocity model containing a constant velocity square embedded within a homogeneous medium. While the velocity model itself is rather simple, it is actually very far removed from the characteristics of the random fields that the FNO was trained on and represents a challenging example. We can see that the predicted wavefield does a very good job of approximating the wavefield compared to the ground truth. We believe the small residual errors can be reduced with better hyperparameter selection.

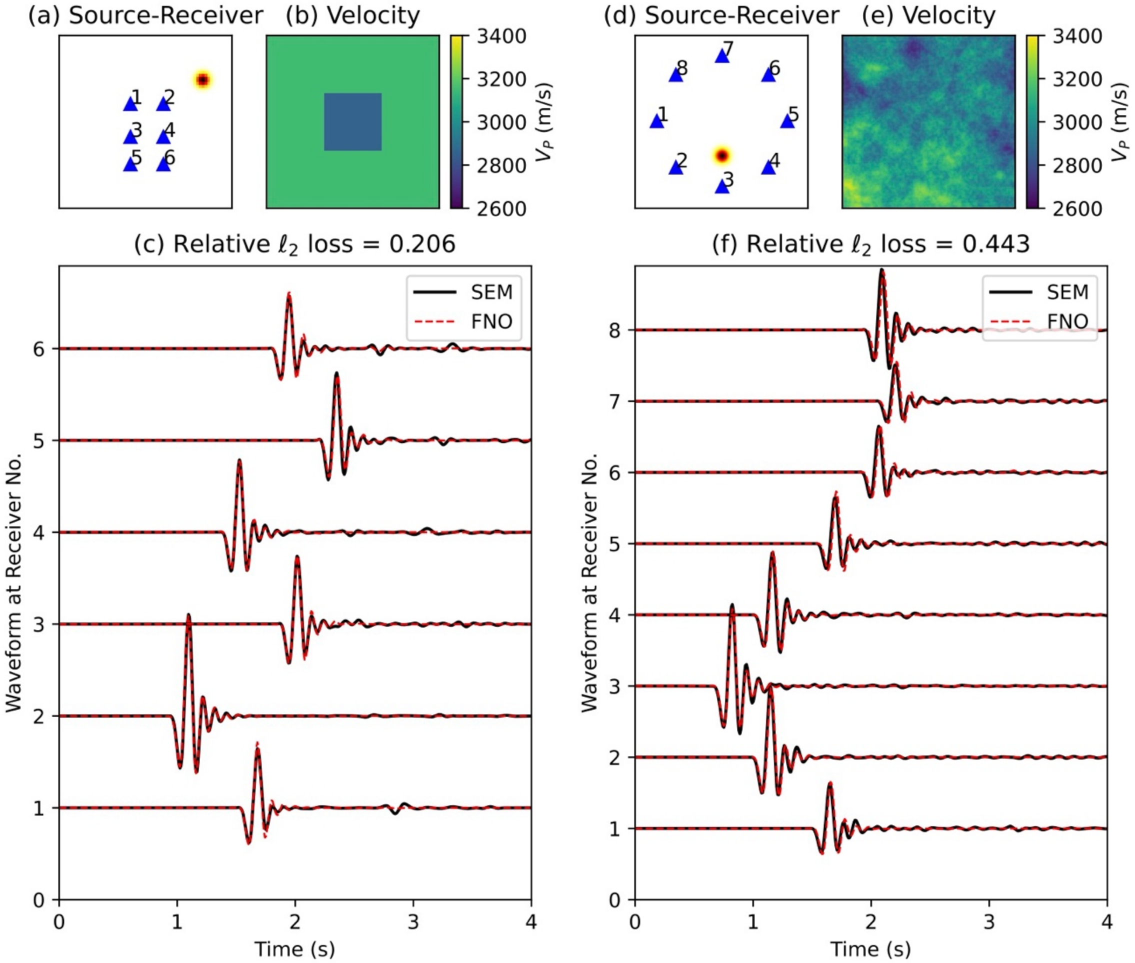

Figure 9.4: Model generalization experiments. (a) the source-receiver locations with receivers in blue and source in red; (b) a velocity model with a homogeneous background of 3 km/s and a 5% square anomaly; (c) waveform simulated with SEM (black) and FNO (red). (d-f) same as (a-c), but for an input velocity model with 2x finer resolution than trained on. These experiments show that the model is not just memorizing the solutions, but is able to generalize to entirely new conditions.

9.4.4 Generalization to higher resolution grids

FNO can be viewed in some sense as a method for learning generalized Green's functions valid for arbitrary boundary conditions. Since it is intrinsically learning a mapping between function spaces, the FNO is theoretically independent of the resolution at which the functions are discretized (this is only a requirement for evaluation on a computer). One important advantage of this is that the FNO can be trained on velocity models with a certain grid spacing, and then be evaluated on velocity models with a different grid spacing at inference time. Here, we are not simply talking about interpolating the wavefield after solving the PDE; but rather, the solutions to the PDE can actually be evaluated on a higher resolution velocity model with negligible extra compute cost. To demonstrate this, Figure 9.4d-f shows the FNO prediction for a random velocity field with 2x higher resolution (128×128) than the models used during training, alongside the spectral element solution. The FNO solution closely approximates the spectral element solution. Note that the velocity models with different meshes have the same roughness as the training data set. Resolving more rough structure with denser spacing can be achieved by training with many more GRFs with varying correlation length scales and variance.

9.4.5 Full waveform inversion with Neural Operators

One of the most useful applications of wavefield simulations is in inversion, to image the Earth's interior. The adjoint-state method is an approach to efficiently compute the gradients of an objective function with respect to parameters of interest and can be used for seismic tomography (e.g., Gebraad et al., 2020; Tape et al., 2009). Neural Operators are differentiable by design, which enables gradient computation with reverse-mode automatic differentiation. Automatic differentiation has been shown to be mathematically equivalent to the adjoint-state method (Zhu et al., 2021). This allows for the gradients of the wavefield to be determined with respect to the inputs (velocity model and source location).

Figure 9.5 demonstrates our FWI performance. For each case, we compute synthetic observations using the source distribution as shown (red circles), taking every point in the 64×64 grid as a receiver. The observations are noise-free for this experiment. Then, we perform tomography by starting with a homogeneous initial velocity model and forward propagating a wavefield with the FNO for each source. We calculate the loss $L = \sum_i \sum_j \left[u^{\mathrm{obs}}\,(x_i, x_j) - u^{\mathrm{pred}}\,(x_i, x_j)\right]^2$, and compute ∇L with automatic differentiation. The velocity model is then iteratively updated with gradient descent for 1000 iterations using the Adam optimizer (Kingma & Ba, 2014)and a learning rate of 0.01. For comparison, Figure 9.5ab shows the imaging result using SEM and adjoint-state method, with a relative ℓ_2 misfit between the inverted and true velocity model of 0.0289. Figure 9.5cd shows the result for the same velocity structure using FNO and automatic differentiation, with a misfit of 0.0319. Figure 9.5ef is designed to demonstrate sharp discontinuous changes with a short wavelength. The results demonstrate the remarkable capabilities of FNO to learn a general solution operator.

We note that our FWI approach does not require an adjoint wavefield to be computed, nor a cross-correlation; the gradients can be rapidly computed with GPUs using automatic differentiation. The rapid simulation makes it substantially more efficient than adjoint methods. For these experiment, 20 sources take ~1 second for one tomographic iteration including the costs of computing the forward model, while the spectral element method with adjoint methods takes ~100 seconds for one tomographic iteration. These time measurements are from using only a single NVIDIA Tesla V100 GPU.

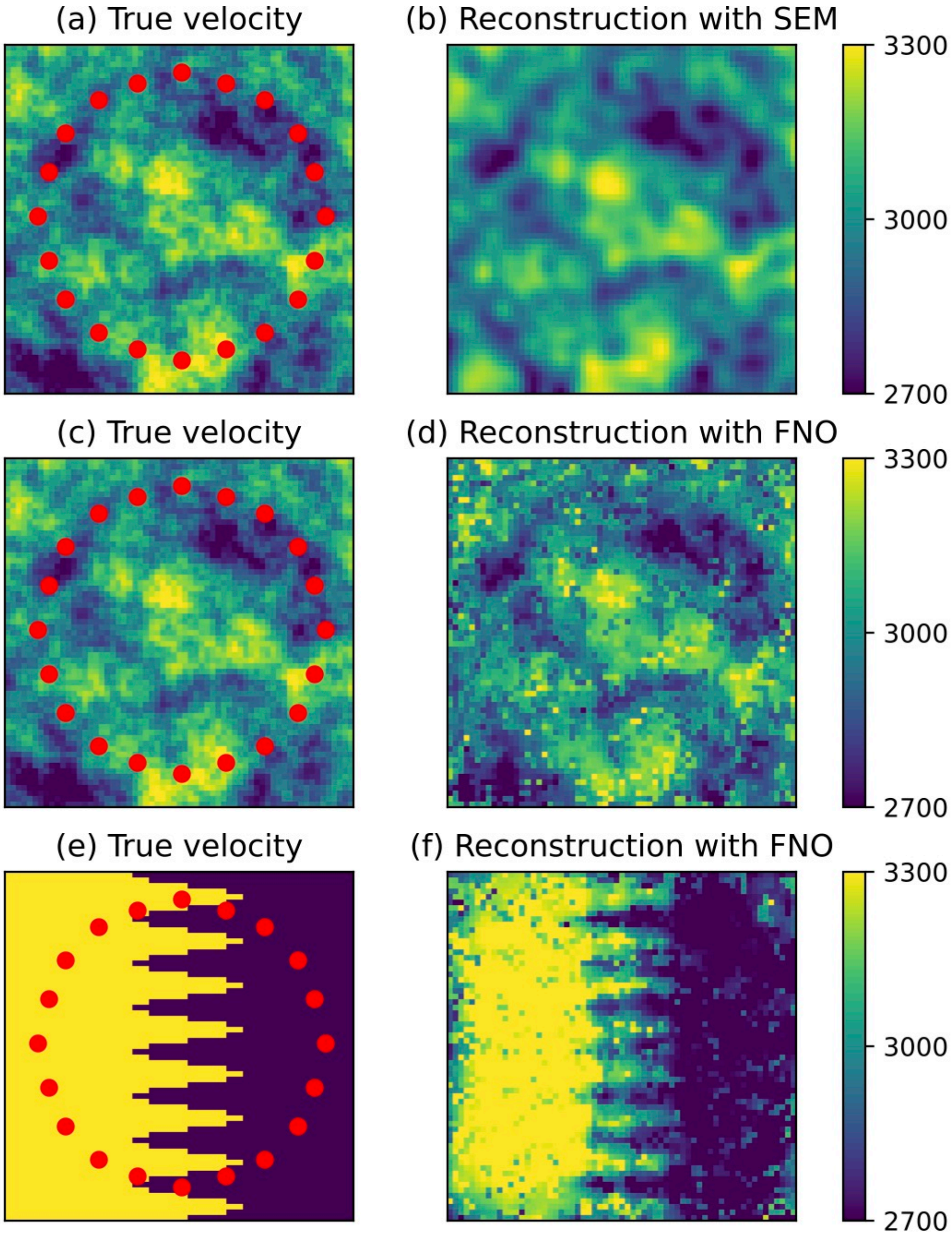

Figure 9.5: Example of a full waveform inversion using FNO. (a)(c)(e) True velocity models with source locations indicated by red circles and receivers placed at every node of the 64×64 grid (10 km×10 km region). (b) Reconstruction using SEM and adjoint tomography. (d)(f) Reconstruction using FNO as the forward model and automatic differentiation to compute gradients. No regularization is used for these experiments.

9.5 Discussion

This study presents a prototype framework for applying Neural Operators to the 2D acoustic wave equation. We anticipate that the general framework would also be suitable for the 3D elastic wave equation with relatively little modification. Indeed the FNO method was applied successfully to the Navier-Stokes equations (Li et al., 2020a), which can be more challenging to solve than the elastic wave equation. In our tests, we found that only a few thousand simulations were needed to train a FNO model, and from there, required negligible time to compute a new solution. Since FNO can be trained on lower resolution simulations and then generalize to higher resolution solutions once trained, this results in substantially faster computations than using traditional numerical methods at the full resolution.

One of the limitations of the approach is that the solutions are approximate, as seen in several of the figures. However, since this is a learning-based approach, the performance can be improved in the future by using a better model architecture, thorough tuning of hyperparameters, improving the size of the training dataset, using a more appropriate objective function, and various other factors. Additionally, as new developments within machine learning emerge in this area, they would be able to be incorporated. Thus, these performance metrics should only be viewed as a starting point. For some applications, the error may be enough of an issue and traditional numerical methods may be preferable; however for many other situations in geophysics, a reasonably accurate solution may be acceptable.

Among the most exciting benefits of our approach is that by training the FNO on random velocity models, the FNO is able to produce solutions for arbitrary velocity models. This is because FNO learns a general solution operator to the PDE, and not specifically the velocity model. This means that the model does not need to be retrained for each region. Thus, the approach offers the potential for a single FNO model to be used by the entire seismology community for any region of a similar size. While the initial cost of training a FNO and performing the training simulations may be expensive, it only needs to be done a single time for the community as a whole.

Supplementary Material

This Supplemental Material demonstrates that the misfit between the simulations using spectral element method (SEM) and the Fourier Neural Operator (FNO) is minimal.

Given a homogeneous velocity model, we have the analytical solution for the acoustic equation with Green's functions

$$\partial_t^2 G(\boldsymbol{x}, t; \boldsymbol{x_0}, t_0) - c^2 \Delta G(\boldsymbol{x}, t; \boldsymbol{x_0}, t_0) = \delta(\boldsymbol{x} - \boldsymbol{x_0})\delta(t - t_0),$$

where c is speed, δ is the Dirac delta function, and $G(\boldsymbol{x}, t; \boldsymbol{x_0}, t_0)$ gives the pressure at $(\boldsymbol{x}, t)$ that results from the unit force function applied at $(\boldsymbol{x_0}, t_0)$. In the 2D case, the Green's function is given by

$$G(x_1, x_2, t) = \frac{H\left(t - \frac{\sqrt{x_1^2 + x_2^2}}{c}\right)}{2\pi c^2 \sqrt{t^2 - \frac{x_1^2 + x_2^2}{c^2}}},$$

where H is the Heaviside step function. We can convolve a particular source time function with the Green's function to get the analytical solution.

Here we compare the analytical solution with SEM simulation and FNO simulation, as shown in Figure S1. Because the displacement is very close to zero in most time points, the relative $\ell 2$ misfit could be large due to the small denominator. However, we can see the misfit between SEM and FNO (0.239) is small compared to the misfit between SEM and analytical solutions (0.364). This shows the capability of the FNO prediction.

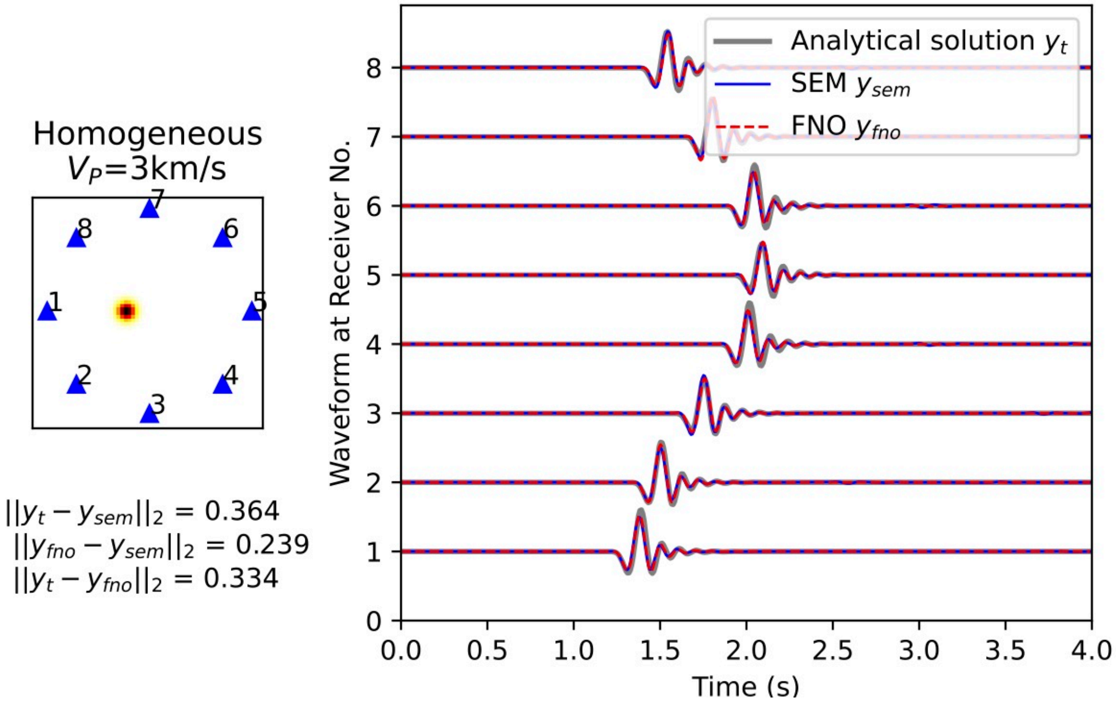

Figure 9.S1: Simulation results from a homogeneous velocity model. The left panel shows the source (red) and receiver locations (blue). The right panel shows the analytical solution (gray), the SEM simulation (blue), and the FNO prediction (red). The text in the lower left annotates the relative ℓ_2 misfit between each two methods, which shows that the FNO prediction has lower error than the SEM simulation when compared to the analytical solution.

References

Afanasiev, M., Boehm, C., Van Driel, M., Krischer, L., Rietmann, M., May, D. A., et al. (2019). Modular and flexible spectral-element waveform modelling in two and three dimensions. *Geophysical Journal International*, *216*(3), 1675–1692. https://doi.org/10.1093/GJI/GGY469

Duputel, Z., Jiang, J., Jolivet, R., Simons, M., Rivera, L., Ampuero, J. P., et al. (2015). The Iquique earthquake sequence of April 2014: Bayesian modeling accounting for prediction uncertainty. *Geophysical Research Letters*, *42*(19), 7949–7957. https://doi.org/10.1002/2015GL065402

Fichtner, A., Kennett, B. L. N., Igel, H., & Bunge, H. P. (2009). Full seismic waveform tomography for upper-mantle structure in the Australasian region using adjoint methods. *Geophysical Journal International*, *179*(3), 1703–1725. https://doi.org/10.1111/J.1365-246X.2009.04368.X

Gebraad, L., Boehm, C., & Fichtner, A. (2020). Bayesian Elastic Full-Waveform Inversion Using Hamiltonian Monte Carlo. *Journal of Geophysical Research: Solid Earth*, *125*(3). https://doi.org/10.1029/2019JB018428

Graves, R., & Pitarka, A. (2016). Kinematic ground-motion simulations on rough faults including effects of 3D stochastic velocity perturbations. *Bulletin of the Seismological Society of America*, *106*(5), 2136–2153. https://doi.org/10.1785/0120160088

Kingma, D. P., & Ba, J. L. (2014). Adam: A Method for Stochastic Optimization. *3rd International Conference on Learning Representations, ICLR 2015 - Conference Track Proceedings*. https://doi.org/10.48550/arxiv.1412.6980

Lee, E. J., Chen, P., Jordan, T. H., Maechling, P. B., Denolle, M. A. M., & Beroza, G. C. (2014). Full-3-D tomography for crustal structure in Southern California based on the scattering-integral and the adjoint-wavefield methods. *Journal of Geophysical Research: Solid Earth*, *119*(8), 6421–6451. https://doi.org/10.1002/2014JB011346

Li, Z., Kovachki, N., Azizzadenesheli, K., Liu, B., Bhattacharya, K., Stuart, A., & Anandkumar, A. (2020a). Fourier Neural Operator for Parametric Partial Differential Equations. https://doi.org/10.48550/arxiv.2010.08895

Li, Z., Kovachki, N., Azizzadenesheli, K., Liu, B., Bhattacharya, K., Stuart, A., & Anandkumar, A. (2020b). Multipole Graph Neural Operator for Parametric Partial Differential Equations. *Advances in Neural Information Processing Systems*, *2020-December*. https://doi.org/10.48550/arxiv.2006.09535

Li, Z., Kovachki, N., Azizzadenesheli, K., Liu, B., Bhattacharya, K., Stuart, A., & Anandkumar, A. (2020c). Neural Operator: Graph Kernel Network for Partial Differential Equations. https://doi.org/10.48550/arxiv.2003.03485

Moseley, B., Nissen-Meyer, T., & Markham, A. (2020). Deep learning for fast simulation of seismic waves in complex media. *Solid Earth*, *11*(4), 1527–1549. https://doi.org/10.5194/SE-11-1527-2020

Moseley, B., Markham, A., & Nissen-Meyer, T. (2021). Finite Basis Physics-Informed Neural Networks (FBPINNs): a scalable domain decomposition approach for solving differential equations. Retrieved from http://arxiv.org/abs/2107.07871

Rodgers, A. J., Pitarka, A., Anders Petersson, N., Sjogreen, B., McCallen, D. B., & Abrahamson, N. (2019). Broadband (0-5 Hz) fully deterministic 3D ground-motion simulations of a magnitude 7.0 Hayward fault earthquake: Comparison with empirical ground-motion models and 3D path and site effects from source normalized intensities. *Seismological Research Letters*, *90*(3), 1268–1284. https://doi.org/10.1785/0220180261

Smith, Jonathan D., Azizzadenesheli, K., & Ross, Z. E. (2021). EikoNet: Solving the Eikonal Equation with Deep Neural Networks. *IEEE Transactions on Geoscience and Remote Sensing*, *59*(12), 10685–10696. https://doi.org/10.1109/TGRS.2020.3039165

Smith, Jonathan D., Ross, Z. E., Azizzadenesheli, K., & Muir, J. B. (2022). HypoSVI: Hypocentre inversion with Stein variational inference and physics informed neural networks. *Geophysical Journal International*, *228*(1), 698–710. https://doi.org/10.1093/gji/ggab309

Tape, C., Liu, Q., Maggi, A., & Tromp, J. (2009). Adjoint tomography of the southern california crust. *Science*, *325*(5943), 988–992. https://doi.org/10.1126/SCIENCE.1175298

Virieux, J., & Operto, S. (2009). An overview of full-waveform inversion in exploration geophysics. *Geophysics*, *74*(6). https://doi.org/10.1190/1.3238367

Wang, X., & Zhan, Z. (2020). Seismotectonics and Fault Geometries of the 2019 Ridgecrest Sequence: Insight From Aftershock Moment Tensor Catalog Using 3-D Green's Functions. *Journal of Geophysical Research: Solid Earth*, *125*(5), e2020JB019577. https://doi.org/10.1029/2020JB019577

Xiao, C., Deng, Y., & Wang, G. (2021). Deep-Learning-Based Adjoint State Method: Methodology and Preliminary Application to Inverse Modeling. *Water Resources Research*, *57*(2). https://doi.org/10.1029/2020WR027400

Ye, L., Lay, T., Kanamori, H., & Rivera, L. (2016). Rupture characteristics of major and great ($Mw \geq 7.0$) megathrust earthquakes from 1990 to 2015: 2. Depth dependence. *Journal of Geophysical Research: Solid Earth*, *121*(2), 845–863. https://doi.org/10.1002/2015JB012427

Zhu, W., Xu, K., Darve, E., & Beroza, G. C. (2021). A general approach to seismic inversion with automatic differentiation. *Computers & Geosciences*, *151*, 104751. https://doi.org/10.1016/J.CAGEO.2021.104751

C h a p t e r 1 0

RAPID SEISMIC WAVEFORM MODELING AND INVERSION WITH U-SHAPED NEURAL OPERATORS

Yang, Y., Gao, A. F., Azizzadenesheli, K., Clayton, R. W., & Ross, Z. E. (2023). Rapid Seismic Waveform Modeling and Inversion With Neural Operators. *IEEE Transactions on Geoscience and Remote Sensing*, 61, 1–12. https://doi.org/10.1109/TGRS.2023.3264210

Abstract

Seismic waveform modeling is a powerful tool for determining earth structure models and unraveling earthquake rupture processes, but it is usually computationally expensive. We introduce a scheme to vastly accelerate these calculations with a recently developed machine learning paradigm called the neural operator. Once trained, these models can simulate a full wavefield at negligible cost. We use a U-shaped neural operator to learn a general solution operator to the 2D elastic wave equation from an ensemble of numerical simulations performed with random velocity models and source locations. We show that full waveform modeling with neural operators is nearly two orders of magnitude faster than conventional numerical methods, and more importantly, the trained model enables accurate simulation for velocity models, source locations, and mesh discretization distinctly different from the training dataset. The method also enables convenient full-waveform inversion with automatic differentiation.

10.1 Introduction

The seismic wave equation relates displacement fields to external forces and the density and elastic structure in the Earth. Solutions to the wave equation form the basis of ground shaking simulations of large earthquakes (R. Graves & Pitarka, 2016; R. W. Graves & Pitarka, 2010; Rodgers et al., 2019) and full waveform inversion for Earth's structure (Fichtner, Kennett, et al., 2009; Gebraad et al., 2020; Tape et al., 2009). Due to the highly heterogeneous nature of the Earth, as exemplified by subduction zones and sedimentary basins, there are no exact analytical solutions for these wavefields. Instead, approximate solutions are made possible by approximating derivatives through discretized spatial and time or frequency domains. Finite difference methods (FDM) have been popular since the early 80s due to their relatively straightforward formulation (Igel et al., 2002; Kelly et al., 1976; Olsen, 2000). The spectral-element method (SEM), a particular case of finite element methods (FEM), which was introduced to seismology in early 2000s, combined the flexibility of FEMs with the accuracy of spectral approaches (Fichtner, Igel, et al., 2009; Komatitsch & Tromp, 2002a, 2002b; Liu & Gu, 2012). These numerical solvers impose a tradeoff between resolution and computation speed, with the computational cost proportional to the fourth power of frequency (Pell et al., 2013). Thus, the cost of wave simulation is a major barrier to using full-waveform techniques for seismic inversion and updating models of the subsurface with new data.

A number of machine learning-based methods have been proposed in the past few years to provide a faster alternative for tackling seismological problems such as signal denoising (Birnie et al., 2021; L. Yang et al., 2022; Zhu et al., 2019), event detection (Mousavi et al., 2020; Ross et al., 2018; Zhu & Beroza, 2019), and phase association (Ross et al., 2019; Zhu et al., 2022). Deep neural networks have also recently been used to solve partial differential equations (PDEs), such as the Eikonal equation and wave equation (Ben Moseley et al., 2020, 2021; Benjamin Moseley et al., 2018; Siahkoohi et al., 2019; Smith et al., 2021). These approaches to solving PDEs offer not only speedup in computational capabilities, but also low-memory overhead, differentiability, and on-demand solutions. Such advantages facilitate deep learning being used for seismic inversion (Kazei et al., 2021; Rasht-Behesht et al., 2022; Sun & Alkhalifah, 2020; Zhang & Curtis, 2021; Zhu et al., 2021). However, one major limitation of these approaches is that the solutions generated by these models are dependent on the specific spatial and temporal discretization in the numerical simulation training set.

Recently, a paradigm named ‘neural operator’ was developed to address the mesh-dependent shortcoming of classical neural networks by creating a single deep learning model that can be applied to different discretizations (Bhattacharya et al., 2020; Z. Li et al., 2020b, 2020c; Lu et al., 2019). This is made possible because neural operators can provably learn mappings between infinite-dimensional function spaces (Kovachki et al., 2021) and therefore are suitable for learning general solution operators to PDEs, which are valid even when the PDE coefficients (e.g. elastic properties) are varied. Since first introduced (Lu et al., 2019), a variety of neural operator models have been developed. In particular, the Fourier neural operator (FNO) is a model that uses the fast Fourier transform as an integral operator, and has been shown to outperform other neural operators in terms of efficiency and accuracy (Z. Li et al., 2020a). The FNO has been applied to many types of scientific problems including weather forecasting (Pathak et al., 2022), CO_2 sequestration (Wen et al., 2022), and coastal flooding (Jiang et al., 2021).

Within the domain of seismology, neural operators were also recently used to learn general solution operators to the 2-D acoustic wave equation, a simplified case of the elastic wave equation (Y. Yang et al., 2021). This pilot study demonstrated that it was possible for a single FNO model to predict a complete wavefield given an arbitrary velocity model and mesh discretization. The success of this limited case highlights the potential of these methods, however, extending the method from the acoustic wave equation to the elastodynamic case requires substantially increased model complexity. By comparison with neural networks, FNO is not considered to be a deep architecture, and is most analogous to the fully-connected neural networks employed heavily until the 2010s. A U-shaped neural operator (U-NO) was recently proposed to enable very deep neural operators and facilitate fast training, data efficiency, and hyperparameter selection robustness (Rahman et al., 2022).

In this paper, we apply the U-NO architecture to full seismic waveform modeling. We train a U-NO model to learn a general solution operator to the 2D elastic wave equation and demonstrate that the trained model enables fast and accurate simulation for source locations, velocity structures and mesh discretization beyond the training dataset. The trained U-NO also allows for efficient full-waveform inversion with automatic differentiation.

10.2 Methods

10.2.1 Neural operator learning

Operators are maps between function spaces, and the purpose of operator learning is to learn the operator given a dataset of input-output pairs. In seismology, it is common to write solutions to the wave equation, $U(x)$ in terms of a linear integral operator acting on a source function, $A(x)$,

$$U(x) = \int G(x,y)A(y)dy, \tag{10.1}$$

where $x \in \mathbb{R}^4$ is the physical domain and G is a so-called Green's function defined for a particular velocity model. Equation 10.1 holds so long as the velocity model is not varied because the wave equation remains a linear operator.

Instead, if we consider the case where the input function, $A(x)$, is a velocity model, the solution operator, $\mathcal{L}$, relating this to $U(x)$ is nonlinear and cannot be written in the form of (10.1), $U(x) = (\mathcal{L}\,A)(x)$. The most general version of the nonlinear solution operator $\mathcal{L}$ for the elastic wave equation is not known in closed form.

Neural operators are a class of models that aim to solve this problem, as they provably can learn a wide array of nonlinear operators. Their basic form consists of a composition of linear operators with nonlinear activations. More specifically, a neural operator with L layers can be written as:

$$\begin{gathered} v_0(x) = (P\,A)(x), \\ v_{l+1}(x) = \sigma\big(W_l v_l(x) + \textstyle\int \kappa_l(x,y)v_l(y)dy\big), l = 0,..,L-1 \\ U(x) = (Q\,v_L)(x), \end{gathered} \tag{10.2}$$

where v_l is the input function at the l^{th} layer, P is a pointwise operator that lifts the input function to a higher dimensionality, Q is a pointwise operator that projects the function back to the desired output dimensionality, W_l is a linear pointwise transformation that can keep track of non-periodic boundary behavior, σ is a pointwise nonlinear activation operator, and κ_l is a kernel function that acts along with the integral as a global linear operator.

A neural operator is parameterized by P, Q, W_l, and κ_l. A critical aspect of this class of models is that these parameters are independent of the numerical discretization of the physical domain, i.e. they are shared across all possible discretizations in a similar way that in convolutional networks, the parameters are shared across neurons. It is this property that allows for the learning of maps between infinite dimensional function spaces, as the discretization can be chosen dynamically at inference time independently of what was used for training.

If we are given a dataset of N numerical simulations, $\{A_i, U_i\}_{i=1}^{N}$, where the A_i are chosen to span the range of the expected function space, we can train a neural operator in a supervised fashion to map from arbitrary A into U.

Due to the expense of evaluating integral operators, neural operators may lack the efficiency of convolutional or recurrent neural networks in finite-dimensional settings. The FNO was proposed to mitigate this difficulty through the fast Fourier transform (Z. Li et al., 2020a). The kernel integral operator in (10.2) can be considered a convolution operator, defined in Fourier space as:

$$\int \kappa_l(x, y) v_l(y) dy = \mathcal{F}^{-1}\big(\mathcal{F}(\kappa_l) \cdot \mathcal{F}(v_l)\big), \tag{10.3}$$

where $\mathcal{F}$ and $\mathcal{F}^{-1}$ denote Fourier Transform and its inverse, respectively. However, FNO imposes that each layer is a map between functions spaces with identical domain spaces, which may cause a large memory usage. The U-NO, an analogy to the U-net architectures, was proposed to allow progressively transforming the input function space with respect to a sequence of varying domains (Rahman et al., 2022; Ronneberger et al., 2015). After the lifting operator P, a sequence of L_1 non-linear integral operators G_i is applied to v_0 and map the input to a set of functions with decreasing dimensional domain. Then a sequence of L_2 non-linear integral operators G_i is applied to v_{L_1+1} and map the input to a set of functions with increasing dimensional domain before the projection operator Q. Skip connections (Ronneberger et al., 2015) are included to add vector-wise concatenation of v_{L_1+i} and v_{L_1-i}. The contracting and expanding parts are symmetric. The architecture of the U-NO used in this study is illustrated in Figure 10.1, and we refer the interested readers to the references (Bhattacharya et al., 2020; Z. Li et al., 2020b, 2020c, 2020a; Lu et al., 2019; Rahman et al., 2022) for more details.

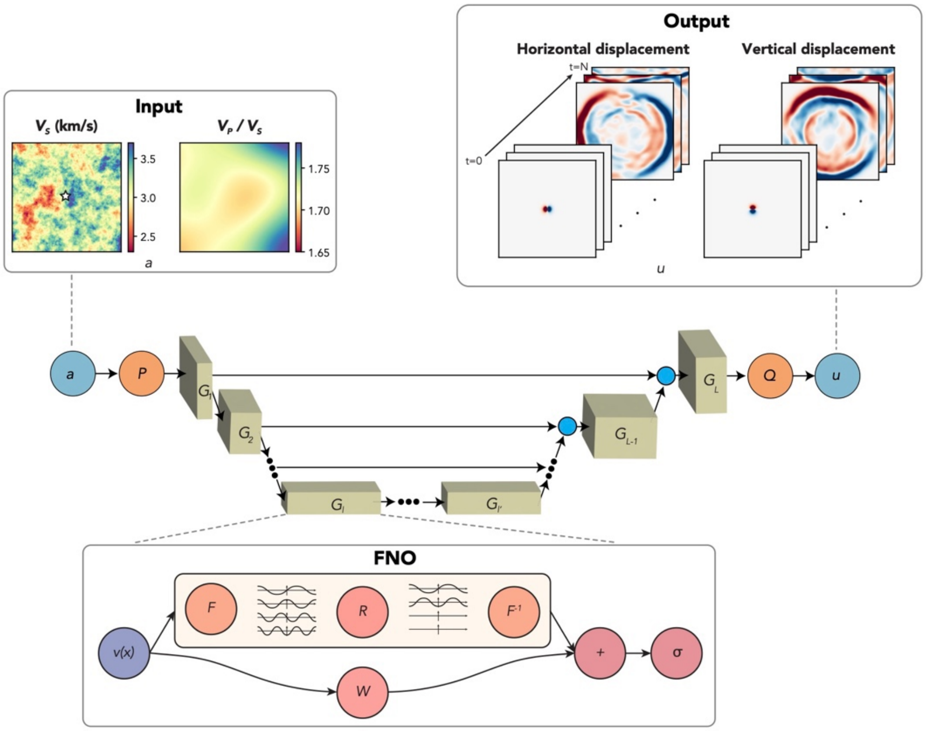

Figure 10.1: Overview of our method for solving the elastic wave equation with neural operators. The inputs, *a*, to the U-NO model are the P- and S-wave velocity (V_P, V_S) model and the source location (indicated by the white star). V_P is calculated from V_S and V_P/V_S, examples of which are shown in the upper left panel. The outputs, *u*, are the horizontal and vertical displacements at each time step, examples of which are shown in the upper right panel. In the middle panel showing the U-NO architecture, orange circles *P* and *Q* denote point-wise operators, rectangles *G* denote general operators, and smaller blue circles denote concatenations in function space. The lower panel shows the architecture of each FNO layer, where *v* is the input of the layer, *F* and F^{-1} are Fourier transform and its inverse, respectively, R and W are a linear transform, and σ is the nonlinear activation function. The expansion (or contraction) factors in equation (5) are set as: $c^s_{1,2} = \frac{3}{4}, c^s_{3,4} = \frac{1}{2}, c^s_{5,6} = 2, c^s_{7,8} = \frac{4}{3}, c^t_1 = \frac{3}{4}, c^t_2 = \frac{2}{3}, c^t_{3,4} = \frac{1}{2}, c^t_{5,6} = 2, c^t_7 = \frac{3}{2}, c^t_8 = \frac{4}{3}, c^c_{1,2,3,4} = 2, c^c_{5,6,7,8} = \frac{1}{2}$.

10.2.2 Numerical simulation

We set up a training dataset of random source locations, S-wave velocity (V_S) models, and P- to S-wave velocity ratios (V_P/V_S). We define the velocity model on a 64 × 64 mesh with 0.16 km grid spacing. The source is set as an isotropic explosive source randomly distributed on the mesh. The V_S has an average background of 3 km/s and perturbed by random fields with a von Kármán covariance function with the following parameters: Hurst exponent κ=0.5, correlation length a_x=a_y=8 grids, and the fractional magnitude of the fluctuation ε=10% background velocity. The power spectral density function of the von Kármán type random field follows a power law (fractal randomness) and can accurately represent the distribution of Earth's heterogeneity (Nakata & Beroza, 2015). The V_P/V_S is simplified to an average background of 1.732 perturbed by a smooth Gaussian random field with the following parameters: correlation length λ=32 grids, standard deviation σ=2% background. This work, as our very first experiment to evaluate the feasibility of solving 2D elastic wave equations, wants to focus on the parameters that the wavefield is most sensitive to. Therefore, we use the empirical relation between density and V_S to compute the density (Brocher, 2005). Other input parameters such as density and attenuation may be explored in future work. A total of 20,000 random sets of models are generated and each of them is input to a GPU based 2D finite difference code in Cartesian coordinates to simulate the 2-D displacement field (D. Li et al., 2014). For simulation, the top boundary is set with a free-surface boundary condition and the other three edges have absorbing boundary conditions. A total of 4-sec wavefield with a time step of 0.01 sec and a major frequency content up to 6 Hz is simulated. Each simulation takes about 1.23 sec with a GPU memory usage of 0.3 GB.

10.2.3 U-NO model training

We developed a framework that applies U-NO to the 2D elastic wave equation. The architecture is depicted schematically in Figure 10.1. U-NO takes the source location and V_P and V_S as inputs, where V_P is calculated from V_S and V_P/V_S. V_P and V_S are then passed through a point-wise lifting operator. A sequence of non-linear integral operators (encoders) are applied that gradually contract the physical domain size after each inverse Fourier transform step, while simultaneously increasing the number of channels in the co-domain.

These operators are followed by a sequence of non-linear integral operators (decoders) that progressively expand the physical domain, and decrease the number of channels. Finally, a point-wise projection operator leads to the output function (Rahman et al., 2022). The output of the U-NO model is the complete horizontal and vertical displacement wavefield function over the medium domain, which can be queried at any mesh points desired, regardless of the input and output training mesh used.

We describe the detailed parameters used in U-NO below following the notations in Figure 10.1. The goal is to learn an operator mapping from the input function a to the output function u. The training is on an input mesh of $X_{\text{in}} \times Y_{\text{in}} \times T_{\text{in}}$ and an output mesh of $X_{\text{out}} \times Y_{\text{out}} \times T_{\text{out}} \times C_{\text{out}}$, where $X_{\text{in}} = Y_{\text{in}} = X_{\text{out}} = Y_{\text{out}} = 64$, $T_{\text{in}} = 3$ representing source, V_S, and V_P/V_S distribution on the mesh, $T_{\text{out}} = 128$ for 32 Hz data output, and $C_{\text{out}} = 2$ representing two displacement components (horizontal and vertical). This work applies the U-NO architecture designed for mapping between 3-D spatio-temporal function domains (x, y, t) without any recurrent composition in time (Rahman et al., 2022). The fourth dimension C_{out} of the output function u can be created in the last step through the projection operator Q. Constructing the operator to learn the mapping between 3-D spatio-temporal function domains:

$$G: \{a: [0,1]^2 \times [0, T_{\text{in}}] \to \mathbb{R}^{d_A}\} \to \{u: [0,1]^2 \times [0, T_{\text{out}}] \to \mathbb{R}^{d_U}\}. \tag{10.4}$$

The operators $\{G_i\}_{i=0}^{L}$ as shown in Figure 10.1 that are used to construct the U-NO are defined as:

$$G_i: \{v_i: [0, \alpha_i]^2 \times \mathcal{T}_i \to \mathbb{R}^{d_{vi}}\} \to \left\{v_{i+1}: [0, c_i^s \alpha_i]^2 \times c_i^t \mathcal{T}_i \to \mathbb{R}^{c_i^c d_{vi}}\right\}, \tag{10.5}$$

where $[0, \alpha_i]^2 \times \mathcal{T}_i$ is the domain of the input function v_i to the operator G_i, and c_i^s, c_i^t, and c_i^c are the expansion or contraction factors for the spatial domain, temporal domain, and co-domain for i^{th} operator, respectively. Note that $\mathcal{T}_0 = [0, T_{\text{in}}]$, $\alpha_0 = \alpha_{L+1} = 1$, and $\mathcal{T}_{L+1} = [0, T_{\text{out}}]$. In this work we set the number of layers to L=8. The details of the expansion and contraction factors c_i^s, c_i^t, and c_i^c are in Figure 10.1. The lifting operator P to convert the input to a higher dimension channel space is a fully-connected neural network with channel number $d_0 = 16$. The projection operator Q to the output domain is also a fully connected neural network. The activation function used in each FNO block is the Gaussian Error Linear Unit (GELU) (Hendrycks & Gimpel, 2016).

With the simulation dataset and the U-NO design, we train the U-NO model in a supervised manner with the objective of learning the general solution operator to the wave equation for arbitrary inputs. We divide the training dataset into 90% training and 10% validation. The model is trained with a batch size of 8. After hyperparameter tuning, the loss function we use in model training is the 90% relative L1 loss plus 10% relative L2 loss. The incorporation of L1-norm loss is more resistant to outliers. We use an Adam optimizer (Kingma & Ba, 2014) with a learning rate of 10^{-3} and a weight decay of 10^{-5}. We trained for 100 epochs, which takes approximately 40 minutes per epoch using a single NVIDIA Tesla V100 GPU with 24GB memory usage. A 70% of loss decrease is achieved in the first 10 epochs. Once the U-NO model is trained, the model parameters require GPU usage of 3.8 GB and the time for an evaluation on a new source and velocity model takes only 0.02 sec with GPU usage of 0.9 GB.

10.3 Results

10.3.1 The number of simulations needed for training

Once completely trained, the U-NO model can be evaluated on a new input with very little computational cost (0.02 sec compared to the FDM runtime of 1.23 sec). The number of training simulations is the main factor in the computational cost. In the training process, we split the entire training dataset to 90% for training and 10% for validation. We test the performance of the model on the velocity models out of the training data set. We can see that the U-NO model trained on a dataset of 5000 simulations can already predict the major phase arrivals, while increasing the dataset size from 5000 simulations to 20000 provides better fit to the amplitudes (Figure 10.2). With a training dataset of 20000 simulations, the validation and training loss are very close, indicating there is no overfitting of the training data.

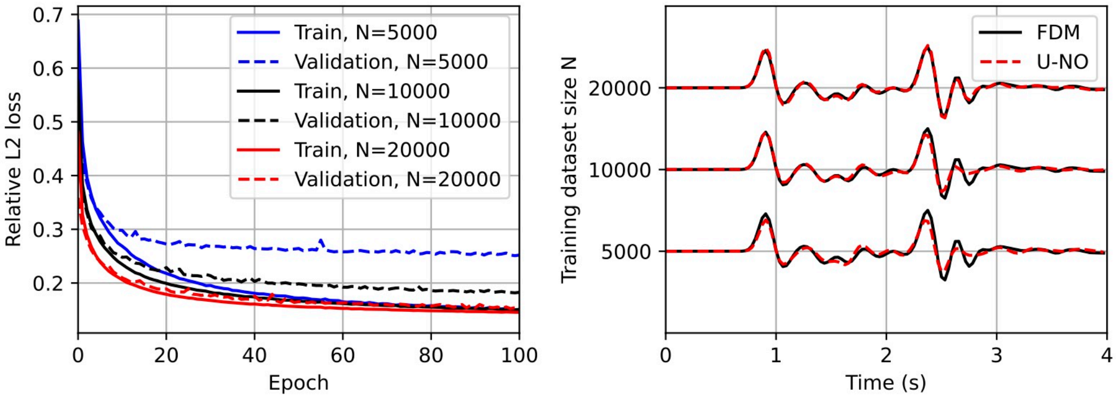

Figure 10.2: Model performance as a function of the number of training samples. Left panel: relative L2 loss curves for the training and validation data. Right panel: Example of simulated waveform comparison between FDM (black solid) and U-NO (red dashed). N means the number of simulations in the training dataset, including 90% for training and 10% for validation.

10.3.2 Generalizability to arbitrary velocity structure or discretization

The U-NO model is trained on random velocity models generated with the von Karman correlation function, which can best mimic the Earth's heterogenous velocity distribution (Mai & Beroza, 2002; Nakata & Beroza, 2015). We show by example that the U-NO model, although trained on random velocity models with some certain parameters, is applicable to arbitrary velocity models. These outcomes are in fact expected from theoretical grounds because most physical functions can be approximated to arbitrary accuracy by random fields.

Our first example is with velocity models from a von Karman-type random distribution, but with a different covariance function than the one used for the training data. We increase the roughness of the velocity structure by a factor of four by decreasing the correlation length of V_S and V_P/V_S to only one-fourth that of the training data. As shown in Figure 10.3, the wavefield snapshot has more coda than with the smoother models because of the scattering from increased heterogeneity. However, the coda waves are well modeled by U-NO when compared to the ground truth simulation by FDM.

The velocity models used in the training data do not have coherent structures with discontinuities as in the real Earth, but wavefields for such models can still be simulated with our method. As mentioned before, this is because discontinuous functions can be approximated to arbitrary accuracy by random fields. Figure 10.4 shows a simple model with a dipping 'slab' embedded in a homogeneous background. The slab has 20% higher V_S and 5% lower V_P/V_S. The wavefield snapshots show that the reflections from the high velocity anomaly are clearly predicted by U-NO. A more complex example is shown in Figure 10.5, where a random subpanel of the Marmousi model, a 2D velocity model with complex vertical and horizontal structures used in exploration studies (Versteeg, 2012), is used. The reflected and refracted waves are very complicated due to the presence of folding and faulting, but the U-NO predictions still closely approximate the numerical solutions (Figure 10.5).

One of the most important advantages of a neural operator compared with a neural network is its mesh-free nature, since it intrinsically learns the mapping between function spaces. A model trained on a particular mesh can be evaluated on any other mesh, even at finer spacing. The Fourier layers may learn from and evaluate functions on any discretization because parameters are directly learned in Fourier space and resolving the functions in physical space is simply projecting on the basis (Z. Li et al., 2020a). The example in Figure 10.6 shows the U-NO trained on a grid of 64*64 nodes applied to an input velocity model with 160*160 nodes. Here both the input velocity model and the output wavefield can be seen at a much higher resolution, yet U-NO provides comparable prediction with the FDM solver. Note that if the resolution is increased by a factor of 2, a grid-based numerical solver like FDM takes about 6 times greater computational time; however, the evaluation using U-NO takes only about 2.5 times longer, providing additional computational efficiency.

We evaluate the overall generalization performance of the trained U-NO by performing a thousand random realizations on each of these cases. The distribution of the relative L2-norm misfit and cross-correlation coefficient are plotted in Figure 10.7. In the case of the Marmousi model, the extended tail of the histogram is attributed to the model's imbalanced complexity.

In general, however, we see a very high cross-correlation coefficient (>0.95) between U-NO prediction and ground truth, confirming its robust generalizability.

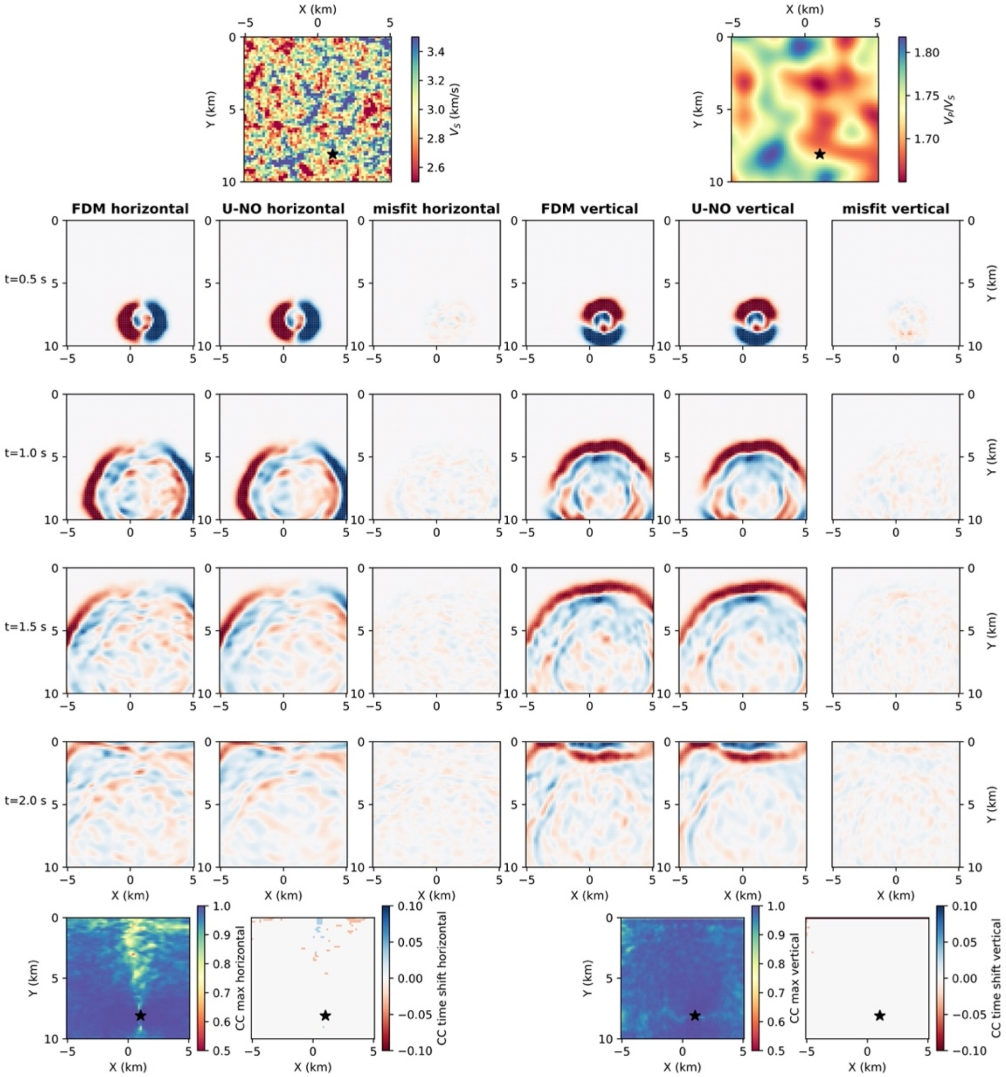

Figure 10.3: Model generalization experiments 1: random fields of Vs and Vp/Vs model with 4-times roughness of the training data. The top row shows the Vs and Vp/Vs. From the second row to the fifth row, the wavefield snapshots at 0.5 s-2.0 s are shown. From left to right, the first three columns show the horizontal displacement of the FD simulation, U-NO prediction, and their misfit in the same color scale. The latter three columns show the vertical component. The horizontal and vertical displacement waveforms at each grid are cross-correlated between FD and U-NO, with the maximum cross-correlation value and its

associated time shift shown in the bottom row. For this case, the relative L2 loss of the U-NO simulation is 0.182.

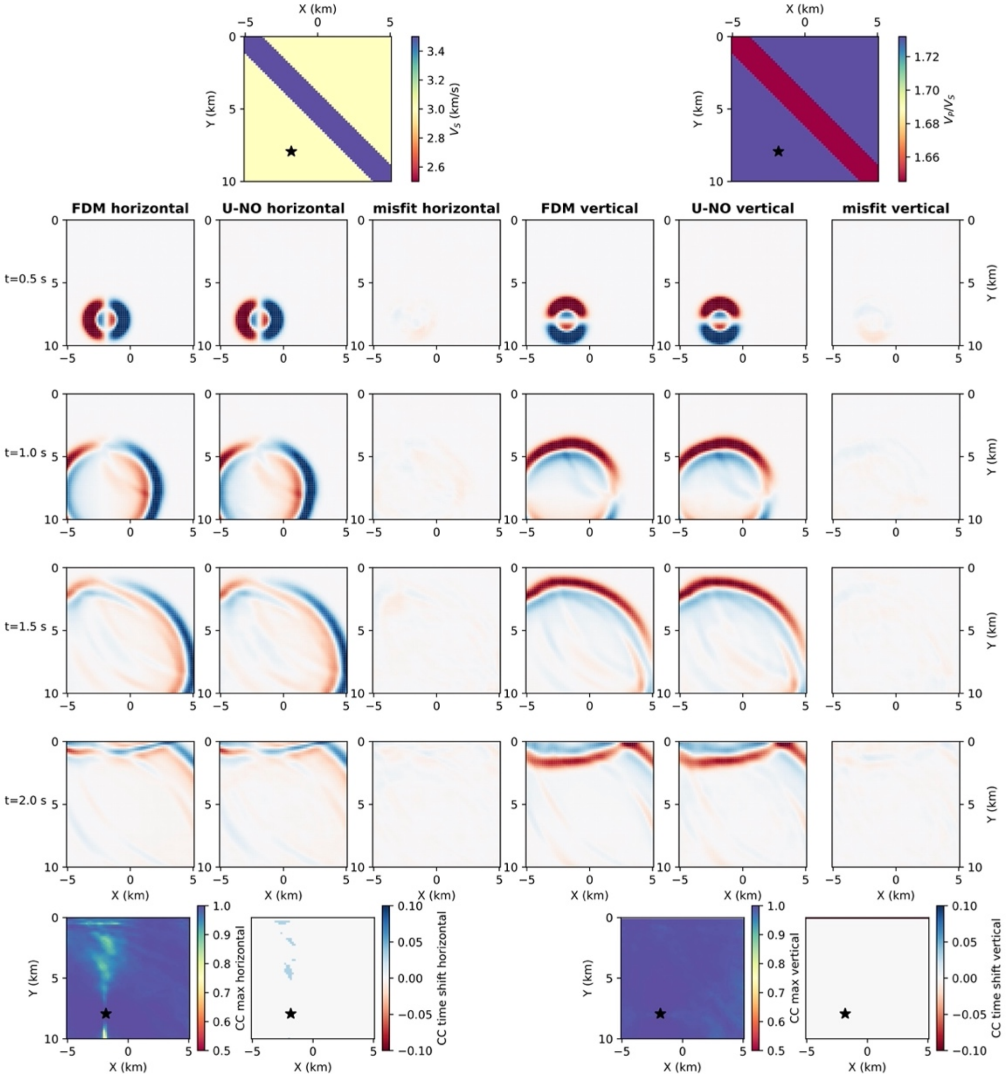

Figure 10.4: Model generalization experiments 2: Similar as Figure 10.3, but for a homogeneous background model embedded with a ‘slab’ with 20% higher Vs and 5% lower Vp/Vs. Relative L2 loss of the U-NO simulation is 0.090.

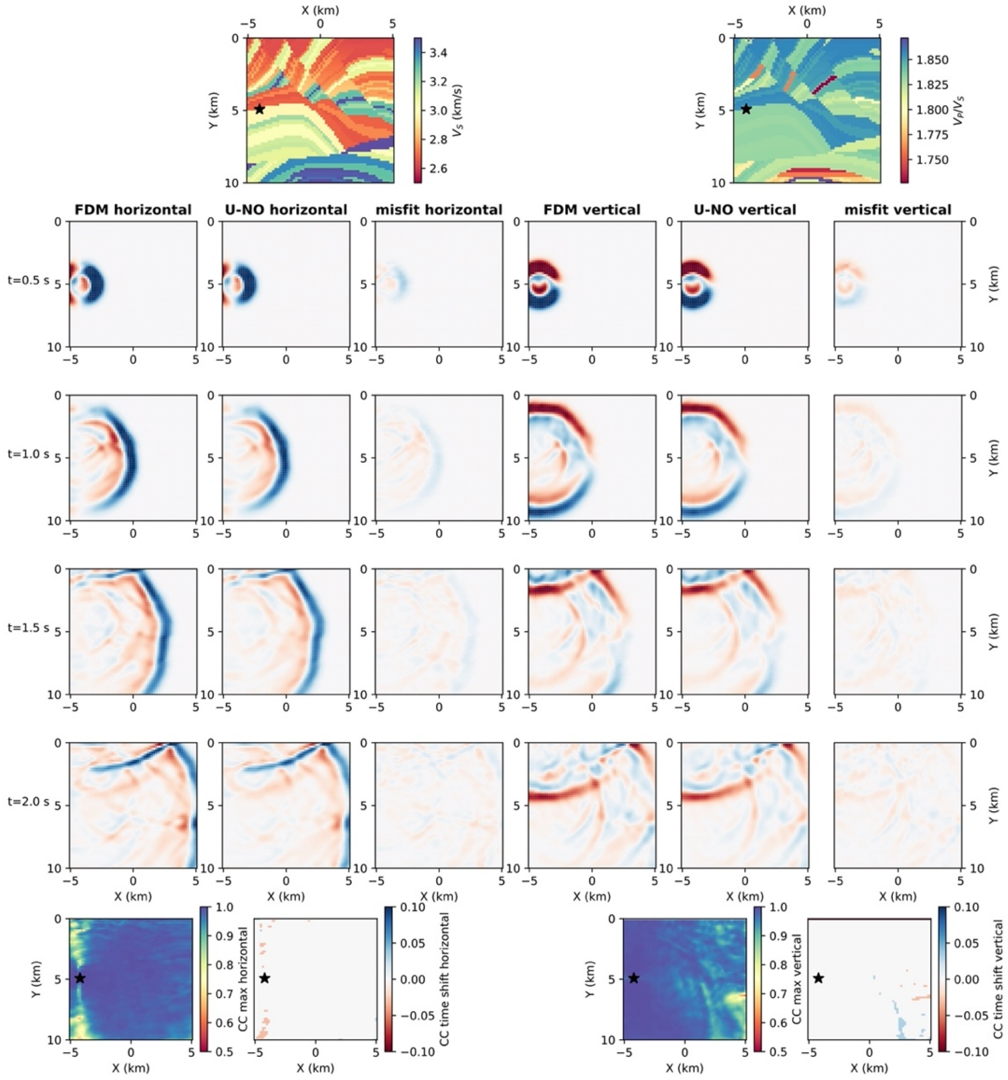

Figure 10.5: Model generalization experiments 3: Similar as Figure 10.3, but for a random subpanel from the Marmousi model. The velocity perturbation range is normalized to 30% of the average velocity. Relative L2 loss of the U-NO simulation is 0.225.

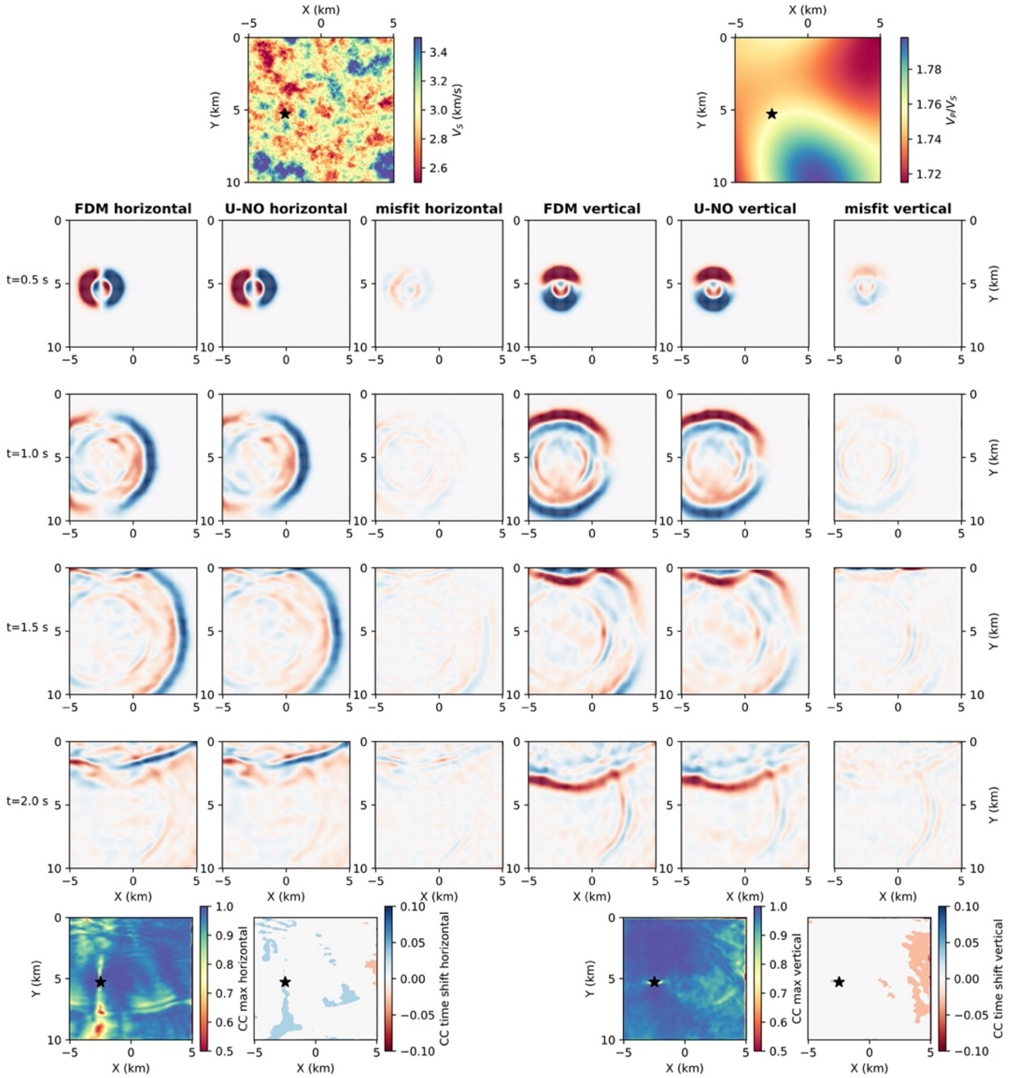

Figure 10.6: Model generalization experiments 4: Similar as Figure 10.3, but Vp and Vs model mesh discretization is increased from 64*64 to 160*160. Relative L2 loss of the U-NO simulation is 0.385.

10.3.3 Application to full-waveform inversion

One of the most important applications of wavefield simulations is in full-waveform inversion (FWI), which uses the full recorded waveform to image the Earth’s interior. The adjoint-state method is the traditional approach for computing the gradients of an objective function with respect to parameters of interest (Fichtner, Kennett, et al., 2009; Tape et al., 2009). Neural operators are differentiable by design, which enables gradient computation with reverse-mode automatic differentiation. It has been shown that automatic differentiation and the adjoint approach are mathematically equivalent (Zhu et al., 2021). Hence, the trained U-NO model allows for convenient FWI and the associated speed and accuracy should depend only on the forward modeling part.

We demonstrate the inversion performance using the velocity structure of random subpanels in the Marmousi model (Versteeg, 2012). The synthetic waveform data are simulated with FDM (D. Li et al., 2014) using 14 sources distributed in a ring shape. In Figure 10.8, we use the true source location, receivers on all 64*64 grids and noise-free waveform data; the goal here is not to demonstrate resolution, but rather the computational accuracy of the method. We then invert for V_P and V_S simultaneously by starting with homogeneous initial V_P and V_S models and forward propagating the wavefield with the U-NO for each source. The misfit is defined by the mean square error between the forward modeled and true wavefield. The gradient of the misfit with respect to V_P and V_S can be computed through automatic differentiation. V_P and V_S are then iteratively updated with gradient descent for 100 iterations using the Adam optimizer (Kingma & Ba, 2014) with a learning rate of 0.01. Each iteration takes only about 1.4 sec by taking advantage of U-NO forward computation. The results in Figure 10.8 show a relative L2-norm misfit between the true and inverted model of only 3%. This successful inversion, in turn, further validates the accuracy of forward modeling with U-NO.

Besides the fact that the inversion target velocity model is quite different from the smooth random fields in the training dataset, this experiment itself is difficult due to conventional problems in full-waveform inversion, such as cycle skipping (multiple local maxima in the least-squares misfit function). We also show that if we only use 64 receivers on the surface, the inversion results in the region with ray path coverage are still reasonably accurate (Figure 10.9). Inversion with a biased homogenous initial model is also capable of producing relatively accurate results (see Supplementary Materials).

10.4 Discussion and conclusions

We use the relative L2 loss between the FDM and U-NO predictions to evaluate the performance of the trained model for generalization. The relative L2 loss is defined as the L2-norm of the difference between the prediction and ground truth divided by the L2-norm of the ground truth. This ratio is used to evaluate the performance of the trained model. When using the same mesh discretization as the training data, the relative L2 loss is around 10–20 percent, but this number rises to 30–40 percent when the tests are performed on finer grids (Figure 10.7). These values are misleading, however, because the relative L2 loss imposes equal weights to the entire sparse matrix of waveforms that is dominated by small amplitudes close to 0. Alternatively, the cross-correlation coefficient is a quantity that is more sensitive to the seismic phases with amplitudes larger than background noise. A cross-correlation coefficient larger than 0.95 suggests the coherence of the U-NO prediction is excellent, even for the scenarios with large relative L2 loss (Figure 10.7). In addition, the FWI results confirm that the large L2 loss is not so important since even challenging models can still be properly recovered (Figure 10.8).

Besides the more than an order of magnitude higher speed, the most important advantage of the neural operator-based full waveform modeling is its generalizability to arbitrary velocity models or discretization. This is because the neural operator learns a general solution operator to the wave equation instead of a specific instance of input velocity models. Once the neural operator is trained, it can be used by the entire seismology community for any region of a similar size without the need for retraining. Since the full waveform modeling with a neural operator has easily accessible gradients for convenient FWI, we anticipate that this approach will eventually make FWI as affordable as travel time tomography.

One of the main limitations of the method is the domain extent. For a trained neural operator, the function is defined on a fixed domain extent (e.g. it could be a unit cube). We can evaluate at a different grid size but cannot change the extent. We are now working on an extension of the work, where we recursively predict the wavefield. Through this way, a trained neural operator is essentially taking the first few time steps as input and then output the next few time steps, and there will be no need for retraining.

The scalability of evaluation using a trained neural operator with respect to the grid size and the number of time steps is a little different from conventional FDM. Assuming the original dimension is (Nx_1, Ny_1, Nt_1), where Nx_1, Ny_1 are the number of grids in the x and y domain, respectively, and Nt_1 is the number of time steps. If the new dimension is (Nx_2, Ny_2, Nt_2), the memory becomes $\frac{Nx_2 \cdot Ny_2 \cdot Nt_2}{Nx_1 \cdot Ny_1 \cdot Nt_1}$ times the original memory, which is consistent with the FDM. In the example presented in this paper, evaluation using U-NO takes 3 times the GPU memory of the FDM approach, and this scaling should be consistent with increasing grid points. In terms of computational cost, the majority of it for UNO is on the Fourier transform and its inverse. The computational cost of fast Fourier transform with dimension (Nx_1, Ny_1, Nt_1) is proportional to $Nx_1 \cdot Ny_1 \cdot Nt_1 \cdot \log(Nx_1 \cdot Ny_1 \cdot Nt_1)$, and therefore, the new computational time becomes $\frac{Nx_2 \cdot Ny_2 \cdot Nt_2 \cdot \log(Nx_2 \cdot Ny_2 \cdot Nt_2)}{Nx_1 \cdot Ny_1 \cdot Nt_1 \cdot \log(Nx_1 \cdot Ny_1 \cdot Nt_1)}$ times the original computational time. This scaling is slightly higher than that of FDM, however, considering the 60 times acceleration in the example presented in this paper, UNO evaluation on an increased dimension of 1024*1024*1024 should still have ~40 times the acceleration.

The most compute- and memory-intensive part of the UNO method is the one-time training process. The cost of training for the 2D case is tractable on a single GPU. For the extension from 2D to 3D modeling, the computation and memory will increase due to the larger dataset and the larger number of parameters to learn. Therefore, the next step is to enhance data compression and parallelization to accelerate the training process and reduce the storage. Since this is a learning-based approach, the model performance can be improved by fine-tuning the model parameters and increasing the size of the training dataset. More importantly, any future advancements made in neural operator model architectures will be able to be directly incorporated into the system as they occur. For example, the improvement from linear layers of FNO to U-NO enables faster training convergence. As a result, we should only take current performance metrics as a starting point.

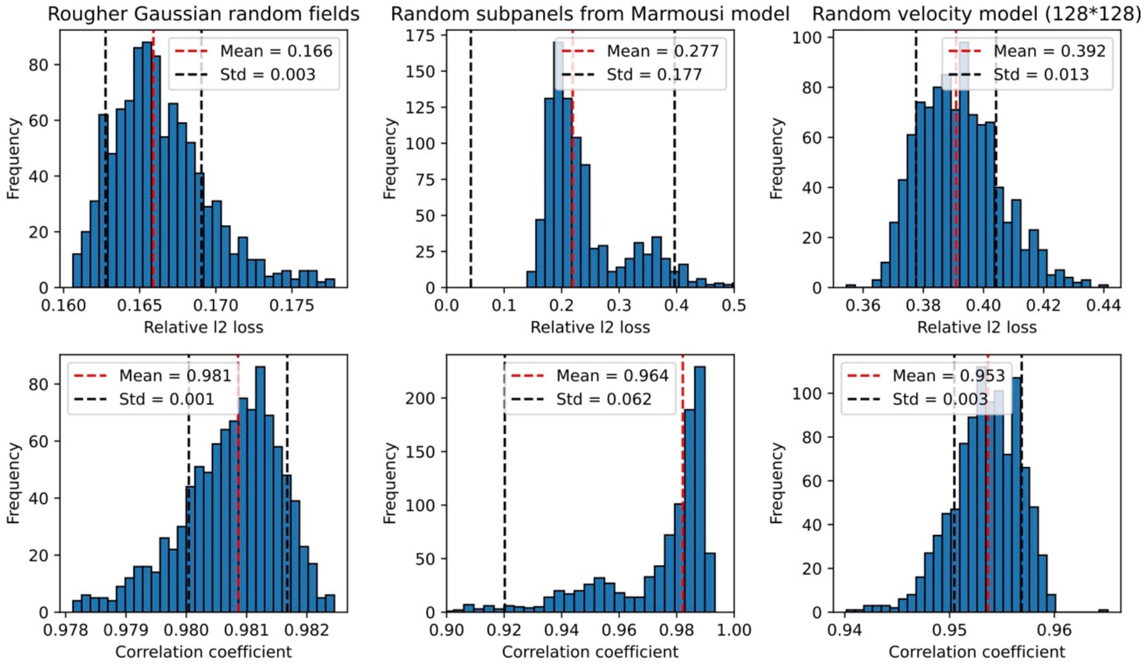

Figure 10.7: Output evaluation. Distribution of Relative L2 loss (top) and correlation coefficient (bottom) between the U-NO predictions and ground truth. From left to right, the columns are corresponding to the experiments in Figure 10.3, 5, 6. The red and black dashed lines mark the mean and standard deviation of the histograms.

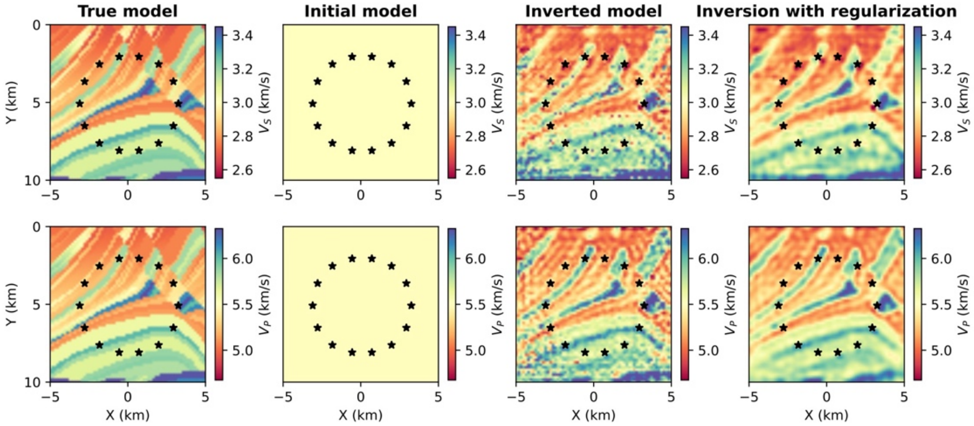

Figure 10.8: Full waveform inversion. The inversion for a random subpanel from the Marmousi model. 14 sources are placed in a ring shape (black stars) and receivers are placed at every node of the 64*64 grid. From left to right, the columns represent true velocity model,

initial model for inversion, inverted model without regularization, and inverted model with 0th and 1st order Tikhonov regularization. The top and bottom rows are the models for Vs and Vp, respectively.

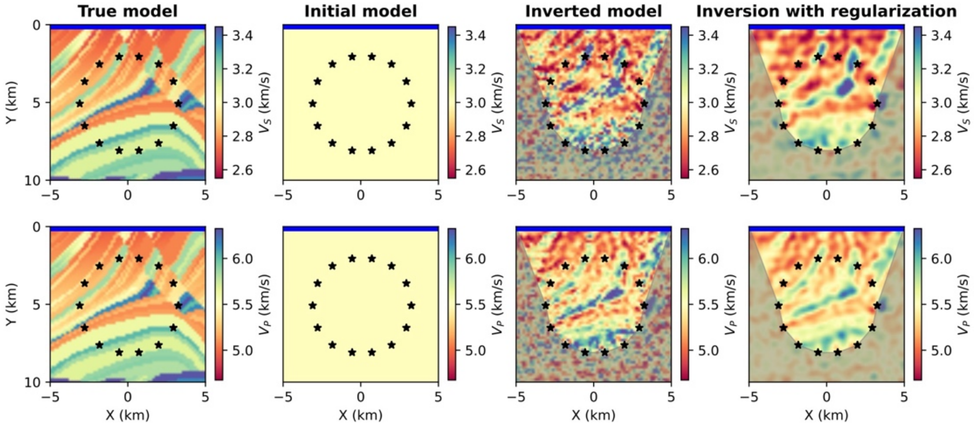

Figure 10.9: Full waveform inversion. Same as Figure 10.8, but the receivers are only placed on the 64 grids on the surface (blue line on the top of each subpanel). The gray shaded areas mask the areas without ray path coverage.

Supplementary Material

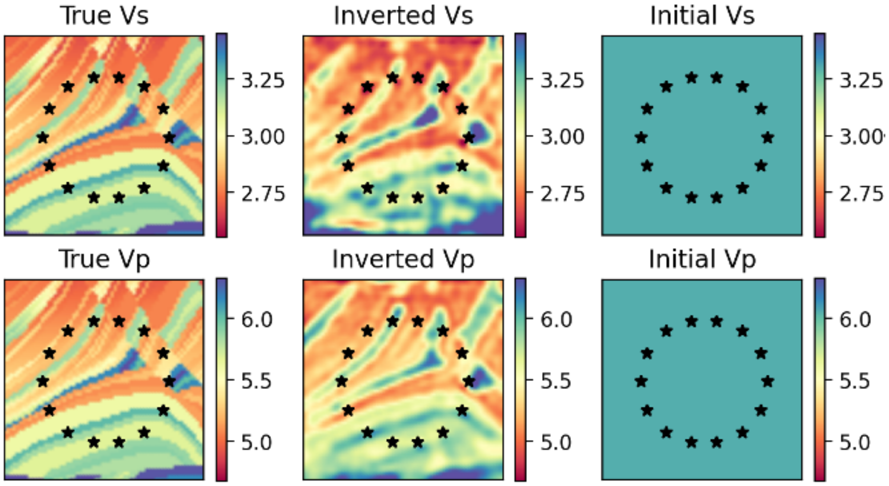

Figure 10.S1: Full-waveform inversion example. The true model is the same as Figure 10.8 in the main text but we use an initial model with homogeneous velocity 10% higher than the average value of the true model for inversion. The misfit curve of the inversion is shown in the lower right panel.

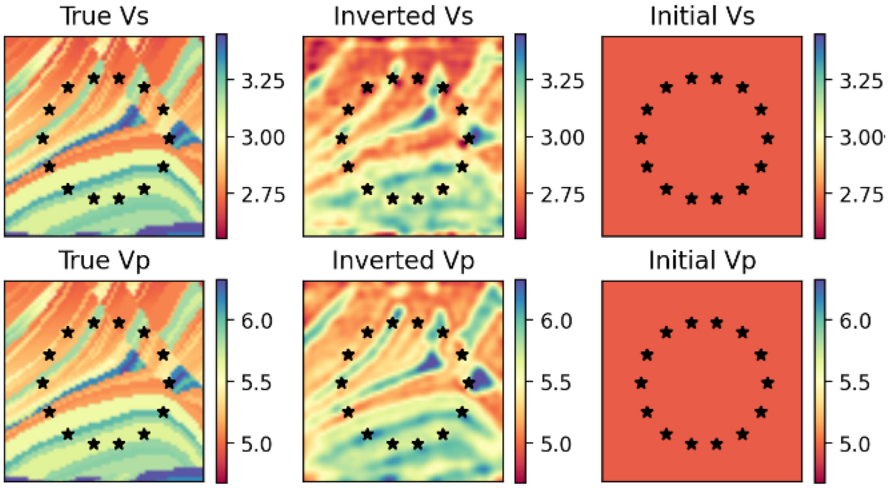

Figure 10.S2: Same as Figure 10.S1 but for an initial model with homogeneous velocity 10% lower than the average value of the true model.

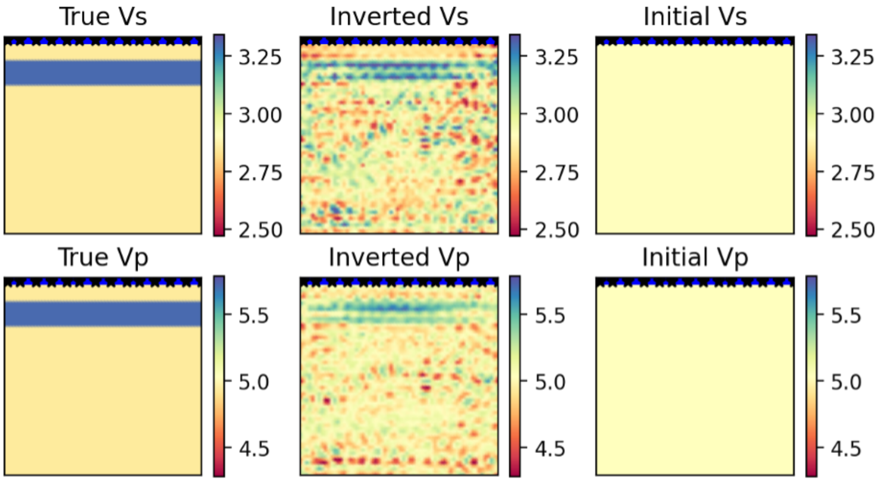

Figure 10.S3: Full-waveform inversion example. The true model is the same as Figure 10.8 in the main text but we use an initial model with homogeneous velocity 10% higher than the average value of the true model for inversion. The misfit curve of the inversion is shown in the lower right panel.

References

Bhattacharya, K., Hosseini, B., Kovachki, N. B., & Stuart, A. M. (2020). Model Reduction and Neural Networks for Parametric PDEs. *SMAI Journal of Computational Mathematics*, *7*, 121–157. https://doi.org/10.48550/arxiv.2005.03180

Birnie, C., Ravasi, M., Liu, S., & Alkhalifah, T. (2021). The potential of self-supervised networks for random noise suppression in seismic data. *Artificial Intelligence in Geosciences*, *2*, 47–59. https://doi.org/10.1016/j.aiig.2021.11.001

Brocher, T. M. (2005). Empirical Relations between Elastic Wavespeeds and Density in the Earth's Crust. *Bulletin of the Seismological Society of America*, *95*(6), 2081–2092. https://doi.org/10.1785/0120050077

Fichtner, A., Kennett, B. L. N., Igel, H., & Bunge, H. P. (2009). Full seismic waveform tomography for upper-mantle structure in the Australasian region using adjoint methods. *Geophysical Journal International*, *179*(3), 1703–1725. https://doi.org/10.1111/J.1365-246X.2009.04368.X

Fichtner, A., Igel, H., Bunge, H. P., & Kennett, B. L. N. (2009). Simulation and inversion of seismic wave propagation on continental scales based on a spectral-element method. *Journal of Numerical Analysis, Industrial and Applied Mathematics*, *4*(1–2), 11–22.

Gebraad, L., Boehm, C., & Fichtner, A. (2020). Bayesian Elastic Full-Waveform Inversion Using Hamiltonian Monte Carlo. *Journal of Geophysical Research: Solid Earth*, *125*(3). https://doi.org/10.1029/2019JB018428

Graves, R., & Pitarka, A. (2016). Kinematic ground-motion simulations on rough faults including effects of 3D stochastic velocity perturbations. *Bulletin of the Seismological Society of America*, *106*(5), 2136–2153. https://doi.org/10.1785/0120160088

Graves, R. W., & Pitarka, A. (2010). Broadband ground-motion simulation using a hybrid approach. *Bulletin of the Seismological Society of America*, *100*(5 A), 2095–2123. https://doi.org/10.1785/0120100057

Hendrycks, D., & Gimpel, K. (2016). Gaussian Error Linear Units (GELUs). https://doi.org/10.48550/arxiv.1606.08415

Igel, H., Nissen-Meyer, T., & Jahnke, G. (2002). Wave propagation in 3D spherical sections: effects of subduction zones. *Physics of the Earth and Planetary Interiors*, *132*(1–3), 219–234. https://doi.org/10.1016/S0031-9201(02)00053-5

Jiang, P., Meinert, N., Jordão, H., Weisser, C., Holgate, S., Lavin, A., et al. (2021). Digital Twin Earth – Coasts: Developing a fast and physics-informed surrogate model for coastal floods via neural operators. https://doi.org/10.48550/arxiv.2110.07100

Kazei, V., Ovcharenko, O., Plotnitskii, P., Peter, D., Zhang, X., & Alkhalifah, T. (2021). Mapping full seismic waveforms to vertical velocity profiles by deep learning. *GEOPHYSICS*, *86*(5), R711–R721. https://doi.org/10.1190/geo2019-0473.1

Kelly, K. R., Ward, R. W., Treitel, S., & Alford, R. M. (1976). Synthetic seismograms: a finite -difference approach. *GEOPHYSICS*, *41*(1), 2–27. https://doi.org/10.1190/1.1440605

Kingma, D. P., & Ba, J. L. (2014). Adam: A Method for Stochastic Optimization. *3rd International Conference on Learning Representations, ICLR 2015 - Conference Track Proceedings*. https://doi.org/10.48550/arxiv.1412.6980

Komatitsch, D., & Tromp, J. (2002a). Spectral-element simulations of global seismic wave propagation-I. Validation. *Geophysical Journal International*, *149*(2), 390–412. https://doi.org/10.1046/j.1365-246X.2002.01653.x

Komatitsch, D., & Tromp, J. (2002b). Spectral-element simulations of global seismic wave propagation-II. Three-dimensional models, oceans, rotation and self-gravitation. *Geophysical Journal International*, *150*(1), 303–318. https://doi.org/10.1046/j.1365-246X.2002.01716.x

Kovachki, N., Li, Z., Liu, B., Azizzadenesheli, K., Bhattacharya, K., Stuart, A., & Anandkumar, A. (2021). *Neural Operator: Learning Maps Between Function Spaces* (No. arXiv:2108.08481). arXiv. Retrieved from http://arxiv.org/abs/2108.08481

Li, D., Helmberger, D., Clayton, R. W., & Sun, D. (2014). Global synthetic seismograms using a 2-D finite-difference method. *Geophysical Journal International*, *197*(2), 1166–1183. https://doi.org/10.1093/gji/ggu050

Li, Z., Kovachki, N., Azizzadenesheli, K., Liu, B., Bhattacharya, K., Stuart, A., & Anandkumar, A. (2020a). Fourier Neural Operator for Parametric Partial Differential Equations. https://doi.org/10.48550/arxiv.2010.08895

Li, Z., Kovachki, N., Azizzadenesheli, K., Liu, B., Bhattacharya, K., Stuart, A., & Anandkumar, A. (2020b). Multipole Graph Neural Operator for Parametric Partial Differential Equations. *Advances in Neural Information Processing Systems*, *2020-December*. https://doi.org/10.48550/arxiv.2006.09535

Li, Z., Kovachki, N., Azizzadenesheli, K., Liu, B., Bhattacharya, K., Stuart, A., & Anandkumar, A. (2020c). Neural Operator: Graph Kernel Network for Partial Differential Equations. https://doi.org/10.48550/arxiv.2003.03485

Liu, Q., & Gu, Y. J. (2012). Seismic imaging: From classical to adjoint tomography. *Tectonophysics*, *566–567*, 31–66. https://doi.org/10.1016/J.TECTO.2012.07.006

Lu, L., Jin, P., & Karniadakis, G. E. (2019). DeepONet: Learning nonlinear operators for identifying differential equations based on the universal approximation theorem of operators. *Nature Machine Intelligence*, *3*(3), 218–229. https://doi.org/10.1038/s42256-021-00302-5

Mai, P. M., & Beroza, G. C. (2002). A Spatial Random Field Model to Characterize Complexity in Earthquake Slip. *Journal of Geophysical Research: Solid Earth*, *107*(B11), ESE 10-1-ESE 10-21. https://doi.org/10.1029/2001JB000588

Moseley, Ben, Nissen-Meyer, T., & Markham, A. (2020). Deep learning for fast simulation of seismic waves in complex media. *Solid Earth*, *11*(4), 1527–1549. https://doi.org/10.5194/SE-11-1527-2020

Moseley, Ben, Markham, A., & Nissen-Meyer, T. (2021). Finite Basis Physics-Informed Neural Networks (FBPINNs): a scalable domain decomposition approach for solving differential equations. Retrieved from http://arxiv.org/abs/2107.07871

Moseley, Benjamin, Markham, A., & Nissen-Meyer, T. (2018). Fast approximate simulation of seismic waves with deep learning. Retrieved from http://arxiv.org/abs/1807.06873

Mousavi, S. M., Ellsworth, W. L., Zhu, W., Chuang, L. Y., & Beroza, G. C. (2020). Earthquake transformer—an attentive deep-learning model for simultaneous earthquake detection and phase picking. *Nature Communications*, *11*(1), 1–12. https://doi.org/10.1038/s41467-020-17591-w

Nakata, N., & Beroza, G. C. (2015). Stochastic characterization of mesoscale seismic velocity heterogeneity in Long Beach, California. *Geophysical Journal International*, *203*(3), 2049–2054. https://doi.org/10.1093/gji/ggv421

Olsen, K. B. (2000). Site Amplification in the Los Angeles Basin from Three-Dimensional Modeling of Ground Motion. *Bulletin of the Seismological Society of America*, *90*(6B), S77–S94. https://doi.org/10.1785/0120000506

Pathak, J., Subramanian, S., Harrington, P., Raja, S., Chattopadhyay, A., Mardani, M., et al. (2022). FourCastNet: A Global Data-driven High-resolution Weather Model using Adaptive Fourier Neural Operators. https://doi.org/10.48550/arxiv.2202.11214

Pell, O., Bower, J., Dimond, R., Mencer, O., & Flynn, M. J. (2013). Finite-Difference Wave Propagation Modeling on Special-Purpose Dataflow Machines. *IEEE Transactions on Parallel and Distributed Systems*, *24*(5), 906–915. https://doi.org/10.1109/TPDS.2012.198

Rahman, M. A., Ross, Z. E., & Azizzadenesheli, K. (2022). U-NO: U-shaped Neural Operators. https://doi.org/10.48550/arxiv.2204.11127

Rasht-Behesht, M., Huber, C., Shukla, K., & Karniadakis, G. E. (2022). Physics-Informed Neural Networks (PINNs) for Wave Propagation and Full Waveform Inversions. *Journal of Geophysical Research: Solid Earth*, *127*(5), 1–21. https://doi.org/10.1029/2021jb023120

Rodgers, A. J., Pitarka, A., Anders Petersson, N., Sjogreen, B., McCallen, D. B., & Abrahamson, N. (2019). Broadband (0-5 Hz) fully deterministic 3D ground-motion simulations of a magnitude 7.0 Hayward fault earthquake: Comparison with empirical ground-motion models and 3D path and site effects from source normalized intensities. *Seismological Research Letters*, *90*(3), 1268–1284. https://doi.org/10.1785/0220180261

Ronneberger, O., Fischer, P., & Brox, T. (2015). U-net: Convolutional networks for biomedical image segmentation. *Lecture Notes in Computer Science (Including Subseries Lecture Notes in Artificial Intelligence and Lecture Notes in Bioinformatics)*, *9351*, 234–241. https://doi.org/10.1007/978-3-319-24574-4_28/COVER/

Ross, Z. E., Meier, M. A., & Hauksson, E. (2018). P Wave Arrival Picking and First-Motion Polarity Determination With Deep Learning. *Journal of Geophysical Research: Solid Earth*, *123*(6), 5120–5129. https://doi.org/10.1029/2017JB015251

Ross, Z. E., Yue, Y., Meier, M. A., Hauksson, E., & Heaton, T. H. (2019). PhaseLink: A Deep Learning Approach to Seismic Phase Association. *Journal of Geophysical Research: Solid Earth*, *124*(1), 856–869. https://doi.org/10.1029/2018JB016674

Siahkoohi, A., Louboutin, M., & Herrmann, F. J. (2019). Neural network augmented wave-equation simulation. https://doi.org/10.48550/arxiv.1910.00925

Smith, J. D., Azizzadenesheli, K., & Ross, Z. E. (2021). EikoNet: Solving the Eikonal Equation with Deep Neural Networks. *IEEE Transactions on Geoscience and Remote Sensing*, *59*(12), 10685–10696. https://doi.org/10.1109/TGRS.2020.3039165

Sun, B., & Alkhalifah, T. (2020). ML-descent: An optimization algorithm for full-waveform inversion using machine learning. *GEOPHYSICS*, *85*(6), R477–R492. https://doi.org/10.1190/geo2019-0641.1

Tape, C., Liu, Q., Maggi, A., & Tromp, J. (2009). Adjoint tomography of the southern california crust. *Science*, *325*(5943), 988–992. https://doi.org/10.1126/SCIENCE.1175298

Versteeg, R. (2012). The Marmousi experience: Velocity model determination on a synthetic complex data set. *Https://Doi.Org/10.1190/1.1437051*, *13*(9), 927–936. https://doi.org/10.1190/1.1437051

Wen, G., Li, Z., Azizzadenesheli, K., Anandkumar, A., & Benson, S. M. (2022). U-FNO—An enhanced Fourier neural operator-based deep-learning model for multiphase flow. *Advances in Water Resources*, *163*, 104180. https://doi.org/10.1016/J.ADVWATRES.2022.104180

Yang, L., Liu, X., Zhu, W., Zhao, L., & Beroza, G. C. (2022). Toward improved urban earthquake monitoring through deep-learning-based noise suppression. *Science Advances*, *8*(15), 3564. https://doi.org/10.1126/SCIADV.ABL3564/SUPPL_FILE/SCIADV.ABL3564_MOVIES_S1_AND_S2.ZIP

Yang, Y., Gao, A. F., Castellanos, J. C., Ross, Z. E., Azizzadenesheli, K., & Clayton, R. W. (2021). Seismic Wave Propagation and Inversion with Neural Operators. *The Seismic Record*, *1*(3), 126–134. https://doi.org/10.1785/0320210026

Zhang, X., & Curtis, A. (2021). Bayesian Geophysical Inversion Using Invertible Neural Networks. *Journal of Geophysical Research: Solid Earth*, *126*(7), e2021JB022320. https://doi.org/10.1029/2021JB022320

Zhu, W., & Beroza, G. C. (2019). PhaseNet: A deep-neural-network-based seismic arrival-time picking method. *Geophysical Journal International*, *216*(1), 261–273. https://doi.org/10.1093/gji/ggy423

Zhu, W., Mousavi, S. M., & Beroza, G. C. (2019). Seismic Signal Denoising and Decomposition Using Deep Neural Networks. *IEEE Transactions on Geoscience and Remote Sensing*, *57*(11), 9476–9488. https://doi.org/10.1109/TGRS.2019.2926772

Zhu, W., Xu, K., Darve, E., & Beroza, G. C. (2021). A general approach to seismic inversion with automatic differentiation. *Computers & Geosciences*, *151*, 104751. https://doi.org/10.1016/J.CAGEO.2021.104751

Zhu, W., Tai, K. S., Mousavi, S. M., Bailis, P., & Beroza, G. C. (2022). An End-To-End Earthquake Detection Method for Joint Phase Picking and Association Using Deep Learning. *Journal of Geophysical Research: Solid Earth*, *127*(3), 1–13. https://doi.org/10.1029/2021JB023283

Chapter 11

CONCLUSIONS

In this thesis, I aim to better understand the near surface structure and dynamics through dense seismic observation. Sharing this common thread, I present a diverse range of case studies: utilizing DAS, seismometers, and accelerometers; ambient noise, active surveys, and earthquakes, in both urban and glacial settings. Beyond observation, I introduce advanced data processing and analysis techniques to effectively handle the large volumes of data collected. The key insights from each study are as follows.

In Chapter 2, I develop a Python tool for seismic ambient noise analysis with DAS, leveraging PyTorch for computational efficiency. The significant acceleration achieved through GPU utilization underscores the potential of our approach in data-intensive seismology tasks. The challenges of data transfer and I/O operations in large DAS datasets emphasize the need for strategic data management and the potential benefits of cloud computing in future seismological studies. As the field progresses, such Python tools will be pivotal, offering a balance between computational efficiency for experts and versatility for beginners, ensuring that researchers can effectively tackle the complexities of modern seismological data.

In Chapter 3, I demonstrate that DAS-based noise tomography can capture subsurface structural heterogeneities that cause ground shaking variability at sub-kilometer scales. Such fine-scale seismic hazard microzonation can significantly improve urban seismic risk management. Although the physics linking the shallow structure and site amplification quantitatively requires further investigation, the observation reported here highlights the potential of DAS for high-resolution urban seismic hazard mapping as an efficient and inexpensive tool.

In Chapter 4, I report clear surface wave scattering in noise cross-correlation functions including scattered coda waves and spurious arrivals that do not exist in true Green's functions. The travel times and amplitudes of the scattered waves are used to map the faults and to characterize the geometry and velocity reduction of the mapped faults. These results suggest a viable application of DAS for refining prior fault maps or imaging hidden faults at top 100 meters at high lateral resolution in urban areas.

In Chapter 5, I demonstrate the viability of fiber-seismic sensing for monitoring high-resolution vadose zone soil moisture dynamics at high spatiotemporal resolution. Future work involving direct in-situ measurements for different soil types and regional scale modeling will increase the robustness of the inverted vadose zone soil moisture dynamics. Given the escalated regional drought risk under climate change, our findings highlight the promise of fiber-optic seismic sensing as a large-scale, long-term and cost-effective observational tool to enhance our climate resilience in semi-arid regions.

In Chapter 6, I derive a new empirical relation between density and P- and S-wave velocities for the low precipitation and cold polar firn regime using a DAS array at the South Pole. This refined firn model represents an improvement over previous empirical relationships for this site, effectively reducing the underestimation of firn air content. The new relation may be applicable to extensive regions of the Antarctic Plateau and interior Antarctica with comparable environmental conditions. This study, more generally, highlights the effectiveness and future potential of fiber-optic sensing technology in glacial seismology.

In Chapter 7, I map the depth of the LA basin using basin converted phases recorded by two urban dense seismic arrays. The mapping offers independent constraints that supplement previous seismic tomography, receiver function, and gravity surveys. The results indicate that a substantial part of the central LA Basin is deeper than previously estimated. This improved depth mapping enhances our understanding of the basin's geological structure and contributes to better seismic hazard assessments.

In Chapter 8, I use three dense urban exploration seismic networks in the Long Beach area to detect and locate local seismicity. The results support the previous conclusion that the Newport-Inglewood fault is a wide splayed fault in this area. The seismicity pattern also compares well with some newly identified faults from reflection seismic surveys. The shallow events call for attention on the potential shallow seismicity-related hazard.

In Chapter 9, I present a prototype framework for applying neural operators to the 2D acoustic wave equation. By training on an ensemble of simulations with random velocity models and source locations, the neural operator can efficiently compute solutions for any velocity structure or source location. The differentiable nature of the neural operator also facilitates full waveform inversion. Building on this, in Chapter 10, I extend the work to 2D elastic wave equation using a U-shaped neural operator. Not surprisingly, full waveform modeling with neural operators is nearly two orders of magnitude faster than conventional numerical methods. The trained model enables accurate simulation for velocity models, source locations, and mesh discretization distinctly different from the training dataset. Its easily accessible gradients allow for convenient and robust full waveform inversion for complex geological model despite of the initial model. Since this is a learning-based approach, the model performance can be improved by fine-tuning the model parameters and increasing the size of the training dataset. More importantly, any future advancements made in neural operator model architectures will be able to be directly incorporated into the system. Despite these advancements, this approach is in its early stages. Enhancing computational capabilities, incorporating more geophysical parameters, and testing models on real-world seismic data are necessary next steps.